Nanomaterials

Edited by
D CHAKRAVORTY

NANOMATERIALS
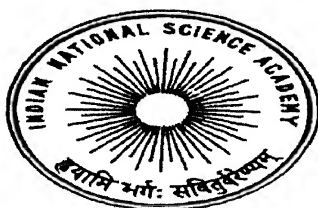
NANOMATERIALS

Edited by

Professor D Chakravorty, FNA

INDIAN NATIONAL SCIENCE ACADEMY
NEW DELHI

NANOMATERIALS   *Edited by:* D. CHAKRAVORTY

Price: Rs. 400/-   US $ 50/-

EDITOR'S REMARKS

"Nanomaterials" has become an exciting area of modern research, because of the special properties this class of materials possess and the great technological applications they promise. Therefore, Indian National Science Academy is pleased to bring out this special volume on "Nanomaterials".

The present volume covers a wide range of topics, *viz.* synthesis, structure and applications. I am indebted to the authors who have contributed to this volume and specially Professor D Chakravorty, who has taken great pains to edit this volume after collecting the articles from several scientists. I am really grateful to Professor S K Malik, who during his tenure as Editor, PINSA-A, conceived the idea for such a volume and requested Professor Chakravorty to take up this responsibility. Lastly, I would like to thank our editorial staff, Mr A K Tagore and Mr M Ranganathan, for their valuable editorial/production assistance for bringing out this publication.

N Satyamurthy
Editor, PINSA-A

PREFACE

Nanomaterials has become an area of intense research activities during the last decade. With particle size in such systems generally ranging from 1 to 100 nm, their physical properties neither correspond to those of free atoms or molecules making up the particle nor to those of the bulk solids having identical chemical composition. Materials with such a structure in the nanometre scale are characterized by large surface to volume ratio implying that a major fraction of atoms reside at the grain boundary. Because of the ultrafine dimensions, the physical properties are dominated by quantum mechanical effects. As a consequence, novel properties are expected and have been found in several systems of such nanostructural characteristics. With a well developed non fabrication ability, the researcher can now conceive of new structures in this dimensional domain and thereby general novel quantum mechanical properties. This also opens up a fascinating new realm of fundamental physics. Nanomaterials, therefore, provide challenging opportunities for physicists, chemists, materials scientists and engineers to contribute to the development of nano electron devices and a myriad of sensor systems. It is expected that nanomaterials will play a dominant role in device technology in the next few decades.

The present volume is a modest effort to focus for the general researcher some of the basic aspects of preparation and properties of nanostructured materials. The authors are experts in this field. They review different aspects of this subject in the articles of this volume. The first three papers (S K pabi *et al.*; A Gupta; P Pramanik *et al.*) deal with the synthesis of nanocrystalline materials, *viz.*, by mechanical attrition of metals and alloys, by controlled crystallization of amorphous alloys and by chemical methods for ultrafine oxides. The fourth paper (by P Ayyub) examines the effect of particle size (in the nanometre scale) on the ferroelectric properties of conventional titanates. The fifth one (by S Ramasamy *et al.*) delineates the electrical properties of nanostructured materials synthesized by various methods. The sixth article (by S N Sahu *et al.*) discusses the theoretical aspects of nanocrystalline semiconductors and examines their possible applications. The seventh paper (by A K Pal *et al.*) reviews the absorption and photoluminescence phenomena in nanocrystalline ZnS and ZnSe materials.

I take this opportunity to thank all the authors for their efforts in writing the review papers. I also thank Professor S K Malik and Professor N Sathyamurthy for their help and support in bringing out this Special Volume on Nanomaterials.

D Chakravorty
Guest Editor
Special Volume on
"Nanomaterials"

CONTENTS

MECHANISM AND KINETICS OF ALLOYING AND NANOSTRUCTURE FORMATION BY MECHANICAL METHODS

S K PABI, J JOARDAR AND B S MURTY*

Department of Metallurgical and Materials Engineering, Indian Institute of Technology, Kharagpur-721 302 (India)

Nanocrystalline materials have become a subject of both scientific and industrial importance in the past one decade. The present paper reviews the work being carried out world over, on the synthesis of nanocrystalline metals, alloys, intermetallics and nanocomposites by mechanical means, in particular, by high energy ball milling process. Many high melting intermetallics, that are difficult to prepare by conventional processing techniques, could be easily synthesized in nanocrystalline state with homogeneous structure and composition by this route. The present understanding of the nature of these materials and the phase transitions induced during nanocrystallization are critically reviewed in the present paper.

Key Words: Nanocrystalline Materials; Nanocomposites; High Energy Ball Milling; Nanocrystalline Intermetallic Compounds; Mechanical Alloying; Mechanical Milling; Devitrification; Plastic Deformation

1 Introduction

Nanocrystalline materials (NCM) are solids composed of crystallites with characteristic size (at least on one dimension) of a few nanometers. The discovery of these materials by Gleiter[1] can be viewed as one of the most fascinating ones of the past decade. The importance of these materials can be easily gauged by the launch of the International Journals like Nanostructured Materials and Nanotechnology even when the field is in its infancy. A biannual International Conference Series on these materials has been launched in 1992 and the fifth one in the series is scheduled in 2000[2-6]. The importance of the field can be recognized by the large number of international conferences being held regularly on nanophase materials[7-17]. Various aspects of these materials have been reviewed by a number of investigators[1,18-25].

The NCMs can be zero (clusters), one (lamellar), two (filamentary) or three (equiaxed particles)-dimensional in nature (Fig. 1)[26,27] and can be obtained by a number of techniques as shown in Table I. These are the materials characterized by a large volume fraction of grain boundaries as shown schematically in Fig. 2. The fraction of atoms associated with the boundaries, C is given by $C=3t/d$, where t is the thickness of the boundary and d is the diameter of the nanocrystal. Thus, the volume fraction of atoms at the grain boundaries can be of the order of 50% for 5 nm grains and a mere 3% for 100nm grains (Fig. 3). A number of physical and mechanical properties of materials are significantly altered in the nanocrystalline state as shown in Table II[28]. Nanostructured materials can be synthesized starting from vapour (inert gas condensation, sputtering, plasma processing, vapour deposition), liquid (electrodeposition, rapid solidification) and solid state (high energy ball milling, sliding wear, spark erosion). Among the solid state techniques, high energy ball milling has become quite popular in recent years due to its simplicity, low capital cost, higher productivity and scalability (Table III). The synthesis of NCM by the mechanical routes (high energy ball milling, sliding wear, spark erosion, cold rolling as well as devitification of mechanically induced amorphous phases) will be reviewed in the present paper.

High energy ball milling technique has been developed in 1966 by Benjamin and his co-workers[29] at the INCO's Paul D Merica Research Laboratory as a part of the programme to produce oxide dispersion strengthened (ODS) Ni-base superalloys for gas turbine applications. NCMs can be synthesized either by high energy ball milling of elemental blends (known as mechanical alloying (MA)) or that of individual

Present Address: National Research Institute for Metals, Tsukuba 305-0047, Japan.
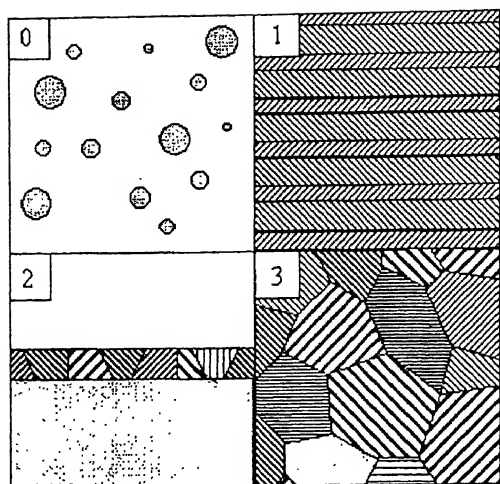
Fig. 1 Schematic of the four types of nanocrystalline materials[27]
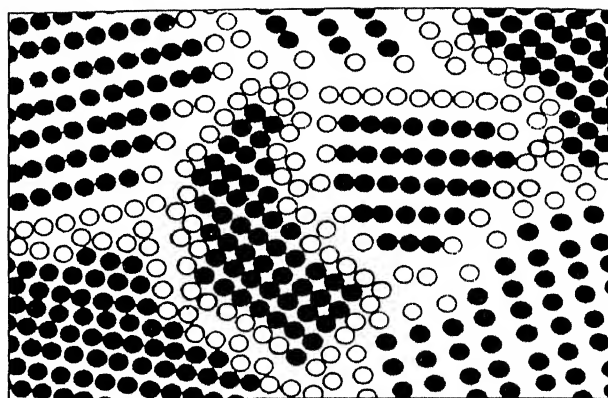
Fig. 2 Schematic representation of equiaxed nanocrystalline metal distinguishing between atoms associated with the individual grains (O) and those constituting grain boundary network (●)[1]

Table I

Classification of Nanocrystalline Materials

Dimensionality	Designation	Typical method(s) of synthesis
Three	Crystallites (equiaxed)	Gas condensation, mechanical alloying
Two	Filamentary	Chemical vapour deposition
One	Layered (lamellar)	Vapour deposition, electrode position
Zero	Clusters	Sol-gel method

Table II

Changes in the Properties in the Nanocrystalline State

Property	Change in the nanocrystalline state
Electrical	Higher conductivity in ceramics and magnetic nanocomposites
	Higher resistivity in metals
Magnetic	Increase in coercivity until a critical size
	Decrease in coercivity below a critical size leading to superparamagnetic behaviour
Mechanical	Increase in strength and hardness in metals and alloys
	Enhanced ductility, toughness and formability in ceramics and intermetallics
Optical	Blue shift of optical spectra in quantum-confined crystallites
	Increase in luminescent efficiency of semiconductors

Table III

Comparative Evaluation of MIGC, HEBM, Spray Conversion and Sol-Gel Methods (adopted and modified from[33])

| Features	MIGC	HEBM	Spray conversion	Sol gel
Smallest grain size attainable	~2nm	~5nm	~10-20nm	~5nm
Contamination	<1%	High (unless milled with proper media under inert atmosphere)	High	High
Composition control	Sometimes difficult	Very good	Good	Difficult
Process control	Excellent	Good	Difficult	Difficult
Production rate (in laboratory unit)	Low	Good (~2kg/day)	Excellent	Good
Capital expenditure (in Indian Rupees)	>5 million	0.3-1 million	~4 million	~0.2 million
Production cost	High	Low	Low	Low
Possibility of scaling up	Difficult	Easy	Easy	Easy
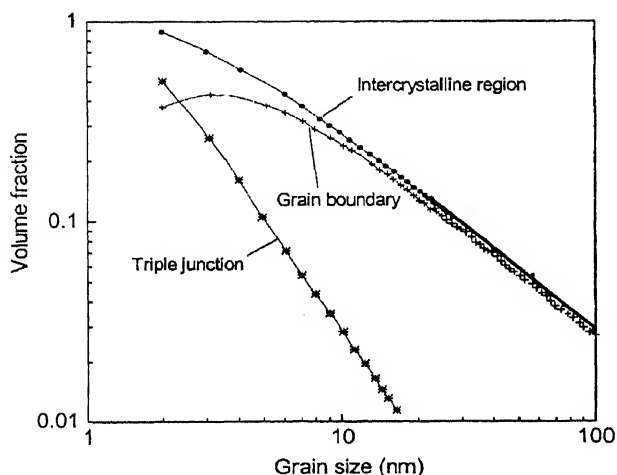
Fig. 3 Estimated volume fraction of grain boundaries, intercrystalline regions and triple junctions at various grain sizes, assuming grain boundary thickness of 1nm[22]

elements, alloys and intermetallics (known as mechanical milling (MM)). The formation NCMs during MA was first suggested by Koch et al.[30]. It was Fecht et al.[31], who have first synthesized elemental nanocrystals by high energy ball milling of their powders of a few micrometers in size. Over the past one decade, nanocrystalline metals, alloys, intermetallics, ceramics and nanocomposites have been synthesized in a number of systems by this technique[32-43]. Nanocrystals have also been synthesized through sliding wear[44], spark erosion[45] and severe plastic deformation[46], though these techniques have not become quite popular. Cold rolling has also been used to synthesize amorphous materials[47-50], that can be devitrified in a controlled fashion to yield nanocrystals.

2 High Energy Ball Milling

2.1 High Energy Ball Mills

MA/MM is usually carried out in high energy mills such as vibratory mills (Spex 8000 mixer/mill), planetary mills (Fritsch and Retsch mills) and attritor mills (Szegvari attritor). The energy transfer to the powder particles in these mills takes place by a shearing action or impact of the high velocity balls with the powder. An attritor was the first high energy ball mill used for MA by Benjamin[29]. The attritor, invented in 1922 by Szegvari for a quick dispersion of fine sulfur particles during the vulcanization of rubber, has a vertical cylindrical tank in which the

powder and balls are charged. The movement of the balls and powder is achieved by the horizontally rotating impellers attached to a vertical shaft (Fig.4a)[32]. Set progressively at right angles to each other, the impellers energizes the grinding balls causing the size reduction of powder by impact. Due to the higher capacity of these attritor mills (Table IV), they are usually preferred in an industry rather than in research laboratories. The tumbler mills (Fig.4b)[32], which are traditionally used in mineral processing can also be used for MA, if their diameters are sufficiently large (of the order of meters) and if mills are operated close to the critical speed beyond which the balls stick to the inner walls of the mill. For large scale production, tumbler mills are more economical when compared to the attritor and other high energy ball mills[56]. Vibratory tube mills[57] are also used for pilot scale production in which a cylindrical container with the powder and ball charge is vibrated.

The laboratory mills, though have smaller capacities[58], offer a higher velocity for the balls[59-61]. Among the laboratory mills, Spex 8000 shaker mill and Fritsch Pulverisette have found wide use. In the Spex mill, most widely used in U.S.A., the vial containing the balls and powder is vibrated in three mutually perpendicular directions with amplitude of 50mm and a frequency of 20Hz. In the Fritsch planetary mill (P5 and P7), commonly used in the European countries, the disc and the vial mounted on the disc rotate in the opposite directions. This gives a centrifugal force to the balls (Fig.4c)[52]. In the basic models (P5 and P7) the speeds of the vial and disc can not be independently varied, however, this has been achieved in the modified versions (G5 and G7)[61-63]. It may be noted that even though the linear velocity of the balls in Fritsch mill is higher than that of Spex mill, the frequency of impacts is much more in the case of the Spex mill[59,60] which makes it a higher energy mill in comparison with the Fritsch mill. Due to the low energies of milling in the case of the attritor, it takes a longer period to achieve alloying when compared to the laboratory mills. It has been shown[64] that alloying in the case of Ti-Mg system takes place after 16h in the Spex mill, while the attritor took 100h to achieve the same result.

The Anutech uni-ball mill is the other high energy ball mill, which has found wide acceptance among the Australian investigators[51,65]. This mill consists
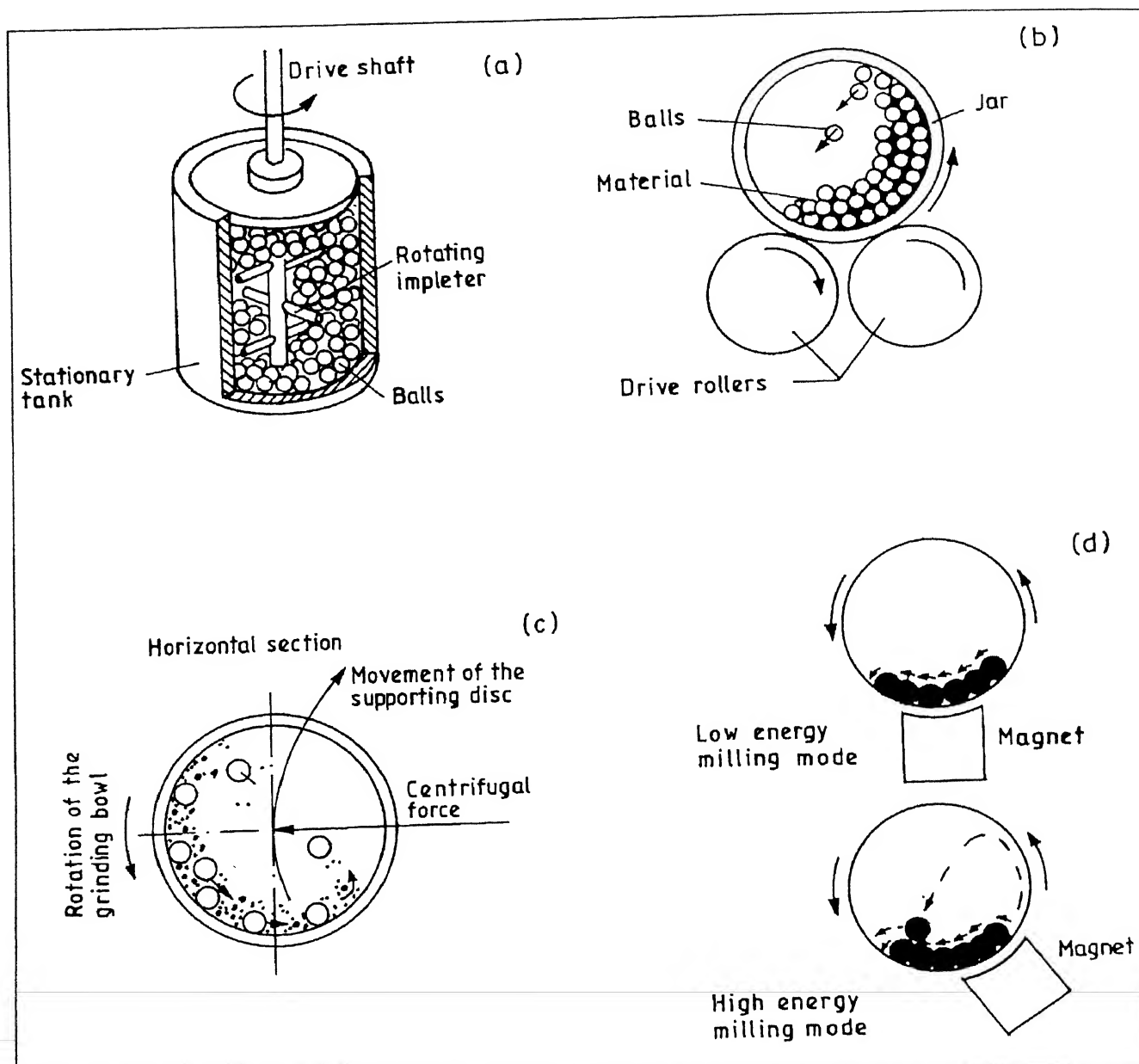
Fig. 4 Schematic of the milling processes in some of the ball mills (a) attritor, (b) tumbler mill, (c) Planetary ball mill (P-5) and (d) uni-ball mill

Table IV

Comparison of Various High Energy Ball Mills

Type of Mill	Capacity[52]	Ball velocity (m/s)	Reference
Mixer Mills	up to 2x20 g	<3.9	53
Planetary Mills	up to 4x250 g	<11.24	54,55
Attritor Mills	0 5-100 kg	<0.8	53
Uni Ball Mill	up to 4x2000 g		

```
                              Power scale
   10^-10        10^-8        10^-6        10^-4        10^-2  (eV/at s)

                        Solid state solicitation
                              Forming
            Conventional tests              High freq.fatigue
         e Van de graf                    Ion implantation
              nuclear reactor              HVEM
                         Ball milling
                            G5
                            G7
                         Pulv. P5
              Spex  6000
                              
              Attritor       Pulv P0
```
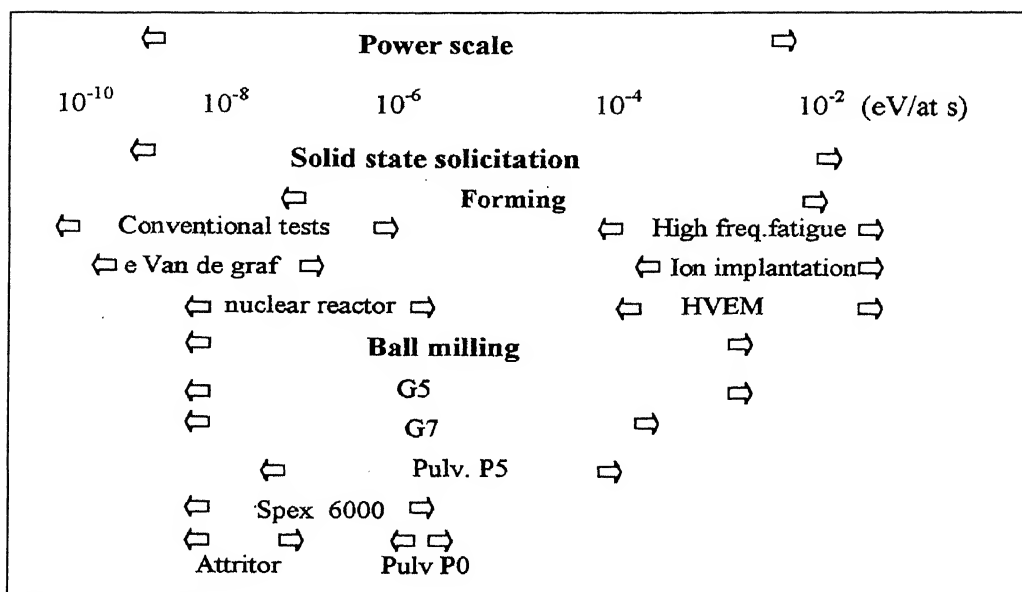
Fig. 5 Injected power levels in various mills[62, 71]

of a stainless steel horizontal cell with hardened steel balls. The movement of balls is confined to the vertical plane by the cell walls and is controlled by external magnetic field, whose intensity and direction can be adjusted. Depending on the position of the magnet, the mill can run in either high energy mode (impact prominent) or in low energy mode (shear prominent) (Fig. 4d)[51]. Another interesting feature of this mill is that the impact velocity and frequency can be independently controlled[51], which is not usually possible in the other mills unless some modifications are incorporated[57,63]. In addition to the above mills, several other mills such as Fritsch pulverisette P0 (single large ball in a vibrating frame mill)[66], rod mill[67], modified rod mill[68] and other specially designed mills[69,70] have been used for MA/MM. The capacities and linear velocities of the balls in various high energy ball mills are compared in Table IV. Fig. 5 compares the injected power levels in various mills[62,71].

2.2 Milling Parameters

Though the ultimate nanocrystalline grain sizes reported by high energy ball mills[72-74] and conventional low energy ball mills[75] are quite similar, the kinetics of nanocrystalline phase formation during MA/MM depend on the energy transferred to the powder ingredients from the balls during milling. The energy transfer is governed by various parameters e.g., the

type/design of the mill, milling speed, type, size and size distribution of the balls, ball to powder weight ratio (BPR), extent of filling of the vial, temperature of milling, grinding media and the milling atmosphere and finally the duration of milling. The kinetic energy of the balls will be higher with higher speeds of milling and with heavier balls (e.g. tungsten carbide (WC) better than steel). Joardar et al.,[76] have recently shown that nanocrystalline NiAl formation and its disordering tendency during MA are enhanced with increasing milling intensity. It has also been reported recently[77], that the reaction rate for the formation of nanocrystalline TiC during MA increases exponentially with the density of the balls. The size and size distribution and the number of the balls should be so chosen as to achieve optimum packing of the vial. Too dense packing of the balls decreases the mean free path of the ball, while loose packing minimizes the collision frequency. BPR of 5 to 10 is widely used and is found to be effective.

2.3 Contamination during Milling

Most of the MA work reported so far has been carried out using stainless steel (SS) or hardened chrome steel (CS) milling media (balls and container). These can introduce large amount of Fe contamination into the milled powder. It has been shown during the synthesis of NiAl from Ni and Al blend using SS milling media that the Fe contamination is to

the tune of about 18at.%[78]. However, with CS milling media (having better wear resistance than SS), the contamination level was ~5at.%[78]. The level of contamination not only depends on the milling media but also on other milling conditions such as the type of mill and milling speed etc. Contamination levels are expected to be more in high energy ball mills such as Spex mill. In order to minimize contamination, less energetic mills such as the vibratory mill may be used[32]. Contamination can be avoided by milling the powders with a milling media made up of the same material as that of the powders being milled[32]. However, the proposal is difficult to put into reality in many cases.

It has been shown recently[78-80] that Fe contamination from milling media can be a blessing in disguise. During the MA of elemental blend of Ni and Al, it was observed that completely disordered (long range order parameter, S=0) nanocrystalline NiAl forms when milled with SS media, while partially ordered (S=0.55) NiAl forms when milled in tungsten carbide[78]. Milling with CS media has resulted in NiAl having an intermediate value of S (0.48)[78]. Fig. 6[81] shows the X-ray diffraction (XRD) patterns of Ni and Al powder mixture of $Al_{75}Ni_{25}$ composition milled in Fritsch Pulverisette (P-5) at 300rpm for 30h using SS and WC milling media. The presence of (100) superlattice reflection of NiAl can be clearly seen (indicated by arrowhead in the figure) in the case of WC, while it is absent when milled in SS. In

recent years, it has been argued that some ductility can be introduced into the otherwise brittle intermetallics by grain refinement[82] and/or by the introduction of disorder[83]. Fe is known to reduce the ordering energy of NiAl[83,84]. Thus, it is not surprising that Fe contamination during milling has resulted in the formation of disordered NiAl[78,81]. The above results suggest that Fe contamination from milling media may be helpful in improving the formability in some otherwise brittle aluminides.

Another example of the usefulness of Fe contamination was observed during MA of Cu-Ni elemental blends[79]. Complete alloying and the formation of solid solution was observed when an elemental blend of $Cu_{50}Ni_{50}$ was milled in Fritsch Pulverisette (P-5) at 300rpm for 20h in SS and CS milling media, while no alloying was observed when milled in WC under identical conditions (Fig. 7)[79]. Interestingly, in the case of CS and SS milling media, the Cu and Ni crystallites reached nanocrystalline state (<20nm) within 10h of milling, while in the case of WC media they remained coarse (>100nm) even after 20h of milling. This could be attributed to the change in the deformation characteristics of Cu and Ni due to Fe contamination during milling in SS and CS media. In fact Pabi et al.,[85] have recently shown that nanocrystallization is a prerequisite for alloying during high energy ball milling at least in slow diffusing systems such as Cu-Ni.
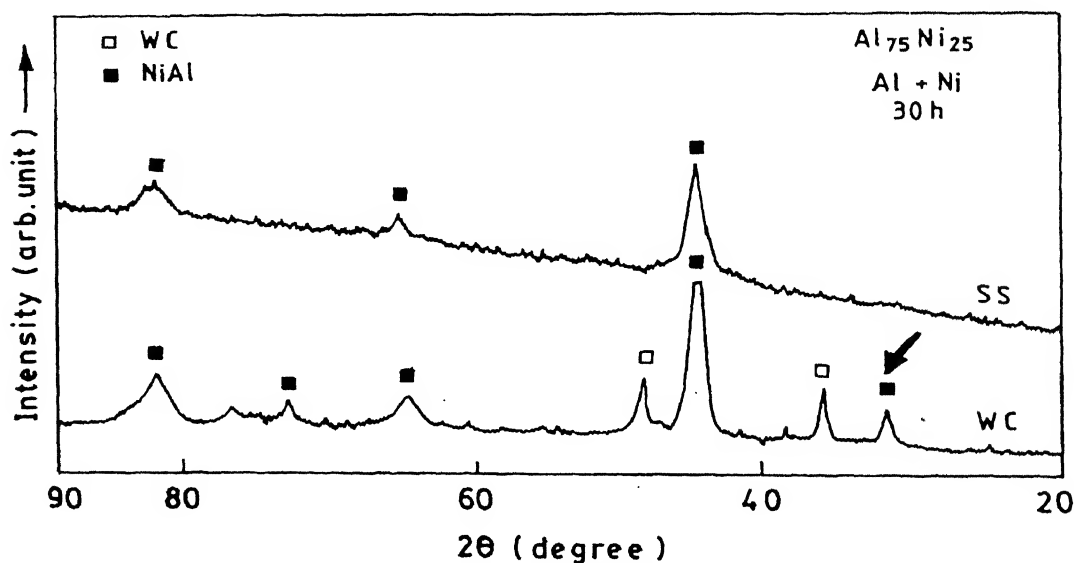

Fig. 6 Influence of WC and SS grinding media on the ordering characteristics of mechanically alloyed NiAl
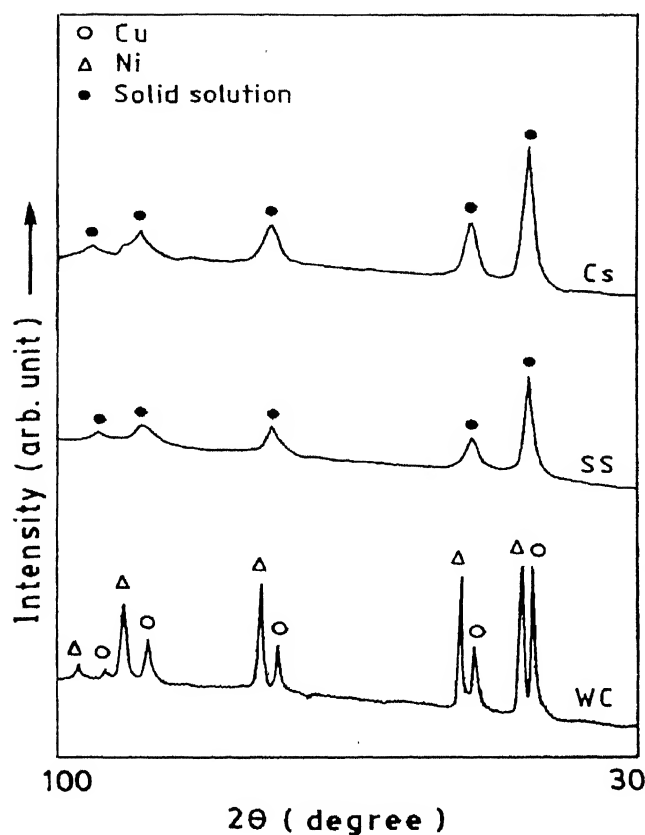
Fig. 7 Influence of grinding media on the alloying, behaviour during MA of $Cu_{50}Ni_{50}$ elemental blend

2.4 Temperature of Milling

High energy ball milling is characterized by repeated cold welding and fragmentation of the ·powder ingredients. The extent of welding and fracturing is decided by the deformation behaviour of the powder and the temperature at the point of ball-powder-ball impact. Thus, the kinetics of nanocrystal formation during milling is expected to be a function of the milling temperature. Indeed the milling time at which a given nanocrystalline grain size was attained in TiNi intermetallic was found to be a function of milling temperature[86]. Shen and Koch[87] have observed smaller crystallite size for Cu and Ni when milled at 188K when compared to those milled at room temperature. The crystallite size of CoZr intermetallic was also smaller at low milling temperature[88]. Milling at subzero temperatures prevents excessive welding, while fracturing is favoured due to the change in the deformation characteristics of the powder[89] at low temperatures.

There have been a number of reports wherein the macroscopic temperature of the mill has been measured. Davis[90] and McDermott[91] have measured the maximum temperature of the Spex mill to be 323K (313K without balls) and concluded that most of the heat comes from motor and bearings. Kimura and Kimura[92] reported a maximum macroscopic temperature of 445K in the attritor. Borzov and Kaputkin[93] have measured a temperature in the range of 373-488K for attritor using SiC and diamond sensors. Substantial temperature rise (120K) is also reported by Kuhn et al.,[53] in vibratory mills. Thus the macroscopic temperature during mill appears to be low and sensitive to the mill design[94,95].

However, the microscopic temperature of the powder just after the impact can be quite high. In fact, Yermakov et al.,[96,97] have attributed amorphization during milling to the local melting and rapid solidification of the powders. As it is not practically feasible to measure the microscopic temperature rise at the point of ball-powder-ball impact during milling, investigators have taken recourse to two approaches for its estimation. One of the approaches being to ascertain it on the basis of appropriate models and the other being to infer from the structural/ microstructural changes during milling. However, there can be large temperature rise due to some exothermic reactions during milling. But this is not considered in these models.

Assuming that particles trapped between colliding balls (head-on collision assumed) deform by localized shear, Schwarz and Koch[55] estimated a microscopic temperature rise of about 40K for $Ni_{32}Ti_{68}$ and $Ni_{45}Nb_{55}$ powders in a Spex mill. Davis and Koch[98] calculated the ball velocities and used the expression and materials of Schwarz and Koch[55] to predict a raise in temperature ΔT of $\leq 112K$. They[98] have also estimated the maximum ΔT to be about 350K. Maurice and Courtney[99] have also developed an expression for the adiabatic temperature rise during milling by modelling the deformation of powder as equivalent to microforging. However, they assumed ΔT to be low such that the material is in the cold working regime. Magini et al.,[100] have also calculated the adiabatic temperature in a planetary mill and reported the maximum temperature to be of the order of 400K after calculating the amount of powder trapped between the balls assuming a Hertzian collision. Bhattacharya and Arzt[101] calculated the contact

temperature of the powder compact surfaces, assuming Hertzian elastic collisions, which are higher (623K) than those calculated by others. However, they show a rapid decrease of the temperature to ambient temperature at the center of the compact. Davis and Koch[98] calculated the ΔT due to sliding friction to be very low ($\leq$10K). Miller et al.,[102] used microsecond time resolved radiometry to observe a temperature rise during impact on various materials. They observed ΔT of the order of about 400K.

In view of the difficulties in modelling of the temperature rise during milling, the microstructural changes occurring during ball milling provides a better alternative for realistic estimation. The observation of deformation bands and slip lines by optical microscopy[103] and the high dislocation densities and deformation bands seen in transmission electron microscopy[104] indicate that the microscopic temperatures are much below the recrystallization temperature. However, in some cases it is reported[92,105] that the temperature is above the crystallization temperature of the amorphous phase. Davis and Koch[97] studied the tempering of martensite in Fe-1.2%C steel during ball milling and concluded that the maximum microscopic temperature to be about 548K. Davis and Koch[98] have also milled Bi powder and concluded that the temperature of milling is below the melting point of Bi (544K). The milling temperature obtained by both calculations and experiments is compiled in Table V. The results suggest that there is only a moderate temperature rise at the point of ball-powder impact during milling, and the possibility of local melting can be ruled out.

3 Nanocrystalline Phases by High Energy Ball Milling

3.1 Nanocrystalline Metals

Nanocrystalline structures were obtained by high energy ball milling of a number of elemental powders such as Cr, Nb, W, Hf, Zr and Co[106], Fe[107,108], Ni[109], Ag[110], Si[111,112] and graphite[113,114]. The crystallite sizes of the nanocrystals obtained by MA/MM are usually calculated from X-ray peak broadening after eliminating the strain and instrumental broadening constituents using standard methods[115,116]. TEM and HREM results have confirmed the nanocrystalline nature of these milled elements[72]. The initial results have shown an indication that the minimum crystallite

Table V
Estimated Temperature Rise (ΔT) during Milling

Method of Estimation	ΔT (K)	Reference
Calculation	$\leq$ 10	98
	40	54
	130	99
	$\leq$ 350	98
	350	101
	400	100
Experimentation	50	90,91
	120	52
	100-215	93
	172	92
	< 271	98
	400	102

size obtained by MM varies inversely with the melting point of the elements. It was argued[106] that in case of elements with low melting points, the tendency for cold welding dominates, resulting in larger crystallite sizes. Very recently, Koch[41] has compiled the minimum crystallite sizes reported so far for various elements by MM (Fig. 8). The figure clearly brings out the fact that for fcc elements having lower melting points (Al, Ag, Cu and Ni) the minimum crystallite size varies inversely with their melting point[74]. However, in case of bcc, hcp elements[72,73] and fcc elements with higher melting points (melting point of Pd)[74], the minimum crystallite size is virtually insensitive to their melting points. Thus, the understanding of the reasons for the minimum crystallite size is presently in a primitive stage. However, the fact that similar crystallite sizes were
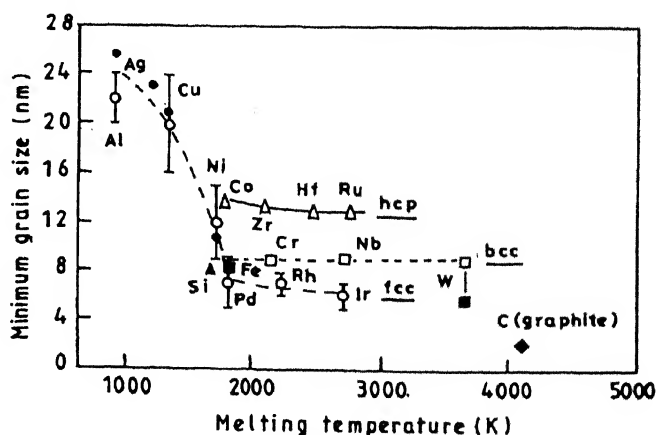

Fig. 8 Effect of melting temperatures on the minimum crystallite sizes of various elements as attained by MM[41]

obtained both in conventional ball mills[75] as well as in the high energy ball mills suggests that it is the total strain, rather than the milling energy, that decides the minimum attainable grain size by MM.

The phenomenology of the development of nanocrystalline microstructure during high energy ball milling as summarized by Fecht[40] consists of three stages. In the first stage, deformation localization occurs in shear bands containing high dislocation density. In the second stage, dislocation annihilation/recombination/rearrangement occurs to form cell/subgrain structure in nanoscale and further milling extends this structure throughout the sample. In the third stage, the orientation of subgrains becomes random. It has been suggested that the ultimate grain size achievable is determined by the minimum grain size that can sustain dislocation pile-up within the grain and the rate of recovery during milling[74]. This means that the minimum crystallite size should be inversely proportional to the hardness[117]. A decreasing crystallite size with solute concentration has been observed in a number of alloy systems which exhibit solution hardening such as Cu(Fe)[118,119] Ti (Cu), Nb(Cu), Cu(Ni) and Cu(Co)[119]. The grain size of Ni(Co), where the hardness does not change significantly on alloying does not show any appreciable change during MA[87]. Similarly, an increase in grain size has also been observed in systems showing solid solution softening such as Ni(Cu), Fe(Cu) and Cr(Cu)[118].

3.2 Solid Solutions

3.2.1 Extension of Solid Solubility

Nanocrystalline solid solutions have been synthesized in a number of systems by MA of elemental powder mixtures such as Ti-Si[120], Ti-Ni, Ti-Cu[121], Ti-Mg[65] and Ti-Al[122,123]. Shen and Koch[119] have recently shown the formation of nanocrystalline solid solutions in Ti-Cu (0-8at.%Cu), Nb-Cu (0-20at.%Cu), Ni-Cu (0-50at.%Cu), Cr-Cu (0-20at.%Cu), Fe-Cu (0-15at.%Cu), Cu-Ni (0-50at.%Ni), Cu-Fe (0-50at.%Fe) and Cu-Co (0-50at.%Co) systems. They suggested that the solid solution hardening or softening is mainly governed by the hardening or softening of the grain boundaries. The extension of terminal solid solubility by MA has not been studied thoroughly so far, as the emphasis of most of the investigators was more either on the ODS alloys or on amorphization. The limited data available on the extension of terminal

solid solubility achieved in different alloy systems by MA is shown in Table VI. The formation of solid solution in the entire composition range in the eutectic Ag-Cu system[125] has highlighted the potential of MA in achieving large extensions of terminal solid solubilities even in systems with positive enthalpies of mixing in the solid state. This is supported by the results of Suryanarayana and Froes[65], wherein a terminal solid solubility of 6at.% of Mg in Ti has been achieved by MA while these elements are immiscible in the solid state under equilibrium conditions. They have attributed this extension of solid solubility to the nanocrystalline structure formed during MA. The large volume fraction of grain boundaries present in the nanocrystalline state are expected to enhance the solid solubility in these materials. Murty et al.,[121] could show in Ti-Ni and Ti-Cu systems that the extension of solid solubility in these systems is limited by the onset of amorphization. In another report, Murty and Pabi[141] could correlate the limit of extension of solid solubility of NiAl during MA to its crystallite size. Thus, MA can be used very effectively to extend the solid solubility of one element in the other so as to obtain stronger alloys.

3.2.2 Alloying in Immiscible Systems

In the initial stages of development of MA, Benjamin[103] could demonstrate the formation of homogeneous mixtures of Fe-Cu and Cu-Pb by MA. Later, a significant solid solubility was reported in Fe-Cu system by MA[119,142-148]. Alloying has also been reported in Cu-W[149,150], Cu-V[151,152], Cu-Ta[153-155] and Cu-Co[156-158] systems by MA. Significantly, Huang et al.,[159] have reported continuous series of solid solutions in Cu-Co system. Alloying in liquid immiscible systems by MA is an interesting phenomenon and there have been efforts to understand the driving force for such a behaviour during high energy ball milling. Yavari et al.,[143,160] have attributed this to the capillarity effect in the nanocrystalline state. They argued that high energy ball milling results in the formation of small fragments with tip radii of the order of 1nm. The capillarity pressure at these tips forces the atoms on these fragments to dissolve. Gente et al.,[158] and Huang et al.,[159] have proposed that the formation of homogeneous solid solution is energetically more favoured when the crystallite size of the constituents is reduced below a critical size which is of the order of 1-2nm. Murty et al.,[79] Pabi et al.,[85] and Huang et al.,[161-163] have shown that

Table VI
Extension of Terminal Solid Solubility by MA

Solvent	Solute	Solid Solubility at room temperature (at %)		Reference
		Equilibrium[124]	MA	
Ag	Cu	0.3	100.0	125
	Ni	0.7	3.8	126
Al	Cr	0.0	5.0	127
	Fe	0.0	4.5	126
	Mg	2.1	23.0	126
	Mn	0.0	18.5	128
	Nb	0.0	25.30	126
	Ti	0.0	6.0	122
	Zr	0.0	9.1	126
Cd	Zn	0.0	50.0	129
Co	C	0.0	6.0	130
	Cr	0.0	40.0	131
	V	9.1	33.0	131
	Zr	0.0	5.0	131
Cr	Co	9.0	40.0	131
	Cu	0.0	20.0	119
Cu	Co	0.0	90.0	119,132
	Fe	0.0	50.0	119
	Hg	0.0	70.0	129
	Zn	30.0	50.0	80
Fe	Al	18.5	50.0	133
	Cu	0.0	15.0	119
	Mg	0.0	20.0	134
	Si	9.0	27.5	135,136
Mg	Ti	0.0	4.2	126
Mn	Co	4.0	50.0	131
Nb	Al	21.5	60.0	126
	Cu	0.0	20.0	119
	Ni	7.0	10.0	129
Ni	Ag	2.0	9.0	126
	Al	10.0	27.0	129
	C	0.0	12.0	130
	Nb	6.0	15.0	137
Ti	Al	36.0	55.0	138
	Cu	0.0	8.0	119
	Mg	2.9	60.0	65,139
V	Co	7.0	40.0	131
Zr	Al	0.5	15.0	140
	Co	0.0	4.0	131

nanocrystallization is a prerequisite for MA in immiscible or partially miscible systems.

3.3 Nanocrystalline Intermetallic Compounds

The intermetallics constitute some of the most technologically prospective engineering materials. This stems from their novel attributes such as excellent high temperature strength and thermal stability apart from the high corrosion/oxidation resistance and unique electrical and magnetic properties. However, the high melting temperatures and the poor formability of the intermetallics poses a major impediment to their conventional processing. Under this perspective, MA has been envisaged as an extremely promising solution. Over the past one decade, a considerable volume of work has been reported on the synthesis of a large number of intermetallic compounds through MA[42]. The possibility of producing these intermetallics in the nanocrystalline state by MA (Fig. 9a and b) has increased the popularity of this technique, as it can induce some formability in these otherwise brittle materials[164]. Fig. 10 shows that the increase in hardness is quite significant (by 4 to 5 orders) in case of metals on nanocrystallization[165], while in
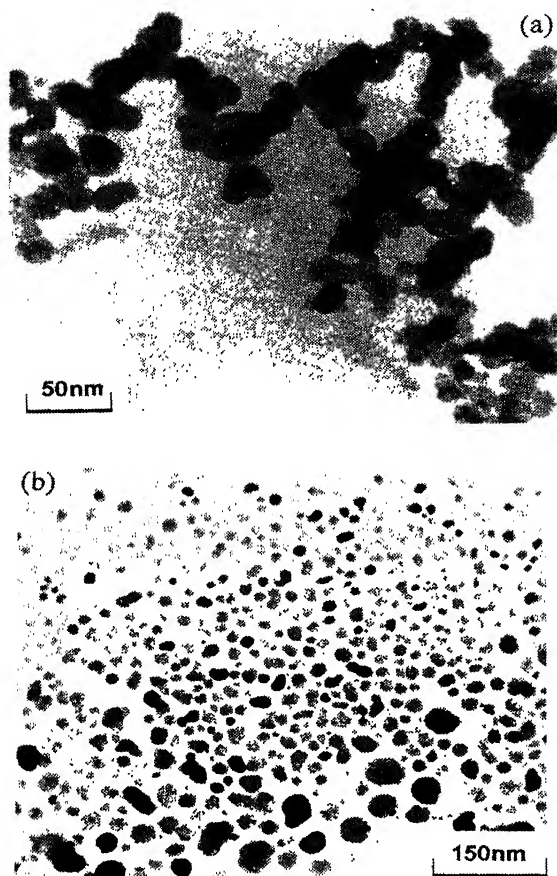
Fig. 9 TEM images of nanocrystalline (a) NiAl and (b) NiSi crystallites

Fig. 10 Variation in hardness with $d-1/_2$ for Fe and Nb_3Sn, where d=average grain diameter[39,165]

case of intermetallics (Nb_3Sn) it is quite marginal (10-20%)[39]. Dymek *et al.,*[166] have demonstrated sufficient compressive ductility (>11.5%) in fine grained (<1μm) NiAl. Jain and Christman[167] have shown that nanocrystalline FeAl (Fe-28Al-2Cr crystallites of 80nm) is brittle in tension, but is superplastic in compression. The bulk of these efforts have been on the aluminides and to some extent on the silicides.

3.3.1 Aluminides

Overwhelming interest in the MA of nanocrystalline aluminides has been instigated by their possible applications in aerospace and automotive industries owing to their high specific strength and corrosion/oxidation resistance at elevated temperatures. Among all aluminides, MA of Ni, Ti and Fe aluminides have so far received major attention.
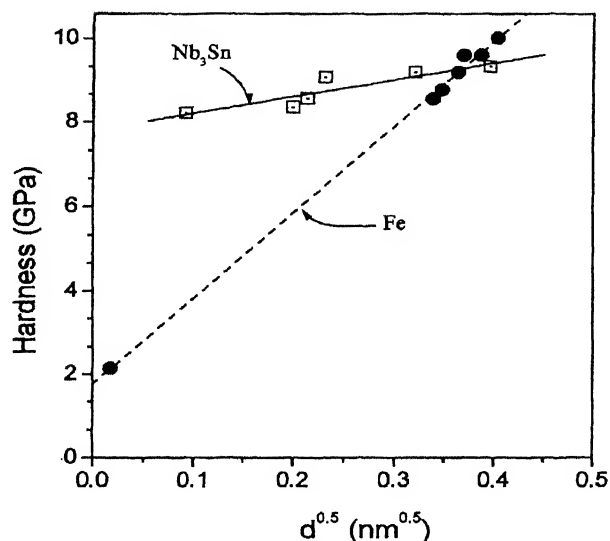
Ni-Aluminides: The formation of nanocrystalline Ni-aluminides, such as $NiAl_3$, NiAl and Ni_3Al through MA has been established at various compositions in the binary Ni_xAl_{100-x} (32<x<90) elemental blends[168]. Subsequent efforts[169-173] have confirmed the previous results of solid state synthesis in the Ni-Al system. Though a considerable extension of phase fields in the Ni_3Al, NiAl and even in the line compound $NiAl_3$ have been observed under intensive milling conditions[169,171], Ni_2Al_3 and Ni_5Al_3 phases were found metastable under similar conditions[169]. It is of interest to note that, in a marked contrast to the gradual temperature rise (~348K) during MA of Ni-aluminides in laboratory ball mill under air[168], formation of NiAl in Spex 8000 mill under Ar atmosphere[170] was accompanied by an exothermic reaction within a short duration of milling following an interruption after 2h of continuous milling. A similar observation has also been reported recently[174] on low energy ball milling of $Ni_{50}Al_{50}$ as well. Recent studies by Liu *et al.,*[175] have revealed a delayed initiation of the exothermic NiAl phase formation reaction on addition of ternary alloying elements such as Ti and Fe as indicated in Fig. 11. The occurrence of explosive reaction was also observed on opening the vial following milling[174]. This suggests the possible role of energy liberated during oxidation of Al in promoting the Ni-Al reaction. On the other hand, the absence of catastrophic reaction when milled in air[168] could be attributed to the continuous oxidation of the
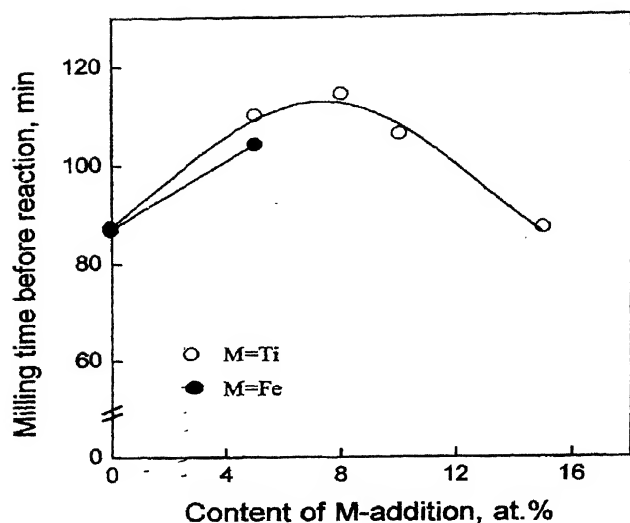
Fig. 11 Influence of ternary additions on the initiation of exothermic NiAl phase formation reaction[175]

Fig. 12 Extended phase fields of Ni-aluminides under MA
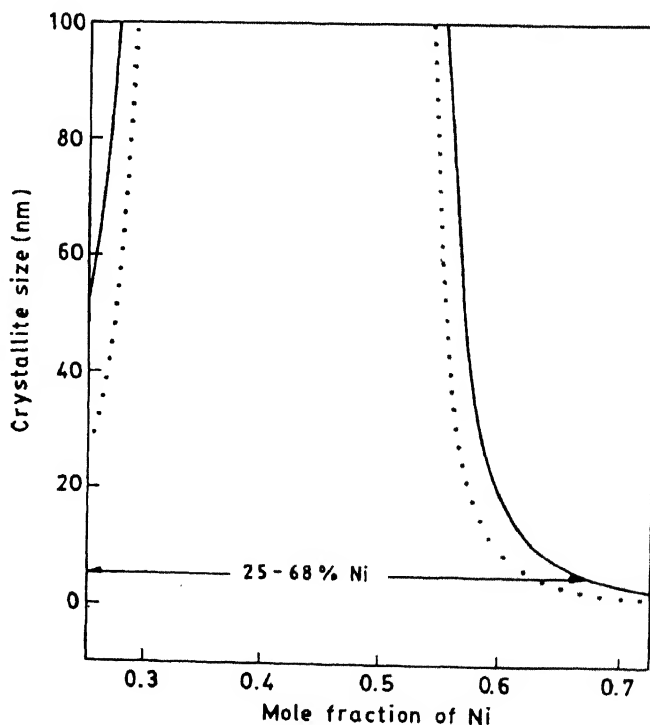
Fig. 13 Role of crystallite size on the thermodynamic stability of NiAl over an extended phase field

elements and the slow diffusion between the oxide coated ingredients, which results in reduced reaction kinetics. Pabi and Murty[176] have observed wide phase fields for the Ni aluminides (Fig. 12) in the nanocrystalline state and could explain the large extension in the NiAl phase field in the nanocrystalline state based on thermodynamic considerations (Fig. 13)[141].

Ti-Aluminides: Investigations on Ti-Al intermetallics have revealed stiff resistance to alloying during MA. For example, prolonged milling for 100h in Fritsch P-5 planetary mill at a BPR of 10 has failed to produce Ti-Al compounds[177]. The formation of Ti-Al intermetallics could be achieved on adopting a two stage process involving MA and subsequent annealing[178]. This is evidenced by the MA efforts for the synthesis of TiAl and TiAl$_3$, which required annealing of the ball milled ingredients at 873 and 813K respectively[179]. Several other reports on the production of Ti-Al intermetallics such as TiAl$_3$, Ti$_2$Al$_3$, TiAl and Ti$_3$Al through a 'mechanically activated annealing process' involving intense ball milling followed by annealing process are also available[180,181]. It is, however, quite obvious that the annealing temperatures would vary considerably depending on the final crystallite sizes which dictates the diffusion distance. On the other hand, there also exist some reports of direct synthesis of Ti-Al intermetallics by MA. For example, the formation
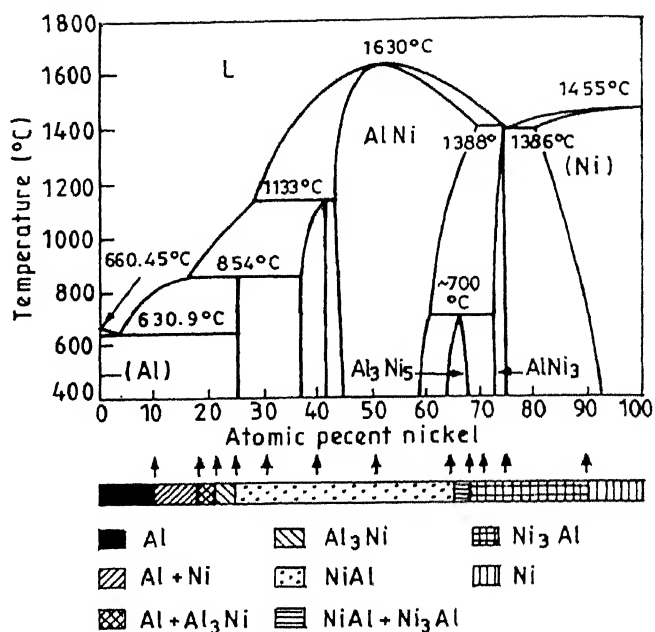
of TiAl and Ti_3Al has been reported during MA of $Ti_{40}Al_{60}$ and $Ti_{50}Al_{50}$ elemental blends[182]. Moreover, investigations by Park et al.,[183] have shown successful synthesis of TiAl and Ti_2Al through direct MA in vibratory mill in stainless steel grinding media with 12.7 and 19.1mm diameter grinding balls. However, the extent of Fe-contamination and its possible role in triggering such a reaction during MA remain to be looked into. Suryanarayana et al.,[184] could synthesize TiAl by MA of $TiAl_3$ and TiH_2.

Fe-Aluminides: $FeAl_3$ formation during MA of $Fe_{20}Al_{80}$ and $Fe_{25}Al_{75}$ blends in Fritsch P-5 planetary ball mill is quite well documented[185,186]. Interestingly, the initiation of $FeAl_3$ formation occurred within $40h$ in the $Fe_{25}Al_{75}$ blend as against $65h$ in $Fe_{20}Al_{80}$. Such a delayed synthesis of $FeAl_3$ in $Fe_{20}Al_{80}$ is quite explicable due to the off-stoichiometric composition. No intermetallic compound has been detected in Fe-87.5at.%Al blend even after $80h$ of MA[185,186]. Subsequent annealing at 773K, however, resulted in $FeAl_3$ phase. The formation of such non-stoichiometric $FeAl_3$ may be an indication of an extended $FeAl_3$ phase field, though, any possible Al loss due to oxidation may also be responsible for such observation. MA of Fe-rich composition, e.g., Fe-25at.%Al, which incidentally lies in the Fe_3Al phase field, has been found to produce FeAl instead[187]. Subsequent annealing, on the other hand, has led to B2- Fe_3Al instead of the usual DO_3 structure. The formation of FeAl during MA in preference to $AlFe_3$ has been attributed to its more negative Hf (–31.8kJ/mol) when compared to that of Fe_3Al (–18kJ/mol). The formation of metastable Fe_2Al_5 through MA has also been demonstrated[188] within $0.5h$ in Spex 8000 mill at a BPR of 6, which finally transformed to a more stable FeAl on MA for $5h$.

Other Aluminides: Apart from the above mentioned Ni, Ti and Fe aluminides, MA has demonstrated its ability in the synthesis of several other aluminides including ternary aluminides. Some of these aluminides includes Cu-Al, Nb-Al, Mo-Al, Zr-Al, Al-Ni-Fe, etc. A list nanocrystalline aluminides synthesized by MA is presented in Table VII.

3.3.2 Silicides

The MA of silicides has gained significant interest in recent years[206], particularly because of their potential applications as structural materials in the field of microelectronics and electrical technology.

Ni-Silicides: The initial efforts by Radlinski and Calka[207] on the synthesis of Ni-Si intermetallics through MA of an equiatomic blend of Ni-Si failed to produce the desired product even after prolonged milling for $1000h$. However, subsequent annealing treatment at 973K for a period of $1h$ did result in the formation of NiSi. On the other hand, studies on MA of $Ni_{100-x}Si_x$ (x=25, 28, 33, 40 and 50) in Fritsch P-5 at a very high vial speed of 642rpm revealed crystalline phase formation in Ni_3Si, Ni_3Si_2 and NiSi compositions and an amorphous phase in Ni_5Si_2, Ni_2Si compositions[208]. Recently, Datta et al.[209,] studied the MA characteristics of the entire range of composition in Ni-Si system. They have observed that only congruent melting silicides form in the nanocrystalline state and the formation of non-congruent silicides is suppressed even at their
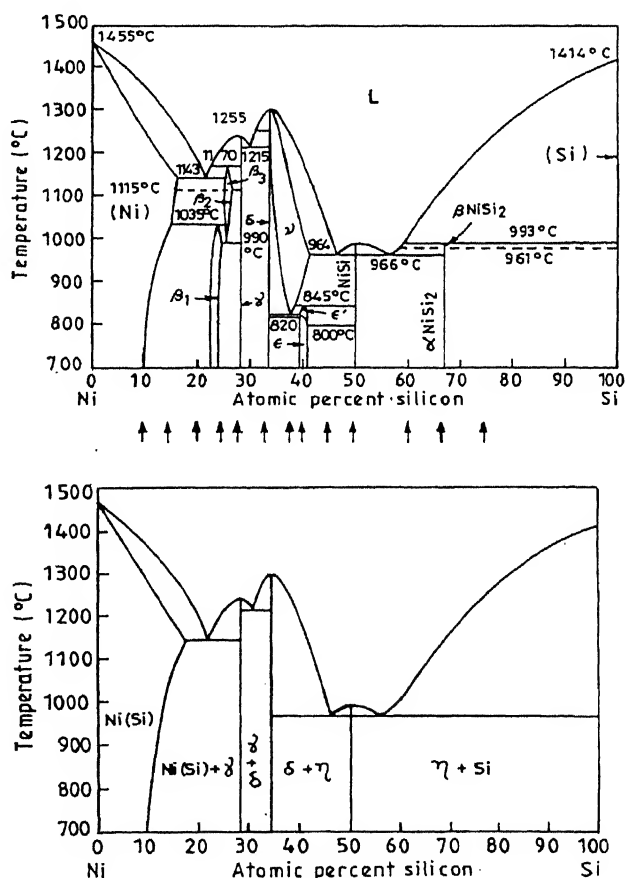

Fig. 14 (a) Equilibrium Ni-Si phase diagram indicating compositions subjected to MA and (b) metastable phase diagram at nanocrystalline state

Table VII
Nanocrystalline Aluminides Synthesized by MA

Phase	Structure	ΔH_f (kJ/mol)[187]	Synthesis Route	Reference
AlCo	B2	-43	MA	190
Al_4Cu_9	$D8_2$	-8	MA	191
Al_3Hf	$L1_2$	-51	MA	192
Al_3Mg_2	Fcc	-3	MA	193
$Al_{12}Mg_{17}$	A12	-3	MA	193
Al_6Mn	Orthorh	-15	MA	194
AlMn	B2	-43	MA	194
$Al_{12}Mo$	Bcc	-5	MA+HT	195
Al_5Mo	hex	-10	MA+HT	195
Al_4Mo	Monocl	-13	MA+HT	195
Al_8Mo_3	Monocl	-17	MA+HT	195
$AlMo_3$	Monocl	-15	MA+HT	195
Al_3Nb	DO_{22}	-29	MA	196,197
$AlNb_2$	$D8_2$	-36	MA+HT	197
$AlNb_3$	A15	-28	MA+HT	198-200
AlZr	Orthorh	-83	MA	197
Al_3Zr_2	Orthorh	-80	MA	197
Al-49Ni-2Cr	B2		MA	201
Al-46Ni-8Cr	B2		MA	201
Al-42Ni-16Cr	B2		MA	201
Al-40Ni-20Cr	A2		MA	201
Al-Ni-Fe	B2		MA	175,202
Al-49Ni-2Fe	B2		MA	201
Al-46Ni-8Fe	B2		MA	201
Al-42Ni-16Fe	B2		MA	201
Al-40Ni-20Fe	A2		MA	201
Al-Ni-Ti	B2		MA	171,175,203
Al-25Zr-3Fe	$L1_2$		MA	197
Al-25Zr-8Fe	$L1_2$		MA	204
Al-25Zr-8Ni	$L1_2$		MA	204
Ti-24Al-11Nb	B2		MA	197,205
Ti-25Al-25Nb	B2		MA	205
Ti-28 5Al-23 9Nb	B2		MA	197
Ti-37 5Al-12 5Nb	B2		MA	197

HT : Heat treatment

equilibrium compositions. Thus, in the nanocrystalline state the phase fields of silicides are given by the metastable phase diagram in comparison to the stable phase diagram as shown in Fig. 14(a) and (b).

Fe-Silicides: MA efforts with elemental $Fe_{33}Si_{67}$ blend[210] have shown the formation of a mixture of low temperature-tetragonal α–$FeSi_2$, high temperature-orthorhombic β–$FeSi_2$ and the cubic FeSi phases. MA studies on $Fe_{100-x}Si_x$ (x=5, 25, 37.5 and 50) in Fritsch P-7 at a BPR of 12 have revealed the formation of FeSi, Fe_2Si, Fe_5Si_3 and $FeSi_2$ respectively[211]. However, MA of Fe-6.5wt.%Si has shown the formation of a solid solution[212]. In fact, extremely high intensity MA[213] has demonstrated the formation of Fe-Si solid solution over an extended phase field up to Fe-37.5wt.%Si. On the other hand, MA studies in the Si-rich composition regimes in horizontal ball

mill[214] have revealed the formation of β–$FeSi_2$ phase for Si>70at.% and ε+β–$FeSi_2$ at 50at.%<Si<70at.%.

Ti-Silicides: In the initial studies on MA of Ti-Si system by Veltl et al.[215] in planetary ball mill, no intermetallic formation in the intermediate stages of milling have been detected possibly due to fast amorphization reaction in the high energy milling. However, the generation of TiSi intermetallic phase prior to amorphization during MA has been observed within 4h in Vibro mill at higher BPR[216]. MA results reported by Oehring and Bormann[217] and Park et al.,[218] demonstrate the formation of crystalline Ti_5Si_3, which remained stable even on prolonged milling. Such a high stability of Ti_5Si_3 against amorphization during milling is in conformity with its large negative free energy of formation (~ -71kJ/mol at 673K). Recent studies on MA of elemental blends of compositions

$Ti_{33}Si_{67}$ and $Ti_{42}Si_{58}$ have shown the formation of crystalline Ti_5Si_3 and Ti_5Si_4 embedded in an amorphous matrix after 60h of milling in Vibro mill[219]. $TiSi_2$ and TiSi phases were also detected in the preliminary stages of milling (4h) in this study, which paved way to the more stable phases with the progress of milling.

Mo-Silicides: Most of the research work on MA of Mo-silicides has been primarily focused on the Mo-disilicide ($MoSi_2$), which is a well-known refractory intermetallic (melting point=2323K) with considerable technological importance. Successful synthesis of $MoSi_2$ by MA has been reported by Schwarz *et al.*,[220] in Spex 8000 mill within 70h. More recently, nanocrystalline $MoSi_2$ has been synthesized by MA of $Mo_{33}Si_{67}$ in planetary ball mill (Fritsch P-5) at a disc speed of 280rpm[221]. Interestingly, both the low temperature as well as the high temperature phases *viz.*, α and β-$MoSi_2$ occurred during MA, with the extent of β phase increasing with milling time. Lee *et al.*[222,] have reported that the formation of $MoSi_2$ during MA is quite sensitive to the type of mill used. While both α and β-$MoSi_2$ could be obtained by MA in Spex mill, MA in planetary mill could not yield the silicide even after subsequent annealing treatment. In a significant report, Liu and Magini[223] have shown that high energy ball milling results in a self propagating high temperature synthesis (SHS) reaction leading to stable α-$MoSi_2$, while low energy milling leads to metastable β-$MoSi_2$ without any such reaction.

Other Silicides: The development of silicides other than the Ni, Fe, Ti and Mo-silicides through MA has evoked only limited interest so that only a handful of such reports is available. Some of these have been on the Pd-silicides. It is interesting that while high energy ball milling[224] resulted in the formation of the line compound Pd_3Si along with an amorphous phase from a mixture of composition Pd-16-23at.%Si elemental blend, low energy milling[225] of Pd-17at.%Si led only to an amorphous phase. The direct synthesis of Pd_2Si has been reported on MA of Pd-Si blends with Si>33at.% while at Si>50at.%, initial product of Pd_2Si is destabilized on prolonged milling and gradually transformed to the high temperature PdSi phase[226]. Nb_5Si_3 and Ta_5Si_3 compounds have also been synthesized through MA of elemental blends[227]. Lou *et al.*,[228] have shown that milling without interruption leads to the abrupt formation of $NbSi_2$, while regular interruption results in its gradual formation. Unlike in $MoSi_2$ where

prolonged milling resulted in the transformation of the low temperature phase (α) to the high temperature phase (β), the progress of MA of Nb_5Si_3 in Spex mill[229] led to the formation of more of the room temperature phase (α) at the expense of the high temperature phase (β).

3.3.3   Other Intermetallics

Though the aluminides and silicides have stolen the lime light in the field of research on MA of intermetallics, several other intermetallics deserve notable mention due to fundamental aspects as well as technological importance. The formation of various compounds in the Cu-Zn system *viz.*, β-CuZn, γ-Cu_5Zn_8 and ε phases, through MA has been extensively studied over the last decade[80,230,231]. Studies have shown that a sequence of phase formation is maintained during milling of elemental Cu-Zn blends in Fritsch P-5, wherein, the Zn-rich phases e.g. ε, and/or γ were always the first to form[80]. This is attributed to the much higher diffusivity of Cu in Zn than *vice versa*[80]. The progress of milling has shown the gradual formation of the Cu-rich phases through a continuous diffusive mechanism. The synthesis of superconducting intermetallics by MA e.g., Nb_3Sn has also been successful[232], while efforts on MA of superconducting Nb-Ge system has led to successful production of a number of phases *viz.*, Nb_3Ge, Nb_5Ge and $NbGe_2$ depending on the composition of the starting blend[233,234]. A list of non-aluminide and non-silicide intermetallics produced by MA is presented in Table VIII.

A number of metastable intermetallics have been obtained during MA in the nanocrystalline state. A bcc phase has been obtained at an elemental composition ratio for Nb_3Al instead of the equilibrium A15 compound[120] and a hcp phase at Ti_3Al, where the equilibrium structure is DO_{19}[177]. Similarly, $TiSi_2$ phase with metastable C49 structure has been obtained both by MM of equilibrium C54 structure and by MA of Ti and Si[249]. Formation of hexagonal C14 phase, metastable at room temperature has been obtained in stead of stable C15 cubic Cr_2Nb during MA[250].

3.4   Nanocomposites

In recent years, there have been considerable efforts to produce *in-situ* nanocomposites by MA. Zhu *et al.*,[251] have synthesized Pb-Al and Fe-Cu nanocomposites by MA. In a similar attempt,

Table VIII

Nanocrystalline Intermetallics other than Aluminides and Silicides Synthesized by MA

Phase	Structure	ΔH_f (kJ/mol)[189]	Synthesis Route	Reference
Co_3C	hex	+6	MA	235,236
Cr_7C_3	hex	-13	MA+HT	237,238
Cr_3C_2	orthorh	-16	MA+HT	237,238
Cr_2Nb	C15	-10	MA	239
β-CuZn	B2	-8	MA	80,230,231
γ-Cu_5Zn_8	$D8_2$	-4	MA	80,230
ε-$CuZn_4$	hex.	-2	MA	80,230
Fe_3C	orthorh.	+25	MA	236
$FeSn_2$	C16	-1	MA	240
Fe_3Sn_2	monocl	-2	MA+HT	240
$FeSn$	B35	-2	MA+HT	240
Fe_3Sn	DO_{19}	-2	MA	241
Fe_3Si	DO_3	-21	MA	242
$FeTi$	B2	-25	MA	241
Fe_3Zn	$D8_2$	-2	MA	241
Mg_2Ge	C1	-115	MA	243
Mg_2Ni	hex	-52	MA+HT	244
Mg_2Si	C1	-79	MA	243
Mg_2Sn	C1	-80	MA	243
Nb_3Ge	A15	-28	MA	233,234
Nb_5Ge	orthorh	-19	MA	234
$NbGe_2$	C40	-29	MA	234
Nb_3Sn	A15	-16	MA	232
Ni_3B	cubic	-21	MA	245
Ni_3C	cubic	+7	MA	235,236
Ni_3Sn_2	hex	-24	MA	240
TiB_2	hex	-74	MA	207
TiC	$L1_2$	-77	MA	246-248
$TiNi$	B2	-52	MA	248

Provenzano and Holtz[252] have shown the formation of Ni-Ag and Cu-Nb nanocomposites by MA. Du et al.,[253] have produced Al-BN composites by high energy ball milling. In an interesting report, Naser et al.[254], have showed that no grain growth occurs in the matrix close to its melting point when Cu and Mg are reinforced with nanocrystalline Al_2O_3 by mechanical alloying. Wu et al.,[255] have reported the formation of nanocrystalline TiC in an amorphous Ti-Al matrix by MA. A solid state reaction leading to the formation of AlN and AlB_2 was reported by them during further processing of these nanocomposites. $TiAl$-Ti_5Si_3 nanocomposites have been reported by Liu et al.,[256] by MA followed by thermal treatment. They attribute the formation of these nanocomposites to the crystallization of amorphous phase obtained by MA in Ti-Al-Si system. These nanocrystalline compounds appear to be quite stable and no significant coarsening was observed even after heat treatment for 1h at 1273K. Similar nanocomposites have been obtained by Senkov et al.,[257] by MA and subsequent heat treatment of a mixture of TiH_2 and Al-Si alloy powders. $NbAl_3$-NbC nanocomposites have been
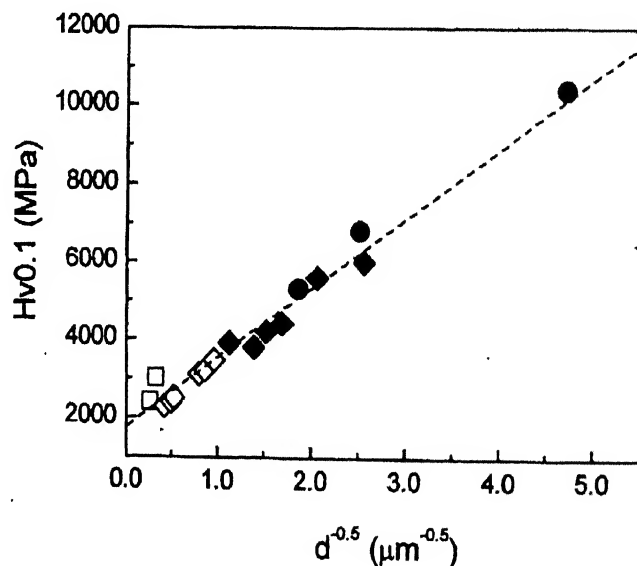

Fig.15 Change in the microhardness of Ti-Al alloys with d-$^1/_2$($\bullet$), mechanically alloyed Ti-46at %Al-5at %Si and Ti-20at %Al-17at %Si-9 5at %Nb; ($\blacklozenge$), mechanically alloyed binary Ti-Al; ($\downarrow$), conventional powder-processed material; ($\lrcorner$), ingot material of similar composition[260]

obtained by MA of Al and Nb powders[258]. Interestingly, NbC in this case appears to have formed by the reaction of Nb with the methanol medium in which the milling was performed. Manna et al.,[259], have recently synthesized nanocomposites of Cu-NbAl$_3$ by the codeposition of nanocrystalline NbAl$_3$ during the electrodeposition of Cu. Pfullmann et al.,[260] have mechanically alloyed TiAl base alloys with Si to synthesize nanocomposites with Ti$_5$Si$_3$ dispersions in TiAl and Ti$_3$Al and found significant improvement in microhardness in the nanocrystalline state (Fig.15).

4 Mechanism of Nanocrystalline Phase Formation during MA

The phase formation processes to a great extent are influenced by the chemical driving force provided by the free energy/enthalpy difference. In case of nanocrystalline materials, the contribution of interfacial energy term becomes comparable with the chemical free energy term, and hence has a decisive role in dictating the stability of equilibrium phases in the milled product. For instance, precipitation of second phase particles in nanocrystalline supersaturated solid solution is going to be difficult due to further increase in interfacial areas. For this reason, reactions like discontinuous precipitation or peritectoid transformations are expected to be suppressed in nanocrystalline alloys. The large density of dislocations generated in the as milled products under heavy cold work involved during MA can also contribute to the enhanced diffusivity values and thereby significantly influence the alloying mechanism[261]. The studies on ball milling induced alloying has broadly led to three major type of mechanisms as discussed below:

(a) Continuous Diffusion (CD) of Reacting Species

The mechanism is characterized by a continuous change in the lattice parameter of the solvent with the progress of milling at the expense of the depleting solute content. Zbiral et al.,[262] have proposed two different mechanisms (I and II) occurring via CD mode. In mechanism I, for a lower solubility of A in B compared to B in A in the A-B system, alloying is achieved by diffusion of the B into A. Such mechanism has been suggested to be relevant to binary model systems e.g., Ni+Al, Ni+Ti, Ni+Cr, Ni+Mo, Ni+W. While mechanism II has been proposed to operate in systems with good mutual solubilities e.g., Ni+Cu, Ni+Ta and Ni+Zr. Fig.16 illustrate the two alloying mechanisms and indicate the direction of diffusion and alloy growth.
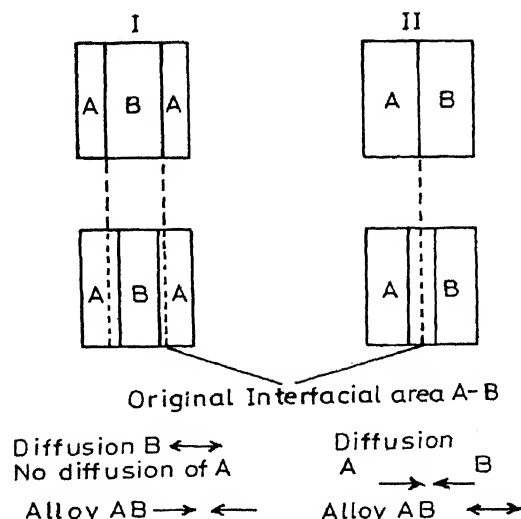

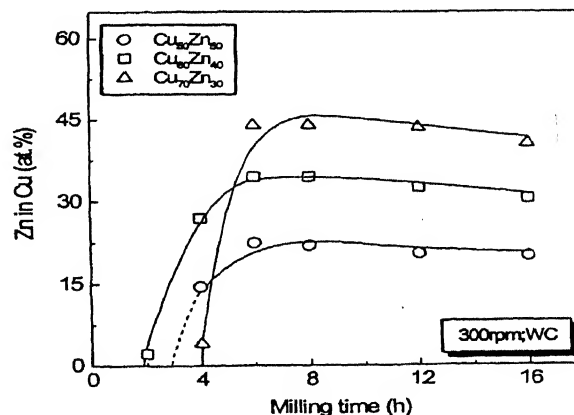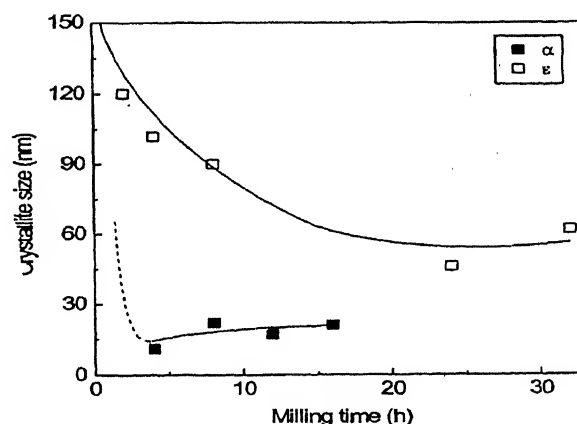Fig. 16 Alloying mechanism by continuous diffusive mode[262]

Fig. 17(a) Changes in the crystallite size of α and ϵ and (b) variation in the solubility of Zn in Cu during MA of different Cu-Zn blends

Recently, the mechanism of mixing has also been analyzed in Cu-Zn model system[80], which is characterized by $\Delta H_f \sim$ -6 to -9kJmol[-1]. As evident from Fig.17a, the formation of α and ε-phases occur with the reduction in crystallite sizes of (Cu). A concomitant increase in the amount of Zn dissolved in Cu at the initial stages of milling is also estimated (Fig.17b), which indicates fast diffusion of the species at nano-grain sizes. Interestingly, alloying was found to initiate by the diffusion of Cu into Zn so that even at a Cu-rich composition in equilibrium α phase field, the Zn-rich phases *viz.* η or ε were first to form. These Zn-rich phases were however metastable, and paved way for the more stable phase(s) at the particular composition. The above behaviour may be easily understood if one looks into the diffusivities of Cu and Zn in each other (extrapolated at the probable milling temperature of ~473K from high temperature data[263]) which indicate nearly eight order of magnitude higher $D_{Cu\ in\ Zn}$ (2.99x10^{-14}cm[2]/s) when compared to $D_{Zn\ in\ Cu}$(8.21x10^{-23}cm[2]/s). Similar mixing behaviour has also been observed in Cu-Ni system as reported by Pabi *et al.*[264]

(b) Self-Sustaining Reaction (SR)

Though, in real sense SR mechanism is more a reaction synthesis mechanism rather than a MA mechanism, it deserves attention because of the indications in several reports that similar process possibly play the crucial role in the overall alloying behaviour by increasing the milling temperature drastically, which in turn promotes the desired reaction. For example, the synthesis of Ni-Al intermetallic from Ni-Al blend has been reported to be associated with an exothermic reaction due to oxidation during milling which supports the reaction leading to generation of phase(s)[170,265]. The role of crystallite size and lattice strain, however, has been overlooked and warrants critical assessment. In an effort to develop a well defined criteria for self sustaining reaction it has been suggested[60] that for the reaction to occur the required diffusion distance, must decrease relatively more rapidly than the accomplished diffusion distance (X_D) increases (Fig.18).

(c) Discontinuous Additive (DA) Mixing

The mechanism is characterized by the typical behaviour of the crystallite size refinement whereby the crystallite size of the product at the onset of its
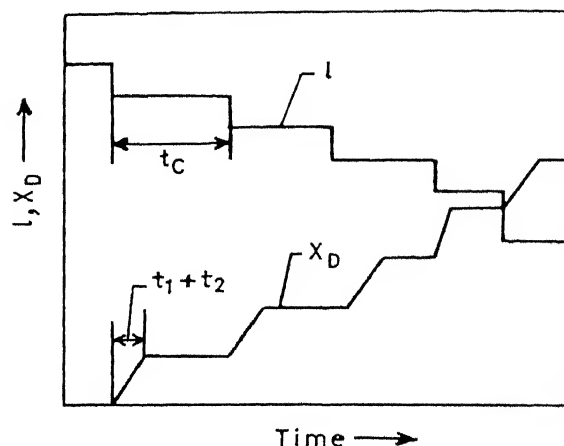

Fig. 18 Schematic of a reaction process where the phase evolution occurs at a time, t, when the required diffusion distances (l) as well as the accomplished diffusion length (X_D) converges[60]

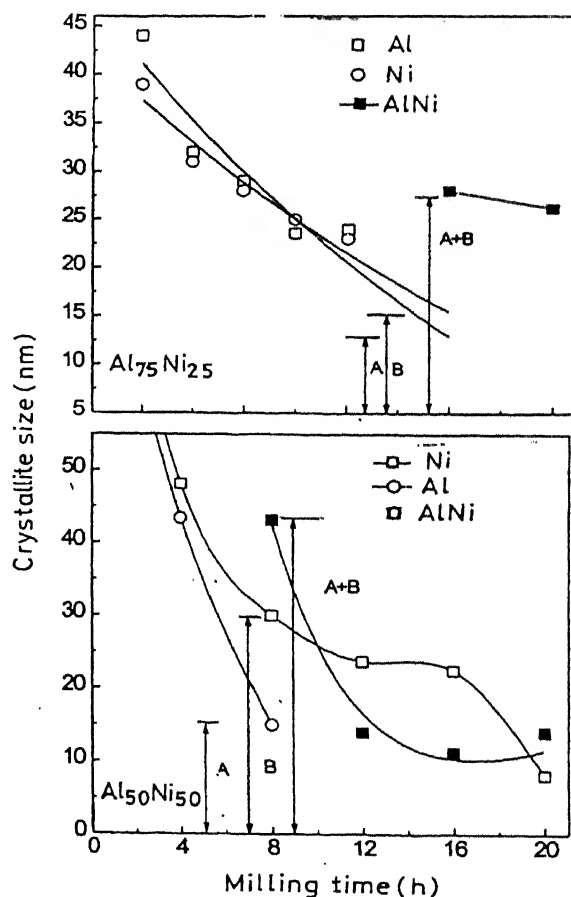Fig. 19 Discontinuous additive mixing during NiAl formation from (a) $Ni_{25}Al_{75}$ and (b) $Ni_{50}Al_{50}$ blend compositions by MA

formation is equal to the sum of the individual crystallite size of the constituents[264]. It may be noted that the mixing behaviour during MA of binary Ni-Al blends as analyzed in various prototype compositions viz. $Ni_{21}Al_{79}$, $Ni_{25}Al_{75}$, and $Ni_{50}Al_{50}$ have revealed similar behaviour. Interestingly, the formation of ordered NiAl from $Ni_{25}Al_{75}$ and $Ni_{50}Al_{50}$ blends initiates when the crystallite sizes of the ingredients, Ni and Al, at the onset of the reaction shows an additive relation when compared to that of the product, NiAl (Fig.19(a) and (b)). Furthermore, the critical crystallite size of the constituents, at which the DA mixing is triggered, depends on the composition and it is largest at the stoichiometric composition (i.e., $Ni_{50}Al_{50}$) apparently for maximum available driving force[264]. This does not fit to the conventional continuous diffusive mixing mechanism. It may be recalled that earlier reports[170,265] have indicated the association of a sudden exothermic reaction in the vial during the synthesis of NiAl from a stoichiometric blend composition, which is suggestive of reactive mixing as stated in the previous section. However, in reactive mixing the reaction front usually propagates in unpredictable direction and is, therefore, unlikely to show additive rule as observed by Pabi et al.[264] In addition, as milling in these studies were performed under liquid (toluene) bath, high temperature build-up at the collision point is unlikely. The temperature estimates from earlier studies 94 points to a modest rise in temperature (~ 473-573K). It is noteworthy to mention in this connexion that studies on external heating of Ni-Al powder compacts in atomic volume of 1:3 at a heating rate of 8.33 x 10^{-2}K/s shows the initiation of a self propagating high temperature reaction (SHS) at ~823K[266]. While, studies on Ni-Al foils at overall compositions between Ni-25 to 75at.%Al have indicated that the initiation of SHS required a temperature of greater than or equal to the melting point of Ni[267]. Thus, the discontinuous additive mode of mixing is quite unique, which may, however, be looked upon as a low temperature version of reaction synthesis.

4.1 Factors Controlling the Mixing Mechanisms

It may be noted that the mechanically induced energy may even supersede any thermodynamic or kinetic barrier to instigate reaction in otherwise immiscible systems. The difference in the alloying behaviour in various systems may be, therefore, evaluated within a framework delineated by distinct ranges of enthalpy of formation/mixing. On the other hand, recent investigations also point to the possible influence of the ordered structure of the mechanically alloyed products in determining the mode of alloying. These aspects need greater attention for an in-depth understanding of the underlying fundamentals, which has not been attempted so far.

4.1.1 Influence of ΔH_{mix}

I $\Delta H_{mix} < 0$

The above condition thermodynamically favours alloy formation. However, the occurrence of the reaction during MA from elemental blends is likely to be decided by the kinetic factors. The system has to surmount the activation energy barrier by the mechanical energy impounded into the ultra-fine-crystal ensembles and once it crosses this barrier the reaction is sustained by an enhanced downhill diffusion. Though, there exist no distinct criteria defining the alloying mechanism involved during MA, three different modes have been reported to operate in several systems viz. a continuous diffusion induced transformation, a self sustaining reaction assisted by some exothermic process accompanying ball milling and also the discontinuous additive mixing mode observed in aluminides as discussed in previous section.

II $\Delta H_{mix} > 0$

The positive heat of mixing in system implies lack of chemical driving force for alloying and as such, the formation of intermediate phases or solid solution is thermodynamically not feasible under equilibrium conditions. The mechanism underlying the solid solution formation in systems with positive ΔH_{mix} under the non-equilibrium MA processing have been found to be of CD type. The alloying process in these systems has opened up several possibilities based on the source of driving force as mentioned below. It may be noted that all these mechanisms suggested for systems with positive heat of mixing could well be applicable for systems showing negative enthalpy of mixing.

(a) Energy Stored in Grain Boundary

The large grain boundary energy has been correlated to the occurrence of solid state alloying based on the observation that reaction proceeds as the crystallite sizes of elemental constituents drops down to nanometric level[154]. Substantial amount of enthalpy is expected to be stored in the nanocrystalline metal due to large grain boundary area[31].

(b) Oxygen Induced Mixing

The possible reduction in the enthalpy of mixing of systems by the dissolution of oxygen has also been suggested to induce alloy formation in liquid immiscible systems e.g., Cu-Ta and Cu-W, both of which have tendency to form amorphous phases on milling[39]. This has been supported by the reported reduction in the heat of transformation of amorphous $Cu_{30}Ta_{70}$ to elemental state of only 3-11kJ/g atom[153,267] from the expected value of ~20kJ/g atom. However, no such change in the enthalpy of mixing has been reported in Cu-Co system[148] even for higher amounts of oxygen.

(c) Capillary Pressure Mechanism

The mechanism suggested by Yavari et al.,[143] for composites of Cu with Fe or other high-melting bcc metals, having positive ΔH_{mix}, considers fracturing of the composite on deformation, with the formation of fragments of small tip radii. Such structure leads to capillary pressure build-up at the small tips, which in turn forces, the atoms of the fragments to dissolve. Yavari et al.,[143] has further shown that for an incoherent Cu/Fe interface enthalpy of 1.4J/m2, dissolution of Fe atom in Cu occurs for a tip diameter ≤14nm.

(d) Dislocation Assisted Alloying

High dislocation density may also contribute to a substantial increase in the mutual solubility in systems with positive ΔH_{mix}[144]. This is due to change in the chemical potential of the solute atoms in the strain field of an edge dislocation. Such mechanism has been extended to account for the metastable solid solubility in Cu-Fe system under ball milling[144].

(e) Influence of Coherent Interface

Apart from the excess structural enthalpy of the system on account of the grain refinement during ball milling, coherent interface formation in systems, e.g., Cu-Co (between Cu and Co regions) has been considered to play significantly in the solid solution formation[158]. It has been argued that the formation of such coherent interface between Cu and Co regions does not change the crystallite size so that the thickness of the elemental components in the final state may be much smaller than their crystallite sizes, enhancing the chemical contribution of the interface. The critical size, d_c, below which the chemical contribution of the Cu-Co interface enthalpy exceeds the free energy of the solid solution, has been calculated from simple energy relations, neglecting the small entropy contribution to the free energy of interface. The enhancement in the chemical contribution of interface enthalpy with the refinement of microstructure has been shown in Fig.20 for different sizes of Cu and Co regions. Considering an enthalpy of $0.3Jm^{-2}$ for the coherent Cu/Co interface for d_C ~1nm, the ΔH_{chem} for $Cu_{50}Co_{50}$ composite raises above 6kJ/g atom which is sufficient to allow for a phase transformation of the composite into solid solution provided the interface temperature reaches ~673K during ball milling operation.

4.1.2 Influence of Ordering Characteristics

The various mechanisms controlling the phase formation reactions during MA have been investigated in Cu-Al, Nb-Al, Ni-Al and Fe-Al systems having $\Delta H_f \ll 0$. It has been attempted to generalize the theory propounded for these systems by comparing with alloying mode in Cu-Zn possessing less negative Hf and Cu-Ni with $\Delta H_f > 0$. Table IX presents the various alloying mechanisms operating in these systems during MA. As it evolves from the above table (Table IX)[268], there exists contrasting mode of mixing in the ordered products viz. $NiAl_3$ and NiAl on one hand and the disordered products e.g., Ni_3Al and FeAl on the other. The Table reflects the possible role played by the structural order in the product phase in determining the synthesis mechanism. This is elucidated by the influence of a highly disordered
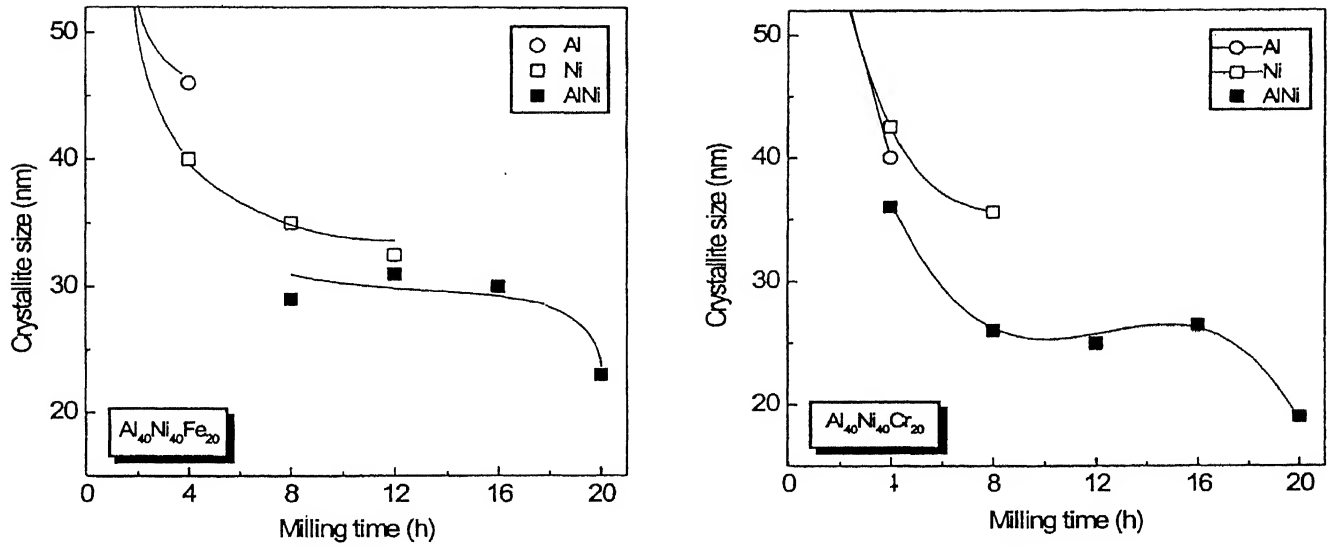

Fig. 20 Chemical contribution of interface enthalpy with the refinement of microstructure[158]

Fig. 21 Crystallite size variation with milling time in the formation of NiAl during MA of (a) $Ni_{40}Al_{40}Fe_{20}$ and (b) $Ni_{40}Al_{40}Cr_{20}$ blends

Table IX
Alloying Mechanism in Different System during MA[26*]

System	Composition	Product phase	C S (nm)	Product nature	ΔH_f (kJ/mol)	Alloying mechanism
Cu-Ni	$Cu_{50}Ni_{50}$	Cu(Ni)	20	DO	2	CD
Cu-Zn	Cu-15 to 50at %Zn	α	20	DO	-9	CD
Cu-Al	$Cu_{80}Al_{20}$	Cu(Al)	10	DO	-8	CD
Fe-Al	Fe-25 to 50at %Al	FeAl	15	DO	-31	CD
Ni-Al	Ni-21at %Al	$NiAl_3$	20	ORD	-39	DA
	$Ni_{50}Al_{50}$	NiAl	10	ORD	-72	DA
	$Ni_{75}Al_{25}$	Ni_3Al	30	DO	-42	CD
Ni-Al-Fe/Cr	$Ni_{40}Al_{40}Fe_{20}$	NiAl	25	DO	–	CD
	$Ni_{40}Al_{40}Cr_{20}$	NiAl	20	DO	–	CD
Nb-Al	$Nb_{25}Al_{75}$	Nb_3Al	9	ORD	-20	CD

C.S. =crystallite size after 20h of MA; ORD=ordered; DO=disordered (S≤0.3); CD=continuous diffusive mixing; DA=discontinuous additive mixing;

ball milled NiAl, caused by Fe or Cr additions as described in ref. [47], on the mixing phenomenon (see ref. [28]). Interestingly, the crystallite sizes at the onset of the formation of the highly disordered NiAl in NiAl(+Fe/Cr) blends do not demonstrate the usual additive relation as evident from Fig.21(a) and (b). However, a gradual shift in the lattice parameter of Ni caused by the gradual consumption of Al with progress of milling is observed (Fig.22), that evidences a continuous diffusive mixing mode in the disordered NiAl. It may be noted that though Fig. 22 reports the variation of Ni peak in $Ni_{40}Al_{40}Cr_{20}$ only up to 8h its presence was evident till 16h. However, it was difficult to ascertain the lattice parameter as well as crystallite size because of its highly diffused nature. Furthermore, it may be mentioned that a considerably higher diffusivity values are usually
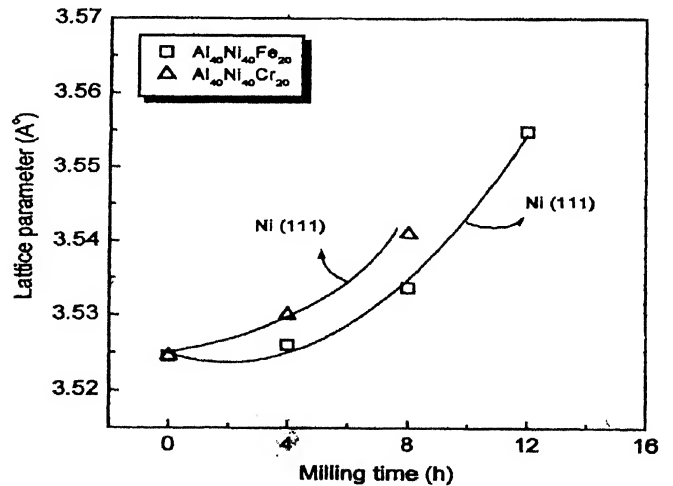
Fig.22 Shift in lattice parameter of Ni during MA of $Ni_{40}Al_{40}Fe_{20}$ and $Ni_{40}Al_{40}Cr_{20}$ blends

expected in the disordered state of a phase when compared to that in its ordered state e.g., the diffusivity of Cu in Zn at 773K in disordered β'-phase ($D_{Cu\,in\,Zn}=4.8\times10^{-13}$ m^2/s at 773K in β') under identical condition is $\sim$ 35 times higher than that in ordered β($D_{Cu\,in\,Zn}= 1.4\times10^{-14}$ m^2/s at 773K in β), while the diffusivity of Zn in Cu in disordered β exceeds that in ordered β by about 144 times ($D^{\beta'}_{Zn\,in\,Cu}=1.3\times10^{-11}$m^2/s; $D^{\beta}_{Zn\,in\,Cu}=9.0\times10^{-14}$m^2/s at 773K)[263]. Such situation is expected to prevail in the highly disordered AlNi structure as well, which perhaps assist the phase formation reaction by the continuous diffusive mechanism as observed in the present investigation. However, it may be noted that the formation of Nb$_3$Al during MA follows a continuous diffusive mechanism in spite of it being ordered on MA. It may be noted that the ΔH_f for Nb$_3$Al is less negative when compared to that of NiAl or NiAl$_3$. The above studies, therefore, indicate that the mode of mixing is continuous diffusive if either $\Delta H_f >$ -40kJ mol^{-1} for a given phase or the as milled product is disordered.

5 Kinetics of Alloying during MA

It is well known for over three decades that mechanical deformation enhances the diffusion rate and the process has been termed as "mechanical diffusion" by Balluffi and Rouff[269]. Gleiter[270] has shown that a large potential gradient leads to a high rate of diffusion in the vicinity of a dislocation even at temperatures where self-diffusion is not possible. Gleiter had also shown that the passage of dislocations through Ni$_3$Al particles in Ni-rich matrix causes pronounced reversal of solute to the matrix from the precipitates, thus resulting in their dissolution at large deformation. Thus, the deformation-enhanced diffusivities can play a significant role in deciding the alloying kinetics during MA.

Recent development of a kinetic model based on a modified version of the iso concentration contour migration (ICCM) method developed earlier[271] to estimate the rate of diffusion controlled dissolution in a two phase planar and multilayered aggregate[268], has been a significant step in kinetic analyses of the MA process. Fig. 23 shows the experimental and calculated results of the respective variation of solubility of Ni, Al and Zn in Cu for Cu$_{50}$Ni$_{50}$, Cu$_{80}$Al$_{20}$ and Cu$_{70}$Zn$_{30}$, as a function of milling time[268]. These experimental results are obtained from

the XRD peak shifts of Cu in the above-mentioned elemental blends during MA. The results clearly indicate that the effective mass transport phenomenon operative during MA attains a rate intermediate between that of volume diffusion and grain boundary diffusion. The enhanced diffusion rate in course of MA have been considered to be equivalent to that of volume diffusion at some elevated temperature T_{eff}, that has been determined by comparing the experimental values of solid solution rate with that predicted by the MICCM model. The results of these analyses demonstrate that the equation of ballistic diffusion[62] is not able to account for the extremely large enhancement in the diffusivity values as encountered in MA. It is also clear from the results
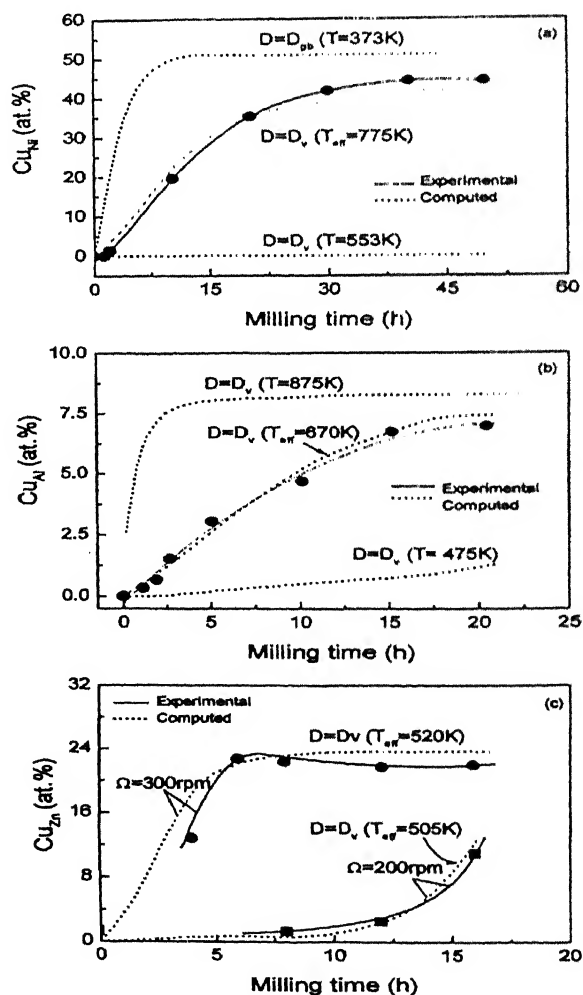

Fig. 23 Experimental and calculated results of the respective variation of solubility of Ni, Al and Zn in Cu for Cu$_{50}$Ni$_{50}$, Cu$_{80}$Al$_{20}$ and Cu$_{70}$Zn$_{30}$, as a function of milling time

Table X

Variation in the T_{eff} and the Homologous Temperature, θ_{eff} obtained from Experimental Data through MICCM model

Composition	rpm	$T_{solidus}$ (K)	T_{eff} (K)	θ_{eff} (T_{eff}/Tsolidus)
$Cu_{70}Zn_{30}$	200	1190	505	0.42
$Cu_{70}Zn_{40}$	300	1190	520	0.44
$Cu_{60}Zn_{40}$	300	1150	560	0.49
$Cu_{50}Ni_{50}$	300	1533	755	0.49
$Cu_{20}Ni_{80}$	300	1633	785	0.48
$Cu_{80}Al_{20}$	300	1317	670	0.51

of the $Cu_{70}Zn_{30}$ that though the alloying kinetics are remarkably slower at milling disc speed of 200rpm when compared to that at 300rpm in the planetary ball mill P-5, the T_{eff} changes only marginally from 505 to 520K. Furthermore, it is of interest to note that the homologous temperature ($T_{eff}/T_{solidus}$) lies in the range of 0.42 to 0.51 (Table X) in each of these systems, indicating that the effective mass transfer during MA is related to the solidus temperature of the system concerned. It is also evident from these calculations that the crystallite size of the constituent(s) has to be reduced to nanoscale (< 100nm) to achieve any significant rate of alloying by high energy ball milling. It is expected that these results would suffice for predicting the alloying kinetics in diverse systems.

6 Nanocrystallization by Devitrification

Devitrification under controlled conditions has been found to induce nanocrystalline structure[272]. The process may be grouped under two categories depending on the route leading to the nanocrystalline phase evolution *viz.* (i) mechanical deformation induced crystallization and (ii) thermally assisted crystallization of metallic glasses. However, the thermal devitrification has not been discussed here as it is beyond the scope of this review.

The crystallization of amorphous Zr-Ni alloys at higher milling intensities after being amorphized at low intensity milling have been shown by Eckert *et al.*[273] and Trudeau *et al.*,[274] have milled Metglas 2605Co ($Fe_{66}Co_{18}Si_1B_{15}$) and Metglas 2605S-2 ($Fe_{78}Si_9B_{13}$) and found that both crystallize on milling, with Co containing metallic glass crystallizing at shorter milling times. The crystallization of these glasses during milling was attributed to the local rise in the temperature during ball milling, while the early crystallization of the Co containing glass was thought to be due to its lower crystallization temperature (714K

as against 826K of Metglas 2605S-2). In an interesting experiment, they[274] have mechanically alloyed Co and Ni to Metglas 2605S and found that Co addition induces rapid crystallization while Ni stabilizes the amorphous phase. This is interesting because Ni addition is known to lower the crystallization temperature to Metglas 2605S to 648K. This work has suggested that a lower crystallization temperature of a metallic glass is not sufficient for it be crystallized during high energy ball milling. Crystallization of metallic glass in Fe-B-Si system by MM has been observed by other several other investigators[275,276]. Enhancement of diffusion due to heavy deformation[277] is also an explanation offered to the nanocrystallization of metallic glasses by high energy ball milling. It appears that temperature rise during milling alone can not explain the crystallization of amorphous phases observed during milling. Chemistry changes during milling and the local temperature rise during milling can enhance the crystallization kinetics. It is possible that the defects introduced during milling accelerate the diffusion and in turn the crystallization kinetics during milling.

7 Nanocrystalline Materials Synthesized by Severe Plastic Deformation

Recent studies have shown that nanocrystalline structure can be synthesized by severe plastic deformation (SPD) either by torsion straining under high pressure (SPTS)[46,278-283] or by equal-channel angular pressing (ECAP)[284-293]. The major advantage of SPD techniques over high energy ball milling and inert gas condensation is that bulk nanocrystalline samples and semi-finished products without any residual porosity can be obtained without the need for compaction and sintering[46]. The concept of ECAP can be traced back to Segal *et al.*,[284] who have pressed the test samples through a die containing two channels, equal in cross section, intersecting at an angle. As
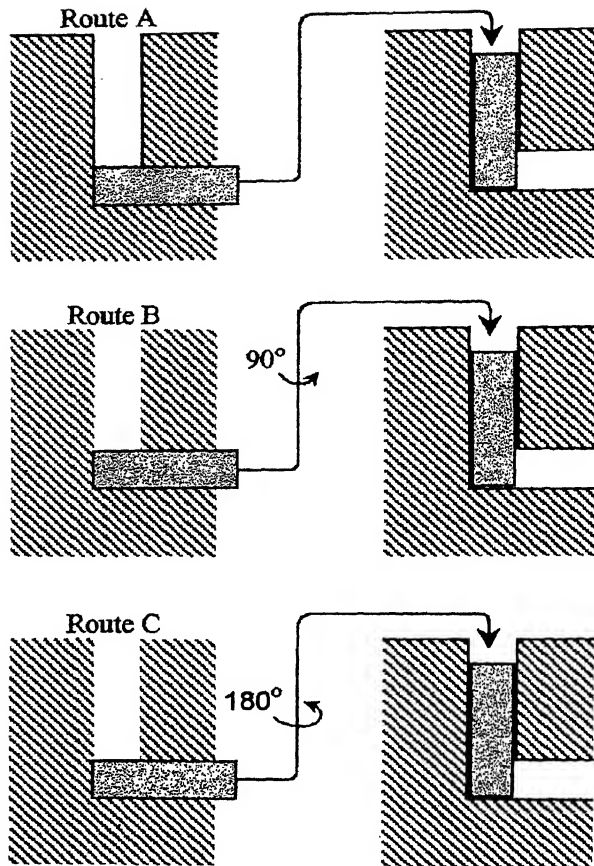
Fig. 24 Schematic of the route adopted during ECAP[293]

Fig. 25 Change in the microhardness with $d^{-1/2}$ for Al-3%Mg produced by torsion straining[298]
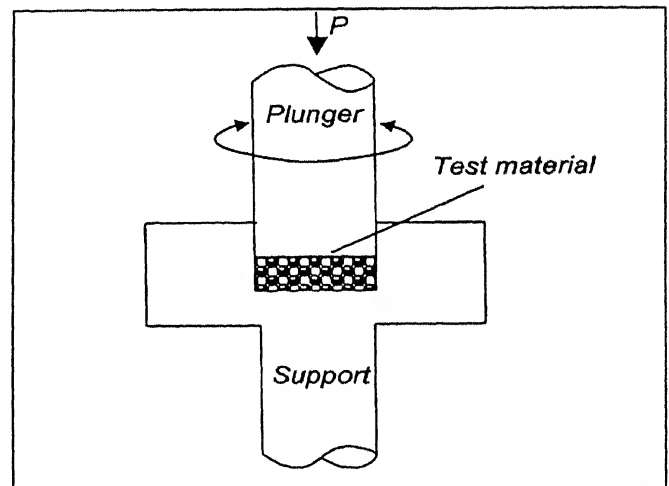
Fig. 26 Schematic of the SPTS route for nanocrystalline structure[46]

a result of pressing the samples undergoes simple shear but retains the same cross section so that the pressing can be repeated for several cycles. The SPD techniques have been shown to produce nanocrystals as small as 50nm[294]. Interestingly, a number of structure insensitive properties such as modulus of elasticity[288], Debye[285] and Curie temperature[287] have been shown to change significantly on nanocrystallization using SPD. Fig. 24[293] shows a schematic of the routes adopted during ECAP. In route A the samples is pressed repetitively without rotation, in route B the samples is rotated by 90° between each pressing and in route C the sample is rotated by 180° between pressings. Nanocrystalline state could be achieved in a number of materials such as Al[295-299], Cu[288,300], Mg[301,302], Ni[303] and intermetallics (γ-TiAl)[291]. It has been shown in case of Al-Mg alloy that the nanocrystalline microstructure

developed by ECAP can be useful till $0.5T_m$[296]. Furukawa et al.,[297] have shown that the Hall-Petch relation is valid till the finest crystallite size (~90nm) obtained by them by SPD. However, the Hall-Petch slope appears to decrease at fine grain sizes (Fig. 25) which has been attributed to the increased participation of mobile extrinsic dislocations in the boundary regions. An Al-Mg alloy (AZ91) has shown superplasticity with an elongation of 661% and a strain rate sensitivity of 0.3 at $0.5T_m$ after ECAP[302].

The principle of SPTS is illustrated in Fig. 26[46]. In this technique, high hydrostatic pressure of 5-15Gpa is applied at room temperature. An extension of the

solid solubility of Fe in Al to the extent of 2.2wt% has been observed by this technique due to nanocrystallization[283]. This has led to an increase in the microhardness values from 750 to 1750MPa[283]. Subsequent aging at 373K has led to a further increase in the microhardness to 3020MPa due to decomposition of the supersaturated solid solution[283]. A significant increase in the coercivity of Pr-Fe-B-Cu hard magnet has also been observed on SPTS[46].

8 Concluding Remarks

The present paper reviews some of the intriguing facets of the mechanical alloying (MA) and nanostructure formation that have emerged from recent works. The paper highlights the success of MA route in the synthesis of large number of intermetallics and solid solutions in several metallic systems. The works in this field have revealed that the various milling parameters, the milling temperatures, the nature of the product(s) and the presence of more than single phase during MA have a pronounced influence on the limiting grain size attainable by controlling the degree of coalescence of the grains. Present level of work identifies broadly three types of alloying mechanisms, *viz.* continuous diffusive (CD), self-sustaining reactions (SR) and the discontinuous additive (DA) mode. Studies have emphasized the role of enthalpy of formation, ΔH_f, and the ordering characteristics of the phases during alloying in some of the Al and Cu based systems. So far, the DA mechanism is evident only in the case of NiAl and NiAl$_3$ phase formation, having a very highly negative enthalpy (ΔH_f, of -72 and -39kJ mol^{-1} respectively) as well as an ordered structure in the as-milled state, while in the case of rest of the phases CD mechanism is observed. Studies also indicate a switch over from DA to CD mode on disordering of the as-milled NiAl by ternary additions. The kinetic analysis of the phase formation process during MA, on the other hand, shows that the effective mass transfer rate during MA by CD mode attains a value in between the volume diffusion and grain boundary diffusion, and the rate is not so sensitive to the milling intensity. Moreover, this rate in Cu-Ni, Cu-Zn and Cu-Al systems could be correlated with the melting temperature of the systems. It is also revealed that the enhanced rate of mass transfer caused by deformation during MA is inexplicable by the existing ballistic diffusion model. The success and advantages of the recently developed mechanical methods of porosity-free bulk nanostructure production *viz.* severe plastic deformation by torsion straining (STPS) and by equal-channel angular pressing (ECAP) have also been reviewed.

References

1　H Gleiter *Prog Mater Sci* 33 (1989) 223

2　B H Kear, R W Siegel and T Tsakalakos (Eds.) Proc First Int Conf Nanostructured Materials 1992 *Nanostructured Mater* 2 (1993)

3　H E Schaefer, R Wurschum, H Gleiter and T Tsakalakos (Eds.) Proc Second Int Conf on Nanostructured Materials 1994 *Nanostructured Mater* 6 (1995)

4　M L Trudeau, V Provenzano, R D Shull and J Y Ying Proc Third Int Conf on Nanostructured Materials (Nano'96) 1996 in *Nanostructured Mater* 9 (1997)

5　Nano'98

6　Nano'2000

7　L E McCandlish, B H Kear, D E Polk and R W Siegel (Eds.) MRS Symp Proc on Multicomponent Ultrafine Microstructures, Pittsburgh (PA), MRS 132 (1989)

8　D C V Aken (Ed.) *Symp Proc Microcomposites and Nanophase Materials* Warrendale (PA) TMS (1991)

9　G Kostorz, I Gorynin and V Trefilev (Eds.) Symp Proc Materials under Extreme Conditions and Nanophase Materials 1992 *Mater Sci Eng A* 168 (1993)

10　S Komarneni, J C Parker and G J Thomas (Eds.) MRS Symp. Proc Nanophase and Nanocomposite Materials Pittsburgh (PA) MRS 286 (1993)

11　R D Shull (Ed.) Symp Proc Nanophase and Nanocrystalline Structure Warrendale (PA) TMS (1993)

12　R D Shull (Ed.) Proc of Special Symp on Nanocrystalline Materials New York (NY) Pergamon Press (1993)

13　R D Shull and J M Sanchez (Eds.) Symp Proc on Nanophase and Nanocrystalline Materials Warrendale (PA) TMS (1994)

14　G C Hadjipanayis and R W Siegel (Eds.) Symp Proc on *Nanophase Materials - Structure, Properties and Applications* Kluwer Netherlands (1994)

15　R D Shull (Ed.) *Symp Proc on Structure and Properties of Nanophase Materials* 1995 *Nanostructured Mater* 7 (1996)

16　C Suryanarayana, J Singh and F H Froes (Eds.) *Symp Proc Processing and Properties of Nanocrystalline Materials* Warrendale (PA) TMS (1996)

17　D L Bourell (Ed.) *Symp Proc Synthesis and Processing of Nanocrystalline Powder* Warrendale (PA) TMS (1996)

18　C Suryanarayana *Bull Mater Sci* 17 (1994) 307

19　H Gleiter *Nanostructured Mater* 1 (1992) 1

20　H Gleiter *Nanostructured Mater* 6 (1995) 3

21　R W Siegel *Mater Sci Eng A* 168 (1993) 189

22　C Suryanarayana *Int Mater Rev* 40 (1995) 41

23　R Birringer *Mater Sci Eng A* 117 (1989) 33

24　R W Siegel *Ann Rev Mater Sci* 21 (1991) 559

25 V G Gryaznov and L I Trusov *Prog Mater Sci* **37** (1993) 289

26 C Suryanarayana and F H Froes *Metall Trans A* **23** (1992) 1071

27 R W Siegel *Nanostructured Mater* **4** (1994) 121

28 M N Ritter and T Abraham *Int J Powder Metall* **34** (1998) 33

29 J S Benjamin *Metall Trans* **1** (1970) 2943

30 C C Koch, O B Cavin, C G Mckamey and J O Scorbrough *Appl Phys Lett* **43** (1983) 1017

31 H J Fecht, E Hellstern, Z Fu and W L Johnson *Metall Trans A* **21** (1990) 2333

32 C C Koch *Materials Science and Technology – A Comprehensive Treatment* (Ed. R W Cahn) Weinheim VCH **15** (1991) 193

33 S K Pabi and A Das, *Metals Mater Processes* **9** (1997) 229

34 B S Murty and S Ranganathan *Int Mater Rev* **43** (1998) 101

35 C C Koch *Nanostructured Mater* **2** (1993) 109

36 A R Yavari *Mater Trans JIM* **36** (1995) 228

37 E Gaffet, M Abdellaoui and N M Gaffet *Mater Trans JIM* **36** (1995) 198

38 H J Fecht *Nanostructured Mater* **1** (1992) 125

39 C C Koch and Y S Cho *Nanostructured Mater* **1** (1992) 207

40 H J Fecht *Nanostructured Mater* **6** (1995) 33

41 C C Koch *Nanostructured Mater* **9** (1997) 13

42 C C Koch *Mater Sci Eng A* **244** (1998) 39

43 C C Koch and J D Whittenberger *Intermetallics* **4** (1996) 339

44 D A Rigney *Ann Rev Mater Sci* **18** (1988) 141

45 A E Berkowitz and J L Walter *J Mater Res* **2** (1987) 277

46 V V Stolyarov and R Z Valiev *Mater Sci Forum* **307** (1999) 185

47 M Atzmon, J D Veerhoven, E D Gibson and W L Johnson *Appl Phys Lett* **45** (1984) 1052

48 L Schultz *Rapidly Quenched Metals* V (Eds. S Steeb and H Warlimont) Amsterdam North-Holland (1984) 1585

49 A Sagel, H Sieber, H J Fecht and J H Perepezko *Acta Mater* **46** (1998) 4233

50 F Boordeaux and A R Yavari *J Appl Phys* **67** (1990) 2385

51 A Calka and A P Radlinski *Mater Sci Eng* A **134** (1991) 1350

52 V Arnhold, J Baumgarten and H C Neubing *Proc World Conf Powder Metallurgy* (PM'90), London UK The Institute of Metals **2** (1990) 259

53 W E Kuhn, I L Friedman, W Summers and A Szegvari *Metals Handbook, Powder Metallurgy* Metals Park Ohio ASM **7** (1985) 56

54 I Kerr *Metal Powder Rep* **48** (1993) 36

55 R B Schwarz and C C Koch *Appl Phys Lett* **49** (1986) 146

56 M Abdellaoui and E Gaffet *J All Comp* **209** (1994) 351

57 M Abdellaoui and E Gaffet *Acta Metall Mater* **43** (1995) 1087

58 T H Courtney *Mater Trans JIM* **36** (1995) 110

59 M Magini and A Iasonna *Mater Trans JIM* **36** (1995) 123

60 T H Courtney and D Maurice *Scripta Mater* **34** (1996) 5

61 E Gaffet, N Malhouroux and M Abdellaoui *J All Comp* **194** (1993) 339

62 R Watanabe, H Hashimoto and G G Lee *Mater Trans JIM* **36** (1995) 102

63 E Gaffet *Mater Sci Eng A* **132** (1991) 181

64 C Suryanarayana and F H Froes *J Mater Res* **5** (1990) 1880

65 A Calka and A P Radlinski *Appl Phys Lett* **58** (1991) 119

66 A W Weeber, A J H Wester, W J Haag and H Bakker *Physica B* **145** (1987) 349

67 M S El-Eskandarany, K Aoki and K Suzuki *J Less Common Metals* **167** (1990) 113

68 M Abdellaoui and E Gaffet *Acta Metall Mater* **44** (1996) 725

69 D Basset, P Matteazzi and F Miani *Mater Sci Eng A* **168** (1993) 149

70 T Aizawa, K Tatsuzawa and J Kihara *Proc 1993 Powder Metallurgy World Congress* (Eds. Y Bando and K Kosuge) Kyoto Japan *Jap Soc Powder and Powder Metallurgy* (1993) 96

71 M Martin and E Gaffet *Colloque de Phys* **51** (1990) 71

72 E Hellstern, H J Fecht, C Garland and W L Johnson *J Appl Phys* **65** (1989) 305

73 E Hellstern, H J Fecht, C Garland and W L Johnson *MRS Symp Proc* **132** (1989) 137

74 J Eckert, J C Holzer, C E Krill III and W L Johnson *J Mater Res* **7** (1992) 1992

75 D Oleszak and P H Shingu *J Appl Phys* **79** (1996) 2975

76 J Joardar, S K Pabi and B S Murty *Proc Int Conf on Recent Adv Metallur Process* (Eds. D H Sastry, E S Dwarakadasa, G N K Iyengar and S Subramanian) New Age Int Publ New Delhi India **1** (1997) 647

77 G B Schaffer and J S Forrester *J Mater Sci* **32** (1997) 3157

78 B S Murty, J Joardar and S K Pabi *Nanostructured Mater* **7** (1996) 691

79 B S Murty, D Das, I Manna and S K Pabi *Acta Mater* (Communicated)

80 S K Pabi, J Joardar and B S Murty *J Mater Sci* **31** (1996) 3207

81 K H S Singh *Production of Nanocrystalline Nickel Aluminides by Mechanical Alloying* M Tech Thesis, Indian Institute of Technology Kharagpur India (1995)

82 R Birringer *Mater Sci Eng A* **117** (1989) 33

83 R D Noebe, R R Bowman and M V Nathal *Int Mater Rev* **38** (1993) 193

84 D B Miracle *Acta Metall Mater* **41** (1993) 649

85 S K Pabi, D Das, T K Mahapatra and I Manna *Acta Mater* **41** (1998) 3501

86 K Yamada and C C Koch *J Mater Res* **8** (1993) 1317

87 T D Shen and C C Koch *Mater Sci Forum* **179-181** (1995) 17

88 D K Pathak, Ph D Thesis North Carolina State University Raleigh USA (1995)

89 R L White Ph D Thesis Stanford University Stanford USA (1979)

90 R M Davis M S Thesis North Carolina State University Raleigh USA (1987)

91 B T Mcdermott M S Thesis North Carolina State University Raleigh USA (1988)

92 H Kimura and M Kimura *Solid State Powder Processing* (Ed. A H Clauer and J J Debarbadillo) Warrendale (PA) TMS-AIME (1990) 365

93 A B Borzov and E Y Kaputkin *Mechanical Alloying Structural Applications* (Eds. J J deBarbadillo and A H Clauer) Addendum Materials Park Ohio ASM International (1993)

94 C C Koch *Int J Mechanochem Mech Alloying* 1 (1994) 56

95 E T B Levinson, A A Kolesnikov and I V Fine *Mater Sci Forum* **88-90** (1992) 113

96 A E Yermakov, E E Yurchikov and V A Barinov *Phys Met Metall* **52** (1981) 50

97 A E Yermakov, V A Barinov and E E Yurchikov *Phys Met Metall* **54** (1982) 935

98 R M Davis and C C Koch *Scripta Metall* **21** (1987) 305

99 D R Maurice and T H Courtney *Metall Trans* A **21** (1990) 289

100 M Magini, N Burgio, A Iasonna, S Martelli, F Padella and E Paradiso *J Mater Syn Proc* 1 (1993) 135

101 A K Bhattacharya and E Arzt *Scripta Metall Mater* **27** (1992) 749

102 P J Miller, C S Coffey and V F Devost *J Appl Phys* **59** (1986) 913

103 J S Benjamin *Sci Am* **234** (1976) 40

104 W Schlump and H Grewe *New Materials by Mechanical Alloying* (Eds. E Arzt and L Schultz) Oberursel Germany Deutsch Gesellschaft Fuer Metallkunde (1989) 307

105 L Schultz *Mater Sci Eng A* **97** (1988) 15

106 H J Fecht, E Hellstern, Z Fu and W L Johnson *Metall Trans A* **21** (1990) 2333

107 T R Malow and C C Koch *Acta Mater* **45** (1997) 2177

108 C Moelle and H J Fecht *Nanostructured Mater* **6** (1995) 421

109 R Z Valiev, R S Mishral, J Grozal and A K Mukherjee *Scripta Mater* **34** (1996) 1443

110 J Xu, J S Yin and E Ma *Nanostructured Mater* **8** (1997) 91

111 E Gaffet and M Harmelin *J Less Common Metals* **157** (1990) 201

112 T D Shen, C C Koch, T L McCormick, R J Nemanich, J Y Huang and J P Huang *J Mater Res* **10** (1995) 139

113 T D Shen, W Q Ge, K Y Wang, M X Quan, J T Wang, W D Wei and C C Koch *Nanostructured Mater* **7** (1996) 393

114 H Hermann, T Schubert, W German and N Maltern *Nanostructured Mater* **8** (1997) 215

115 B E Warren and B L Averback *J Appl Phys* **21** (1950) 595

116 G K Williamson and W H Hall *Acta Metall* **1** (1953) 22

117 T G Nieh and J Wadsworth *Scripta Metall Mater* **25** (1991) 955

118 J Eckert, J C Holzer, C E Krill III and W L Johnson *J Mater Res* **7** (1992) 1980

119 T D Shen and C C Koch *Acta Mater* **44** (1996) 753

120 M Oehring and R Bormann *Mater Sci Eng A* **134** (1991) 1330

121 B S Murty, M Mohan Rao and S Ranganathan *Nanostructured Mater* **3** (1993) 459

122 B S Murty, M D Naik, S Ranganathan and M Mohan Rao *Mater Forum* **16** (1992) 19

123 R Nagarajan, B S Murty and S Ranganathan *Chinese J Mater Res* (1994) 215

124 T B Massalski (Ed) Binary Alloy Phase Diagrams ASM Metals Park OH (1986)

125 K Uenishi, K F Kobayashi, K N Ishihara and P M Shingu *Mater Sci Eng A* **134** (1991) 1342

126 F H Froes, C Suryanarayana, K Russell and C G Li *Mater Sci Eng A* **192/193** (1995) 612

127 K F Kobayashi, N Tachibana and P H Shingu *J Mater Sci* **25** (1990) 3149

128 C Suryanarayana and R Sundaresan *Mater Sci Eng A* **131** (1991) 237

129 C Suryanarayana *Metals and Mater* **2** (1996) 195

130 T Tanaka, K N Ishihara and P H Shingu *Metall Trans A* **23** (1992) 2431

131 J Eckert, L Schultz and K Urban *Europhys Lett* **13** (1990) 349

132 J Y Huang, Y D Yu, Y K Wu, D X Li and H Q Ye *J Mater Res* **12** (1997) 936

133 S Enzo, R Frattini, R Gupta, P P Marci, G Principi, L Schiffini and G Scipione *Acta Mater* **44** (1996) 3105

134 A Hightower, B Fultz and R C Bowman Jr *J All Comp* **252** (1997) 238

135 M Abdellaoui, T Barradi and E Gaffet *J All Comp* **198** (1993) 155

136 M Abdellaoui, C M Djega and E Gaffet *J All Comp* **259** (1997) 241

137 V K Portnoy, V I Fadeeva and I N Zaviyalova *J All Comp* **224** (1995) 159

138 G Walkowiak, T Sell and H Mehrer *Z Metallkde* **85** (1994) 332

139 M Hida, K Asai, Y Takemoto and A Sakakibara *Mater Sci Forum* **235-238** (1997) 187

140 H J Fecht, G Han, Z Fu and W L Johnson *J Appl Phys* **67** (1990) 1744

141 B S Murty and S K Pabi *(unpublished work)*

142 K Uenishi, K F Kobayashi, K Nasu, H Hatemo, K N Ishihara and P M Shingu *Z Metallkde* **83** (1992) 132

143 A R Yavari, P J Desre and T Benameur *Phys Rev Lett* **68** (1992) 2235

144 J Eckert, J C Holzer, C E Krill III and W L Johnson *J Appl Phys* **73** (1993) 2794

145 E Ma, M Atzmon and F E Pinkerton *J Appl Phys* **74** (1993) 955

146 E Gaffet, M Harmelin and F Faudot *J All Comp* **194** (1993) 23

147 J Y Huang, A Q He, Y K Wu, H Q Ye and D X Li *J Mater Sci* **31** (1996) 4165

148 B Mazumdar, M M Raja, A Narayanaswamy and K Chattopadhyay *J All Comp* **248** (1997) 192

149 E Gaffet, C Louison, M Hermelin and F Faudot *Mater Sci Eng A* **134** (1991) 1380

150 C S Xiong, Y H Xiong, H Zhu, T F Sun, E Dong and G X Liu *Nanostructured Mater* **5** (1995) 425

151 F Fukunaga, M Mori, K Inoue and M Mizutani *Mater Sci Eng A* **134** (1991) 863

152 K Sakurai, M Mori and U Mizutani *Phys Rev B* **46** (1992) 5711

153 K Sakurai, Y Yanada, C H Lee, T Fukunaga and U Mizutani *Mater Sci Eng A* **134** (1991) 1414

154 G Veltl, B Scholz and H D Kunze *Mater Sci Eng A* **134** (1991) 1410

155 T Fukunaga, K Nakamura, K Suzuki and U Mizutani *J Non-Cryst Sol* **117/118** (1990) 700

156 J G C Moreno, V M Lopez, H H A Calderon and J C Angels *Scripta Metall Mater* **28** (1993) 645

157 M Baricco, N Cowlam, L Schiffini, P P Maira, R Frattini and S Enzo *Phil Mag B* **68** (1993) 957

158 C Gente, M Oehring and R Bormann *Phys Rev A* **48** (1993) 13244

159 J Y Huang, Y K Wu, A Q He and H Q Ye *Nanostructured Mater* **4** (1994) 293

160 A R Yavari *Mater Sci Eng A* **179/180** (1994) 20

161 J Y Huang, A Q He and Y K Wu *Nanostructured Mater* **4** (1994) 1

162 B L Huang, R J Perez, E J Lavernia and M J Luton *Nanostructured Mater* **7** (1996) 69

163 J Y Huang, Y D Yu, Y K Wu, D X Li and H Q Ye *Acta Mater* **45** (1997) 113

164 R Bohn, T Hanbold, R Birringer and H Gleiter *Scripta Metall Mater* **25** (1991) 811

165 J S C Jang and C C Koch *Scripta Metall Mater* **24** (1990) 1599

166 S Dymek, M Dollar, S J Hwang and P Nash *Mater Sci Eng A* **152** (1992) 160

167 M Jain and T Christman *Acta Metall Mater* **42** (1994) 1901

168 E Ivanov, T Grigorieva, G Gdubkova, V Boldyrev, A B Fasman, S D Mikhailenko and O T Kalimna *Mater Lett* **7** (1988) 51

169 B S Murty, K H S Singh and S K Pabi *Bull Mater Sci* **19** (1996) 565

170 M Atzmon *Phys Rev Lett* **64** (1990) 487

171 T Itsukaichi, M Umemoto and J G C Moreno *Scripta Metall Mater* **29** (1993) 583

172 F Cardellini, G Mazzone, A Montone and M V Antisari *Acta Metall Mater* **42** (1994) 2445

173 B L Huang, J Vallone and M J Luton *Nanostructured Mater* **5** (1995) 411

174 R Maric, K N Ishihara and P H Shingu *J Mater Sci Lett* **15** (1996) 1180

175 Z G Liu, J T Guo and Z A Hu *Mater Sci Eng A* **192/193** (1995) 577

176 S K Pabi and B S Murty *Mater Sci Eng A* **214** (1996) 146

177 M Oehring, Z H Yan, H Klassen and R Bormann *Phys Stat Solidi (a)* **131** (1992) 671

178 B S Murty Ph D Thesis Indian Institute of Science Bangalore India (1992)

179 R C Baun, P K Mirchandani and A S Watwe *Proc Mod Dev Powder Metallurgy* APMI **18** (1988) 479

180 K Y Lee, H K Cho and J H Ahn *J Mater Sci Lett* **15** (1996) 1324

181 C Suryanarayana, G H Chen, A Frefer and F H Froes *Mater Sci Eng A* **158** (1992) 93

182 W Guo, S Martelli, N Burgio, M Magini, F Padella, E Padadiso and I Soleta *J Mater Sci* **26** (1990) 6190

183 Y H Park, H Hashimoto and R Watanabe *Mater Sci Forum* **88-90** (1992) 59

184 C Suryanarayana, R Sundaresan and F H Froes *Mater Sci Eng A* **150** (1992) 117

185 M A Morris and D G Morris *Mater Sci Eng A* **136** (1991) 59

186 M A Morris and D G Morris *Mater Sci Forum* **88-90** (1992) 529

187 G H Fair and J V Wood *Powder Metall* **36** (1993) 123

188 F Cardellini, V Contini and G Mazzone *J Mater Sci* **31** (1996) 4175

189 F R de Boer, R Boom, W C M Mattens, A R Miedema and A K Niessen *Cohesion in Metals - Transition Metal Alloys Cohesion and Structure* (Eds. F R deBoer and D G Pettifor) North-Holland Publications Co Amsterdam Holland **1** (1988)

190 L M Di, H Bakker and F R de Boer *Physica B* **182** (1992) 91

191 S X J Zhou, D Zhang and X Wang *Mater Lett* **26** (1996) 245

192 R B Schwarz, S Srinivasan and P B Desch *Mater Sci Forum,* **88-90** (1992) 595

193 D C Crew, P G Mccormic and R Street *Scripta Metall Mater* **32** (1995) 315

194 M R Pachauri, D L Zhang and T B Massalski *Mater Sci Eng A* **174** (1994) 119

195 Z Zdujic, D Poleti, L Karanovic, K F Kobayashi and P H Shingu *Mater Sci Eng A* **185** (1994) 77

196 Z Peng, C Suryanarayana and F H Froes *Metall Mater Trans A* **27** (1996) 41

197 H J Ahn and K Y Lee *Mater Trans JIM* **36** (1995) 297

198 S Kawanashi, K Ionishi and K Okazaki *Mater Trans JIM* **34** (1993) 43

199 J Saida, Y Tanaka and K Okazaki *Mater Trans JIM* **37** (1996) 265

200 C Rock and K Okazaki *Nanostructured Mater* **5** (1995) 643

201 L Schultz, E Hellstern and G Zorn *Z Phys Chem* **157** (1988) 203

202 H Schropf, C Kuhrt, E Arzt and L Schultz *Scripta Metall Mater* **30** (1994) 1569

203 J G C Moreno, T Itsukaichi and M Umemoto *Mater Sci Eng A* **181/182** (1994) 1202

204 C Suryanarayana, W Li and F H Froes *Scripta Metall Mater* **31** (1994) 1465

205 G H Chen, C Suryanarayana and F H Froes *Scripta Metall* **25** (1991) 2537

206 R Radhakrishnan, S Bhaduri and C H Hanegar Jr *J Metals* **49** (1997) 41

207 A P Radlinski and A Calka *Mater Sci Eng A* **134** (1991) 1376

208 K Omuro and H Miura *J Appl Phys* **30** (1991) L851

209 M K Datta, S K Pabi and B S Murty *(unpublished work)*

210 M Gaffet and E Gaffet *J All Comp* **198** (1993) 143

211 A G Escorial, P Adveda, M C Cristina, A Martin, F Carmona, F Cebollada, V E Martin, M Leonato and J M Gonzalez *Mater Sci Eng A* **134** (1991) 1394

212 O Kohmoto, N Yamaguchi and T Mori *J Mater Sci* **29** (1994) 3221

213 M Abdellaoui, E Gaffet, T Barradi and F Faudot *IEEE Trans Mag* **30** (1994) 4887

214 M Umemoto *Mater Trans JIM* **36** (1995) 373

215 G Veltl, B Scholz and H D Kunze *New Materials by Mechanical Alloying* (Eds. E Arzt and L Schultz) Deutsch Gesellschaft fur Metallkunde Oberursel Germany (1989) 79

216 D Parlapanski, S Denev, S Ruseva and E Gatev *J Less Common Metals* **171** (1991) 231

217 M Oehring and R Bormann *Mater Sci Eng A* **134** (1991) 1330

218 H Park, H Hashimoto and R Watanabe *Mater Sci Eng A* **181/182** (1994) 1212

219 N Zotov and D Parlapanski *J Mater Sci* **29** (1994) 2813

220 R B Schwarz, S R Srinivasan, J J Petrovic and C J Maggiore *Mater Sci Eng A* **155** (1992) 75

221 L Liu, F Padella, W Guo and M Magini *Acta Metall Mater* **43** (1995) 3755

222 P Y Lee, T R Chen, J L Yang and T S Chin *Mater Sci Eng A* **192/193** (1995) 556

223 J Liu and M Magini *J Mater Res* **12** (1997) 2281

224 M Magini, N Basili, N Burgio, G Ennas, S Martelli, F Padella, E Paradiso and P Susini *Mater Sci Eng A* **134** (1991) 1406

225 T Nasu, K Nagaoka, T Takahashi, T Fukunaga and K Suzuki *Mater Trans JIM* **30** (1989) 146

226 D L Zhang and T B Massalski *J Mater Res* **9** (1994) 53

227 R K Viswanandhan, S K Mannan and S Kumar *Scripta Metall* **22** (1988) 1011

228 T Lou, G Fau, B Ding and Z Hu *J Mater Res* **12** (1997) 1172

229 K S Kumar and S K Mannan *MRS Symp Proc MRS* Pittsburgh PA **133** (1989) 415

230 B T Mcdermott and C C Koch *Scripta Metall* **20** (1986) 669

231 F Cardellini, V Contini, G Mazzone and M Vittori *Scripta Metall Mater* **28** (1993) 1035

232 H Kimura, M Kimura and F Takada *J Less Common Metals* **140** (1988) 113

233 R L White and W D Nix *New Developments and Applications in Composites*, (Eds. D K Wilsdorf and W C Harrigan) Warrendale (PA) TMS (1979) 78

234 M S Kim and C C Koch *J Appl Phys* **62** (1987) 3450

235 T Tanaka, K N Ishihara and P H Shingu *Metall Trans A* **23** (1992) 2431

236 K Tokumitsu *Mater Sci Forum* **235-238** (1997) 127

237 L Li and J Jang *J All Comp* **209** (1994) L1

238 H Huang and P G Mccormick *J All Comp* **256** (1997) 258

239 M A Morris and D G Morris *Solid State Powder Processing* (Eds. A H Clauer and J J Debarbadillo) Warrendale (PA) TMS-AIME, 299 (1990)

240 C W Pan, M P Hung and Y H Chang *Mater Sci Eng A* **185** (1994) 147

241 L B Hong, C Bausal and B Fultz *Nanostructured Mater* **4** (1994) 949

242 M L Trudeau, R Schulz, L Zaluski, S Hosatte, D H Ryan, C B Doner, P Tessier, J O Strom-Olsen and A V Neste *Mater Sci Forum* **88-90** (1992) 537

243 C R Clark, C Wright, C Suryanarayana, E G Baburaj and F H Froes *Mater Lett* **33** (1997) 71

244 L Aymard, M Ichitsubo, K Uchida, E Sekreta and F Ikazaki *J All Comp* **259** (1997) L5

245 A Corrias, G Ennas, G Morangiu, A Musinu, G Paschina and D Zedda *Mater Sci Eng A* **204** (1995) 211

246 M S El-Eskandarany *Metall Mater Trans A* **27** (1996) 2374

247 A Teresiak, N Mattern, H Kubsch and B F Kieback *Nanostructured Mater* **4** (1994) 775

248 L L Ye, J Y Huang, Z G Liu, M X Quan and Z Q Hu *J Mater Res* **11** (1996) 2092

249 Z H Yan, M Oehring and R Bormann *J Appl Phys* **72** (1992) 2478

250 M A Morris *J Mater Sci* **26** (1991) 1157

251 M Zhu, B L Li, Y Gao, L Li, K C Luo, H X Sui and Z X *Scripta Metall Mater* **36** (1997) 447

252 V Provenzano and R L Holtz *Mater Sci Eng A* **204** (1995) 125

253 Y Du, S Li, K Zhang and K Lu *Scripta Metall Mater* **36** (1997) 7

254 J Naser, W Reinhemann and H Ferkel *Mater Sci Eng A* **234** (1997) 467

255 N Q Wu, J M Wu, G X Wang and Z Z Li *Mater Lett* **32** (1997) 259

256 K Liu, J Zhang, J Wang and G Chen *Scripta Metall Mater* **36** (1997) 1113

257 O N Senkov, F H Froes and E G Baburaj *Scripta Mater* **37** (1997) 575

258 T Kaneyoshi, T Takahashi, Y Hayashi and M Motayama (Eds. E D Capus and R M German) *Proc 1992 Powder Metallurgy World Congress* New Jersey Metal Powder Industries Federation 7 (1992) 421

259 I Manna, P P Chatterjee, V Srinivasa Rao and S K Pabi *Scripta Mater* **40** (1999) 409

260 Th Pfullmann, M Oehring, R Bohn and R Bormann *Mater Sci Forum* **225-227** (1996) 757

261 A K Bhattacharya and E Arzt *Scripta Metall Mater* **27** (1992) 635

262 J Zbiral, G Jangg and G Korb *Mater Sci Forum* **88-90** (1992) 19

263 R C Weast (Ed) CRC Handbook of Chemistry and Physics 58th Edn CRC Press Ohio (1977) F-62

264 S K Pabi, J Joardar, I Manna and B S Murty *Nanostructured Mater* **9** (1997) 149

265 Z G Liu, J T Guo, L L He and Z Q Hu *Nanostruct Mater* **7** (1994) 787

266 K A Philpot, Z A Munir and J B Holt *J Mater Sci* **22** (1987) 159

267 U A Tamburini and Z A Munir *J Appl Phys* **66** (1989) 5039

268 S K Pabi, I Manna and B S Murty *Bull Mater Sci* **22** (1999) 101

269 R W Balluffi and A L Rouff *Appl Phys Lett* **1** (1962) 59

270 H Gleiter *Acta Metall* **16** (1967) 455

271 S K Pabi *Phys Status Solidi (a)* **51** (1979) 281

272 K Lu, *Mater Sci Eng R* **16** (1996) 161

273 J Eckert, L Schultz and E Hellstern *J Appl Phys* **64** (1988) 3224

274 M L Trudeau, R Schulz, D Dusault and A V Neste *Phys Rev Lett* **64** (1990) 99

275 C Bansal, B Fultz and W L Johnson *Nanostructured Mater* **4** (1994) 919

276 B Huang, R J Perez, P J Crawford, A A Sharif, S R Nutt and J Lavernia *Nanostructured Mater* **5** (1995) 545

277 M L Trudeau *Appl Phys Lett* **64** (1994) 3661

278 R Sh Musalimov and R Z Valiev *Scripta Metall Mater* **27** (1992) 1685

279 R Z Valiev, A V Koznikov and R R Mulyukov *Mater Sci Eng A* **168** (1993) 141

280 J Languillaume, F Chemilik, G Kapelski, F Bordeaux, A A Nazarov, G Canova, C Esling, R Z Valiev and B Baudelet *Acta Mater* **41** (1993) 2953

281 Y Ma, Z Horita, M Furukawa, M Nemoto, R Z Valiev and T G Langdon *Mater Lett* **23** (1995) 283

282 Y V Ivanisenko, A V Korznikov, I M Safarov and R Z Valiev *Nanostructured Mater* **6** (1995) 433

283 O N Senkov, F H Froes, V V Stolyarov, R Z Valiev and J Liu *Nanostructured Mater* **10** (1998) 691

284 V M Segal, V I Rexnikov, A E Drobyshevsky and V I Kopylov *Russian Metallurgy* **1** (1981) 99

285 R Z Valiev, R R Mulyukov, V V Ovchinnikov and V A Shabashov *Scripta Metall Mater* **25** (1991) 841

286 N A Akhmadeev, V I Kopylov, R R Mulyukov and R Z Valiev *Izvest Akad Nauk SSSR Metally* **5** (1992) 96

287 K Y Mulyukov, S B Kaphizov and R Z Valiev *Phys Status Sol (a)* **133** (1992) 447

288 N A Akhmadeev, N P Kobelev, R R Mulyukov, Y M Soifer and R Z Valiev *Acta Metall Mater* **41** (1993) 1041

289 J Wang, Z Horita, M Furukawa, M Nemoto, N K Tsenev, R Z Valiev, Y Ma and T G Langdon *J Mater Res* **8** (1993) 2810

290 V M Segal *Mater Sci Eng A* **197** (1995) 157

291 S L Semiatin, V M Segal, R L Goetz, R E Goforth and T Hartwig *Scripta Metall Mater* **33** (1995) 535

292 Y Iwahashi, J Wang, Z Horita, M Nemoto and T G Langdon *Scripta Mater* **35** (1996) 143

293 Y Iwahashi, Z Horita, M Nemoto and T G Langdon, *Acta Mater* **46** (1998) 3317

294 R Z Valiev and R Sh Musalimov *Phys Metal Metall* **78** (1994) 666

295 J Wang, M Furukawa, Z Horita, M Nemoto, R Z Valiev and T G Langdon *Mater Sci Eng A* **216** (1996) 41

296 J Wang, Y Iwahashi, Z Horita, M Furukawa, M Nemoto, R Z Valiev and T G Langdon *Acta Mater* **44** (1996) 2973

297 M Furukawa, Z Horita, M Nemoto, R Z Valiev and T G Langdon *Acta Mater* **44** (1996) 4619

298 M Kawazoe, T Shibata, T Mukai and K Higashi *Scripta Mater* **36** (1997) 699

299 Y Iwahashi, Z Horita, M Nemoto and T G Langdon *Acta Mater* **45** (1997) 4733

300 R Z Valiev, E V Kozlov, Y F Ivanov, J Lian A A Nazarov and B Baudelet *Acta Metall Mater* **42** (1994) 2467

301 M Mabuchi, H Iwasaki and K Higashi *Mater Sci Forum* **243-245** (1997) 547

302 M Mabuchi, H Iwasaki, K Yanase and K Higashi *Scripta Mater* **36** (1997) 681

303 V M Segal *Mater Sci Eng A* **197** (1995) 157

NANOCRYSTALLINE SOFT-MAGNETIC ALLOYS PRODUCED BY CONTROLLED CRYSTALLIZATION OF AMORPHOUS ALLOYS

AJAY GUPTA

Inter-University Consortium for DAE Facilities, University Campus, Khandwa Road, Indore-452 017 (India)

A controlled partial crystallisation of FeSiB alloy with small amounts of Cu and Nb results in formation of nanocrystalline grains dispersed in a residual amorphous matrix. Both the nanocrystals as well as the amorphous matrix are ferromagnetic at room temperature. This composite material posses excellent soft magnetic properties, which even surpass those of transition metal-metalloid metallic glasses. The present article reviews the formation, structure and magnetic properties of such alloys. Although a number of other amorphous alloys also have been found to result in nanocrystalline phase formation, most of the examples taken in this article are for the system FeCuNbSiB which happens to be the most promising system from the application point of view.

Key Words: Alloys; Nanocrystalline; Metallic Glasses; Crystallization; Microstructure; Soft-Magnetic Material; Coercivity; Anisotropy; Superparamagnetism

1 Introduction

Development of soft magnetic materials with large saturation magnetisation B_s, high effective permeability μ_e and low coercive field H_c is an important area of research and development. Efforts are being made to achieve better soft magnetic properties in order to conserve energy by reducing the losses in transformer cores and also for the achievement of higher efficiency and resultant miniaturisation of electronic components[1]. This involves developing new compositions as well as microstructures. In addition to improving the properties of conventional crystalline soft magnetic materials, efforts are being made to develop metastable structures with improved soft magnetic properties. For example, the technique of rapid quenching from melt has been used in order to achieve Fe-Si alloys with enhanced Si solubility. In early 70's, development of transition metal-metalloid type of metallic glasses using melt-spinning technique was a major advance towards achieving better soft magnetic properties in metastable/non-equilibrium alloy phases. The metallic glass composition suitable for soft magnetic applications are either based on Fe or on Co. The Fe based amorphous alloys possess high saturation magnetisation but at the same time they have high magnetostriction, thus resulting in strong stress induced anisotropy causing the coercive field to increase. On the other hand Co based amorphous alloys can have almost zero magnetostriction but their saturation magnetisation is relatively low as compared to Fe based alloys. Thus a compromise between high saturation magnetisation and low coercive field has to be reached. In late 80s Yoshizawa et al., discovered another class of non-equilibrium microstructure[2,3] consisting of nanocrystalline grains dispersed in amorphous matrix (Fig.1) which possess soft magnetic properties far superior to those of amorphous alloys. Yoshizawa et al., found that FeSiB alloy containing small amount of Cu and Nb, when subjected to controlled partial crystallisation resulted in precipitation of a primary Fe-Si crystalline phase with grain size ~ 10nm. This composite structure consisting of nanocrystalline grains of Fe-Si alloy dispersed in the remaining amorphous matrix was found to possess a unique combination of low losses, high permeability and nearly zero magnetostriction similar to the Co based amorphous alloy, but at the same time possessing a very high saturation magnetisation of upto 1.3 Tesla which is even better than that possessed by Fe based amorphous alloys. This result was some what unexpected because it is well known that the crystallisation of amorphous alloys optimised for soft magnetic application results in drastic deterioration of their soft magnetic properties. Further, the combination of small grain size and soft magnetic properties is rather surprising because generally particle size reduction is done in order to improve the hard magnetic properties. The reduction
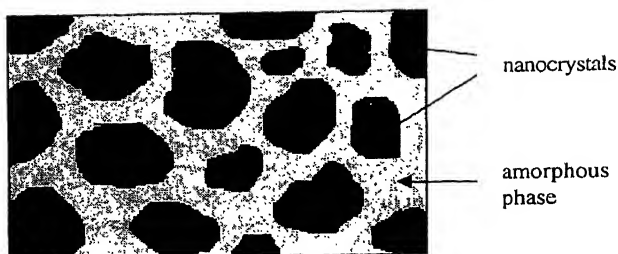
Fig. 1 Schematic presentation of the microstructure of nanocrystalline alloys

Fig. 2 Grain size dependence of the coercivity H_c of various soft magnetic materials[4]

of particle size to the regime of the domain wall size is a well known approach to subdivide the material into single domain particles, which increases the coercive field H_c towards a maximum value determined by the anisotropy present. However, if the particle size is reduced further, the coercivity decreases again due to thermal effects. This point becomes clear from the Fig. 2 where coercive field is plotted as a function of grain size for different magnetic materials[4]. Conventionally, in order to increase the soft magnetic property, attempts have been to make the grain size as large as possible so as to obtain low coercivities and high permeability. However, from Fig. 2, it is evident that low coercivity can also be achieved by going to particle size of a few tens of nanometers. This situation is realised in the case of superparamagnetic particles where the coercivity decreases because of thermal excitations in isolated or weakly coupled particles.

In the superparamagnetic regime although the coercivity vanishes, the permeability also goes down drastically, as large magnetic fields are needed to produce appreciable change in magnetisation. Thus, superparamagnetic nanocrystalline particles with weak intergranular magnetic interactions are not good soft magnetic materials. In contrast to this, in the case of nanocrystalline alloys produced by partial crystallisation of amorphous phase, strong magnetic interaction between individual grains exists via the intervening amorphous matrix, and thus at room temperature the grains are aligned ferromagnetically with respect to each other. Magnetic softening occurs because the grain size as well as the intergranular spacing is smaller than the ferromagnetic exchange length, so that the local anisotropies are randomly averaged out by the exchange interaction and the average anisotropy becomes very low[5]. The role of intergranular interaction via the amorphous matrix is evident from the temperature dependence of the
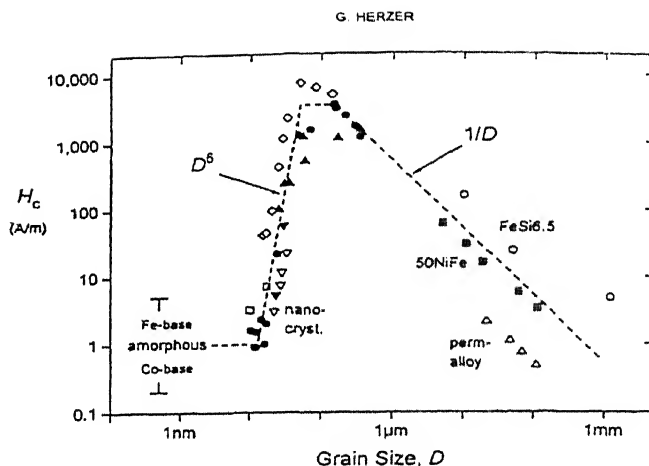
coercive field as well as the initial permeability as depicted in Fig. 3. Further the magnetostriction of the amorphous and nanocrystalline phases being opposite in sign, they tend to cancel each other and therefore, the average magnetostriction of this composite material decreases with progressive degree of nanocrystallisation (Fig. 4), and thus, a very low magnetostriction is achieved for optimum volume fraction of nanocrystalline phase[6]. Thus, the peculiar soft magnetic properties of this composite material arise as a result of combined magnetic response of the nanocrystalline grain and amorphous matrix, which are both in ferromagnetic state at room temperature.

The pioneering work of Yoshizawa et al. has lead to intensive activities in this field aiming at developing

Fig. 3 Temperature dependence of the coercive field H_c and initial permeability μ_i of nanocrystalline $Fe_{73.5}Cu_1Nb_3Si_{13.5}B_9$ [4]

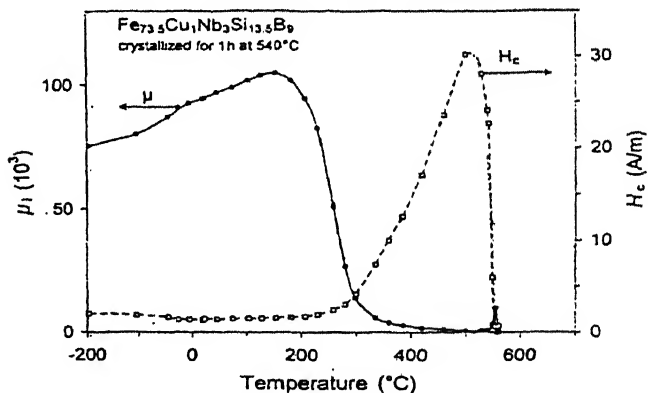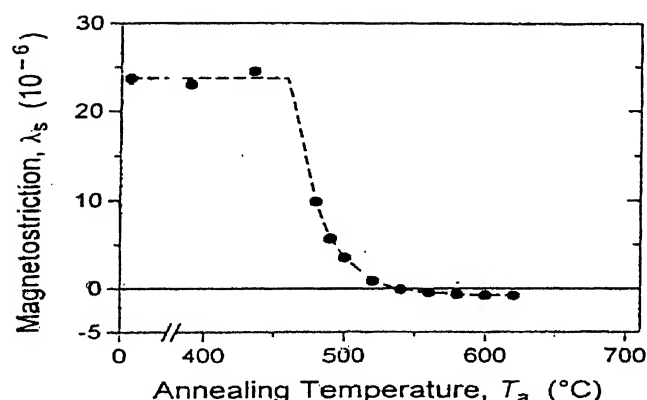Fig. 4 The saturation magnetostriction l_s of $Fe_{73.5}Cu_1Nb_3Si_{16.5}B_6$ as a function of increasing degree of nanocrystallization achieved by annealing at successively higher temperature (T_a) for 1 h

a detailed understanding of the formation of nanocrystalline phase, and their unique magnetic properties. Extensive efforts are also being made for finding alternative alloy compositions. In addition to FeCuNbSiB alloys, a number of other amorphous alloy compositions like FeZrB[6], FeHfC[7] have been found which also exhibit similar nanocrystallisation behaviour and improved soft magnetic properties. From the application point of view efforts are also being made to improve the mechanical properties of nanocrystalline alloys; the nanocrystalline alloys achieved through conventional heat treatment are extremely brittle and thus very difficult to handle. It has been shown that nanocrystallisation achieved through Joule heating by passing an electrical current of sufficient density through the sample results in nanocrystallisation with improved ductility[8]. For some specific applications material with anisotropies along specific directions are desirable. Various external perturbations like magnetic field and stress application during nanocrystallisation have been used to induce such anisotropy[9,10].

2 Formation of Nanocrystalline Phase

Although nanocrystalline alloys can be produced in a variety of ways like, gas phase condensation, plasma processing, mechanical alloying, etc., however, the requirements of a strong intergranular magnetic interaction and other microstructural requirements necessary for the soft magnetic properties rule out most of these techniques. Till now the only technique suitable for obtaining nanocrystalline soft magnetic

alloys is the controlled partial crystallisation of amorphous alloys. The typical amorphous alloy composition which yields nanocrystalline structure with good soft magnetic properties is $Fe_{73.5}Cu_1Nb_3Si_{13.5}B_9$. Fig. 5 gives the DSC thermogram of the amorphous $Fe_{73.5}Cu_1Nb_3Si_{13.5}B_9$. Since the alloy composition is hypoeutectic, it is expected to crystalise in two steps: in the first step a primary phase would precipitate out till the composition of the remaining a-phase becomes eutectic. In the second step the remaining a-phase crystallises through eutectic transformation. Accordingly the DSC thermogram exhibits two exothermic peaks. Nanocrystalline phase is obtained by annealing the amorphous alloy at temperatures in the range of the first crystallisation peak in the DSC thermogram, i.e., 450 to 600°C. The resulting microstructure consist of randomly oriented ultra fine grains of bcc FeSi alloy dispersed in the remaining amorphous matrix. Volume fraction occupied by the nanocrystalline grains primarily depends upon the boron concentration and ranges from 70-80%. Nanocrystalline microstructure and the resultant soft magnetic properties are rather insensitive to the precise annealing treatment within a wide range of annealing temperature and time[11]..
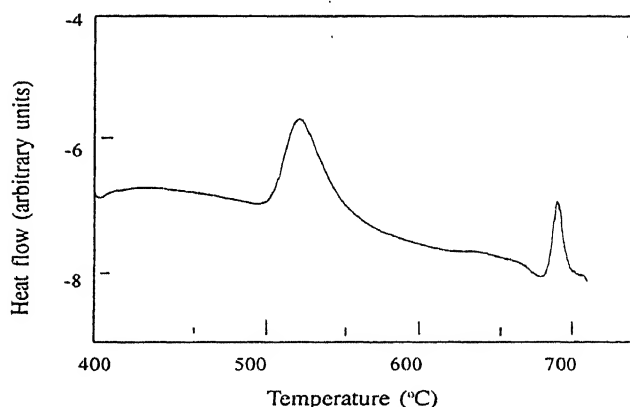
Fig. 5 DSC thermogram of the amorphous $Fe_{73.5}Cu_1Nb_3Si_{13.5}B_9$

The kinetics of nanocrystalline phase formation has been studied using time resolved X-ray diffraction and small angle X-ray scattering measurements[12,13]. Time resolved XRD measurements[12] showed that the nanocrystalline grains grow via a diffusion controlled mechanism (Fig. 6). Variation of lattice parameter with annealing time was taken as an evidence for a significant change in the composition of the nanocrystalline grains with increasing crystal size.

$r = a\sqrt{Dt}$
$D = 10^{-19} m^2 s^{-1}$
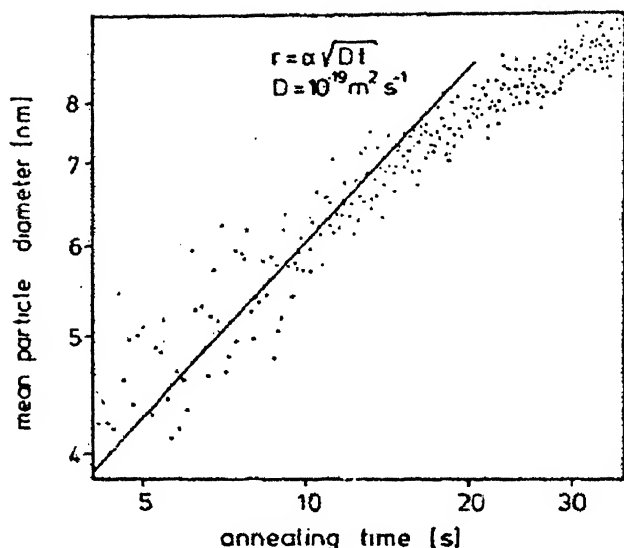
Fig. 6 Growth of nanocrystals during annealing of $Fe_{73.4}Cu_1Nb_{3.1}Si_{13.4}B_{9.1}$ at 490 °C. A linear fit to the data of crystallite diameter verses $t^{1/2}$ gives a diffusivity of 10^{-19} m²s⁻¹ [12]

In a subsequent time resolved X-ray diffraction study of the nanocrystalline transformation in $Fe_{72}Cu_1Nb_{4.5}Si_{13.5}B_9$ alloy, a DC current of 7.8A was passed through the specimen for *in-situ* heating during the measurements. With annealing time the crystallite size grows and saturates at a value of about 16nm (Fig. 7a). The lattice parameter initially shows a large decrease with. increasing volume fraction of nanocrystallite phase, however for larger annealing times it shows a slow increase (Fig. 7b).

Fig. 7 Fractional area, grain size and lattice parameter of crystalline component vs. annealing time as deduced from the time resolved wide angle scattering 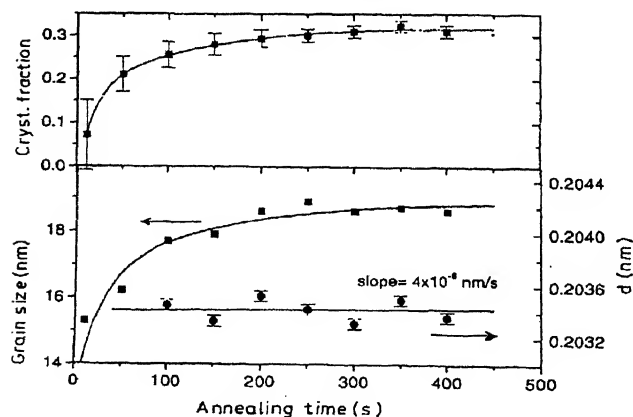patterns of $Fe_{72}Cu_1Nb_{4.5}Si_{13.5}B_9$ amorphous alloy submitted to *in situ* 7.8 A current annealing for the times indicated

The initial decrease in the lattice parameter may be either because of a variation in the composition of the nanocrystalline grain as suggested by Köster *et al.*[12] and also by Varga *et al.*[14] or the other possibility is that the decrease in *d*-spacing is because of variation in the tensile stress on the nanocrystalline grains exerted by the surrounding amorphous phase[15,16]. Since the density of the crystalline phase is higher than that of the amorphous matrix, formation of nanocrystalline grain is accompanied by a shrinkage in the volume. Therefore, the amorphous matrix will exert a tensile stress on the nanocrystalline grain causing an increase in the lattice parameter. With increasing size and amount of nanocrystalline grains, the magnitude of the tensile force exerted by the amorphous matrix decrease causing the lattice parameter to decrease. A strong correlation between the decrease in the lattice spacing and increase in the grain size suggest that the initial decrease in parameter is primarily due to decrease in the tensile stress exerted by the surrounding amorphous matrix. The slower increase in the lattice parameter for longer annealing time may be due to some out diffusion of Si from the nanocrystalline grains. Mössbauer studies provide some indirect evidence of variation of Si concentration in the nanocrystalline grains with annealing time[15].

The effect of the variation of the Si and Nb concentration in the parent amorphous phase on the nanocrystallisation process was studied through the amorphous to crystalline transformation in four specimens of compositions: $Fe_{73.5}Cu_1Nb_3Si_{16.5}B_6$ (specimen A), $Fe_{73.5}Cu_1Nb_3Si_{13.5}B_9$ (specimen B), $Fe_{70.5}Cu_1Nb_{4.5}Si_{16}B_8$ (specimen C), $Fe_{72}Cu_1Nb_{4.5}Si_{13.5}B_9$ (specimen D)[16]. Table I gives the lattice parameter and the crystallite size of the nanocrystalline grains after the completion of the first crystallisation step. From Table I, it may be seen that the average crystallite size in specimens C & D is lower as compared to that in specimen A & B respectively. This shows that both addition of Nb as well as Si causes the final crystallite size to decrease.

Presence of Cu and Nb, though in small quantities, is crucial for the formation of nanocrystalline structure. In the absence of Cu and Nb, crystallisation of FeSiB amorphous alloy results in formation of rather coarse grains with size ~ 100nm and shows a distinct variation with the annealing temperatures and time. Small amounts of Cu and Nb strongly affect the Nucleation as well as growth process and result in the formation

Table I

The line position, integral width and the crystallite size of the specimens after the completion of the first crystallization step

Specimen	Line position (degrees)	Integral width (degrees)	Crystallite size (Å)
$Fe_{73.5}Cu_1Nb_3Si_{16.5}B_6$	45.12	0.016	103
$Fe_{73.5}Cu_1Nb_3Si_{13.5}B_9$	45.12	0.132	126
$Fe_{70.5}Cu_1Nb_{4.5}Si_{16}B_8$	44.95	0.021	78
$Fe_{72}Cu_1Nb_{4.5}Si_{13.5}B_9$	45.11	0.016	106

of nanocrystalline structure. Fig. 8 shows the DSC thermograms of FeSiB metallic glass without any addition as well as with addition of Cu or Nb or both of them. One can see that the crystallisation kinetics gets strongly effected by the addition of Cu and Nb. Table II summarises crystallization temperature of various crystallisation steps and their activation energies. The DSC thermogram of the specimen without Cu and Nb consists of two somewhat overlapping exothermic peaks. The first step corresponds to precipitation of bcc FeSi alloy while in the second step Fe-B compound precipitates out[17,18]. However, addition of just one percent Cu results in substantial lowering of the activation energies of the first crystallisation step bringing out a clear separation between the two. On the other hand addition of Nb increases the stability of the amorphous phase markedly and the amorphous to crystalline transformation occurs in a single step. Addition of both Cu and Nb causes the two crystallisation steps to separate again and also significantly effects the shape of the crystallisation peaks: Both the crystallisation peaks are very flat and wide suggesting much slower kinetics of crystallisation for this alloy. It has been suggested that due to low solubility of Cu in Fe, addition of Cu in the amorphous alloy leads to the formation of Cu rich clusters which act as nucleation site for the crystalline phase. Thus addition of Cu would enhance drastically the nucleation rate of the crystallites bringing down the activation energy of the first crystallisation step. The presence of Nb seems to promote further the formation of Cu rich cluster[19]. In some recent 3D atom probe (3DAP) field ion microscopy formation of Cu clusters prior to crystallization has been observed[20]. Figs. 9 (a), (b) and (c) show 3DAP elemental maps of Cu within analysed volumes of 10 x 10 x 40 nm in the as-melt-spun specimen and in the specimens annealed for 5
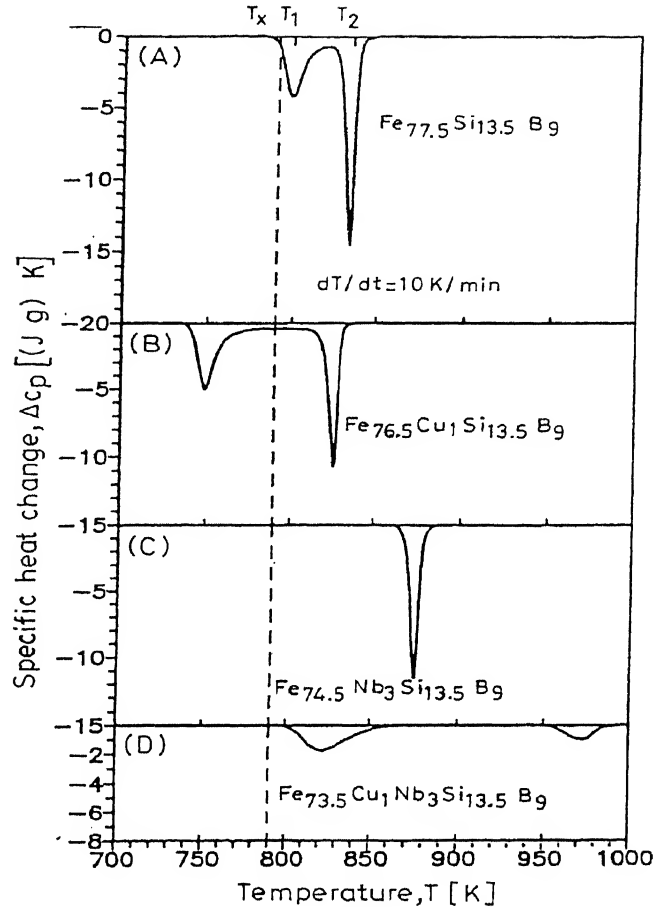
Fig. 8   DSC thermograms of FeSiB metallic glass without any addition as well as with addition of Cu or Nb or both of them

Table II

Crystallization temperature T_x and activation energies E for the various crystallization steps in FeSiB metallic glass without any addition as well as with addition of Cu or Nb or both of them

Alloy Composition	first step		second step	
	T_x (K)	E (kJ/mol)	T_x	E (kJ/mol)
$Fe_{77.5}Si_{13.5}B_9$	799	295±9	835	287±8
$Fe_{76.5}Si_{13.5}Cu_1B_9$	749	235±8	826	252±1
$Fe_{74.5}Nb_3Si_{13.5}B_9$	875	347±8		
$Fe_{73.5}Cu_1Nb_3Si_{13.5}B_9$	822	321±8	972	456±19

and 60 min at 400°C, respectively. In the as-melt-spun specimen, Cu distribution is uniform, confirming that the as-melt-spun specimen is a chemically homogeneous solid solution. In the specimen annealed for 5 min at 400°C, heterogeneous distribution of Cu atoms is apparent, indicating that clustering of Cu
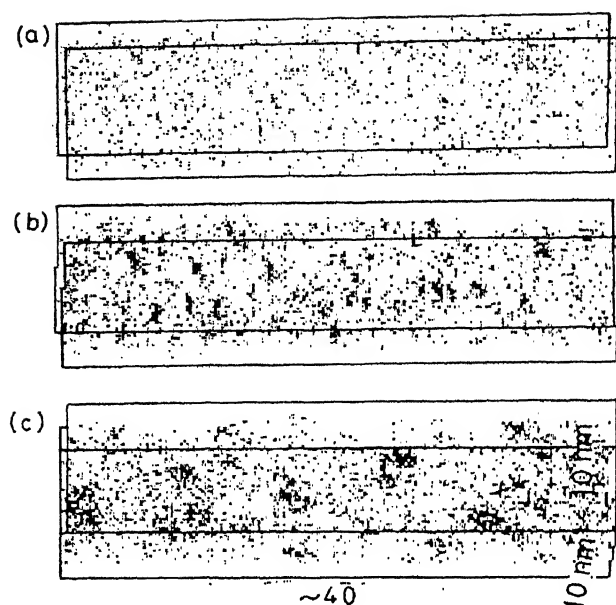
Fig. 9 3DAP elemental mapping of Cu of melt-spun $Fe_{73.5}Cu_1Nb_3Si_{13.5}B_9$ alloy ribbon (a) as-quenched, (b) annealed for 5 min at 400°C, and (c) annealed for 60 min at 400°C[20]

atoms occurs. After a 60 min annealing at 400°C, clustering of Cu atoms is observed more clearly. Separate TEM observation results confirmed that no crystallization occurs up to 60 min at 400°C, thus the clustering observed in this analysis occurs in the amorphous phase. The number of atoms in each cluster is in the range of 50 to 100, and the size of the clusters is approximately 3 nm. The density of the Cu clusters estimated from the analyzed volume is in the order of 10^{24} m^{-3}. Based on the extended X-ray absorption fine structure (EXAFS) measurement results, Sakurai et al.,[21] and Ayers et al.,[22] reported that Cu atoms form clusters having near-fcc symmetry from the very early stage of the heat treatment with some evidence of their presence even in the as-melt-spun amorphous alloy. Thus, the Cu clusters observed in the 3DAP data are believed to have a fcc-like short range structure. Such Cu clustering appears to be common in Cu containing Fe based amorphous alloys. For example, Suzuki et al.[23] reported that the addition of 1 at.% of Cu in Fe-Zr-B amorphous alloy causes a reduction of the grain size leading to better soft magnetic properties in the final nanocrystalline microstructure. Clustering of Cu in this system was also confirmed prior to the crystallization reaction by AP analysis[24]. The assumption that Cu clusters serve as

heterogeneous nucleation sites for the α-Fe primary crystals is quite reasonable, but direct evidence for this mechanism is very difficult to obtain because the sizes of the Cu clusters and the primary particles are both extremely fine. However, in the case of a nanocrystalline Fe-Zr-B-Cu alloy, Cu clusters were found in intimate contact with the primary α-Fe particles by APFIM[25]. Fig. 10 shows 3DAP elemental maps near a Cu precipitate in the $Fe_{73.5}Si_{13.5}B_9Nb_3Cu_1$ alloy annealed at 550°C for 10 min. The Cu precipitate
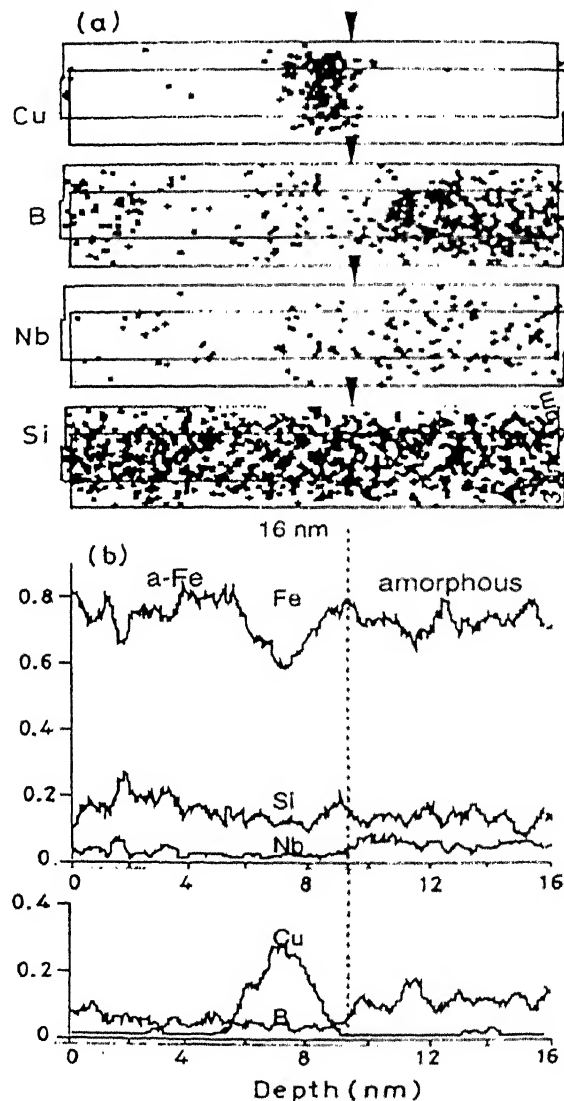

Fig. 10 3DAP elemental mappings of Cu, Nb, B and Si atoms near a Cu cluster in a melt-spun $Fe_{73.5}Si_{13.5}B_9Nb_3Cu_1$ alloy annealed for 60 min at 400°C and (b) the corresponding concentration depth profiles obtained from the same analyzed volume[20]

is in direct contact with the Fe-Si particle, which suggests that Cu provides nucleation sites for the Fe-Si primary crystals[20]. The Fig. 11 illustrates schematically the amorphous to nanocrystalline transformation in Fe-Cu-Nb-Si-B system. Addition of Nb also retards the growth of the crystallites. Thus, an enhanced nucleation rate due to Cu addition and retardation of the growth process owing to the presence of Nb results in restricting the grain size to about 10 nm.

function of annealing time at 540°C. The Mössbauer spectra were fitted with 5 overlapping sextets; one broad sextet corresponding to the remaining amorphous phase and four sharp sextets corresponding to different Fe sites in the nanocrystalline phase. The following analysis of Mössbauer spectra shows that the nanocrystalline grains are essentially nonstoichiometric Fe_3Si phase with small degree of disorder (i.e., a small fraction of Si atoms also occupy iron sites).

Fe–13.5 Si–9 B–3 Nb–1Cu amorphous alloy (FINEMET)
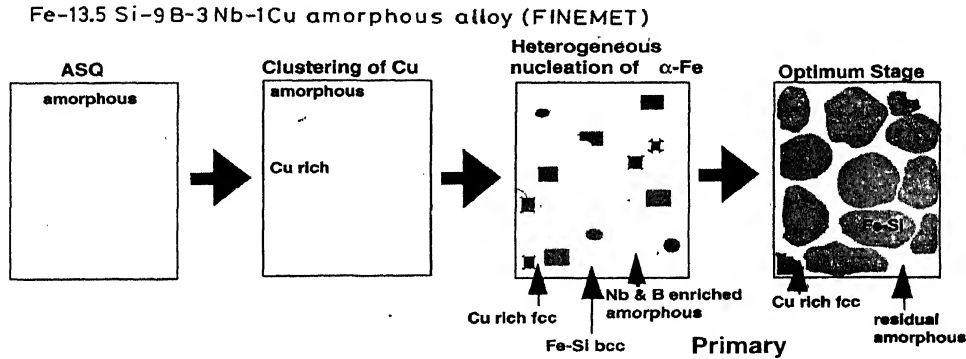
Fig. 11 Schematic representation of microstructural evolution in melt-spun $Fe_{73.5}Si_{13.5}B_9Nb_3Cu_1$ amorphous alloy during primary crystallization[20]

3 Structure of the Nanocrystalline Grains

X-ray diffraction measurements suggest that the nanocrystalline grains have bcc structure with lattice parameters about 5% smaller than that of α iron. Mössbauer spectroscopy provides a much more detailed information about the stoichiometry and structure of the nanocrystalline grains[26]. Fig. 12 gives the Mössbauer spectrum of the specimen $Fe_{73.5}Cu_1Nb_3Si_{16.5}B_6$ as a
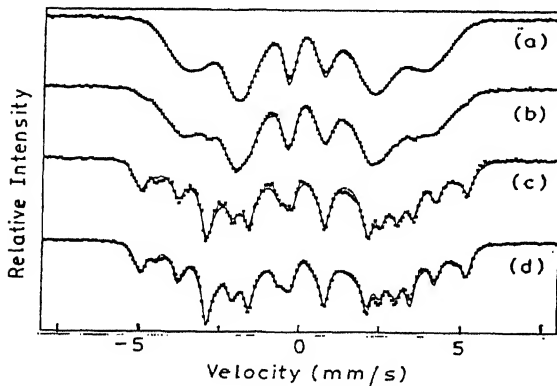
Fig. 12 Room-temperature Mössbauer spectra of amorphous Specimen $Fe_{73.5}Cu_1Nb_3Si_{16.5}B_6$ as a function of annealing time at 540 °C: (a) 0 min; (b) 2 mins; (c) 10 mins; and (d) 25 mins

The possible structure of nanocrystalline grains, having an overall concentration, c, of Si ($c = 0.25$), can be as follows:

i) *A Random Solid Solution of Si in α-Fe:* This would be the case when all the Fe sites are equivalent and they are randomly occupied by Si atoms with a probability 'c'. In this configuration the probability of an Fe atom having 'r' Si nn and $(8-r)$ Fe nn will be given by:

$$P(r) = {}^8C_r c^r (1-c)^{(8-r)} \quad \text{... (1)}$$

The values for these probabilities for $c=0.2$ and the corresponding hyperfine fields as taken from literature[27] are given in Table III.

ii) *An Ordered Stoichiometric Fe_3Si Structure:* In this case, there will be only two possible Fe sites: a) Fe atoms on A site with 4 Fe nn and 4 Si nn and b) Fe atoms on D sites having all 8 Fe nn. The relative number of A and D sites are 2:1. Therefore, the area ratio of the two Mössbauer subspectra corresponding to A and D sites will also be 2:1. The hyperfine field values of A and D sites, as taken from Stearns[28], are 31.1 T and 20.2 T respectively (Table III).

Table III

The possible Fe sites and their hyperfine field parameters in α-Fe(Si) solid solution as well as ordered/disordered and/or stoichiometric/nonstoichiometric Fe₃Si. Sites S8, S7, S6 and S5 correspond to Fe atoms in α-Fe lattice with 8 Fe, 0 Si nn; 7Fe, 1Si nn; 6Fe, 2 Si nn and 5 Fe, 3 Si nn respectively. Site D8 is the D site in DO₃ structure with 8 Fe nn, A4, A5, A6 are the A sites in DO₃ structure with 4 Fe, 4Si nn; 5 Fe, 3 Si nn and 6 Fe, 2 Si nn respectively

Configuration	Sites	Bhf (T)	Probability for c=0.25	Probability for c=0.2
	S8	32.4		0.17
α-Fe(Si)	S7	30.5		0.33
solid solution	S6	28.2		0.29
	S5	23.6		0.15
Ordered-stoichiometric	D	31.1	0.33	
Fe₃Si	A	20.2	0.66	
	D8	31.1		0.33
Ordered	A4	19.5		0.27
nonstoichiometric	A5	24.3		0.27
Fe₃Si	A6	28.2		0.1

iii) *An Ordered Nonstoichiometric Fe₃Si*: In case the overall concentration c of Si, is less than 0.25, some of the Si sites will be replaced by Fe atoms. Thus there will be more than 1 environment for Fe atoms sitting at A site: 4 Fe nn, 4 Si nn (A4); 5 Fe nn, 3 Si nn (A5); 6 Fe nn, 2 Si nn (A6). The probability of an iron atom on A site having an environment of (4-r) Si and (4+r) Fe nn is given by

$$P(A_r) = {}^4C_r C^r (1-C)^{(4-r)} \quad \dots (2)$$

where, $C=4(0.25-c) = (1-4c)$, is the fraction of Si sites (in DO₃ structure) occupied by Fe atoms.

The above expression is written by arguing that in a Si deficient Fe₃Si the probability that one of the Si atom is replaced by an Fe atom is C. The hyperfine field of these environments are given in Table III[28]. All the Fe atoms on D site will still have 8 Fe nn only and thus only one possible environment with a corresponding hyperfine field of 31 T. In the Mössbauer spectra the area of the subspectra corresponding to D site relative to that of the sum of all the A sites will be (0.5-c):0.5. Thus, for c<0.25 the area of D site will be more than half of the area under all the A sites together.

iv) *A Partially Disordered Non-stoichiometric Fe₃Si*: In the most general case one can assume that the system is slightly disordered, i.e., a small fraction

of A sites (say c_A) is occupied by Si and also the system is nonstoichiometric, *i.e.* the fraction of D sites occupied by Si atoms c_D is less than 50%. In this case the probability of an Fe atom on A site having (4-r) Si and (4+r) Fe nn (1-2C_D) fraction if Si sites occupied by Fe given by

$$P(A_r) = {}^4C_r C^r (1-C)^{(4-r)} \quad \dots (3)$$

where $C = (1-2c_D)$

The Fe atoms at D sites can have nn configurations as 8 Fe, 0 Si (D8); 7 Fe, 1 Si (D7); 6 Fe, 2 Si nn (D6) etc., with the probability of having r Si and (8-r) Fe nn given by

$$P(r) = {}^8C_r c_A{}^r (1-c_A)^{(8-r)} \quad \dots (4)$$

Assuming that the substitution of 1 Fe nn by Si causes the hyperfine field to decrease by about 4 T, the hyperfine field of sites with 8 Fe, 0 Si nn; 7 Fe, 1 Si nn and 6 Fe, 2 Si nn will be approximately 31 T, 27 T and 23 T respectively.

It may be noted that the hyperfine field of site A5 is approximately equal to that of site D6 and that of site A6 approximately equal to that of site D7. Thus, in this case also one will have only four subspectra with hyperfine field of 31 T, 28 T, 24 T and 20 T. However, the area under the subspectra with 31 T hyperfine field can be even less than half of the sum of the area under the subspectra (28 T+ 24 T + 20 T), depending upon the value of c_A. The overall concentration of Si in the grains would be $\frac{c_A+c_D}{2}$.

In Table IV the relative areas of the four subspectra are given for the values of c_A and c_D which best fit the experimental data of the nanocrystallized specimen. One may note that the relative areas of the four subspectra agree very well with the calculated values. On the other hand, field values and the expected relative areas on the basis of the other three models do not agree with the experimental values. This suggests that the nanocrystallized grains consist of partially disordered nonstoichiometric Fe₃Si with Si concentration ~22%. However, the degree of disorder in the system is very small, the fraction of A sites occupied by Si being about 1% only. It may also be noted that the Si concentration in nanocrystalline grains is significantly higher than the overall Si concentration in the parent amorphous alloy.

Role of Nb in Inhibiting Grain Growth

From a number of studies, it is well accepted that presence of Nb in the parent amorphous phase causes

Fitted $(RA)_F$ and calculated $(RA)_C$ values of relative areas and the corresponding concentration of Si occupying A sites, c_A, and D site, c_D for the nanocrystallized specimen $Fe_{73.5}Cu_1Nb_3Si_{16.5}B_6$

B_{hf} (T)	$(RA)_F$ (%)	$(RA)_C$ (%)	c_A	c_D
31.7	30.4	31.6		
28.6	8.9	10.6	0.95	21.4
24.7	25.0	23.2		
19.8	35.7	34.0		

inhibition of the grain growth resulting in the nanocrystalline structure[29,30]. The possible mechanism for the inhibition of the grain growth has been suggested as out-diffusion of Nb from the nanocrystals and its segregation at grain boundaries, thus, inhibiting the further growth of the grains. In a high resolution transmission electron microscopic study of nanocrystallisation in $Fe_{75.5}Cu_1Nb_3Si_{12.5}B_8$, selective area energy dispersive X-ray analysis was used to obtain the elemental composition of the nanocrystalline grains and the remaining amorphous matrix[31]. Using the beam spot size of about 2.4 nm, measurements were done from the amorphous as well as crystalline regions. It was concluded that the crystalline phase contains less Nb than the amorphous phase. However, in this study an upper estimate for the Si concentration in the crystallined phase was obtained as $C^x_{Si} = 13.5$, which is significantly lower than that estimated from other measurements. In order to get further information about the presence of Nb in the crystalline phase, the Mössbauer spectra of nanocrystalline grains was compared with that of crystalline alloys of stoichiometric Fe_3Si with and without 3% Nb i.e., having composition $Fe_{75}Si_{25}$ and $Fe_{72}Nb_3Si_{25}$. The Mössbauer spectra of these two crystalline compounds are shown in Fig. 13, and the results of the computer fitting of the spectra are summarised in Table V. Addition of 3% Nb gives rise to an additional singlet in the spectrum. From Table V one finds that the singlet is formed mainly at the expense of the hyperfine field component with 20 T field, and suggests that Nb preferentially goes to D site and the singlet mainly corresponds to Fe atoms with three Fe nn, one Nb near neighbour and four Si nn. On comparing the Mössbauer spectra of crystalline Fe_3Si and Fe_3Si:3% Nb with the spectra of nanocrystalline phase one finds that in the Mössbauer spectrum of nanocrystalline alloys there is no singlet present. Thus, Nb does not go substitutionally in the nanocrystalline grains as it would have preferentially reduced the area under the

hyperfine field subspectrum corresponding to A4 site. Furthermore, segregation of Nb at the surface of the grains should have given rise to atleast a small singlet corresponding to the fraction of iron atoms on A4 site at the surface. Thus the Mössbauer spectra give evidence against segregation of Nb atoms around the nanocrystalline grains.
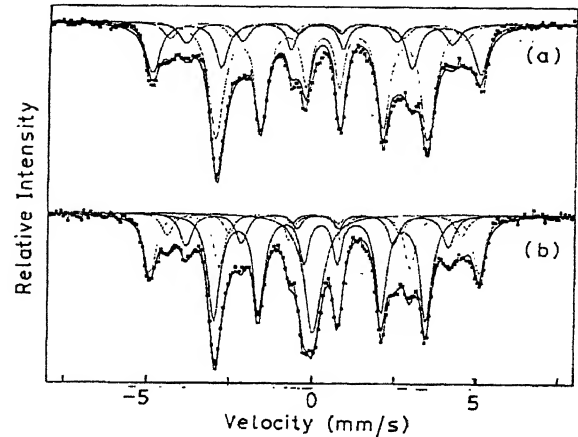
Fig. 13 Room temperature Mössbauer spectra of the alloys (a) Fe_3Si and (b) $(Fe:3\% Nb)_3Si$

Table V

The results of the fits of Mössbauer spectra of the alloys Fe_3Si and Fe_3Si:3% Nb

Alloy composition	Isomer shift (mm/s)	B_{hf} (T)	Rel. Area (%)
Fe_3Si	0.075	30.80	25.2
	0.253	19.85	56.0
	0.108	27.70	8.4
	0.158	24.98	10.4
Fe_3Si:3% Nb	0.072	30.92	22.8
	0.250	19.89	40.6
	0.066	27.70	8.4
	0.157	24.71	12.5
	0.033	0	15.7

In Fig. 14, is plotted the width of hyperfine field distribution of the remaining amorphous component as a function of the degree of crystallization in various specimens[32]. The width of the hyperfine field distribution increases with increasing crystallization due to increasing chemical inhomogenity in the amorphous phase. It may be noted that during the first stage of crystallization primary crystallites of Fe_3Si or a bcc Fe-Si solid solution are formed. Thus the boron atoms from the volume of crystallites are expelled out and they diffuse into the remaining amorphous matrix. Because of the finite diffusivity of boron in the amorphous phase, B will have a concentration gradient

in the amorphous phase, its concentration being higher at the grain boundary. This gives rise to the broadening of hyperfine field distribution of amorphous phase with crystallization. Similarly, the expulsion of Nb from the grains may also contribute to the broadening of the field distribution. From Fig. 14, it may be noted that in the case of Nb-containing amorphous alloys the width of the hyperfine field distribution of the remaining amorphous phase increases at a much faster rate with crystallization as compared to that in amorphous alloy without Nb. Further the slope of $\Delta H/<H>$ versus amount of crystallization is steeper in the case of alloy containing 4.5 % Nb as compared to those containing 3% Nb. Thus, Mössbauer studies suggest that Nb diffuses out of the crystallites but it does not just get segregated at the grain boundaries, rather it diffuses into the amorphous matrix giving rise to a concentration gradient of Nb.

Fig. 14: Width of the hyperfine field distribution, $\Delta H/<H>$, as a function of the amount of crystallization in the specimens A) $Fe_{73.5}Cu_1Nb_3Si_{16.5}B_6$, B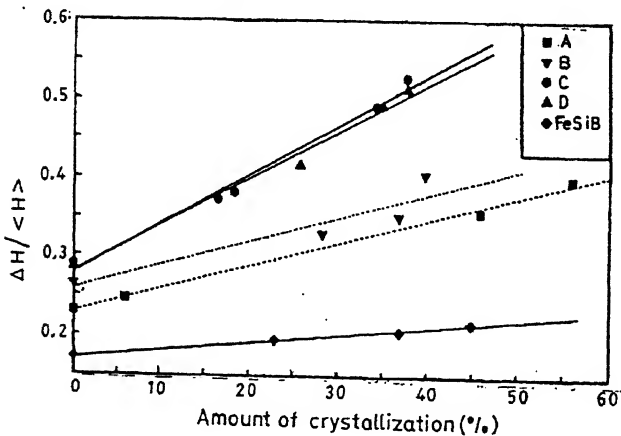) $Fe_{73.5}Cu_1Nb_3Si_{13.5}B_9$, C) $Fe_{70.5}Cu_1Nb_{4.5}Si_{16}B_8$, D) $Fe_{72}Cu_1Nb_{4.5}Si_{13.5}B_9$ and $Fe_{78}Si_9B_{13}$

4 Magnetic Properties

Nanocrystalline alloys with the composition $Fe_{74.5-x}Cu_xNb_3Si_{22.5-y}B_y$ have been investigated[1,33-35] in order to understand their peculiar magnetic properties. In particular the alloy with the composition $x=1$ and $y=9$ shows very soft magnetic properties with coercivities, H_c, of the order of 0.01 A cm^{-1} and initial permeabilities, μ_i, of the order of 10^5 after annealing from the amorphous phase for 1 h in the temperature range 480-550°C[35]. At the same time the saturation

magnetostriction drops to almost zero[5,6]. The excellent soft magnetic properties in the nanocrystalline state is achieved as a result of an averaging of various properties over the exchange correlation length. Individual nanocrystalline grains possess large magnetic anisotropy, however, the easy direction of individual grains are randomly oriented. Within the random anisotropy model[36], in case the exchange length L_{ex} is much greater than the grain size D the effective anisotropy will be obtained by averaging over the nanocrystalline grains within a volume of L^3_{ex} (Fig. 15), and can be written as $<K> \approx K_1 (D/L_{ex})^{3/2}$ where K_1 is the anisotropy of individual grains. One can see that the average anisotropy decreases with the grain size. The exchange length L_{ex} in turn is given by $(A/<K>)^{1/2}$ where A is the exchange stiffness constant. This leads to a reduction in the coercivity according to the relation
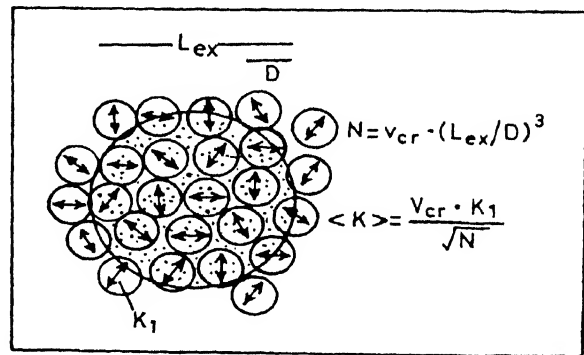
Fig. 15   Schematic representation of the random anisotropy model for nanocrystalline grains embedded in an ideally soft ferromagnetic matrix. The double arrows indicate the randomly fluctuating anisotropy axes, the hatched area represents the ferromagnetic correlation volume determined by the exchange length $L_{ex}=(A/<K>)^{1/2}$ [4]

$$H_c = \frac{K_1^4 D^6}{J_s A^3} \qquad \ldots (5)$$

where J_s is the exchange interaction. Thus for small crystallite size the coercivity decreases as D^6 with decreasing grain size. This behaviour has been confirmed experimentally as shown in Fig. 16. The reduction in the magnetostriction can be explained by a balance between the crystalline and amorphous phases. The saturation magnetostriction[37] of bcc $Fe_{80}Si_{20}$ is $\lambda_s^{FeSi} \sim -6 \times 10^{-6}$, while for the amorphous matrix $\lambda_s^{am} \sim +20 \times 10^{-6}$. Therefore, the average

magnetostriction can be written as $\lambda_s \sim V_{FeSi} \times \lambda_s^{FeSi} +$ $(1-V_{FeSi}) \cdot \lambda_s^{am}$ where V_{FeSi} is the volume fraction of nanocrystalline phase. Thus with the increasing volume fraction of FeSi the average magnetostriction decreases and approaches to a value $\sim 1\times10^{-6}$ as shown in Fig. 17.
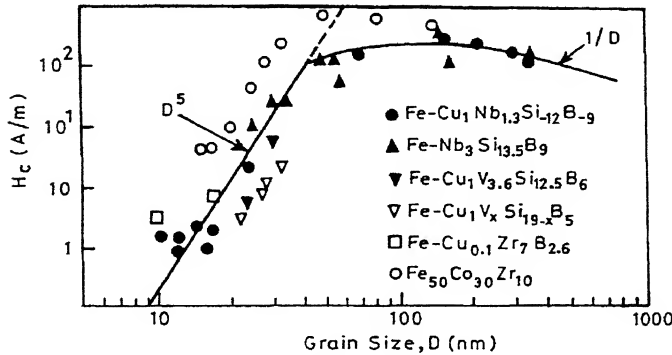
Fig. 16 Grain size dependence of the coercive field of iron based nanocrystalline alloys

Fig. 17 Dependence of the saturation magnetostriction on the volume fraction of the nanocrystalline grains in $Fe_{73.5}Cu_1Nb_3Si_{15.5}B_7$.

The final magnetic properties depend upon microstructure as well as composition of the nanocrystalline and the remaining amorphous phases. For example, value of λ_{cr} as well as λ_{am} depends on silicon content[4]. Therefore, the concentration of boron/silicon can be a very important factor influencing magnetic properties of nanocrystalline Fe-based alloys[18,38].

4.1 Magnetization Behaviour of Nanocrystalline Alloys

Temperature dependent magnetization studies in $Fe_{73.5}Cu_1Nb_3Si_{16.5}B_6$, alloy with different degrees of nanocrystallization have been done using Mössbauer spectroscopy[39]. Some representative Mössbauer spectra are shown in Fig. 18. The spectra can be fitted to obtain the temperature dependent magnetization of the amorphous and nanocrystalline components separately.
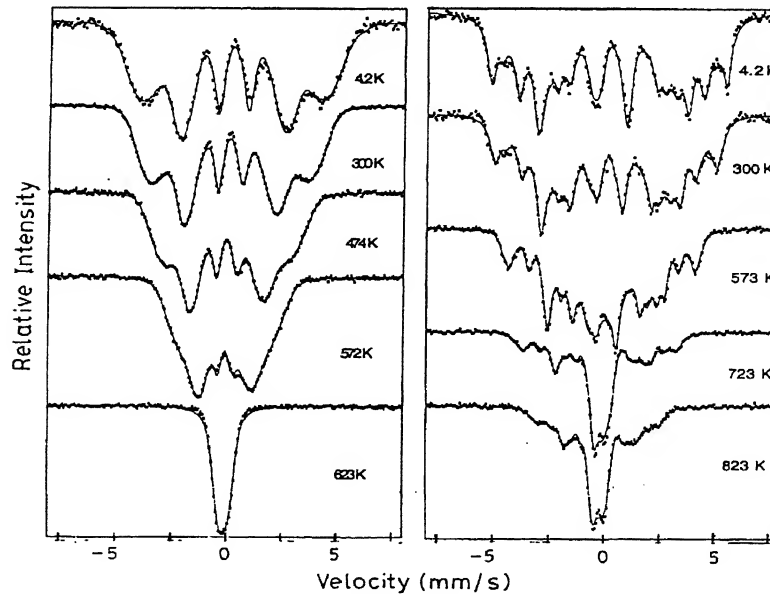
Fig. 18 Temperature dependent Mössbauer spectra of alloy $Fe_{73.5}Cu_1Nb_3Si_{16.5}B_6$: a) in as-prepared amorphous state, and b) after nanocrystallization by annealing at 540°C for 25 min

Magnetic Behaviour of Amorphous Phase

Fig. 19 shows the temperature dependence of the reduced hyperfine field of the amorphous component of the specimens annealed at 540°C for 10 min (A10) and 25 min (A25). In the critical region, the temperature dependence of the hyperfine field may be written as

$$B_{hf}(T) = A(T_c-T)^\beta \qquad \ldots (6)$$

T_C being the Curie temperature. In amorphous ferromagnets this behaviour is found to hold good over a much larger temperature range extending well beyond the critical region[40] and Mössbauer measurements have been used to estimate the critical exponent β. Table VI summarizes the results of the least square fitting of the high temperature data, of specimens with different annealing treatments, with eq. (6). Perusal of Table VI shows that initially the T_C exhibits a small increase upon annealing for 2 mins, which may be attributed to the structural relaxation associated with annealing. For a higher annealing time a decrease in T_C with increasing crystallization is a consequence of the enrichment of the amorphous phase in boron. In the as-received specimen the value of the critical exponent β is close to the theoretical value for a three dimensional Heisenberg ferromagnet[41]. With increasing crystallization the value of β decreases and for the specimen A25 it attains a value in between that for three dimensional and two dimensional systems[41]. It may be noted that as the amount of crystalline phase increases the thickness of the amorphous grain boundary phase would decrease, and for sufficiently thin grain boundary layer the dimensionality cannot be taken as 3, and the low
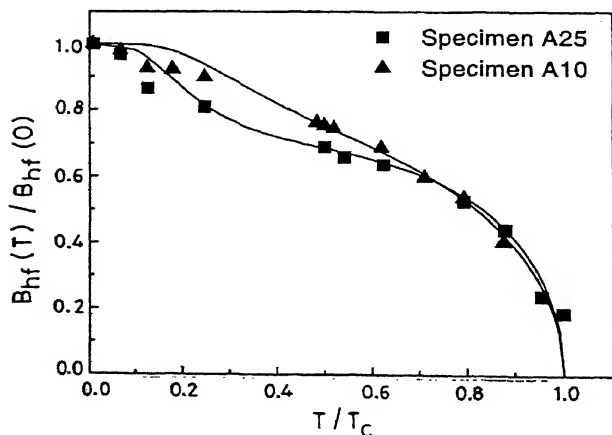
Fig. 19   Temperature dependence of the reduced hyperfine field of the amorphous component of the specimens $Fe_{73.5}Cu_1Nb_3Si_{16.5}B_6$ annealed at 540°C for 10 min (A10) and 25 min (A25)

Table VI

Results of the least square fitting of the high temperature data of the nanocrystalline $Fe_{73.5}Cu_1Nb_3Si_{16.5}B_6$ produced by annealing at 540°C for different periods of time

Annealing time (min)	T_c (K)	β
0	600.5	0.356
2	608.4	0.334
10	567.6	0.336
25	578.0	0.264

dimensional magnetic behaviour should be observed. From the known volume fraction of the nanocrystals and their average diameter, the thickness of the grain boundary layer for the specimen A25 is estimated to be ~ 42 Å. Here it should be noted that, although the spins in the grain boundary layer also interact with those in the crystallites, this interaction is much weaker than that among the spins within the grain boundary layer. This point is supported by the fact that there exists a well defined T_C for the amorphous layer which is only slightly affected by increasing amount of nanocrystalline phase (causing an increase in the interaction of the spins of the amorphous layer with those in crystallites). Thus, the temperature dependence of the magnetization of the amorphous layer is mainly determined by the interaction among the spins within the amorphous layer.

In the low temperature range, the temperature dependence of magnetization comes from the excitation of the long wavelength spin waves. Following the Heisenberg model, the temperature dependence of hyperfine field can be written as

$$\frac{B_{hf}(T)}{B_{hf}(0)} = 1-B\left(\frac{T}{T_c}\right)^{3/2} - C\left(\frac{T}{T_c}\right)^{5/2} \qquad \ldots(7)$$

The low temperature hyperfine field of the parent amorphous phase follows the above equation with values of B and C as 0.33 and 0.23 respectively. These values reasonably agree with those for the specimens with similar composition[42]. On the other hand, in the specimens with substantial nanocrystallization, the low temperature hyperfine field does not follow the eq. (7). A temperature dependent interaction between the amorphous and nanocrystalline phases can be one of the possible reasons for the deviation of the temperature dependence of low temperature magnetization from the eq. (7).

Perusal of Fig. 19 shows that around 75K the hyperfine field shows a steeper rise. Taking the dispersion relation for the spin waves as[43]

$$E(\kappa) \cong DK^2 \qquad \ldots (8)$$

the wavelength of the spin waves at a temperature T may be written as:

$$\lambda = 2\pi \left(\frac{D}{k_B T} \right)^{1/2} \qquad \ldots (9)$$

With decreasing temperature, the wavelength of the spin waves will increase. When the wavelength becomes comparable to the width of the grain boundary, the excitation of the spin waves will be hindered, causing a steeper increase in the hyperfine field. For the known value of D, the temperature at which λ becomes comparable to the grain size agrees well with the temperature at which the hyperfine field exhibits a steep increase.

Magnetization Behaviour of Nanocrystalline Components

The size of nanocrystals is small enough to qualify for single domain particles[44]. Several interesting magnetic effects are associated with such a small particle size. In case the thermal energy, $k_B T$, is comparable to the magnetic anisotropy energy, KV, of a single domain particle, the magnetic moment of the particle exhibits superparamagnetic relaxation and the hyperfine field collapses to zero. Even below the superparamagnetic blocking temperature, the hyperfine field may be reduced to a value below that for the bulk system because of the thermally excited fluctuations of the magnetization vector in directions close to an easy direction of magnetization (collective magnetic excitations). On the other hand, an appreciable magnetic interaction among the nanocrystals may give rise to superferromagnetism in the system.

It was found that for small annealing times, when the concentration as well as the size of the nanocrystals is small, the system exhibits superparamagnetism above the Curie temperature of the amorphous phase. For higher concentrations of the nanocrystalline grains, the system exhibits a superferromagnetic behaviour. Fig. 20 gives the temperature dependence of the reduced hyperfine field of the nanocrystallites in specimens A10 and A25. In the low temperature region, the reduced hyperfine field was found not to follow the relation (10). A fit of the data in the
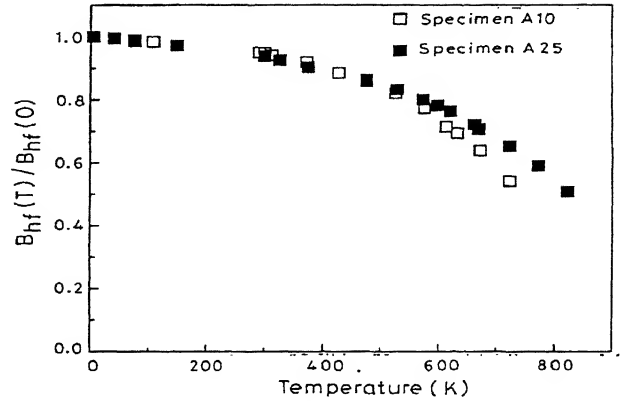
Fig. 20 Temperature dependence of the reduced hyperfine field of the nanocrystallites in specimens $Fe_{73.5}Cu_1Nb_3Si_{16.5}B_6$ annealed at 540°C for 10 min (A10) and 25 min (A25)

temperature range 4.2-150 K, of both the specimens A10 and A25 with a relation.

$$\frac{B_{hf}(T)}{B_{hf}(0)} = 1 + bT^n \qquad \ldots (10)$$

gave the value of the exponent n close to unity, indicating an almost linear temperature dependence in this range. In the high temperature region, the specimen A10 exhibits a faster decrease in $B_{hf}(T)$ as compared to the specimen A25 (Fig. 20), although the composition as well as the size of the nanocrystalline grains in the two specimens are equal. This peculiar behaviour of the magnetization may be understood in terms of the superferromagnetic interaction among the nanocrystalline grains: Since the thickness of the grain boundary layer is quite small, the magnetic dipole interaction between the neighbouring grains would cause a ferromagnetic coupling between them, given by,

$$E_{ij} = K_m^{ij} M_i M_j \qquad \ldots (11)$$

where K_m^{ij} is the magnetic coupling constant for the interaction between the crystallites i and j, and M_i is the magnetization of the ith crystallite. A modified mean field theory for such a system gives the temperature dependent hyperfine field as[45,46]

$$b(T) = \frac{B_{obs}(T)}{B_0(T)} = L \left[\frac{3T_p}{T} \left(\frac{B_0(T)}{B_0(T_p)} \right)^2 b(T) \right] \qquad \ldots (12)$$

where $L[\ ]$ is the Langevin function, $B_0(T)$ is the hyperfine field of the bulk, and T_p is the magnetic transition temperature given by:

$$T_p = \frac{M^2(T_{p'})}{3k_B} \sum_j K_m^{ij} \qquad \text{...(13)}$$

The temperature dependent hyperfine field of nanocrystalline phase at temperature above the Curie temperature of amorphous phase, and in the presence of dipole interaction among the grains, will be given by eq. (12). Since the composition and the size of the nanocrystalline grains of the two specimens are equal, the average magnetization of a grain, M_j, is expected to be equal in the two specimens. However, since the degree of crystallization in the specimen A25 is higher, the average spacing between two nanocrystalline grains in this specimen will be smaller than that in specimen A10. This will lead to a higher value of K_m and hence of T_p in specimen annealed for longer time, and thus to a slower variation of hyperfine field with temperature.

4.2 Magnetic Anisotropy

Generally, it is believed that the initial degrees of topological disorder of the amorphous alloy should not affect the properties of the subsequent crystalline phase. However, it has been found that the initial as-cast state influences the subsequent nanocrystallized specimens. Knoble et al.[47] observed that the increase in initial permeability, μ_p upon nanocrystallization in $Fe_{73.5}Cu_1Nb_3Si_{13.5}B_9$ ribbons is strongly influenced by the initial free volume content of each sample. Samples produced with higher quenching rate exhibited a faster transformation kinetics and stronger enhancement of the initial permeability in the nanocrystalline state. The quenched-in stresses in the as-cast state are found to affect the coercivity of the subsequent nanocrystalline state[48].

The magnetic anisotropy induced in amorphous and nanocrystalline states by annealing in the presence of strong magnetic fields has also been studied. It may be noted that in soft magnetic materials, magnetic anisotropies are generally considered as disturbative factor causing coercive field, H_c, to increase and saturation magnetization to decrease. However, if properly controlled they can also be employed usefully to tailor the shape of the hysteresis loop according to the requirements of a given application. A common way to induce controlled magnetic anisotropy in magnetic materials is by magnetic field annealing. Magnetic field annealing induces a uniaxial

anisotropy K_a with the easy axis being in the direction of the magnetic field applied during the heat treatment. Yoshizawa and Yamauchi[49] and Herzer[50] have extensively studied the magnetic field induced anisotropy in nanocrystalline alloys. The magnitude of K_a is typically 5 to 50 J/m^3 depending upon the annealing conditions and the alloy composition. Almost perfect rectangular and flat loops are obtained after field annealing. This indicates that the induced anisotropy K_a dominates over the magnetocrystalline and magnetoelastic anisotropies. Still K_a is small enough to yield permeabilities of several 10^4.

The field annealed samples mostly reveal a slightly smaller coercivity than the samples annealed without field although the total anisotropy present is several times larger. This can be understood from the fact that the major contribution to coercivity arises from spatial fluctuations of the anisotropy only, and the more simple domain configuration after magnetic field annealing.

Yoshizawa et al.[49] have studied the influence of the annealing conditions on the induced magnetic anisotropy while Herzer[50] has studied in detail, effect of the alloy composition within the Fe-Cu-Nb-Si-B system. The experimental data indirectly suggests that the uniaxial anisotropy is mainly induced in the bcc Fe-Si grains probably by atomic pair ordering of the Si-atoms. This is indicated i) by the fact that the anisotropy is induced at annealing temperatures far above the local Curie temperature of the residual amorphous matrix and ii) by the correlation found between K_a and the nanostructure data[50]. Mössbauer spectroscopy has been used to obtain the spin texture in the nanocrystalline grains and the amorphous grain boundary region separately in the specimens annealed with and without external magnetic fields[51]. The Mössbauer measurements support the earlier observation that the anisotropy is induced mainly in the nanocrystalline grains. The anisotropy normalized to the crystalline volume fraction, i.e. K_a/v_{cr}, is a well defined function of the Si-content in the α-Fe(Si) grains comparable with the corresponding literature data for conventional Fe-Si alloys[52] in particular, the decrease in H_c can be understood from the increasing long-range order (DO_3 superlattice structure) with increasing Si-content which reduces the available lattice sites for directional ordering.

5 Conclusions

Controlled partial crystallisation of some amorphous alloys like FeCuNbSiB leads to the formation of nanocrystallites dispersed in an amorphous matrix. This composite system is found to possess excellent soft magnetic properties, which even surpass those of transition metal-metalloid metallic glasses. Studies have shown that presence of Cu and Nb, though in small quantities, is essential for the formation of nanocrystalline structure. During initial stages of annealing Cu segregates out and forms nanoclusters which act as nucleation sites for the primary phase consisting of bcc Fe-Si. Nb comes out of the primary crystallites and forms a concentration gradient around the crystallites, thus, inhibiting the grain growth. Detailed Mössbauer study with complementary information from X-ray diffraction and other techniques suggest that the nanocrystals consist of partially ordered non-stoichiometric bcc Fe_3Si phase. The Si concentration in the grain is about 20%, which is much higher than the nominal composition of the parent amorphous phase. The excellent soft magnetic properties of this composite material arise because of the fact that the grain size as well as the intergranular spacing is much smaller than the ferromagnetic exchange length, so that the local anisotropies are randomly averaged out by the exchange interaction. Further the magnetostriction of the crystalline and amorphous components being opposite in sign, they tend to cancel the each other, giving rise to a very low average magnetostriction. From the fundamental point of view also these nanocrystalline alloys present a very interesting magnetic system, exhibiting various phenomena like superparamagnetism and super-ferromagnetism. Various annealing treatments like stress annealing or field annealing have been used to introduce magnetic anisotropy in these systems in order to tailor their B-H loop. Excellent thermal stability and the soft magnetic properties which can be tailored by controlling the composition and annealing treatments make them one of the best known soft magnetic materials with great potential in low frequency as well as high frequency devices.

References

1   H R Hilzinger *J Magn Magn Mater* **88** (1990) 370

2   Y Yoshizawa, S Oguma and K Yamauchi *J Appl Phys* **64** (1988) 6044; Y Yoshizawa, K Yamauchi, T Yamane and H Sugihara *J Appl Phys* **65** (1988) 6047

3   Y Yoshizawa and K Yamauchi *Mater Trans JIM* **31** (1990) 307

4   G Herzer *Handbook of magnetic materials* (Ed. K H J Buschow) Elsevier **10** (1997) 415

5   G Herzer *IEEE Trans Magn* MAG-26 (1990) 1397

6   K Suzuki, A Makino, N Kataoka, A Inoue and T Masumota *J Appl Phys* **70** (1991) 6232

7   N Hasegawa, N Kataoka and H Fujimori *IEEE Trans Magn* **7** (1992) 880

8   P Allia, M Baricco, M Knoble, P Tiberto and F Vinai *J Magn Magn Mater* **133** (1994) 243

9   G Herzer *Mater Sci Eng A* **181,182** (1994) 876

10   L Kraus, K Zaveta, O Heczko, P Duhaj, G Vlasak and J Schneider *J Magn Magn Mater* **112** (1992) 275

11   Y Yoshizawa and K Yamauchi *Mater Res Soc Symp Proc* **232** (1991) 183

12   U Köster, U Schünemann, M Blank-Bewersdorff, S Brauer, M Sutton and G B Stephenson *Mater Sci Eng A* **133** (1991) 611

13   Ajay Gupta, N Bhagat, G Principi, A Maddalena, N Malhotra, B A Dasannacharya, P S Goel, H Amenitsch and S Bernstorff, *Intermetallics* (in press); A Maddalena, G Principi, A Gupta, N Bhagat, N Malhotra, B A Dasannacharya, P S Goel, H Amenitsch and S Bernstorff *J Appl Phys* (accepted)

14   L K Varga, E Bakos, E Kisdi-Koszo, E Zsoldos and L F Kiss *J Magn Magn Mater* **133** (1994) 280

15   Ajay Gupta, N Bhagat, G Principi and A Hernando *J Magn Magn Mater* **133** (1994) 291

16   Neeru Bhagat, Ajay Gupta and P Duhaj Formation of nanocrystalline Fe-Cu-Nb-Si-B alloys *Frontiers in Materials Modelling and Design* (Eds. V Kumar, S Sengupta and B Raj) Springer-Verlag (1998)

17   S Budurov, T Spassov, G Stephani, S Roth and M Reibold *Mater Sci Eng* **97** (1988) 361

18   T H Noh, M B Lee, H J Kim and I K Kang *J Appl Phys* **67** (1990) 5568

19   J D Ayers, V G Harris, J A Sprague and W T Elan *Appl Phys Lett* **64** (1994) 974

20   K Hono, D H Ping, M Ohnuma and H Onodera *Acta Meter* **47** (1999) (in press)

21   M Sakurai, M Matsuura, S H Kim, Y Yoshizawa, K Yamauchi, and K Suzuki *Mater Sci Eng A* **179-180** (1994) 469

22   J D Ayers, V G Harris, J A Sprague, W T Elam and H N Jones *Acta Mater* **46** (1998) 1861

23   K Suzuki, A Makino, A Inoue and T Masumoto *Sci Rep RITU, A* **39** (1994) 133

24   Y Zhang, K Hono, A Inoue and T Sakurai *Scripta Metall Mater* **34** (1996) 1705

25   K Hono and T Sakurai *Sci Rep RITU A* **44** (1997) 223

26   Ajay Gupta and Neeru Bhagat *(to be published)*

27 N Saegusa, A H Morrish, *Phys Rev B* **27** (1983) 4027

28 M B Stearns and *Phys Rev* **168** (1968) 588

29 M Müller and N Matterson *J Magn Magn Mater* **136** (1994) 79

30 Y Yoshizawa and K Yamauchi *Mater Sci Eng A* **133** (1991) 176

31 F van Bouwelen *et al. Appl Phys Lett* **61** (1992) 2536

32 Neeru Bhagat, Ajay Gupta and G Principi *Trans Indian Inst Metals* **48** (1995) 159

33 H R Hilzinger *Mater Sci Forum* **62** (4) (1990) 515

34 G Herzer *IEEE Trans Magn* **25** (1989) 3327

35 G Herzer *IEEE Trans Magn* **25** (1989) 515

36 R Alben, J I Budnick and G S Cargin III *Metallic Glasses* (Eds. J J Gillman and H J Leamy) The Metals Park OH ASM Ch 12 P 32 (1978)

37 T Jamamodo *The Development of Sendust and other Ferromagnetic Alloys* (Komiyama Printing, Chiba, Japan 1991) Ch 1-4 p26

38 G Herzer *J Magn Magn Mater* **112** (1992) 258

39 Ajay Gupta Neeru Bhagat and G Principi *J Phys : Condensed Matter* **5** (1995) 2237

40 C L Chien and R Hasegawa *Phys Rev B* **16** (1977) 3024; A K Bhatanagar, B B Prasad and R Jagannathan *Phys Rev B* **29** (1984) 4896

41 M F Thomas and C E Johnson *Mössbauer Spectroscopy* (Ed. D P E Dickson and F J Berry) Cambridge University Press, Cambridge (1986) 143

42 S Yu, K Kim, Y Cho and T Kim, *IEEE Trans Magn* **28** (1992) 5

43 K Moorjani and J M D Coey *Magnetic Glasses* Elsevier Amsterdam (1984) 133

44 S Chikazumi *Physics of Magnetism* John Wiley New York (1966)

45 S Morup *J Magn Magn Mater* **37** (1983) 39

46 S Morup, M B Madsen, J Franck, J Villadsen and C J W Koch *J Magn Magn Mater* **40** (1983) 163

47 M Knoble, J P Sinnecker, J F Saenger and R Sato Turelli *J Magn Magn Mater* **133** (1994) 255

48 Ch Polack, M Knoble, R Grossinger and R Sato Turelli *J Magn Magn Mater* **134** (1994) 1

49 Y Yoshizawa and K Yamauchi *IEEE Trans J Magnetics* **5** (1990) 1070

50 G Herzer *J Magn Magn Mat* **133** (1994) 248

51 Neeru Bhagat *Ph D Thesis* (1998) (unpublished)

52 K Sixtus and Z Angew *Physik* **16** (1962) 270; *ibid* **28** (1970) 270

NANO-PARTICLES OF OXIDES THROUGH CHEMICAL METHODS

A PATHAK AND P PRAMANIK

Department of Chemistry, Indian Institute of Technology, Kharagpur-721 302 (India)

The paper reviews the state of art of the various synthesis methods suitable for the preparation of nano-sized particles of ceramic oxides. The focus is on the various chemical processes that are gaining rapid popularity for large-scale production of fine ceramics. An effort has been made to summarize, with suitable examples, the methods developed by the authors for the preparation of nano-sized oxides.

Three precursor solution based preparative methods that have been developed are discussed. The methods involve evaporation/flame pyrolysis of a polymer/complex based precursor solution. The precursor solutions are constituted of the desired metal ions dispersed in a polymeric reagent or, metal ions complexed with a chelating agent or, metal-ligand complex dispersed in a polymeric reagent. The polymeric reagent used are Polyvinyl alcohol (PVA) or, Sucrose in presence of 10 mole% of PVA while the chelating agents include organic amines such as Diethanolamine (DEA) and Triethanolamine (TEA) and organic acids such as Citric/Oxalic/ Tartaric acid. The polymeric reagents/ the chelating agents used in the precursor solution play a dual role. They help to keep the metal ions uniformly distributed through out the viscous liquid at the time of evaporation and thus circumvent the precipitation /segregation of the metal ions from solution. Again, the carbonaceous materials, obtained from the evaporation of the polymer/chelating agents, provide heat through combustion for the formation of the respective phases. This facilitates the reduction of the external temperature required for the formation of the desired mixed oxide phase. Rapid evaporation of the entire precursor solution results in a voluminous mass rich in mesoporous-carbon pyrolysis of which yields the fine oxide powders. The exothermic decomposition/pyrolysis of the precursor powders is accompanied by the evolution of large amounts of gases. The evolution of various gas (such as : water vapour, CO, CO_2 NO_2, etc.) not only helps the precursor material to disintegrate but also to dissipate the heat of decomposition, thus inhibiting sintering of the fine particles during the process.

Over fifty different ceramic oxides have been synthesized by the authors using the developed processes and the resulting powders are nanosized (10 to 90 nm in diameter), with narrow particle size distribution of high purity and are obtained at relative lower pyrolysis temperatures than those reported in literature so far. The methods are versatile and can be extended for the preparation of a variety of mixed-oxide systems. In addition, the methods are technically simple, and time and energy efficient, which makes the process cost effective and commercially viable for large-scale production of the fine mixed-oxide products.

Introduction

High performance of products or devices made of ceramic material is often limited by both of its high brittleness and statistical variation in their properties. Any attempt to generate ceramics with properties beyond the present limitations has to focus attention on generating microstructures with new types of atomic arrangement or/new chemical compositions. Fine ceramics materials (with grain sizes less than 100 nm) have been shown to have generic properties[1], (such as high elastic modulus, high hardness, high compressive strengths, general refractoriness and low relative density) much improved over those exhibited by conventional ceramics (> 10 μm). It is the combination of unique composition and microstructure that leads to the extraordinary potential of fine ceramics as attractive engineering materials.

Historically, the developments in the research and application of ultrafine microstructure can be divided in two separate periods. During the first period, ranging from about 1870 to about 1970, the microstructure of materials was recognized to be the crucial parameter[2] for controlling many mechanical, magnetic, electronic and optical properties. In fact, the physical understanding of the mechanism by which the ultrafine

microstructures affect the properties of solids received a remarkable boost after World War II. From the advent of the theory of lattice defects–in particular the dislocation theory–and from the availability of new high-resolution research techniques such as electron and field ion microscopy[2]. Both developments helped to elucidate the physical basis for understanding the correlation between the structure sensitive properties and the microstructure of solids. As a matter of fact, the development of most high strength and high temperature materials available today is based on the results of those studies. After the year 1970, the second period of developments in the area of ultrafine microstructures started, when it was recognized that specifically tailored ultrafine microstructures permit the generation of solids with new atomic and/or electronic structures.

Over the years, these fine ceramic materials have reached such high technological levels in various fields of applications that a plethora of names for them have emerged, names such as: 'nano-phase', 'ultrafine-grained', 'submicron grained', 'microcrystalline' or 'nanocrystalline' materials[3]. A unique feature of fine ceramic materials is that a large fraction of their atoms reside in the grain boundaries. Atoms located within a certain distance of a boundary (*i.e.* within the grain boundary thickness) are displaced from their normal sites in a perfect crystal, due to the presence of atoms across the boundary[4]. If one assumes a grain-boundary thickness of approximately 1 nm (*i.e.,* about four nearest-neighbour distances), a fine-grained material with in a mean grain diameter of 5 nm will have nearly 50% of its atoms in its grain boundaries, and an even higher percentage for smaller grain sizes. This falls only to about 30% for a 10 nm grain size, but it is as low as 3% at a 100nm grain size. Thus, as the particle size decreases the interface volume increases.

According to the pioneering work by Gleiter[5,6] and other groups[7-9] the properties of fine or nano ceramic materials are strongly governed by their surface structure and/or interface volume which represents a significant fraction of their total volume. The theory proposed by Gleiter[2] said that the surface atoms in a small crystallite/particle have (i) a lower density, (ii) a lower co-ordination number, (iii) a larger interatomic distance, and (iv) lower symmetry[10-12]. A modified coordination number of the surface atoms

result in the modified electronic structure and related physical/chemical properties of the fine ceramic materials. Thus, obviously, a change of interface volume in small crystallites/particles of size at a nano meter scale causes a significant change in their electronic structure, according to the chemistry of the constituent atoms.

It is thus conceivable that many of the microstructurally based properties (such as: increased strength/hardness, enhanced diffusivity, reduced elastic modulus, higher electrical resistivity, increased specific heat, reduced thermal expansion coefficient, increased specific surface area, and modified magnetic properties, etc.) of fine-grained materials differ from those of conventional bulk materials in which the interface volume fraction is negligible. These powders, because of their crucial microstucturally based properties, have potential application in many areas of technology[13]. For example, Gleiter and coworkers[5] developed a surprising properties of thin ceramic plate of TiO_2 with a ultrafine microstructure that can be plastically deformed at a temperature as low as 180°C. This behaviour opened the way to new ceramic processing and forming techniques. Some of the general functions, properties and applications of fine ceramics are summarized in Fig. 1.

The synthesis of fine ceramic powders with uniform composition is desirable in the improvement of existing ceramics and the development of new ceramic materials. Mechanical mixing of oxides or carbonates followed by calcination and ball milling is the conventional method for preparing ceramics. This method, though successful for large-scale production of bulk ceramic powders because of its low cost and easily adaptability, has several limitations[14] in the production of 'fine ceramics'. High temperatures and long heating schedules, requisites of this route, sinters the final product resulting in coarsening of the particles and high-energy destruction (*i.e.,* the break down force) is required to get the fine powders[15]. Besides, volatilization/melting of the constituent components may occur during the high temperature processing of some of the multi-component mixed-oxide ceramic systems. Thus, a soft chemical method is more suitable for the preparation of 'fine ceramics'. In the last few decades[16,6,7], a lot of research activities have been focussed on the development of new synthetic methods for the production of sinter-active
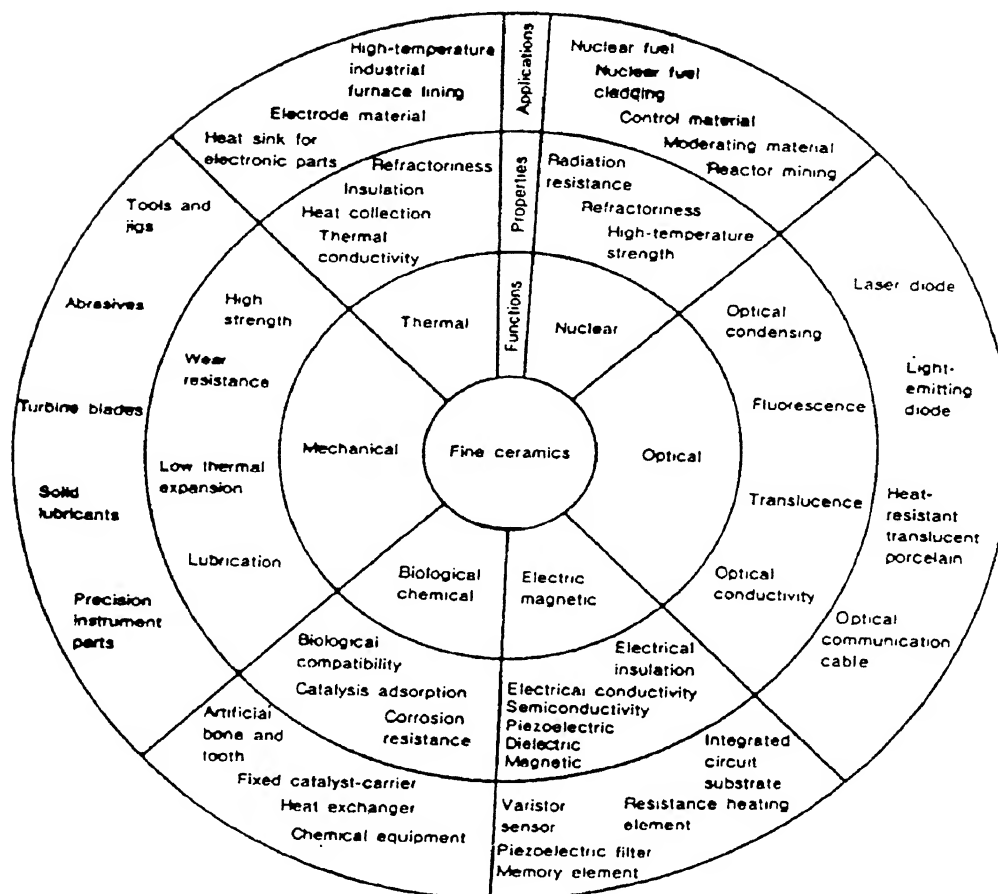
Fig. 1 Functions, Properties and Applications of Fine Ceramics[12]

fine ceramic powders. Details of the state of the art of the powder synthesis are available in various review articles[8,9,17,2].

Synthesis of Fine Ceramics

Recent years have seen a surge of interest in the synthesis and processing of fine ceramic oxide powders. The growing applications of fine ceramics have received increasing interest in the multidisciplinary approach to their synthesis. There are two approaches possible for the synthesis of the fine ceramics. First is the Chemists' approach (*i.e.*, the building-up/or Chemical approach) and the second is the Physicists', approach (*i.e.*, the breaking down/or Physical approach). Inert gas condensation[7], mechanical alloying[18], sputtering[19,20], laser ablation[21], plasma pyrolysis[22], etc. constitute the physical approach methods in this science. Among these processes, gas condensation, mechanical alloying, and spray conversion techniques

are most widely used for a large-scale production of fine ceramics. Chemical processes that are gaining rapid commercialization for at a large-scale production of fine ceramics will be the main focus of the present paper.

The Various Chemical Synthesis Methods

The advanced ceramic materials are often tailor made to suit specific applications, and the chemical synthesis routes play a crucial role in their design and production. Morgen[23] has suggested that the use of chemistry in ceramic fabrication can avoid three major problems − long diffusion paths, impurities and agglomeration. The reasons being that the fine chemically prepared powders allow for shorter diffusion distances and improved homogeneity, the chemical precursors used can be easily refined to increase the purity, and careful control of solvent removal from the precursors could lead to the production of crushable

agglomerates. However, in many cases, the chemical routes generally involve complex techniques compared to the conventional ceramic methods. An improved level of skill is therefore essential if the benefits are to be realized[24].

Uhlmann *et al.*[25] have stressed that better knowledge and understanding of the reactions and mechanism taking place are essential for successful commercial exploitation of the various chemical methods. The synthesis of fine ceramic by a chemical route thus can be categorized under two broad headings of *Vapour Phase Reaction Methods* and *Solution Processing Methods*.

Vapour Phase Reaction Methods

The vapour phase reaction processes (referred to as the Physicists' approach) involve dissociation-vapourization of primary powders (reactants), followed by vigorous quenching of the resulting vapours on to a cold metal substrate. It results in a refined deposit of sample on substrate. The sample, if required, is recovered by scrubbing the deposit from substrate. Generally, the rate and the temperature of decomposition determine the reaction kinetics and rates at which the decomposition products can 'crystallize' on the reaction surface[26]. Inert gas condensation[7], sputtering[18,19], laser ablation[20], plasma spraying[21], processes are some of the important vapour phase reaction methods. Chemical vapour reactions are now receiving considerable attention as techniques for the preparation of high tech ceramics[26-33] for applications in electronic devices.

Solution Processing Methods

The 'solution processing methods' are often considered to be synonymous to the 'chemical synthesis methods'. This technique can be described as consisting of an initial solution preparation step followed by solvent removal and then decomposition of the dried product to the final desired ceramic powders. In general, the solution processing methods offer the advantages of easy preparation of nearly any composition maintaining compositional homogeneity and high purity. The important solution based chemical synthesis methods popularly used for the preparation of fine-grained ceramic products, include: Solvent Vapourization Method, Aerosol Method, Precursor Compound Method, Hydrothermal Method, Co-precipitation Method, Sol-gel Method, Other gel Methods, and the Combustion Method.

Solvent Vapourization Method

In a multi-component system, a slow evaporation of the solution often causes an inhomogeneity in products because of selective crystallization of components with different solubility. To maintain the homogeneity throughout the solvent vapourization process, the solution is broken down in to small droplets (*i.e.*, using spray technique) which results in minimization of solution volume over which segregation can take place. Alternately, the solution can be dried very rapidly so that the segregation is avoided or minimized. The solvent vapourization can be of various types, such as: Flame Spraying[34], Spray roasting[35], Spray drying[36], Emulsion technique[37], Freeze drying technique[38], microwave drying[39], and airless drying[40].

Aerosol Method

Clustered nanoparticles of controlled-sized crystalline and amorphous ceramic materials (especially the chalcogenides) and metals can be prepared through this method. Here the focus is on the novel chemistries developed by the use of surfactant assembly incorporated atomic and molecular clusters. Sharma *et al.*[41] have prepared size selected CdS nanoparticles through the Aerosol method. Aqueous micelles[42], reverse micelles[43], microemulsions, vesicles[44], polymerized vesicles[45], monolayers[46], deposited organized multilayers, and bilayer (black) lipid membranes[47] are the host surfactant assemblies for the clustered particles. J H Fendler[48] has done some pioneering work on the aerosol technique and has published reviews on the detailed working principles and procedures involved with the preparation of atomic and molecular clusters.

Precursor Compound Method

This method involves preparation of a precursor compound. The precursor compounds are usually complex combinations of cations in the proper ratio in their crystalline structures, together with ionic and molecular species containing the necessary oxygen for the formation of solid solutions or the crystalline compounds, the remainder being volatile or decomposable into volatile elements. The pyrolysis of the complex combinations at temperatures between 200°C and 500°C, in an appropriate inert oxidising or reducing atmosphere, depending on the material, gives to nanoscale particles of the desired mixed-oxide system with a good cation stoichiometry. Literature reveals that various organo-metallic

complexes, metal-hydroxides/-carbonates/-oxalates/-citrates,/-ferri-cyanides, and –hydrazine carboxylates etc. are few of the commonly used precursor compounds in this process[49-58].

Hydrothermal Method

Reaction in water above it's boiling points and therefore under pressure, are called hydrothermal reactions. This very general definition illustrates that a variety of very different chemical processes are categorized under the heading of hydrothermal reactions. The different hydrothermal reaction types described in the literature are decomposition, oxidation, crystallization, precipitation, sintering and leaching. For the synthesis of fine oxide ceramics only hydrothermal precipitation and hydrothermal crystallization are usually considered. Hydrothermal precipitation initiates from a clear metal salt solution while the hydrothermal crystallization uses hydroxide gels or sols. Hydrothermal synthesis yields oxide suspension of crystalline metal oxides, which in some cases can even, be used for ceramic processes without a calcination step. A major advantage with the hydrothermal processing is that high temperature calcination is not required for the formation of the oxide. As no solid-state calcination step is needed and thus the formation of hard agglomerates and hard aggregates can easily be avoided unlike in the sol-gel or co-precipitation methods where nano-sized particles are formed and get enlarged and aggregated when the solid-state crystallization to the desired oxide form is performed.

A successful synthesis of material by the hydrothermal synthesis depends on the selection of its precursor. A precursor should be both reactive and cost effective. It should possess appropriate process condition variables, which include temperature, pH and reagent concentrations. A variety of different fine ceramics[59-68] has been successfully synthesized using this hydrothermal technique.

Co-precipitation Method

The co-precipitation process involves the formation of a solid precipitate followed by the separation of the solids with a filtration step. This technique probably is the most widely used method for the preparation of ceramic powders. The precipitation of multi-component system is termed as co-precipitation. For obtaining the co-precipitate with well-defined

stoichiometry of metal ions, the precipitating agent should satisfy the following conditions. The compound should be insoluble in the mother liquor and the precipitation kinetics should be fast. The co-precipitating agents can be a solution of inorganic or organic salt. Various fine-grained ceramic powders have been prepared using inorganic salt solution such as sodium/potassium/ammonium-hydroxides/-carbonates/-oxalates etc.

Use of organic salt solution as the co-precipitating agent circumvents the problems associated with extensive washing of the precipitated precursor material. Moreover, easy volatilization of the organic compounds, in the precursors, during thermal decomposition, facilitates the formation of the ultrafine powders. Pramanik et al., have made significant contribution in the use of organic salt solutions as the co-precipitating agents. The salts include triethylammonium oxalate[69] and triethylammonium carbonate[70,71].

The organic salt-based co-precipitating agents[72-79] are preferred choices for large-scale production of fine powders because of good stoichiometry, purity, homogeneity, and controlled morphology. Several parameters, such as, pH, mixing rates, temperature, and concentration, have to be controlled. For example, microscopic inhomogeneity in the final product arises if the constituent metal ions have widely differing rates of precipitation.

Sol–Gel Method

Sol-gel method involves formation of an amorphous gel from a solution followed by its dehydration at an elevated temperature. The whole process has three key steps[80] as follows:

Step I: The method often uses metal organic precursors where the various components are mixed together in a solvent to get a solution. This 'solution', which in a multi-component composition, is a true ionic or molecular mixture which ensures the atomic-scale mixing (*i.e.*, ultra-homogenization) of the components in the sol-gel technique. The liquid phase for the vast majority of the oxide gels is water or short-chain alcohols, and the solutes may be inorganic nitrates, inorganic chlorides, or a wide variety of metal organic molecules.

Step II: This step is the key step in the sol-gel process. It involves formation of a sol and conversion of it

to a gel so that it retains the chemical homogeneity of the sample during the desiccation. Conversion to a sol is accompanied by adjusting the activity of some species, H^+ and OH^- and other ions, which result in the formation of a dispersed solid phase. In principle, the pH, ionic strength and temperature of the precursor mixture control the gelation of the sol. A manipulation of these parameters is an empirical procedure and it must be worked out independently for each composition. Although the general conditions of *pH* and temperature are known for simple oxides (such as SiO_2 and $AlOOH$) the fine tuning of this step for different staring materials, especially new organic precursors, and multi-component systems has become a major area of current research.

Step III: The last step of the process involves desiccation and heat-treatment of the gels to a ceramic powder.

Many fine ceramics have been prepared by the sol-gel method using different metal ion precursors[81-94]. The particle sizes in this process varied from 50 to 300 nm according to the experimental conditions.

Other Gel Methods : "Citrate–Type Processes"

This is one of the popular chemical synthesis routes used for the preparation of a variety of mixed-oxide powders at relatively low temperatures. Pichini[95] first reported the method in 1968. After his pioneering work, this route is also known as the 'Pechini's Route'. He prepared a variety of fine spinel ferrite systems using citric acid and 15% glycol along with desired aqueous metal salt solutions. Eror and Anderson[96-97] reported preparation of over 100 different mixed-oxide compounds using this method. Since then, a number of mixed-oxide systems have been prepared by the citrate or the modified citrate method by various workers[98-99].

In this process, Amorphous gel mixtures are prepared from solutions containing the required cations and an organic poly-functional acid group such as citric, malic, tartaric, glycolic, or lactic acids. This technique contains a step where the gel is rapidly dehydrated at low temperatures and subsequently pyrolysed to result in the formation of fine oxide powders.

Combustion Method

This method is also known as the 'self-sustaining/propagating high-temperature synthesis process' (*i.e.,*

SHS) and the fire or, furnaceless synthesis. Unlike the Pechini or the amorphous citrate-gel processes, these processes are rapid and may approach direct conversion from the molecular mixture of the precursor solution to the final oxide product, avoiding formation of intermediate crystalline phases that require inter-diffusion for complete reaction. The process makes use of highly exothermic redox chemical reactions between metals and nonmetals, the metathetical (exchange) reaction between reactive compounds or reactions involving redox compound/mixtures. For example[100-105], the combustion approach involves the use of novel combustible precursor which are prepared using carboxylate anion, hydrazine, hydrazine or hydrazinium groups (redox compounds) and redox mixtures as the chelating agents. This method utilized low temperature ignited, gas producing exothermic reactions, which are self-propagating and yield voluminous fine oxides in few minutes. The term 'combustion' covers flaming (gas-phase), smouldering (heterogeneous) as well as explosive type of reactions. Merzhanov, one of the pioneers of the SHS processes, has periodically reviewed[106,107] the developments in SHS and its application for the preparation of carbides, nitrides, borides, silicides, hydrides, chalcogenides, oxides etc. Currently however, several variants of the SHS processes[99,108-110] have gained substantial popularity in the preparation of various ultra-fine multi-component oxide powders. These SHS processes however involve highly explosive type of reactions where a high level of caution and an intricate control of the processing parameters are essential.

The chemical methods generally require a high degree of sophistication and control, in order to obtain the desired characteristic properties in the powders. The benefits that can be obtained from the use of a controlled chemical-processing route are well-recognized[82,111-112] especially for multi-component systems. On the other hand, this invariably increases the cost of the products. Hence, the economic aspects of a particular chemical synthesis process needs to be balanced against the possible improvement in the powder characteristics before it could be considered to be commercially viable.

Although several chemical methods are available for the preparation of a variety of fine mixed-oxide ceramic powders, the author believes that there is scope for improvement of the existing methods, so that less cumbersome, more versatile and cost effective methods can be developed for large scale production

of these ceramics. It is a decade since the authors and their team has been involved with the development of novel chemical routes for the synthesis of nanoparticles of various ceramic oxides. The developed methods are:

1. *Metal ion-polymer based precursor solution method*

2. *Metal ion-ligand complex based precursor solution method*

3. *Metal ion-ligand-polymer based precursor solution method (it is a combination of the two methods)*

The methods involve thermolysis/flame pyrolysis of a polymer/complex based precursor solution. The precursor solutions are constituted of the desired metal ions dispersed in a polymeric reagent or, metal ions complexed with a chelating agent or, metal-ligand complex dispersed in a polymeric reagent. Rapid evaporation of the entire solution results in a voluminous mass rich in mesoporous-carbon pyrolysis of which yields the fine oxide powders. Over fifty different[113-119,58] ceramic oxides have been synthesized by the authors using the developed processes and the resulting powders are nanosized (10 to 90 nm in diameter), narrow particle size distribution of high purity and are obtained at relative lower pyrolysis temperatures than those reported in literature so far. In this paper, we make an effort to summarize the methods developed by the authors with suitable examples.

Experimental

Metal Ion-polymer Based Precursor Solution Method

In this method, the precursor solution is constituted of an aqueous solution of the desired metal salts (predominantly, metal nitrates) mixed with a water-soluble polymer for obtaining the matrix for the dispersion of the cations. The polymer–Polyvinyl alcohol (PVA) easily decomposes exothermally at low ignition temperatures ($\sim 500°C$) leaving behind very little carbon residue. This characteristic of the PVA along with its water-soluble nature motivated the initiation of this method. The method is termed as the *'PVA Evaporation Method'*. By changing the polymeric reagent in the precursor solution the method has been further modified. In the modified method the precursor solution is constituted of an aqueous solution of the desired metal salts (predominantly, metal nitrates) mixed with the polymer -PVA/PAA/carboxylated starch (about 10%) for obtaining the

matrix, in presence of aqueous solutions of monosaccharides, or, disaccharides or, poly hydroxy compounds (such as sorbitol, manitol). Considering the huge volume of the research work, we will restrict our discussions to the precursor solution that consists of the metal salts embedded in the polymer matrix provided by PVA and the disaccharide – Sucrose and we term it as the *'Sucrose Evaporation Method'*.

The methods involve rapid evaporation of the viscous polymeric reagent (*i.e.,* PVA and Sucrose-PVA) added mixed metal nitrate solutions. The complete evaporation of the polymer added mixture results in a fluffy porous mass, which is easily ground to constitute the fine *"precursor powders"*. The precursor powders on pyrolysis (at temperature varying from 300°C to 900°C) results in the formation of the desired fine ceramics. The polymer (PVA/Sucrose) plays a dual role in the process, it acts as a dispersing agent for the cations in the solution and it also serves as a fuel that provide heat through combustion during the calcination of the precursor powders. The details of the reagents required for the preparation of selected few mixed-oxide systems through the *PVA Evaporation method* and the *Sucrose Evaporation method* is listed in Table I and Table II respectively. The flowchart of these two routes is depicted in Fig. 2.

The oxide systems investigated through the methods include (i) Pure oxide [*e.g* α-Al_2O_3, Cr_2O_3, ZrO_2, ZrO_2 stabilized with 5% CaO / MgO / Y_2O_3]; (ii) Spinels [*e.g* $MgAl_2O_4$, $CuFe_2O_4$, $NiFe_2O_4$, $CoFe_2O_4$, $ZnFe_2O_4$]; (iii) Orthoferrites [*e.g* $LaFeO_3$, $NdFeO_3$, $GdFeO_3$, $SmFeO_3$]; (iv) Garnets [*e.g* $Y_3Al_5O_{12}$, $Gd_3Al_5O_{12}$, $Gd_3Fe_5O_{12}$, $Sm_3Fe_5O_{12}$]; (v) Nano Composites [*e.g* Fe_2O_3, NiO, Fe_2O_3, CuO, Fe_2O_3, TiO_2]; (vi) Metal phosphates [*e.g* $Co_3(PO_4)_2$, $Ni_3(PO_4)_2$, $Cu_3(PO_4)_2$, $Ba_3(PO_4)_2$, $AlPO_4$, $CrPO_4$, $FePO_4$]; (vii) Metal vanadates [*e.g* $Ca_3(VO_4)_2$, $Co_3(VO_4)_2$, $Ni_3(VO_4)_2$, $Cu_3(VO_4)_2$, $CrVO_4$, $FeVO_4$, $MnVO_4$]; (viii) Metal molybdates [*e.g* $CaMoO_4$, $NiMoO_4$, $CoMoO_4$, $MgMoO_4$, $Sm_2(MoO_4)_3$, $Gd_2(MoO_4)_3$]; (ix) Metal tungstates [*e.g* $CaWO_4$, $MgWO_4$, $NiWO_4$, $CoWO_4$]; (x) Rare-earth aluminates [*e.g* $LaAlO_3$, $SmAlO_3$, $NdAlO_3$]; and (xi) PZT and PLZT systems.

Metal ion-Ligand Complex Based Precursor Solution Method

In this chemical method, various complexing agents have been used in the precursor solution. The complexing/chelating agents are used to keep the metal

Table I

Stoichiometries (in moles) of the various reagents used for the preparation of few of the representative the mixed-oxide precursors

Sample	Metal ion: PVA* mole ratio	$Fe(NO_3)_3$ (moles)	$M(NO_3)_2$ (moles)	$R(NO_3)_3$ (moles)@	Total PVA (moles)**
MFe_2O_4 System: M = Co(II) / Ni(II) / Zn(II)					
a	1:1	0.0447	0.0223	–	0.0670
b	1:2.5	0.0447	0.0223	–	0.1678
c	1:6	0.0447	0.0223	–	0.4028
$RFeO_3$ System: R = Sm(III) / Nd(III) / Gd(III)					
a	1:1	0.0143	–	0.0143	0.0286
b	1:2.5	0.0143	–	0.0143	0.0715
c	1:6	0.0143	–	0.0143	0.1716
$R_3Fe_5O_{12}$ System: R = Sm(III)					
a	1:1	0.0238	–	0.0143	0.0381
b	1:2.5	0.0238	–	0.0143	0.0953
c	1:6	0.0238	–	0.0143	0.2286

*: Represents the moles of vinyl alcohol monomer unit of PVA;   #: 10% w/v PVA solution;
@: Prepared from stoichiometric amounts of R_2O_3 dissolved in dilute nitric acid.

Table II

The details of the chemicals required for the sucrose evaporation method for the preparation of few of the representative mixed-oxide systems

Metal salts/Preparation condition	Moles of Sucrose (FW-342)	Moles of PVA* (10% w/v aq. solution of PVA)	Total volume of the solution after mixing
Pure Oxide : (α Al_2O_3): 1 mole $Al(NO_3)_3.9H_2O$	2	0.05	1.5 lit.
Lanthanam Aluminate : ($LaAlO_3$) : 0.5 mole La_2O_3 + 3 mole aq. HNO_3 (75% v/v) + 1 mole Al $(NO_3)_3$. $9H_2O$	4	0.05	2.5 lit.
Y_2O_3 stabilized ZrO_2 : 1 mole NH_4OH + 1 mole zirconium oxychloride hexahydrate → zirconium hydroxide obtained dissolved in conc. HNO_3 (1 lit.) with Y_2O_3 (0.04 mole) dissolved in HNO_3 (50 cc)	2.5	0.05	2.5 lit.
Metal Phosphate : ($FePO_4$): Ammonium dihydrogen phosphate (1 mole/500 ml H_2O) + Fe $(NO_3)_3$. $9H_2O$ (1 mole in 1 lit. H_2O) + HNO_3 so that pH = 1	3	0.05	3.0 lit.
Metal Vanadate : (YVO_4): 0.5 mole Y_2O_3+conc. HNO_3 (250 ml) produced $Y(NO_3)_3$ solution + vanadyl salt (obtained from 1 mole ammonium vanadate+4 mole formic acid+4 mole hydrazine hydrate was slowly added and refluxed for 1 hour at 120° C to produce 1 mole vanadyl salt)	2.5	0.05	2 lit.
Metal Tungstate : ($CaWO_4$): Freshly prepared $CaWO_4$ (1 mole) + ethylene diamine tetracetic acid (1.2 mole) + diethylenetriamine (3 mole) dissolved in 1.5 lit. water	1	0.05	2 lit.
Metal Molybdate : ($CaMoO_4$) Freshly prepared $CaMoO_4$ (1 mole) + EDTA (1.2 mole) + ethylenetramine (3 mole) dissolved in 1.5 lit. water	1	0.05	2 lit.

* Represents the moles of vinyl alcohol monomer units of PVA

```
┌─────────────────────────────────┐        ┌──────────────────────────────┐
│ PVA Method:                     │        │ Aqn. Metal nitrate solution  │
│ 10% (w/v) Aqu. solution of PVA  │───────▶│ (with desired cation ratio)  │
│ (with the desired cation: PVA   │        │ Heated at ~ 70-80°C          │
│ monomer ratio)                  │        │                              │
└─────────────────────────────────┘        └──────────────────────────────┘
                                                          │
┌─────────────────────────────────┐                      ▼
│ Sucrose Method:                 │        ┌──────────────────────────────┐
│ 20%(w/v) Aqu. Sucrose Solution  │        │ The Polymeric reagent added  │
│ with PVA mole %w.r.t. Sucrose)  │        │ to the mixed metal nitrate   │
│ (with the desired Cation:Sucrose│        │ solution (10 under hot       │
│ mole ratio)                     │        │ condition (~ 70-80°C)        │
└─────────────────────────────────┘        └──────────────────────────────┘
                                                          │
                                                          ▼
                                           ┌──────────────────────────────┐
                                           │ The resultant viscous mixture│
                                           │ evaporated on hot plate at   │
                                           │ ~ 200°C with stirring        │
                                           └──────────────────────────────┘
                                                          │
                                                          ▼
                                           ┌──────────────────────────────┐
                                           │ Evaporated to dryness at     │
                                           │ ~200°C                       │
                                           └──────────────────────────────┘
                                                          │
                                                          ▼
                                           ┌──────────────────────────────┐
                                           │ Fluffy carbonaceous mass     │
                                           │ obtained                     │
                                           └──────────────────────────────┘
         ┌──────────┐                                     │
         │ TGA/DTA  │◀─────┐                              ▼
         └──────────┘      │          ┌──────────────────────────────────┐
         ┌──────┐          └──────────│ Ground to give the Virgin        │
         │ IR   │◀────────────────────│ Precursor Powder                 │
         └──────┘          ┌──────────└──────────────────────────────────┘
       ┌──────┐            │                              │
       │ XRD  │◀───────────┘                              ▼
       └──────┘      ┌────────────────┌──────────────────────────────────┐
     ┌──────┐        │                │ Virgin Powders Calcined at       │
     │ IR   │◀───────┤                │ different Heat-treatment         │
     └──────┘        │                │ temperatures                     │
   ┌──────┐          │                └──────────────────────────────────┘
   │ TEM  │◀─────────┤
   └──────┘          │
 ┌──────────────────────────┐
 │ Dielectric Measurements  │◀─┘
 └──────────────────────────┘
```
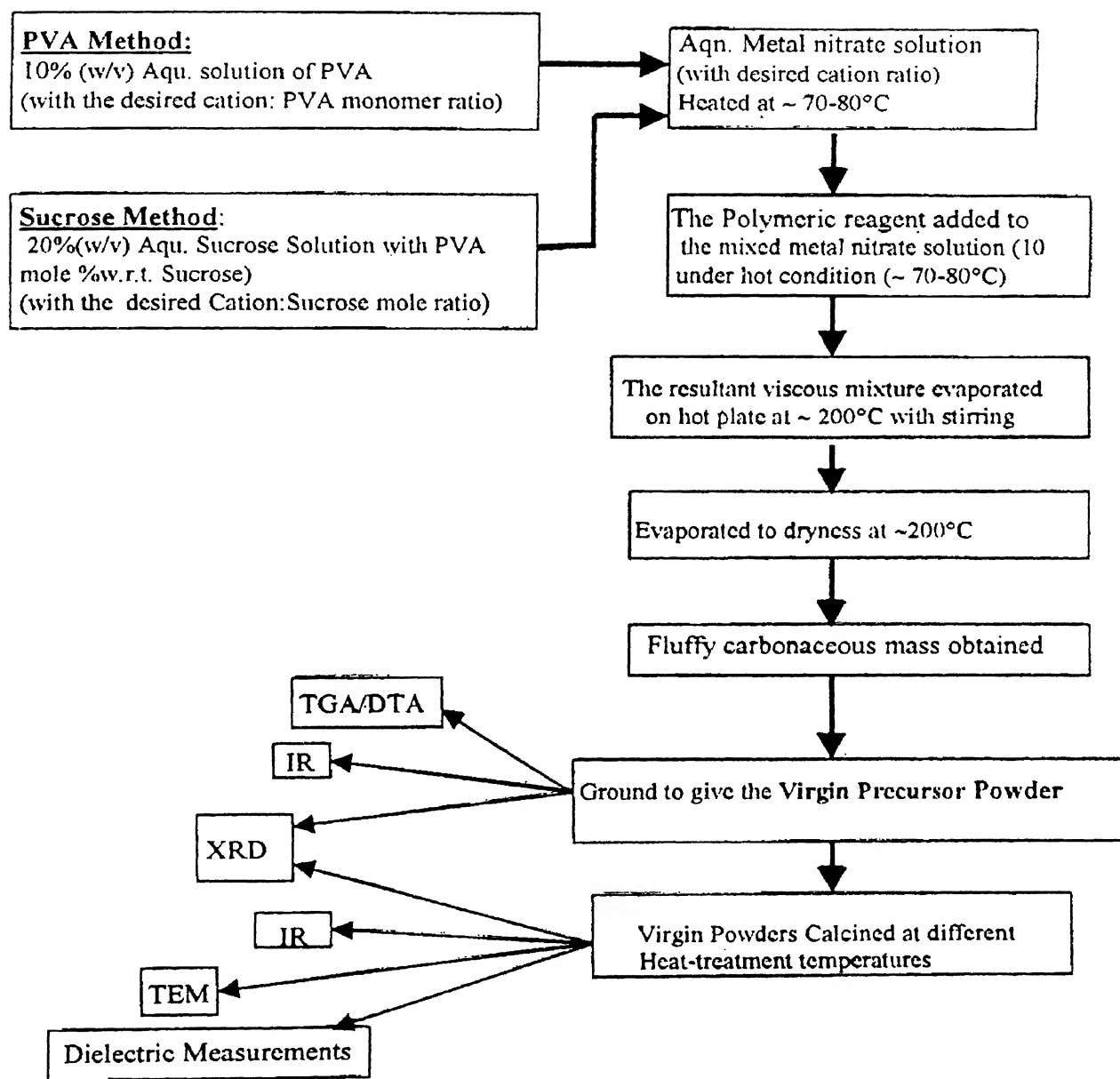
Fig. 2 Schematic representation of the Metal-ion-Polymer based Precursor Solution Method

ions in homogeneous solution, leaving enough flexibility for the system to exist homogeneously throughout the reaction without undergoing precipitation. To ensure this, the moles of the complexing/chelating agent per unit mole of the metal ion in the starting solution has been always kept in excess to the required stoichiometry.

The method involves the complete dehydration of the metal ion-ligand complex precursor solution, which is accompanied by the decomposition of the metal complexes. The decomposition results in a voluminous, organic based, black, fluffy mass. This organic mass is easily crushed to fine powders to generate the *precursor material*. Calcination/heat-
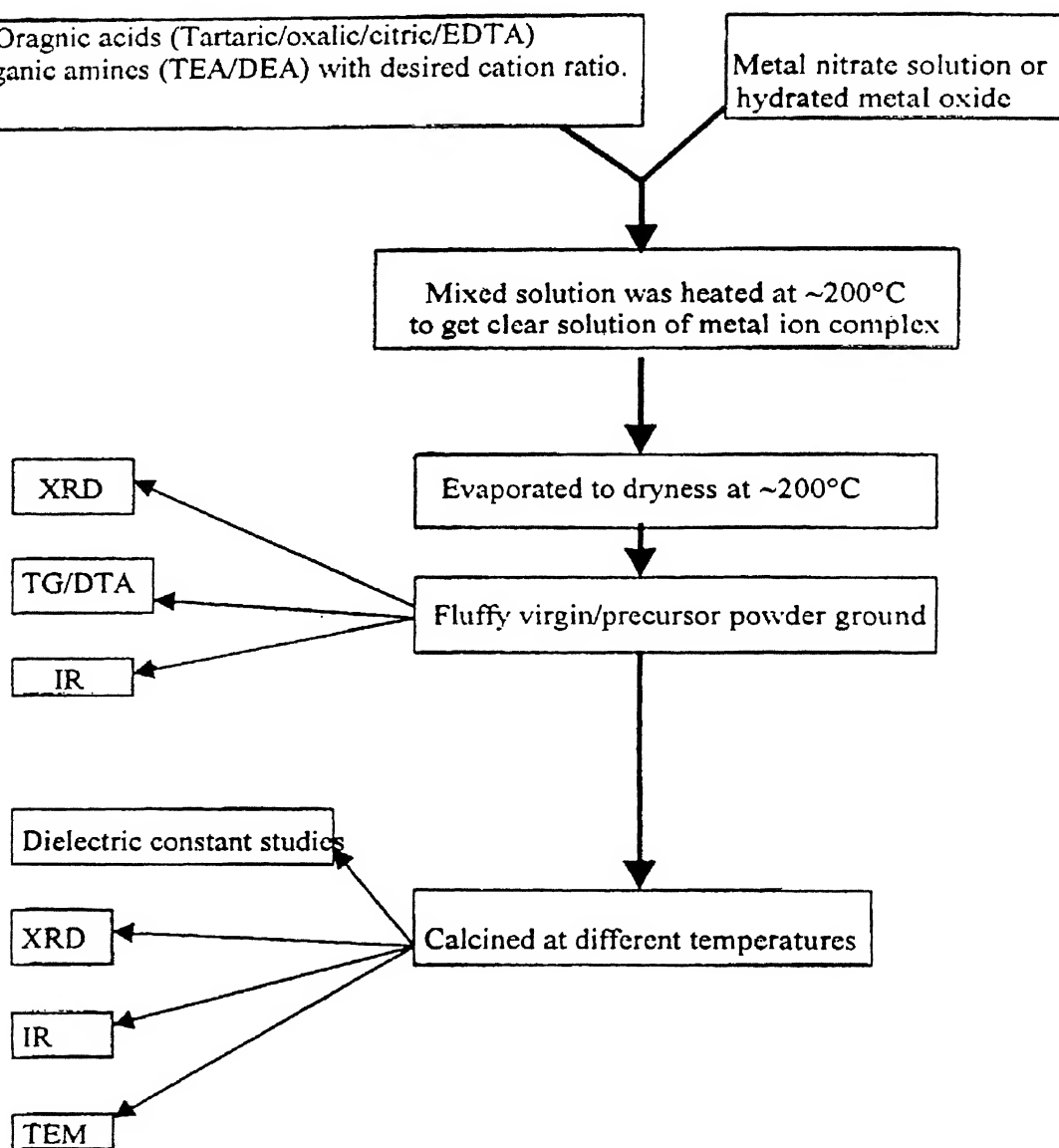
```
┌─────────────────────────────────────────────┐        ┌──────────────────────────┐
│ Aqu. Oragnic acids (Tartaric/oxalic/citric/  │        │ Metal nitrate solution or │
│ EDTA)                                         │        │ hydrated metal oxide      │
│ Or organic amines (TEA/DEA) with desired      │        │                          │
│ cation ratio.                                 │        └──────────────────────────┘
└─────────────────────────────────────────────┘
```

Mixed solution was heated at ~200°C
to get clear solution of metal ion complex

Evaporated to dryness at ~200°C

XRD

TG/DTA   Fluffy virgin/precursor powder ground

IR

Dielectric constant studies

XRD   Calcined at different temperatures

IR

TEM

Fig. 3 Schematic representation of the Metal-ion-ligand complex based Solution Method

treatment of the precursor material results in the respective fine mixed-oxide ceramics. The ligands apart from serving as a chelating agent for the uniform distribution of the cations in the solution also acted as a fuel during calcination of the precursor powders. A generalized process for the preparation of fine ceramic materials using the Metal ion-ligand complex based precursor solution method is depicted in Fig. 3.

The authors have utilized various complexing agents, especially different *organic amines* (namely, *diethanolamine* and *triethanolamine*) and different *organic acids* (namely, *oxalic, tartaric and citric acids*) as the ligands for complexation with the metal ions.

The developed methods using the organic amines and the organic acids follow the same working principle. The organic amines/acids are useful complexing agents for the preparation of multi-component ceramics specially where the constituent

metal complexes have widely different solubilities. For example in the synthesis of PZT [*i.e.*, with composition Pb($Zr_{0.6}Ti_{0.4})O_3$] through the metal ion-organic acid complex based precursor solution method, we use oxalate complexes of Ti^{4+} and Zr^{4+} while Pb^{2+} is complexed with EDTA. Use of oxalate complex is avoided for the Pb^{2+} because of the poor solubility of the Pb(Oxalate) complex compared to that of the oxalate complexes of Ti^{4+} and Zr^{4+}, which would lead to segregation of the Pb^{+2} from the solution. On the other hand, aqueous Pb(EDTA) complex has superior stability to that of the Pb(Oxalate) complex and comparable solubility with that of the oxalate complexes of Ti^{4+} and Zr^4. Thus the use of Pb-EDTA complex circumvents the precipitation of Pb(Oxalate) from the system and the homogeneity of cations is maintained throughout the evaporation process.

The precursor solution when constituted of the metal hydroxides/nitrates and *diethanolamine* (DEA) as the ligand then the method is denoted in the text as the *DEA Evaporation Method*. Similarly, when the ligand used is *triethanolamine* (TEA) the method is represented in the text as *TEA Evaporation Method*. Likewise, when the metal ion and the various organic acids constitute the precursor solution, the methods are illustrated in the text as *Oxalate Evaporation Method*, *Tartarate Evaporation Method* and *Citrate*

Evaporation Method where the corresponding organic acids used are *Oxalic acid, Tartaric acid* and *Citric acid* respectively.

The authors illustrate the *Metal ion-Ligand Complex Precursor Solution Method* through the preparation of the representative *PZT* (with composition Pb$Zr_{0.6}Ti_{0.4}O_3$) powders. The details of the preparative conditions for each of the methods for obtaining the final PZT powders are summarized in Table III.

Metal ion-Ligand-Polymer Based Precursor Solution Method (the Combination Method)

In addition to the mentioned methods, the authors have extended the work to the preparation of *lead magnesium niobate PMN* [Pb($Mg_{1/3}Nb_{2/3})O_3$] and *PFN* [Pb($Fe_{1/3}Nb_{2/3})O_3$] *relaxor materials* through *two* different methods that are combination of the developed two methods (*i.e.*, the polymer based and the complex based precursor solution methods).

In the first method the precursor solution is constituted of the metal nitrates/hydroxides, TEA and tartaric acid in presence of the polymer i.e. PVA. This method is defined as *PVA-TEA-Tartarate Evaporation Method*. The second method is assigned as the *PVA-EDTA-Tartdrte Evaporation Method*. The precursor solution in this method is constituted of the metal nitrates/hydroxides that are complexed with

Table III

Details of Metal ion-ligand complex precursor solution methods for the preparation of PZT (with composition PbZr$_{0.6}$Ti$_{0.4}$O$_3$) powders

---

* Preparative condition for the synthesis of PZT powders through the various methods

DEA Evaporation Method
Stoichiometric amounts of hydrated metal oxides (Pb, Zr, Ti) were reacted with 4-5 moles of DEA per mole of PZT at 200°C to produce a homogeneous red coloured solution of metal ion –DEA complexes.

TEA Evaporation Method
Stoichiometric amounts of hydrated metal oxides of Ti and Zr were reacted with 8 mole of TEA to produce a red solution of metal ion –TEA complexes. The hot metal ion-TEA solution was then mixed with aqueous 30%(w/w) Pb($NO_3)_2$ mixture to produce a homogeneous solution.

Oxalate Evaporation Method
1 mole aqueous Pb(EDTA) was mixed with stoichiometric amounts of Ti-Oxalate and Zr-Oxalate solution to produce a homogeneous solution.

Tartarate Evaporation Method
1 mole aqueous Pb(EDTA) was mixed with stoichiometric amounts of Ti-tartarate and Zr-tartarate solution to produce a homogeneous solution.

Citrate Evaporation Method
1 mole aqueous Pb(EDTA) was mixed with stoichiometric amounts of Ti-citrate and Zr-acetate solution to produce a homogeneous solution.

---

* The homogeneous precursor solutions obtained through each of the preparative methods were evaporated to complete dryness to result in a fluffy carbonaceous powders which were calcined to yield in the PZT phase.

the EDTA and tartaric acid in presence of the polymer *i.e.*, PVA. The preparative conditions for the synthesis of the representative PMN is cited in Table IV and the procedure is illustrated in Figs. 4 and 5.

Results

The final phase and the morphology of the powders prepared through the various developed methods are affected by the following factors, they are:

(1) The amounts of the polymeric reagent/complexing agents used per unit mole of the metal ion present in the precursor solution.

(2) The heat liberated during the complete dehydration of the precursor solution

(3) The bed temperature during the complete dehydration of the precursor solution.

(4) And the time taken for the complete evaporation process.

The characterization studies of the various precursor and heat-treated powders are carried out to get a comprehensive comparative data on the developed methods. For example, the simultaneously recorded thermogravimetry and differential thermal analysis

Table IV
Summary of the two combination methods developed for the preparation of PMN [Pb(Mg$_{1/3}$Nb$_{2/3}$)O$_3$] powders

---

*Preparative conditions for the synthesis of PMN powders through the various combination methods

---

PVA-TEA-Tartarate Evaporation Method
Stoichiometric amounts of Ti-tartarate complex solution and Pb-TEA complex solution were mixed with aqueous Mg(NO$_3$)$_2$ containing 2 moles of PVA solution to produce the homogeneous precursor solution.

PVA-EDTA-Tartarate Evapoartion Method
Stoichiometric amounts of Ti-tartarate complex solution and Pb-EDTA complex solution were mixed with aqueous Mg(NO$_3$)$_2$ containing 2 moles of PVA solution to produce the homogeneous precursor solution.

---

* The homogeneous precursor solutions obtain through each of the preparative route was evaporated to complete dryness to result in black, fluffy, carbonaceous powder which yield the corresponding PMN- phase on heat-treatment.
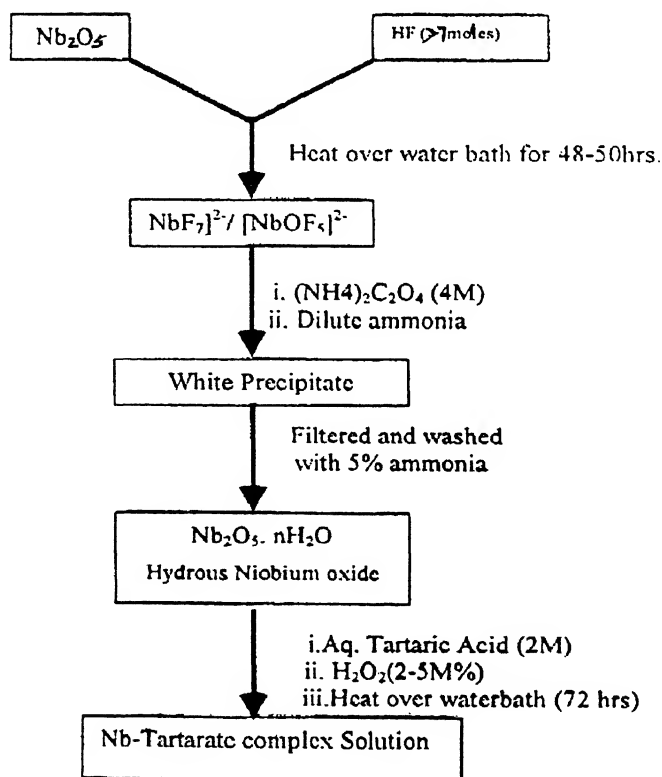

Fig. 4 Flowchart for the preparation of soluble niobium-tartarate complex solution
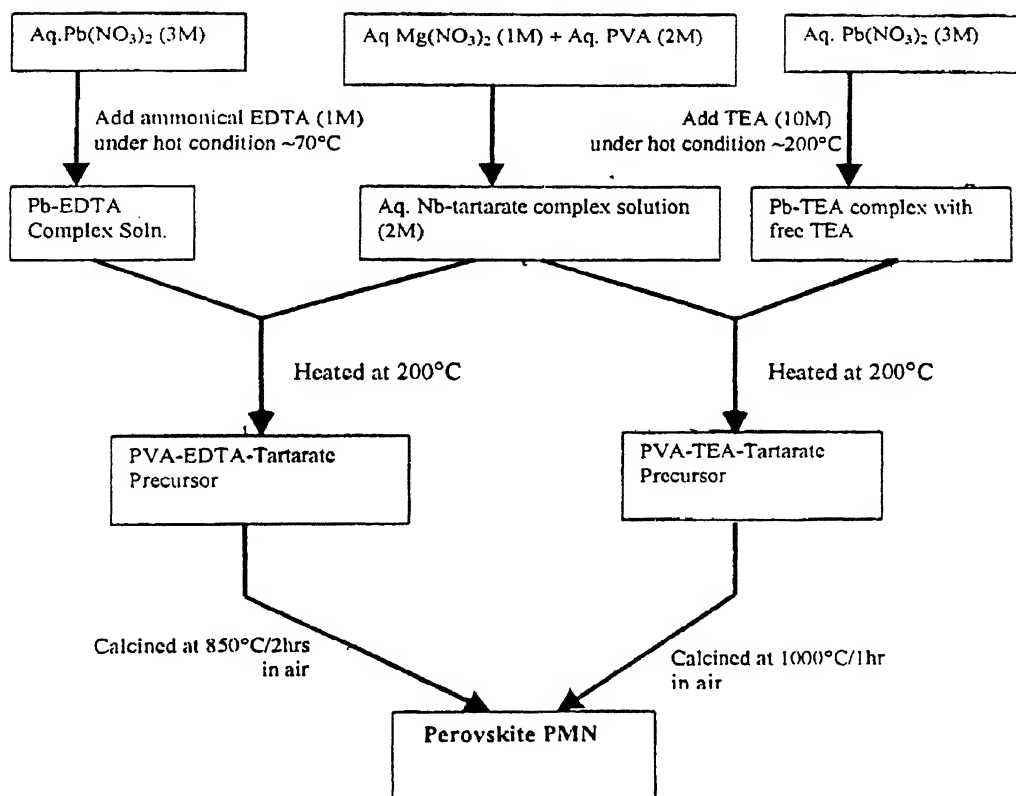
Fig. 5 Schematic representation of the metal ion-PVA-EDTA-tartarate and the metal ion-PVA-TEA-tartarate evaporation method for the synthesis of PMN [Pb(Mg$_{1/3}$Nb$_{2/3}$)O$_3$]

(TG/DTA) studies of the various precursors obtained through the various methods provide information on their thermal effect (*i.e.*, the amount of heat released, the corresponding bed/crucible temperature, the total weight loss etc.).

The X-ray powder diffraction (XRD) patterns of the various precursor and heat-treated powders presents the phase composition of the sample. The X-ray diffractograms of the representative PZT precursor and heat-treated samples that are prepared through the various metal-ion-polymer based precursor solution methods and the various metal-ion –ligand complexed based precursor solution methods are shown in Fig. 6 (A and B) and Fig. 7 (A, B, C, and D) respectively.

Similarly, X-ray diffractograms of the representative PMN [Pb(Mg$_{1/3}$Nb$_{2/3}$)O$_3$] precursors at different heat-treatment temperatures and that of the sintered pellets, produced through the two combinations of the metal-ion-ligand complex and metal-ion-polymer based precursor solution methods, are depicted

in Figs. 8(A and B) and Figs. 9 (A and B) respectively. In these figures the lines (110) and (222) corresponds to the maximum intensity peak in the perovskite and pyrochlore phase respectively.

For ferroelectric materials, such as the PZT system; the dielectric constant measurement are carried out for the heat-treated powders that are palletized and sintered at 1100°C/6h in a lead oxide rich environment provided by PbZrO$_3$ placed in a closed alumina crucible. Variation of dielectric constant with temperatures for the PZT [*i.e.* with composition Pb(Zr$_{0.6}$Ti$_{0.4}$)O$_3$] samples prepared through the PVA method with altering amounts of PVA per unit mole of the metal-ion where the metal-ion : PVA mole ratios are: 1:0, 1:1, 1:2, and 1:3 for the samples P$_0$, P$_1$, P$_2$, and P$_3$ respectively is depicted in Fig. 10. As in normal ferroelectric, the dielectric constant (ε) of prepared PZT powders, with Zr/Ti ratio 60/40, increased gradually with temperature and attained a maxima (ε_{max}) at the Curie temperature (T_c). It is observed that the value of the dielectric constant is
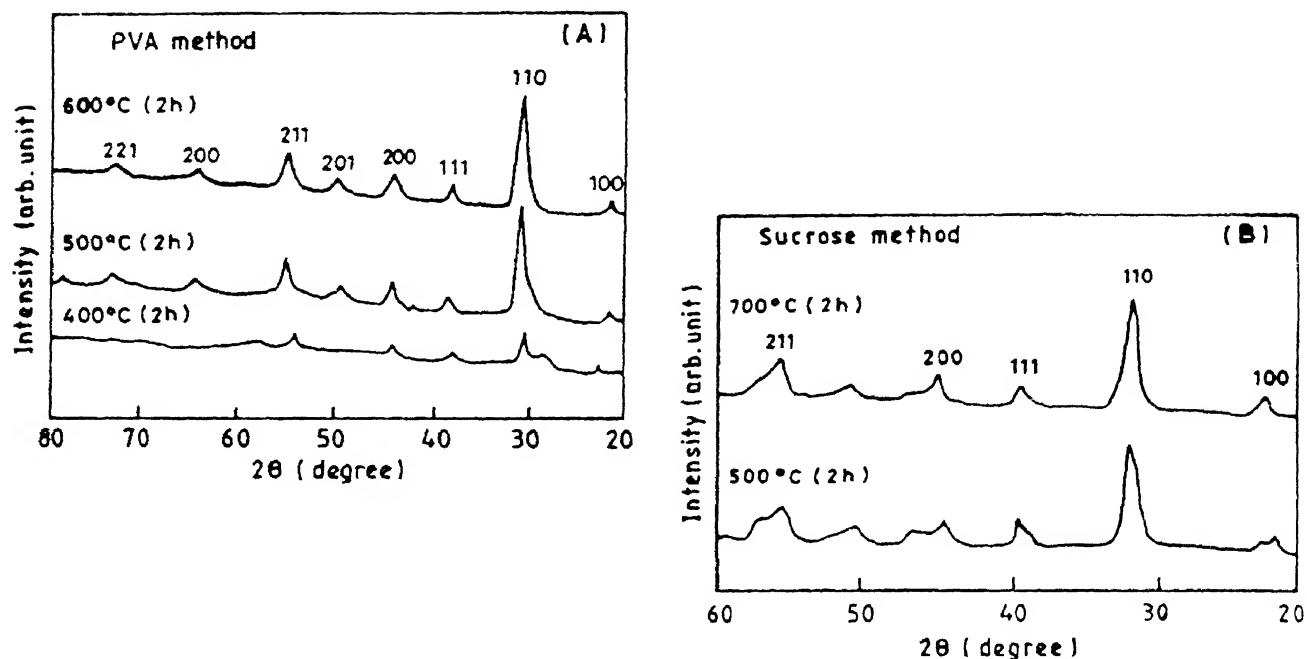
Fig. 6 X-ray diffractograms (using CuK_α radiation) of the PZT [i.e., with composition $Pb(Zr_{0.6}Ti_{0.4})O_3$] precursor powders produced through the metal-ion-polymer based precursor solution method and heated at various temperatures: (A) PVA method, and (B) Sucrose method

maximum when the metal-ion : PVA mole ratio is 1:2. Again, the variation of dielectric constant with temperatures for the sintered (at 1200°C/4h) PZT [i.e. with composition $Pb(Zr_{0.6}Ti_{0.4})O_3$] and PLZT (La = 0.03 mole) pellets prepared through the TEA method is presented in Fig. 11.

Similarly for the dielectric studies, of the PMN [$Pb(Mg_{1/3}Nb_{2/3})O_3$] powders (obtained through the PVA-EDTA-Tartarate and PVA-TEA-Tartarate Evaporation methods after heat-treatment at the 850°C/2h and 900°C/2h respectively) are compacted in to pellets and are sintered at 1200°C/4h under a lead reach atmosphere provided by $PbZrO_3$. The plots of the variation of dielectric constant with temperatures at 1, 10, and 100 kHz and the plot of ln ($1/\varepsilon - 1/\varepsilon_m$) versus ln ($T_m - T$) at 1 kHz and 100 kHz for the sintered PMN [$Pb(Mg_{1/3}Nb_{2/3})O_3$] pellets prepared through the PVA-TEA-tartarate evaporation method are shown in Figs. 12 and 13 respectively.

X-ray $d_{(hkl)}$ line broadening studies are used for the crystallite size calculation of the powders using the Scherrers' formula[120]. Transmission electron microscopy studies of the heat-treated powders provide information on the microstructure and the particle size distribution in the samples. The bright

field TEM micrographs represent the basic powder morphology where the smallest visible ultrafine particles might be identified with the crystallites or their aggregates. The bright field TEM micrographs, and their corresponding SAD patterns for the heat-treated Fe_2O_3 (400°C/3h) and $\alpha-Al_2O_3$ (1025°C/2h) powders prepared through the TEA method are illustrated as representative examples in Fig. 14 (A and B), and Fig. 15 (A and B) and respectively. The presence of the ring in the SAD pattern signify crystallinity in the samples and indicate that each of the particles acted as a single crystallite, with exactly the same atomic array but were oriented differently to each other and were diffracting coherently. Spotty rings or single crystal diffraction patterns replaced these discrete ring patterns as the samples were heat-treated at higher temperatures.

Considering the PZT [i.e., with composition $Pb(Zr_{0.6}Ti_{0.4})O_3$] system as the representative example the major findings of the work is summarized below:

● In the metal ion-polymer based precursor solution method, the optimum amount of the polymer (i.e., PVA and Sucrose-PVA) per mole of the metal ion required for a production of fine ceramic powders is 2:1.
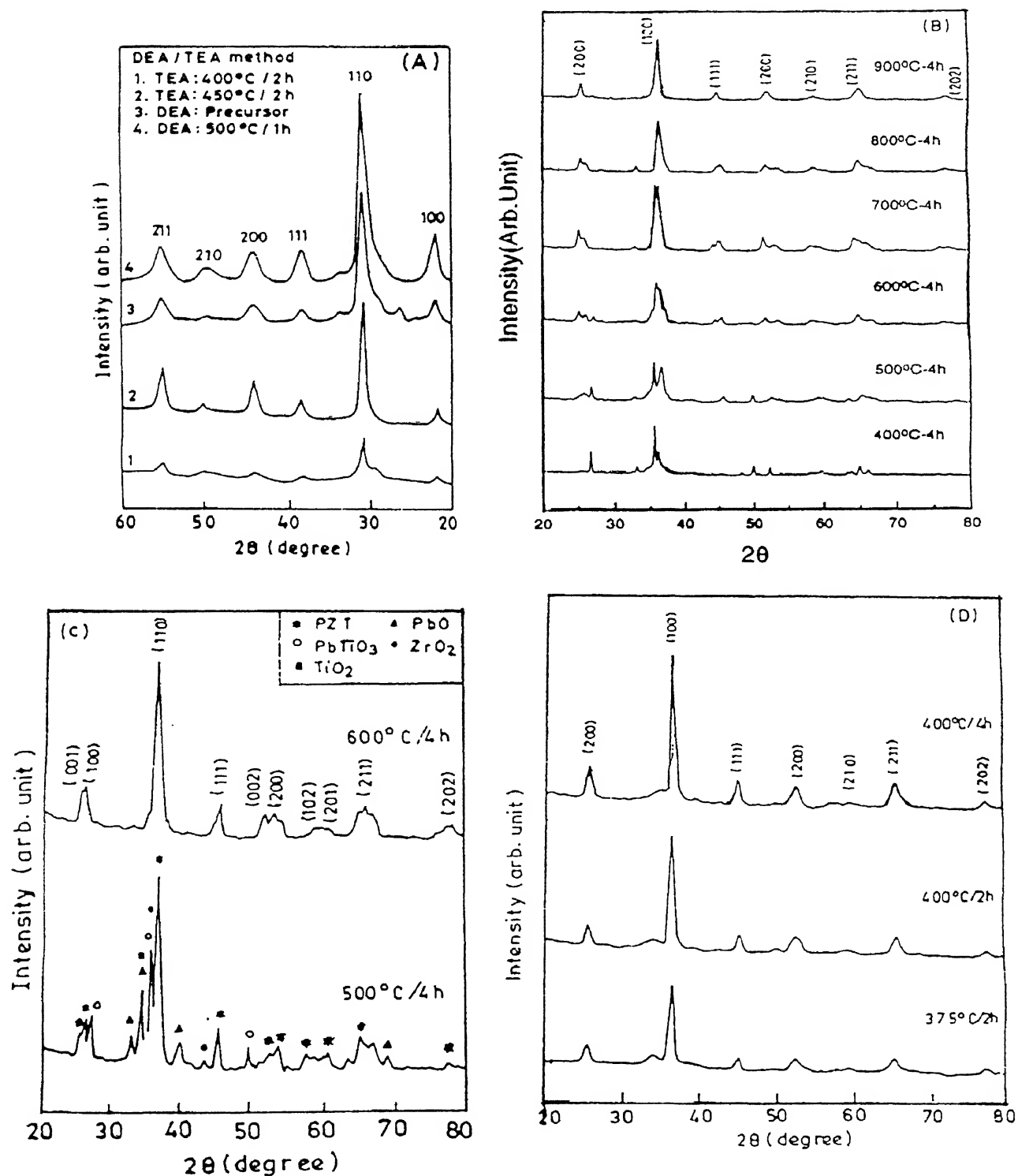
Fig. 7 X-ray diffractograms (using CuK_α radiation) of the PZT [i.e., with composition $Pb(Zr_{0.6}Ti_{0.4})O_3$] precursor powders produced through the metal-ion-ligand complex based solution method and heated at various temperatures: (A) DEA and TEA methods, (B) Citrate method, (C) Oxalate method, and (D) Tartarate method
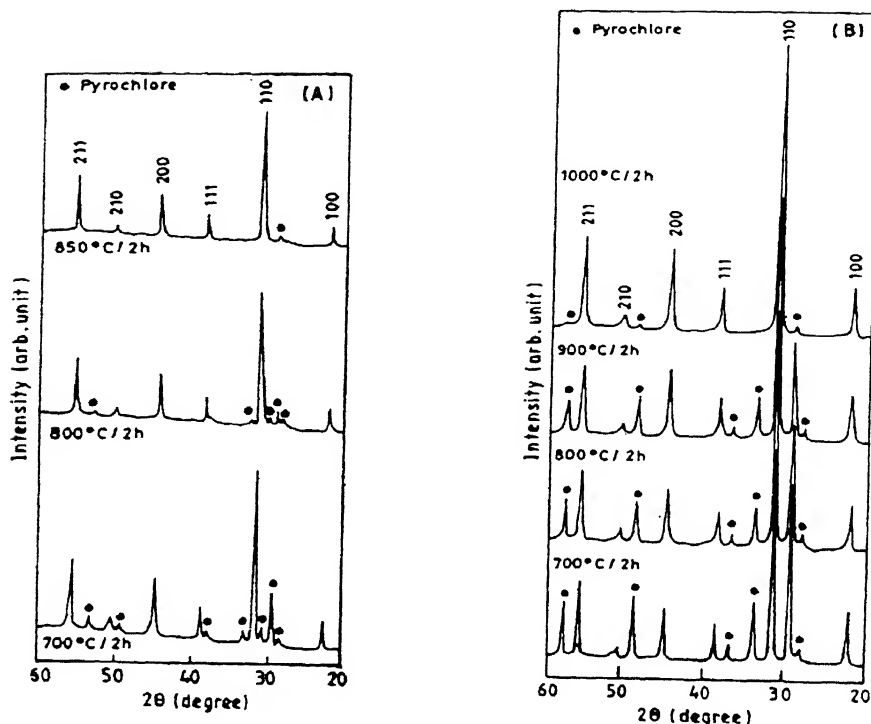
Fig. 8 X-ray diffractograms (using CuK$_\alpha$ radiation) of the PMN [Pb(Mg$_{1/3}$Nb$_{2/3}$)O$_3$] precursor powders produced through the metal-ion-ligand-polymer based combination method and heated at various temperatures: (A) Metal ion-PVA-EDTA-tartarate evaporaion method, and (B) Metal ion-PVA-TEA-tartarate evaporation method
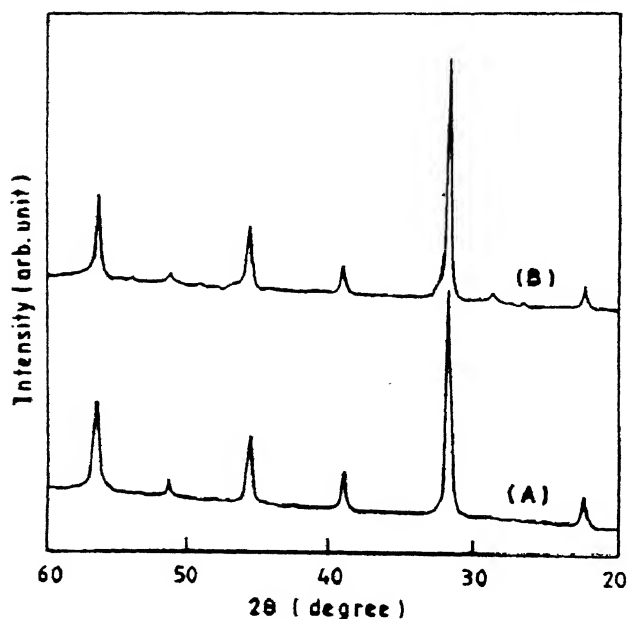

Fig. 9 X-ray diffractograms (using CuK$_\alpha$ radiation) of the sintered (1200°C/4h) PMN [Pb(Mg$_{1/3}$Nb$_{2/3}$)O$_3$] pellets prepared through: (A) Metal ion-PVA-EDTA-tartarate evaporation method, and (B) Metal ion-PVA-TEA-tartarate evaporation method
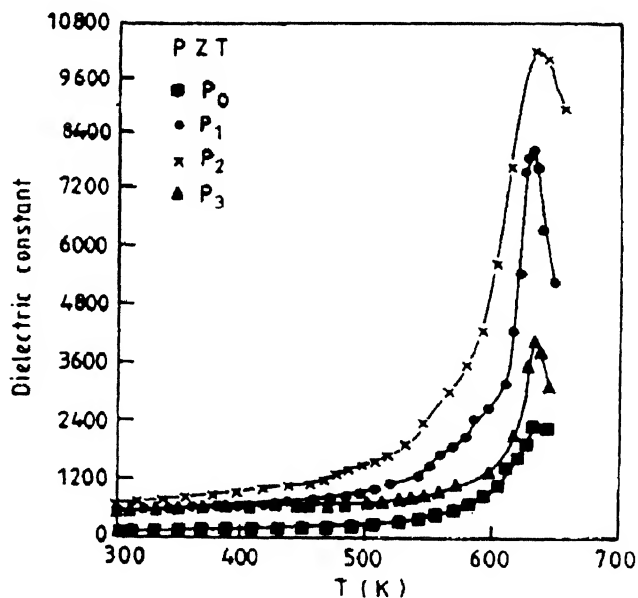

Fig. 10 Variation of dielectric constant with temperatures for the the sintered (at 1200°C/4h) PZT [i.e., with composition Pb(Zr$_{0.6}$Ti$_{0.4}$)O$_3$]pellets prepared through the PVA method with altering amounts of PVA per unit mole of the metal-ion. The metal-ion is to PVA mole ratios are: 1:0, 1:1, 1:2, and 1:3 for the samples P$_0$, P$_1$, P$_2$, and P$_3$ respectively

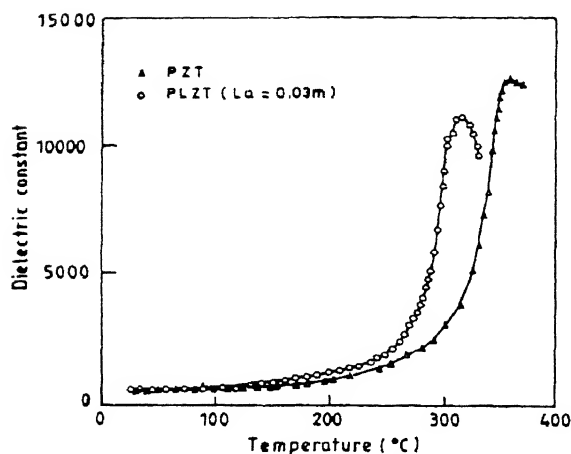Fig. 11 Variation of dielectric constant with temperatures for the sintered (at 1200°C/4h) PZT [i.e., with composition $Pb(Zr_{0.6}Ti_{0.4})O_3$] and PLZT (La = 0.03 M) pellets prepared through the TEA method
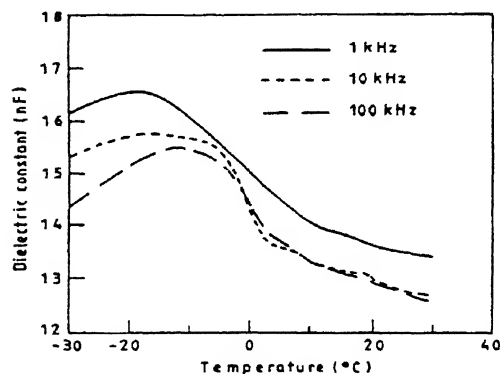

Fig. 12 Variation of dielectric constant with temperatures at 1, 10, and 100 kHz for the sintered PMN [$Pb(Mg_{1/3}Nb_{2/3})O_3$] pellets prepared through the PVA-TEA-tartarate evaporation method

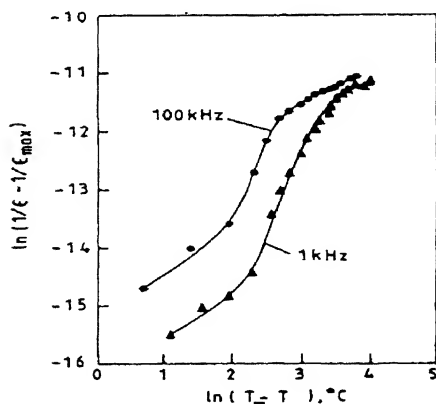Fig. 13 Plot of $\ln(1/\varepsilon - 1/\varepsilon_m)$ versus $\ln(T_m - T)$ at 1 kHz and 100 kHz for the sintered PMN[$Pb(Mg_{1/3}Nb_{2/3})O_3$] pellets prepared through the PVA-TEA-tartarate evaporation method
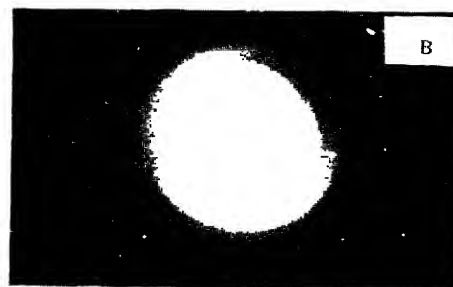

Fig. 14 Fe_2O_3 (heat-treated at 400°C/3h) powders prepared through the TEA method
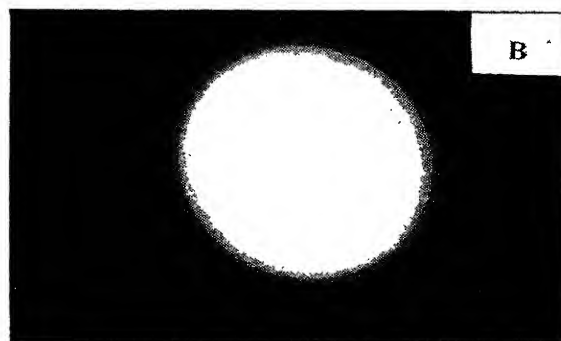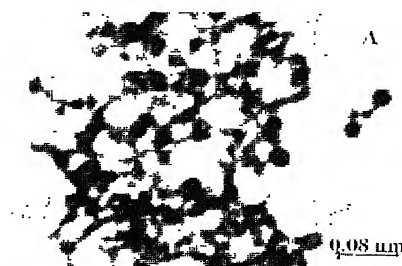(A) Bright field micrographs, and
(B) Corresponding SAD patterns

Fig. 15 α-Al_2O_3 (heat-treated at 1025°C/2h) powders prepared through the TEA method
(A) Bright field micrographs, and
(B) Corresponding SAD patterns

- Of the two polymer based precursor solution methods, the Sucrose method (which involved the addition of 10 mole% of PVA per mole of sucrose in the starting solution) resulted in finer particles with narrow distribution at relatively lower heat-treatment temperatures ($< 500^0$C) compared to that of the PVA method.

- Under similar sintering conditions, the maximum dielectric constant values (*i.e.,* ε_{max}) of the fine mixed-oxide powders change with the change in the preparative methods. It is observed that the ε_{max} approaches the highest value when the particle sizes were comparable to the crystallite size.

- The physical characteristics of the mixed-oxide powders (*i.e.,* the average particle size, dielectric constant and the formation temperature) obtained using the chelating agents DEA (*i.e.,* diethanolamine) and TEA (*i.e.,* triethanolamine) are comparable. However, the use of DEA results in the precursors that facilitate the formation of the oxide phase directly in the virgin precursor state (*i.e.,* before calcination) while the precursors produced using TEA yields the oxide phase after calcination at 450°C.

- Comparison of the various complex-based precursor solution methods reveal that, that of all the methods, the mixed-oxide powders obtained using the organic amines (*i.e.,* DEA and TEA) as the chelating agents produced finer particles at a relatively lower formation temperature.

- Of the various organic acids used (*i.e.,* among the Tartarate, Citrate and Oxalate evaporation methods) as the chelating agent, the tartarate precursors produced the finest (with the average particle size of ~30 nm) powders at the lowest heat-treatment temperature (375°C), and having the highest ε_{max} value.

- Of the various organic acids used as the chelating agent, the use of tartaric acid however results in mixed-oxide powders with average particle size, dielectric constant and formation temperatures comparable with those obtained using the organic amines (*i.e.,* DEA/TEA).

- The physical characterization of the PMN [Pb $(Mg_{1/3}Nb_{2/3})O_3$] powders prepared through the two methods revealed that the PVA-EDTA-Tartarate evaporation method resulted in finer particles (average particle size ~ 20 nm) at a comparatively low formation temperature (~ 850°C).

- Comparative studies of the room temperature dielectric constants also revealed that the PMN [$Pb(Mg_{1/3}Nb_{2/3})O_3$] powders prepared through the PVA-TEA-Tartarate evaporation method have in higher values (~ 13,300) than those obtained through the PVA-EDTA-Tartarate evaporation method (~ 10,500).

The results of the TEM and the dielectric studies for the representative PZT [*i.e.,* with composition $Pb(Zr_{0.6}Ti_{0.4})O_3$] fine powders, prepared through various methods and calcined at various temperatures for 2-4hrs are summarized in Table V. The results of the TEM particle sizes for the representative PLZT system is summarized in Table VI.

Discussions on the Developed Methods

Metal-Ion-polymer Based Precursor Solution Method: the PVA Method

The precursor solution is constituted of stoichiometric amounts of the metal nitrates dissolved in deionized water, and 10% w/v of PVA (molecular weight 1,25,000) maintaining an acidic *p*H. The resulting viscous solution is put to heated over a hot plate with temperature maintained around 200°C. Boiling of the precursor solution in nitric acid medium oxidizes the PVA to the corresponding ketone and at elevated temperatures it is ultimately converted to the carboxylic acid with simultaneous breaking up of the carbon chain. As evaporation proceeds, the nitrate salts are decomposed with the liberation of brown fumes of NO_2. The continuous heating of the solution causes foaming and puffing and constant stirring is required to facilitate the escape of vapour from the solution. Complete evaporation of the PVA-added mixed-metal-nitrate solution results in a voluminous charred fluffy structure, which are easily crushed and ground to compose the precursor powder. On the basis of the experimental findings the carbonaceous precursor powders is presumed to be constituted of mesoporous carbon with some amounts of metal oxides embedded in its matrix, metal-carboxylates (which are expected to form *in-situ*, from the reaction of the metal ions with the residue of the decomposed PVA) and trace amounts of undecomposed metal-nitrates. The composition of the precursor is changeable depending on the reactivity of the constituent metal ion and the various experimental condition such as: sample bed-temperature during the complete evaporation process, amount of PVA in the

Table V
The summary of the characterization studies of the final PZT [with composition $Pb(Zr_{0.6}Ti_{0.4})O_3]$ powders obtained using the various methods

Preparative Methods	Temperature* (°C)	Average Particle size§ (nm)	Dielectric constant** (±50)	Curie Temperature (±2°C)
PZT SAMPLES				
PVA Evaporation Method	500°C/2h	100	10,120	362
Sucrose Evaporation-Method	480°C/2h	80	10,700	365
DEA Evaporation-Method	200°C	25	11,520	364
TEA Evaporation-Method	450°C/2h	20	12,475	362
Oxalate Evaporation-Method	600°C/4h	60	6,500	372
Tartarate Evaporation-Method	400°C/2h	30	11,900	371
Citrate Evaporation Method	900°C/4h	150	5,650	356
PMN SAMPLES ***				
PVA-TEA-Tartarate Method	1000°C/1h	200 nm	13,300	–
PVA-EDTA-Tartarate Method	850°C/2h	20 nm	10,500	–

*   Represents the minimum furnace temperature required to obtain the PZT/ PMN
§   Average particle size from TEM Studies
**   The maximum dielectric constant values for the various PZT samples at a constant frequency of 10 kHz at the respective Curie temperatures.
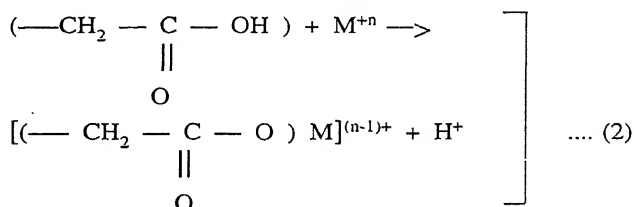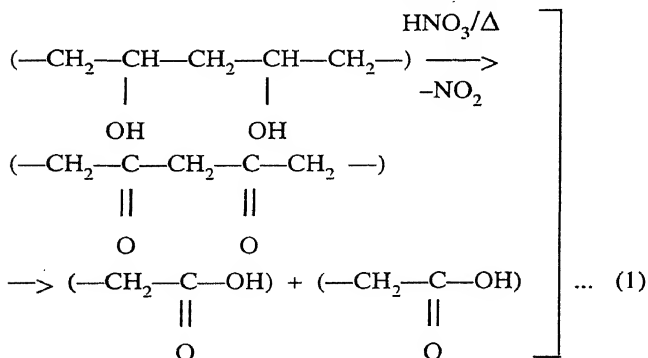***   PMN shows the room temperature (30°C) dielectric constant at 1kHz.

Table VI
The External Formation Temperature and Corresponding Average TEM Particle Size for the Various La Modified PZT Systems

Composition	External formation temperature and corresponding average particle size (nm)			
	PVA	Sucrose	TEA	DEA
$Pb_{1-x}La_x(Zr_{0.6}Ti_{0.4})O_3$ Where x = 0.03, 0.05, 0.07, 0.1, 0.12	500-650°C (80-120 nm)	500-650°C (60-100 nm)	500-600°C (20-40 nm)	200-500°C (25-50 nm)
$Pb_{1-x}(La_{1-z/3}D_z)_x(Zr_{0.6}Ti_{0.4})_{1-x/4}O_3$ Where x = 0.03, 0.05, 0.1, D = Na, K, Li, Cs, Tl and z = 0.1, 0.2, 0.3, 0.5, 0.7	600-750°C (100-150 nm)	600-750°C (60-100 nm)	550-700°C (40-80 nm)	200-500°C (25-50 nm)
$Pb_{1-x}(La_{1-z/3}Bi_z)_x(Zr_{0.6}Ti_{0.4})O_3$ Where x = 0.03, 0.05, 0.1, and z = 0.1, 0.3, 0.5, 0.7	600-750°C (100-150 nm)	600-750°C (60-100 nm)	550-700°C (40-80 nm)	200-500°C (25-50 nm)

starting solution etc. Calcination at temperatures ranging between 400°C to 900°C, results in the formation of nanocrystals of the respective mixed-metal oxides.

The tentative reaction mechanism for the decomposition of PVA is proposed as follows:

$$(-CH_2-CH-CH_2-CH-CH_2-) \quad \xrightarrow[-NO_2]{HNO_3/\Delta}$$
$$\quad\quad | \quad\quad\quad |$$
$$\quad\quad OH \quad\quad OH$$
$$(-CH_2-C-CH_2-C-CH_2-)$$
$$\quad\quad\quad || \quad\quad\quad ||$$
$$\quad\quad\quad O \quad\quad\quad O$$
$$\longrightarrow (-CH_2-C-OH) + (-CH_2-C-OH) \quad .... (1)$$
$$\quad\quad\quad\quad\quad || \quad\quad\quad\quad\quad\quad ||$$
$$\quad\quad\quad\quad\quad O \quad\quad\quad\quad\quad\quad O$$

$$(-CH_2-C-OH) + M^{+n} \longrightarrow$$
$$\quad\quad || $$
$$\quad\quad O$$
$$[(-CH_2-C-O)M]^{(n-1)+} + H^+ \quad .... (2)$$
$$\quad\quad\quad\quad || $$
$$\quad\quad\quad\quad O$$

where M^{+n} represents the metal ion present in the system.

The utility of the polymeric approach comes from the chemical bonding of the cations onto the polymer chains. In the reported process, PVA not only serves as a metal chelating agent but also acts as a fuel which provided heat through combustion during calcination of the precursor. The principal action of PVA in the preparation of the precursor powder changed with the amount of PVA added. The final phase and morphology of the powders were also

affected by metal ion to vinyl alcohol monomer unit of PVA mole ratio in the starting solution.

When the amount of PVA added is small, the polar groups of the long chain of the polymer absorb only some of the cations present in the "precursor solution". This results in segregation and inhomogeneous distribution of the metal ions in the polymeric network structure of PVA, which finally culminated in multi-phase final product on complete evaporation of the PVA-added metal nitrate solution.

The calcination temperature and time, required for the complete solid-phase reaction, are dependent not only on the contact interface among grains but also on the distribution of the various components in the precursor material. In case of non-uniform or, less uniform distribution of the various cations (*i.e.,* segregated products), the atoms must pass through the contact interface among the phases to meet other kinds of atoms. When the amount of PVA added is small, this requirement is achieved only by raising the calcination temperature and prolonging the reaction time. This, however, leads to the growth in the crystallite size and a loss in the fine particle nature of the resulting powder. On the other hand, at lower heat-treatment temperatures, inhomogeneous distribution of the metal ions in the precursor leads to multi-phase final product.

When the amount of PVA is too large, then several layers of the polymer cover the cations in the solution and the dehydration process takes longer time even if the distribution of the cations is more or less uniform. The presence of large amounts of polymer in the system, however, give rise to large amount of carbonaceous mass on complete evaporation of the PVA-added metal nitrate solution. This had a negative effect as it raises the temperature rather high and causes an increase in the heat liberated during calcination. The high temperature leads to the formation of large crystallites that are very strongly agglomerated. The high temperatures or the heat liberated can be lowered and lowering the oxygen content of the flowing gas in the furnace can slow the reaction down. However, doing so can be detrimental since the lowering of the temperature or the heat liberated would cause incomplete burning of all the carbonaceous matter and thus would result in residual carbon content.

When moderate amount of PVA is used, the polar groups of the polymer chain of PVA play a wrapping and covering role for the cations in the solution. As a result, their mutual contact is voided. Thus, the metal ions remain uniformly distributed in the viscous liquid during evaporation and their segregation and precipitation from the solution were avoided. Since the distribution of the various metal ions remains uniform in the precursor material, the metal ions need only a short distance diffusion to complete the solid phase reaction. Hence definite phase formation of the desired oxide system takes place at relatively lower external temperatures and with the liberation of relatively less amount of heat. This results in comparatively finer particles than that of the excess PVA case.

Thus, 2-3 moles of vinyl alcohol monomer unit of PVA per mole of metal ion was found to be the optimum amount of polymer required for obtaining the finest particles at the lowest external temperatures through the reported route.

Metal-Ion-polymer Based Precursor Solution Method: The Sucrose Method

The sucrose solution in presence of small amounts of PVA, shows characteristics similar to that of a polymeric reagent. In this process the precursor solution is constituted of the stoichiometric amounts of the desired metal nitrates; aqueous solution of sucrose and aqueous solution of PVA (10 mole% with respect to the total sucrose). Complete evaporation of the resultant viscous solution is accompanied by the evolution of brown fumes from the decomposition of the metal nitrates. Pyrolysis (at temperatures varying between 300°C and 900°C) of the fluffy voluminous mesoporous carbon-rich mass, produced on the complete evaporation of the precursor solution of metal-nitrate-PVA-sucrose, gives rise to the nanosized powders of the desired oxide phase.

The sucrose, being always in excess to the metal ions, works as a chelating agent and ensured atomistical distribution of the cations throughout the created polymeric network structure. The overall reaction can be represented as follows:

$$C_{12}H_{22}O_{11} + M(NO_3)_x + (CH(OH)-CH_2)_n \longrightarrow C + M_2O_x + NO_2$$
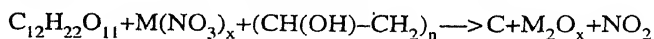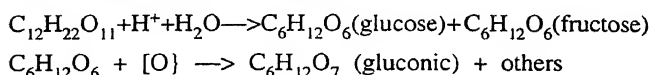
The general idea is to distribute the cations atomistically throughout the polymeric structure so that selective precipitation is prevented during the evaporation process. Stability of the polymeric approach comes from the chemical bonding of the cations onto

the polymeric chain and from the development of extremely high viscosity polymeric solution. Even as the chemical bonding is destroyed during pyrolysis, the high viscosity favours low cation mobility which helps affect the crystallite/agglomerate morphology.

The aqueous solution of sucrose in presence of dilute nitric acid gets hydrolyzed to fructose and glucose that gets further oxidized to gluconic acid (or, a poly hydroxy acid).

$C_{12}H_{22}O_{11} + H^+ + H_2O \longrightarrow C_6H_{12}O_6(glucose) + C_6H_{12}O_6(fructose)$

$C_6H_{12}O_6 + [O] \longrightarrow C_6H_{12}O_7$ (gluconic) + others

The gluconic acid has a carboxylic acid group in one end and five linear hydroxyl groups, which can participate in the complexation of metal ions and it may form branched polymer with PVA. It is observed that sucrose only in presence of PVA, in very small quantity (at 10%) gives rise to crushable, fluffy powder of the oxide system. And it was an empirical observation that the higher the fluffiness of the powders lower was the particle size.

The PVA provides a polymeric matrix structure for the cations and also provides heat through combustion of the carbonaceous remaining of oxidized PVA. In addition, it helps in the polycondensation reaction in presence of oxidized saccharides and gives rise to a branched chain polymer network structure where the metal ion (M^{+x}) are held in the hydroxylic pockets of the branch chain through complex formation. During pyrolysis of these branched chain polymer would release various gases from the pocket making the structure highly porous and fluffy. To substantiate the hypothesis, we performed the experiment with prepolymeric material from gluconic acid and PVA that produces the nanosized oxides very efficiently due to the efficient chelation from branched chain.

For the cases of the phosphates/vanadates/molybdates/tungstates, the immediate precipitation is to inhibited by the addition of EDTA. As EDTA forms stable complexes metal ions and the respective counter ions (e.g. PO_4^{3-}, VO_4^{3-}, MoO_4^{2-}, WO_4^{2-}) remain in the solution because the organoamine-complexes of tungstate/molybdate have poor solubility in the complex-recipe mixture.

Metal-Ion-Ligand Complex Based Precursor Solution Methods

Similar to polymeric reagents used in the metal ion-polymer based precursor solution method, the chelating agents used in the developed synthesis methods play a dual role. They help to keep the metal ions uniformly distributed throughout the viscous liquid at the time of evaporation and thus circumvent the precipitation /segregation of the metal ions from solution. Again, the carbonaceous materials, obtained from the evaporation of the polymer/chelating agents, provide heat through combustion for the formation of the respective phases. This facilitates the reduction of the external temperature required for the formation of the desired mixed oxide phase.

Conclusion

In this paper, we report few simple and versatile chemical processes for the preparation of nanosized ceramic oxides starting from metal-polymer based and metal-ligand complex based precursor solutions. The principle was to atomistically disperse the metal ions in a matrix provided by a polymeric reagent or through complexation with various chelating agents that possess good coordination properties with the metal ions. Evaporation of the precursor solutions resulted in fluffy, voluminous carbonaceous mass that constituted the precursor material. The polymers and the chelating agents used in the developed synthesis methods play a dual role. They help to keep the metal ions uniformly distributed through out the viscous liquid at the time of evaporation and circumvented their precipitation/segregation from the solution. Again, the carbonaceous materials generated from the complete evaporation of the polymer/chelating agents, provided heat through combustion and facilitated the reaction at a reduced value of the external temperature to obtain the desired mixed oxide phase.

On pyrolysis of the precursor powders, the metal ions formed clusters with the oxide ions and were embedded in the resulting matrix of the mesoporous carbon. With the slow oxidation of the carbon, at heat-treatment temperatures ranging between 500°C to 900°C, the cations formed nanocrystals of the respective mixed-metal oxides. The exothermic decomposition/pyrolysis of the precursor powders was accompanied by the evolution of large amounts of gases. The evolution of various gas (such as : water vapour, CO, CO_2 NO_2, etc.) not only helped the precursor material to disintegrate but also to dissipate the heat of decomposition, thus inhibiting sintering of the fine particles during the process.

The developed methods utilize easily available laboratory reagents for the preparation of the fine-

grained mixed-oxide ceramic powders. They are versatile and can be extended for the preparation of a variety of mixed-oxide systems. Moreover, the methods are technically simple, and time and energy efficient, which makes the process cost effective and commercial viable for large-scale production of the fine mixed-oxide products.

References

1   T Page *Future Developments of Metal and Ceramics* (Eds. J A Charles, G W Greenwood and G C Smith) (1992) 121

2   H Glieter *Nanostructured Materials* 1 (1992) 1

3   V G Gryaznov and L I Trusov *Prog Material Science* 37 (1993) 289

4   R W Siegel, S Ramaswamy, H Hanh, Z L, T Lu and R Gronsky *J Mater Res* 3 (1988) 1367

5   J Karch, R Birringer and H Gleiter *Nature* 330 (1987) 550

6   H Gleiter *Prog Mater Sci* 33 (1989) 223

7   R Biringer *Mat Sci & Eng* A 117 (1989) 33

8   D W Johnson *Adv Ceramics* 21 (1987) 3

9   R W Siegel *Mat Res Soc Bull* 15 (1990) 60

10   S Ram, H J Fecht, M Febry and J C Joubert *Nanostructured Materials* 6 (1995) 470

11   S Ram *Phys Rev* B51 (1995) 6280

12   P Frankwicz, S Ram and H J Fecht *Applied Physics Letter* 68 (1996) 282

13   R A Graham and A B Sawaoka High pressure explosive processing ceramics *Trans Tech Publications* Switzerland (1987)

14   D W Johnson and B B Ghate Advances in Ceramics *Proc Am Ceram Soc* (Ed F Y Wang) Columbus OH 15 (1985) 27

15   S T Aruna Ph D Thesis IISc Bangalore India (1987) (submitted)

16   E Matijevic and L L Hench D R Ulrich (Eds) *Ultrastructure Processing of Ceramics Glasses and Composites* J Wiley New York (1984)

17   R W Seigel *Ann Rev Mater Sci* 21 (1991) 559

18   C C Koch *Nanostruc Mater* 2 (1993) 109

19   Y S Kim and H M Jang *Ceram Trans* 43 (1994) 123

20   K Okazaki, H Maiwa and N Ichinose *Ceram Trans* 43 (1994) 15

21   J Frantti and V J Lantto *J Appl Phys* 76 (1994) 2139

22   W W Malinosfsky and R W Babbit *J Appl Phys* 32 (1961) 2375

23   P E D Morgen *Mater Res Soc Symp Proc* (Eds. C J Brinker, D E Clark and D R Ulrich) 32 (1984) 213

24   Y Suyama and A Kato *J Ceram Soc Japan* 88 (1978) 212

25   D R Uhlmann, B J Zelinsky and G E Wrek *Mater Res Soc Symp Proc* (Eds. C J Brinker, D E Clark and DR Ulrich) 32 (1984) 49

26   D W Johnson Jr *Advances in Power Technology* (Ed. G Y Chin) (1982) 23

27   K Kimoto, Y Kamiya, M Nonoyama and R Uyeda *Jpn J Appl Phys* 2 (1963) 702

28   T I Barry, R K Bajlissis and L A Lay *J Mat Sci* 3 (1968) 229

29   C G Granqvist and R A Buhrman *J Appl Phys* 47 (1976) 2200

30   A R Tholen *Acta Metall* 27 (1979) 1765

31   L E McCandish, D E Polk, R W Siegel and B H Kear (Eds) *Mater Res Soc Symp Proc* 132 (1988) 3

32   T Shiosaki, C S Kang, M Shimizu, F Fukagawa, K Nakaya and E Tanikawa *Ceramic Trans* 43 (1994) 27

33   M Faber, J Langguth and P Greil *Ceram Trans* 51 (1995) 63

34   R Zimmermann - Chopin and S Auer *J Sol-gel Sci Technol* 3 (1994) 101

35   M J Ruthener, G G Richter and I L Steniner *J Sol-gel Sci Technol* 1 (1971) 75

36   D W Johnson(Jr) and P K Gallagher *Ceramics Processing Before Firing* (Eds. G Y Onoda Jr and L L Hench) Wiley New York (1978) 125

37   P Reynen and H Basties *Powder Metall Int* 8 (1976) 91

38   P K Gallagher, D W Johnson Jr, E M Vogel and F Schrey *Ceramic Microsturcture* (Eds R M Fulrath and J A Pask) Westview Press Boulder Colo (1977) 423

39   K G K Warrier, P Mukundan, S K Ghosh, S Sivkumar and A D Damodaran *J Mat Sci* 29 (1994) 3415

40   J Fifer *British Ceram Trans* 97 (1998) 80

41   J Nanda, B N Kuruvilla, K V P M Shafi and D D Sharma *Physics of Semiconductor Nanostructures* (Ed. K P Jain) Narosa Publishing House New Delhi (1997) 25

42   H Wennerstrom and B Lindman *Phys Rev* 52 (1979) 1

43   P L Luisi and E Straub *Reversed Micelles* Plenum New York 1984

44   J H Fendler *Acc Chem Res* 13 (1980) 7

45   C M Paleos *Chem Soc Rev* 14 (1985) 45

46   J Gun, R Iscovici and J Sagiv *J Colloid Interface Sci* 101 (1984) 201

47   H T Tien *Bilayer Lipid Membranes(BLM) Theory and Practice* Marcel Dekker New York (1974)

48   J H Fendler *Chem Rev* **87** (1987) 877

49   G H Jonker and AL Stujits *Philips Tech Rev* **32** (1971) 79

50   E M Krieger, E A Nazorova and F T Yakushovskaya *Sov Powder Metall Metal Ceram* **89** (1970) C207

51   H Robbins *Proc Third Int Conf On Ferrites* Central Academy Publishing Co of Japan Tokyo (1982)

52   A Goldman and A M Lang *J Physique* **38** (1977) C297

53   D G Wickham *Inorg Synth* **9** (1967) 152

54   D G Wickham, E R Whipple and E G Larson *J Inorg Nucl Chem* **14** (1960) 217

55   L Patron, E Segal, G Filoti, I Ilie and M Brezeanu *J Mat Sci Lett* **6** (1987) 932

56   P K Gallagher *Mater Res Bull* **3** (1968) 225

57   K Suresh, N R S Kumar and KC Patil *Adv Mater* **30** (1991) 148

58   A Pathak, S D Kulkarni, S K Date and P Pramanik *Nanostructured Materials* **8(1)** (1997) 101

59   A Laudise and W A Ballaman *J Am Chem Soc* **65** (1958) 2655

60   M M D M Bibby and M P Dale *Nature* London **317** (1987) 157

61   M M Lenka and R E Riman *Chem Mater* **5** (1993) 61

62   M M Lenka and R E Riman *J Am Ceram Soc* **76** (1993) 2649

63   M M Lenka and R E Riman *Ferroelectrics* **15** (1994) 159

64   M M Lenka and R E Riman *Chem Mater* **7** (1995) 18

65   M M Lenka, A Anderko and R E Riman *J Am Ceram* **78** (1995) 2609

66   S B Cho, S Venigalla and J H Adair *J Am Ceram Soc* **79** (1996) 88

67   A J Fanelli and J V Burlew *J Am Ceram Soc* **69** (1986) 174

68   F Fievet, M Figlarge and J P Lagier *Solid State Ionics* **32/33** (1989) 198

69   P Pramanik, S Biswas, C Singh, D Bhattarcharya, T K Dey, D Sen, S K Ghatak and K L Chopra *Mat Res Bull* **23** (1988) 1693

70   A Pathak and P Pramanik *Materials Research Society Symposium Proceedings* 1991 Fall meeting Massachusetts USA **249** (1992)171

71   A Pathak PhD *thesis* (1995) Department of Chemistry IIT Kharagpur India

72   C D Mee and J D Jescheke *J Appl Phys* **34** (1963) 1271

73   K Haneda C Miyakawa and H Kojima *J Am Ceram Soc* **57** (1974) 354

74   V R Palkar and M S Multani *Mat Res Bull* **14** (1979) 1353

75   W Roos *J Am Ceram Soc* **63** (1980) 601

76   A Pathak, P Pramanik *Material Manufac Process* **8** (1992) 491

77   K R M Rao, AV P Rao and S Komarneni *Mater Lett* **28** (1996) 463

78   S M Gupta and AR Kulkarni *J Eur Ceram Soc* **4** (1996) 473

79   S E Jacob, C D Pascual, R D Clemente and M L Blesa *J Mat Sci* **32** (1997) 1025

80   R Roy *Science* **238** [**4834**] (1987) 1664

81   F Licci and T Besagni *IEEE Trans Magn* **20** (1984) 1639

82   B J J Zelensky and D R Uhlmann *Phys Chem Solids* **45** (1984) 1069

83   K D Budd, S K Dey and D A Payne *Proc Mat Res Soc* (Eds. C J Birinker, D E Clark and D R Uhlrich) *Mat Res Soc*, Pittsburgh USA (1986) 117

84   R A Lipeles, D J Coleman and M S Leung *Proc Mat Res Soc* (Eds C J Birinker, D E Clark and D R Uhlrich) *Mat Res Soc* Pittsburgh USA (1986) 665

85   T Ikemoto, K Umatsue, N Mizutani, M Kato and Y Mitarai *J Mat Sci* **21** (1986) 2771

86   J C Debsa Kidar *J Non-Cryst Solids* **86** (1986) 231

87   R Rabindranathan, S Komarneni, A S Bhalla, R Roy and L E Cross *Advances in Ceramics Ceramics Powder Science I* (Eds. G L Messing, S Hirano and H Hausner) Am Ceram Soc Westerville OH **21** (987) 82

88   R A Liples and D J Coleman *Ultrastructure Processing of Advanced Ceramics* (Eds. J D Makinzie and DR Ulrich) Wiley New York (1988) 919

89   F Chaput, J P Boilot, M Lejeune, R Papiernik and L G H Pfalzgraf *J Am Ceram Soc* **72** (1989) 1355

90   T Ogihara, N Mizutani and M Kato *J Am Ceram Soc* **72** (1989) 421

91   C Surig, K A Hempel and D E Bonneberg *Appl Phys Lett* **63** (1993) 2836

92   V Kumar, R Marimuthu, S Patil, Y Ohya and Y Takahashi *J Am Ceram Soc* **79** (1996) 2775

93   Y-L Tu, M L Calzada, N J Phillips and S J Melne *J Am Ceram Soc* **79** (1996) 441

94   N N Ghosh, S K Saha and P Pramanik *British Ceram Trans* **97** (1998) 180

95   M Pechini US Pat No 3 330 697 July 1967

96   N G Eror and H U Anderson *Proc Material Research Society Symposia* (Eds. C J Brinker, D E Clark and D R Ulrich) *Mat Res Soc* Pittsburgh PA 73(1986) 571

97   H U Anderson, M J Pennel and J P Guha *Advanced Ceramics Ceramic Powder Science* (Eds. G L Messing, K S Mazdiyasni, J W McCauley and R A Haber) American Ceramic Society Westerville OH **21** (1987) 91

98   C Marcily, P Courty and B Delmon *J Am Ceram Soc* **53** (1970) 56

99   P A Lessing *Amer Ceram Soc Bulletin* **68(5)** (1989) 1002

100 M A Sekar, G Dhanary, H L Bhatt and K C Patil *J Mater Sci Elect Mat* **3** (1992) 237

101 M A Sekar and K C Patil *J Mater Chem* **2** (1992) 749

102 M L Wade and D G Agresty *Materials Res Soc Sym Proc* (Eds W E Rhine, T M Shaw, R J Gottschall and Y Chen) Material Research Society Pittsburgh PA **249** (1992)165

103 K C Patil *Bull Mater Sci* 16 (1993) 533

104 K C Patil and M A Sekar *Int J Self-Prop High-Temp Synth* 3 (1994) 181

105 K C Patil, S T Aruna and S Ekambaram *Curr Opinion in Solid State and Mater Sci* 2 (1997) 158

106 AG Merzhanov *Chemistry of Advanced Materials* (Ed CNR Rao) Oxford Blackwell Scientific 19 (1993)

107 A G Merzhanov *Int J Self-Propag High Temp Synth* 2 (1993) 113

108 P Ravindranathan and K C Patil *Amer Ceram Soc Bull* 66(4) (1987) 688.

109 LA Chick, L R Pederson, G D Maupin, J L Bates, L E Thomas and G J Exarhos *Mater Lett* 10(1&2) (1990) 6

110 S S Manoharan and K C Patil *J Amer Ceram Soc* 75 [4] (1992) 1012

111 B K Das *Preparation and Characterization of Materials* (Eds. J M Honig and C N R Rao) Academic Press New York (1981) 75

112 H Schmidt, R Nass and D Sporn *et al. Mater Sci Forum* 34-36 (1988) 833

113 R N Das, A Pathak and P Pramanik *J Amer Ceram Soc (Comm)* 81(12) (1998) 3357

114 S K Saha, A Pathak and P Pramanik *J Mater Sci Lett* 14 (1995) 35

115 A K Adak, A Pathak and P Pramanik *J Mater Sci Lett* 17 (1998) 559

116 A K Adak, S K Saha and P Pramanik *J Mater Sci Lett* 16 (1997) 234

117 A K Adak, A Pathak and P Pramanik *British Ceramic Trans* 98 (4) (1999)

118 S K Saha and P Pramanik *Brit Ceram Trans* 94 (1995) 123

119 S K Saha and P Pramanik *Nanostructured Mater* 8(1) (1997) 29

120 P Klug and L E Alexander *X-ray Diffraction Procedures for Polycrystalline and Amorphous Materials* 2nd edition Wiley New York (1974)

121 R A Graham and AB Sawaoka *Trans Tech Publications* Switzerland (1987)

FINITE SIZE EFFECTS IN FERROELECTRIC NANOMATERIALS AND THIN FILMS

PUSHAN AYYUB

Department of Condensed Matter Physics & Materials Science, Tata Institute of Fundamental Research, Mumbai-400 005 (India)

The study of size effects in ferroelectric nanoparticles is very important because these are strong candidates for high density computer memories, and one would like to know how small one can make such devices before their properties start changing. It is also interesting to understand such effects from the point of view of basic physics. The ferroelectric transition in the technologically important perovskite-type (ABO_3) systems is strongly affected by a reduction in the particle size below 100 nm. With decreasing size, there is a monotonic reduction in the T_C, and in the off-center displacement of the B-ion. Thus, there is a size-induced structural distortion that reverts the crystal to its high-symmetry paraelectric phase (which is normally stable only above T_C) even at room temperature. The dielectric transition at T_C also shows a marked broadening in small particles. Here, the author reviews the data on nanocrystalline ferroelectrics and antiferroelectrics and present a simple microscopic model for structural transitions in displacive ferroelectrics. Finally, it is concluded that many of the 'thickness' effects in ferroelectric thin films can actually be ascribed to grain size effects.

1. Introduction

1.1 Basic Concepts and Motivation for the Study

In recent years, the study of finite size effects in various classes of oxide nanoparticles has acquired great significance since many such systems have important applications, such as in catalysis, sensors, various types of memory elements, micro-electronic and electro-optic devices, and also as precursors for high strength materials. Finite systems have been of great interest to physicists because they exhibit a number of novel phenomena such as quantum size and confinement effects and various types of surface and interfacial effects. In order to predict the performance of a particular device or component based on nanomaterials, it is essential to understand the way in which various structure-property relations change with particle size in such systems. For the purpose of this paper, a 'nanoparticle' is defined as a small solid whose physical dimension lies in the approximate range of a few nm to a few hundred nm. Though one would ideally prefer to study such systems in isolation, a real experiment usually ends up probing a collection of either closely or loosely aggregated nanoparticles.

It is reasonable to expect that the ideal systems in which to investigate finite size effects are the ones which exhibit some form of co-operative (long-range) ordering, such as superconductors, ferromagnets and ferroelectrics. In the present review, we restrict ourselves to the study of various types of size effects in ferroelectric (as well as antiferroelectric) nanoparticles and thin films. A ferroelectric is usually defined as a system which exhibits a spontaneous dielectric polarization (for $T < T_C$, the Curie temperature) that can be reversed by the external application of an electric field. In an antiferroelectric, on the other hand, there exists an antiparallelly ordered array of local dipoles, which results in the net polarization being zero.

Conventionally, a ferroelectric is termed 'displacive' when the elementary dipoles strictly vanish in the paraelectric phase, and 'order-disorder' when these dipoles are non-vanishing but thermally average out to zero in the paraelectric phase. It is

possible to rigorously distinguish between the two types of systems on the basis of the dynamics of their phase transition and the nature of the soft mode involved, whether propagating or diffusive[1]. However, one now recognizes that it is often difficult to classify a particular ferroelectric or antiferroelectric as strictly 'displacive' or 'order-disorder'.

There are a number of interesting current and potential applications that involve ferroelectric and piezoelectric materials. These include sensors, nano-robotic and micro-electromechanical devices[2]. In addition, interest in ferroelectrics is growing rapidly because the high dielectric constant of a ferroelectric can be utilized in dynamic random access memories (D-RAM), whereas its capacity for being polarized in opposite directions makes it an attractive candidate for non-volatile random access memories (NV-RAM). An important motivation for studying particle size effects in ferroelectrics is to determine the ultimate level to which a device based on such systems can be miniaturized. Also, from the point of view of basic physics, it is no less interesting to investigate systems in which the particle size is smaller than the correlation length corresponding to the long range dipolar ordering.

1.2 A Brief Description of the Origin of Ferro-electricity in Perovskite Systems

Many important ferroelectrics and antiferroelectrics, particularly those belonging to the 'displacive' category, possess the well-known perovskite structure. Since much of the finite size work also relates to this class of compounds, it is useful to briefly recapitulate the mechanism of ferroelectric ordering in them. Perovskites are generally oxide ceramics with the general formula ABO_3. They have a cubic unit cell with the mono- or bivalent A cation at the cube corners and the smaller B cation (usually penta- or tetravalent) at the body centre, while the O ions are situated at the face centers (Fig. 1a). The perovskite lattice is basically a three-dimensional network of BO_6 octahedra, as shown in Fig. 1b. The cubic perovskite structure shown in the figure actually represents the high-temperature $(T > T_C)$, high-symmetry paraelectric phase. It is the off-centering of the B-cation in the oxygen octahedron that leads - through a lowering of the symmetry - to the creation of a local dipole moment, and ultimately to the ferroelectric or antiferroelectric ordering. The structural
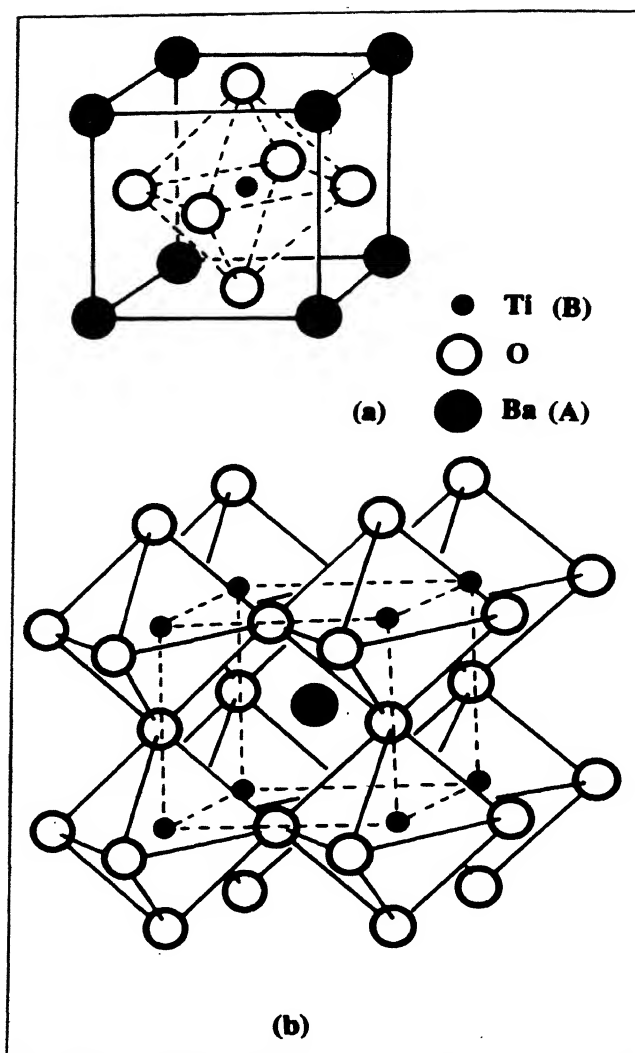

Fig. 1 (a) Typical unit cell of the cubic perovskite structure (ABO_3), (b) The three dimensional network of BO_6 octahedra forming the perovskite lattice

distortion from the cubic (paraelectric) phase is therefore of fundamental importance to the stabilization of ferroelectric order in such 'displacive' systems. This concept is central to the understanding of finite size effects in displacive ferroelectrics.

1.3 Overview of the Contents

I will begin by presenting a historical overview of the study of finite size effects in ferroelectrically ordered systems and point out the various successes as well as inconsistencies in the early studies (Section 2). Then I will present a more upto date account of experimental studies, particularly in nanocrystalline

$BaTiO_3$, $PbTiO_3$ and $PbZrO_3$. Also, I will compare the nature of size effects in ferroelectrics vs. antiferroelectrics, and displacive systems vs. order-disorder systems (Section 3). This will be followed by a discussion of the theoretical techniques that have been used to understand the finite size effects in these systems (Section 4). The observed size-induced structural phase transition is placed in a broader perspective before I discuss, in some details, a simple microscopic model which reproduces the size induced transition and changes in the T_C. A mechanism for the diffuse phase transition observed in nanoparticles is also suggested. The next section is devoted to various types of finite size effects that are observed in thin films (Section 5). The salient points are summarized in Section 6.

2. Size Effects in Ferroelectric Nanoparticles: Early Days

Research on finite size effects in ferroelectric materials was started surprisingly early (in the 1950s) by Känzig and co-workers. The first studies[3] were made on potassium dihydrogen phosphate, KH_2PO_4 (KDP), which is a rather complicated system in the sense that it has characteristics of both displacive and order-disorder mechanisms. It was found that the spontaneous polarization (which is the order parameter in ferroelectrics) is hindered in KDP fine particles embedded in an insulating medium with low dielectric constant when the particle size is less than 150 nm. Below a critical particle size which depends upon the embedding medium, the depolarization field prevents polar, ferroelectric structures. Normal ferroelectric behaviour was exhibited only when the particle size was above 0.5 μm.

A contrasting result was obtained in $BaTiO_3$, which is a predominantly displacive ferroelectric, in which the cubic perovskite paraelectric phase undergoes a tetragonal distortion (of about 1%) below $T_C = 125°C$ to a polar phase. $BaTiO_3$ fine particles in the size range of 30 nm to 2.3 μm (prepared by ball-milling) showed a small *increase* in the T_C and a smearing of the transition with decreasing particle size[4,5]. No critical size (for the destabilization of ferroelectricity) was observed in the above size range. The authors concluded from their electron diffraction studies that the deviation from normal ferroelectric behaviour was due to the existence of a 10-15 nm thick surface layer that was under a higher tetragonal

strain than the bulk and had a higher T_C. This layer also appeared to remain ferroelectric up to a temperature much higher than (by a few hundred degrees) the bulk T_C[4]. They suggested that the misfit between the surface layer and the interior caused the broadening of the transition region and the lattice distortions.

Some of the early results are inconsistent because the samples were often prepared by mechanical grinding, so that the observations were influenced by residual surface stresses, inhomogeneities and imperfect crystallization, rather than by intrinsic size effects. In spite of such difficulties, Känzig's group was able to make the key observation that the spontaneous tetragonal strain (c/a) at room temperature decreases with decreasing particle size.

During the next two decades (60s and 70s) there was considerable progress in the study of grain size effects in ferroelectric *ceramics, i.e.*, sintered compacts. These systems, and the results pertaining to them, differ in certain essential aspects from the quasi-free nanoparticles - which would appear to be more suitable for the study of 'intrinsic' size effects. However, ferroelectric ceramics are technologically important, and one cannot ignore the possibility of enhancing some of their properties by controlling the grain size. The salient observations on ceramic samples of $(Pb_{1-x}La_x)(Zr_{1-y}Ti_y)O_3$ or PLZT[6], $Pb(Zr_{1-x}Ti_x)O_3$ or PZT[7], and other systems can be summarized as follows. With a decrease in the grain size - generally in the 1-5 μm range - (i) there is a decrease in the peak dielectric constant ε_{max}, (ii) the dielectric response peak (near T_C) becomes broader, and (iii) the ferroelectric T_C goes up. Martirena and Burfoot[7] suggested that these observations may be explained in terms of an inter-granular effect (mainly involving the size dependence of the domain wall mobility) and an intragranular effect, for which each grain is assumed to be a monodomain and one considers the effect of different-sized grains having different values of T_C. The dielectric response of the system was simulated using the distribution model due to Diamond[8] wherein it is assumed that the T_C for different grains obeys a Gaussian distribution. Below each individual T_C, the grains are assumed to have a constant dielectric constant, while the Curie-Weiss law is obeyed above T_C.

Martirena and Burfoot also made use of the concept of a diffuse phase transition (DPT). This is

based on the idea that the crystal (or ceramic) consists of many non-interacting micro-regions which can independently switch from a ferroelectric to a paraelectric state (or *vice versa*). Several physical situations that could result in a DPT were proposed. Particularly in the case of solid solutions such as PZT and PLZT, microscopic variations in the local chemical composition could give rise to a T_C distribution and hence a DPT. The DPT effectively leads to a Curie *region* rather than the conventional Curie *peak*. A physically realistic situation will be introduced later which can lead to a DPT even in pure compounds for which one need not assume a compositional variation.

In order to completely understand the grain size effects in ferroelectric ceramics, one may also need to consider the size dependence of the particular transverse optic mode[9], the 'softening' of which (as $T \rightarrow T_C$) causes the ferroelectric distortion of the lattice

3. Ferroelectric Nanoparticles: Current Experimental Situation

After a period of relative inactivity during 1975-87, the study of ferroelectric nanoparticles suddenly stopped being a purely academic exercise (except for piezoelectric ceramics, which had been technologically important for quite some time) because of a revival of the idea of a ferroelectric memory device. Besides, the possible applications of ferroelectrics and piezoelectrics as micro-electromechanical devices, sensors, etc. provides a strong motivation for the study of finite size effects in these systems. So, in the late 80s there was a spurt in both theoretical as well as experimental activities. By this time a lot of progress had also been made in the development and improvement of several synthesis techniques such as sol-gel, co-precipitation, microemulsion, sputtering, evaporation, spray-pyrolysis and laser ablation. This made it possible to study different compounds in the form of phase-pure, ultrafine particles with a narrow size distribution.

Other than direct observations using electron micrography, the most popular and the easiest method for measuring particle size is based on X-ray diffraction line broadening. The coherently diffracting domain size (d_{XRD}) is calculated from the full width at half maximum (FWHM) of the (111) diffraction peak using the Scherrer equation, which assumes that

the small crystallite size is the only cause of line broadening:

$$d_{XRD} = K\lambda/\beta(\theta)\cos\theta \qquad \qquad ...(1)$$

where λ is the X-ray wavelength, $\beta(\theta)$ is the instrument-corrected FWHM of the diffraction line, θ is the diffraction angle and $K \approx 1$ if the particles are assumed to be spherical.

3.1 Size Effects in BaTiO₃

In its paraelectric phase (above $T_C \approx 125°C$), BaTiO₃ has a cubic perovskite structure. It transforms successively to three structurally different ferroelectric phases: a tetragonal phase ($\bar{1}25°C$ to $5°C$), an orthorhombic phase ($5°C$ to $-90°C$) and a rhombohedral phase (below $-90°C$). All three transitions are of the first order.

Kanata *et al.*[10] showed that in BaTiO₃ fine particles, the T_C decreases slightly with decreasing particle size between $20\,\mu m$ and $0.2\,\mu m$. These samples were sintered at high temperature but not hot-pressed. The authors talk about superparaelectricity and the possible presence of internal stresses but have no clear explanation. In this size range, the tetragonal to orthorhombic transition appeared to be insensitive to particle size. However, with a decrease in particle size, there was an increase in the thermal hysteresis, indicating that the latent heat of transition is strongly size-dependent.

Another study of the variation of the tetragonal distortion (c/a) in BaTiO₃ with particle size (in range 0.1 to 1.0 μm) was made by Uchino *et al.*,[11] who prepared the fine particles by co-precipitation and hydrothermal routes. They identified the T_C as the temperature at which c/a drops to unity and determined the critical size for the existence of ferroelectricity (d_{crit}) to be 120 nm. This implies that the T_C drops below room temperature when the particle size is lower than d_{crit}. However, they did not make dielectric or other measurements to support the value of T_C obtained from structure data at different temperatures.

Very detailed X-ray diffraction (XRD) measurements were made in smaller-sized (10 nm to 1 μm) nanocrystalline powders of BaTiO₃ by Schlag *et al.*[12] and the structural phase change associated with the ferroelectric transition was not observed below a critical size of about 50 nm. Such a conclusion was also supported by measurements of the second harmonic generation (SHG) as well as differential

scanning calorimetry. It is, therefore, very interesting that *no change* was observed in the Raman spectra of the tetragonal structure, with a decrease in the particle size. This observation may be explained by the fact that while XRD and SHG probe the average crystal structure over several unit cells, Raman spectral response is determined by the symmetry of individual unit cells. Thus, the authors conclude that the polar distortion of the TiO_6 octahedra continues to be maintained irrespective of the particle size, though the average structure over an ensemble of a few unit cells does become cubic. The authors suggest that such local distortions (in otherwise 'cubic' nanoparticles) exist only at the time scales of light scattering (*i.e.*, $\approx 10^{-13}$s). This is a significant point, but it is not entirely clear whether it is justifiable!

The critical size ($\approx$50 nm) for the occurrence of ferroelectricity that was obtained in the above experiment, contradicts an earlier study of a *suspension* of $BaTiO_3$ particles stabilized by a monolayer of surfactant[13]. The presence of a spontaneous polarization was probed through the electro-optic Kerr effect. The authors claim to have detected a permanent dipole moment even in 10 nm particles. However, such a claim can be contested on at least three grounds. Firstly, the fine particles were prepared by the relatively crude technique of ball-milling the bulk powder and it is quite likely that some relatively large particles may have been left behind. Secondly, ball milling is a mechanical attrition process which may easily create substantial surface damage and induce defects; which may show a 'polar' response. Finally, the size determination process (with arbitrary correction factors) appears questionable.

3.2 Size Effects in PbTiO₃

$PbTiO_3$ is a classical displacive ferroelectric with excellent dielectric, pyroelectric and piezoelectric properties. It has a tetragonal perovskite structure below T_C, and transforms to a cubic paraelectric phase above $T_C = 490°C$. In $PbTiO_3$, the room temperature tetragonal distortion, $(c-a)/_a$, is about 6%, as compared to only 1% in the case of $BaTiO_3$. Due to its obvious applications potential, rigorous size effect studies have been carried out in this system during the past decade.

Ishikawa *et al.*,[14] prepared $PbTiO_3$ fine particles ($22 \leq d_{XRD} \leq 52$ nm) by an alkoxide route and made a Raman study of samples with different average

particle size as a function of temperature. They measured T_C indirectly using the principle that in displacive ferroelectrics, the lowest transverse optic mode, E(1TO), is often identifiable with the ferroelectric soft mode, whose frequency, $\omega_s \to 0$ as $T \to T_C$[15]. For each sample, ω_s was plotted as a function of temperature and the T_C was identified as the temperature at which ω_s extrapolates to zero. They found that T_C decreases monotonically when the average particle size (d) is below 50 nm, and its deviation from the bulk value, $T_C(\infty)$, can be fitted to the equation:

$$T_C(d) = T_C(\infty) - C/(d - d_{crit}) \qquad ...(2)$$

with $d_{crit} = 12.6$ nm and $C = 588.5°C$. Note that d_{crit} is the size at which $T_C \to 0$ K. A problem that may possibly occur with such an indirect measurement is that the surface depolarization fields may also affect the TO mode frequency and lead to unreliable conclusions.

Zhong *et al.*,[16] also made room temperature Raman-scattering measurements on $PbTiO_3$ nanoparticles (20 to 200 nm) prepared by a sol-gel method, and found that the ω_s shifts towards lower frequencies with decreasing particle size. This was interpreted as a lowering of T_C with size. They also performed differential scanning calorimetry (DSC), and identified the T_C as the peak of the heat flow curve. The variation in T_C with particle size again followed eq. (2), but this time with $d_{crit} = 9.1$ nm.

Because it has a large spontaneous polarization, a high T_C, only one structural transition (at T_C), and there is a satisfactory conceptual understanding of its transition mechanism (clearly of the displacive type), $PbTiO_3$ is certainly the candidate of choice for studying *finite size effects* in ferroelectric systems. However, the studies reported above suffer from certain drawbacks: (i) The transition temperature is measured either indirectly, or using only a single method, (ii) there are no proper studies of the size dependence of the dielectric response - which is the single most important property of ferroelectrics, (iii) no clear correlation is made between the dielectric properties and the structural parameters (particularly the ferroelectric distortion). The following experiments[17] were made in order to fill up these lacunae and obtain reliable data that could lead to a clear conceptual understanding of the situation.

Ultrafine $PbTiO_3$ particles ($20 \leq d_{XRD} \leq 200$ nm) were synthesized using a co-precipitation route. The
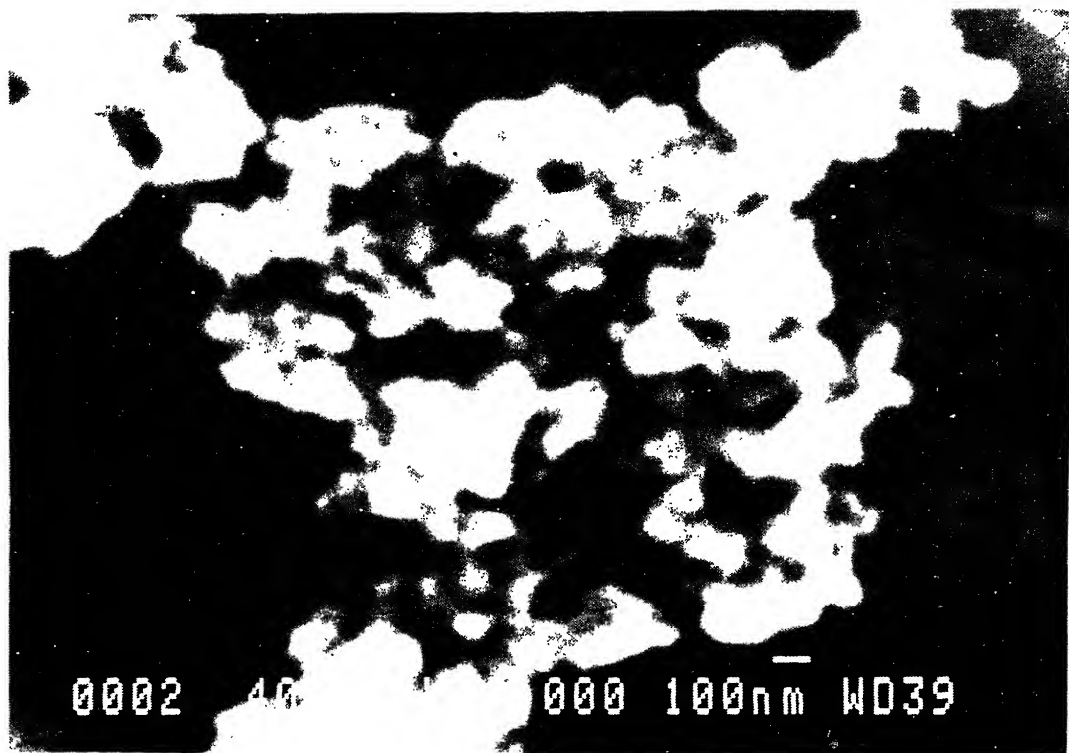
Fig. 2 Scanning electron micrographs of a typical nanocrystalline PbTiO$_3$ sample with an average particle
size (d$_{XRD}$) of 25 nm

X-ray domain size (d_{XRD}) was calculated from eq. (1). The equivalent spherical diameter of the particles was determined from the specific surface area measured by gas adsorption, while the size, shape and size distribution were also studied from scanning electron micrographs (Fig. 2). Since ferroelectric phenomena in displacive systems are controlled by lattice vibrational mechanisms, we expect d_{XRD} to be more relevant to the problem than the other two 'sizes' measured.

The ferroelectric transition was obtained from three complementary measurements: (i) dielectric response vs. temperature, (ii) temperature dependence of the tetragonal distortion (c/a), and (iii) differential scanning calorimetry (DSC). Note that c/a scales with the spontaneous polarization (which is the order parameter) in this class of compounds. XRD measurements were also made at temperatures down to 15 K to confirm that the large change observed in c/a at room temperature is an inherent particle size effect.
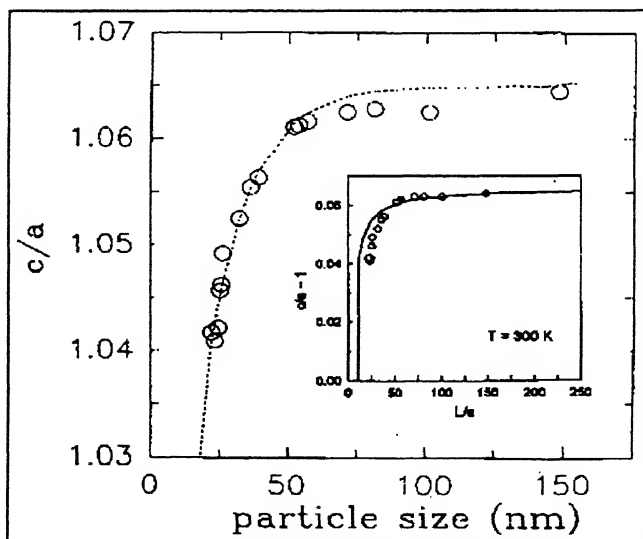

Fig. 3 Dependence of the room temperature tetragonal distortion (c/a) in PbTiO$_3$ on the particle size (d$_{XRD}$). The dashed line is a fit to eq.(3). A plot of ($c/a-1$) as a function of the reduced particle size (L$\equiv$d$_{XRD}$, a = lattice constant) is shown in the inset. The solid line represents a fit with the model described in Section 4.3

Fig. 3 shows the variation of the tetragonal ferroelectric distortion (c/a) with particle size at room temperature. The unit cell dimensions do not change down to ≈ 150 nm, below which c decreases and a increases with decreasing size. The resulting reduction in c/a is especially rapid below ≈ 60 nm. To estimate the critical size at which $PbTiO_3$ transforms to the cubic (paraelectric) phase *at room temperature*, we have fitted the c/a vs. d_{XRD} data to an equation of the form:

$$y = y_\infty - C \ \exp[C(d_{crit} - x)], \qquad \ldots(3)$$

with $x \equiv d_{XRD}$, $y \equiv c/a$, $y_\infty \equiv 1.065$, and $C \equiv y_\infty - 1$. The critical size (d_{crit}) is a fitting parameter. We find - by extrapolation - that $c/a \to 1$ when $d_{crit} \to 7.0$ nm, *i.e.*, ferroelectric order cannot be sustained below this

size. The dielectric, thermal and structural (variable temperature XRD) data all indicate that the T_C decreases monotonically with decreasing particle size[17].

The temperature dependence of the low frequency dielectric response function (ε) in nanoparticle samples is quite instructive. Fig. 4 (bottom) shows that with a decrease in the particle size, T_C decreases, ε_{max} decreases and the peaks become increasingly broader. For samples with $d_{XRD} \leq 26$ nm, no peaks were observed in the ε vs. T curves. In bulk $PbTiO_3$ ($d_{XRD} \geq 60$ nm), a decrease in frequency leads to an increase in the ε_{max}, but the ferroelectric T_C remains constant at $\approx 500°C$. In smaller particles of $PbTiO_3$ ($d_{XRD} = 31$ nm), however, we find that the T_C moves up with an increase in frequency from 476°C at 500 kHz to 488°C at 1 MHz. Also, for a particular frequency, the temperature interval between the maxima in $\tan \delta$ (dielectric loss tangent) and ε is larger in finer particles. These properties are typical of materials with a diffused phase transition, and will be discussed later.

With a reduction in the particle size, the nature of the changes in the 'dielectric' and the 'thermal' transitions (observed by DSC) were found to be qualitatively similar. Thus, the peak in the heat flow shifted towards lower temperature and became broader and flatter with decreasing size in $PbTiO_3$ - as shown in Fig. 4(top).

3.3 Size Effects in Antiferroelectric $PbZrO_3$

Unlike ferroelectrics, in which size effects have been studied for over 35 years, there were no detailed investigations in nanocrystalline antiferroelectrics, prior to the study of $PbZrO_3$ by Chattopadhyay *et al.*,[18]. $PbZrO_3$ is orthorhombic at 300K with eight formula units per crystallographic unit cell. This structure is derived from a cubic perovskite prototype (the high-temperature paraelectric phase) by *antiparallel* displacements of the Pb ions along one of the original [110] directions - which becomes the *a*-axis of the orthorhombic phase. If the displacements of the Pb ions are ignored (so as to compare the unit cells of the paraelectric and the ferroelectric phases), we obtain a pseudo-tetragonal unit cell in the ordered phase, whose lattice constants (a_T, c_T) are related to the real orthorhombic unit cell (a, b, c) through: $a_T = a/\sqrt{2}$, and $c_T = c/2$. $PbZrO_3$ shows a strong dielectric anomaly at $T_C \approx 500K$.
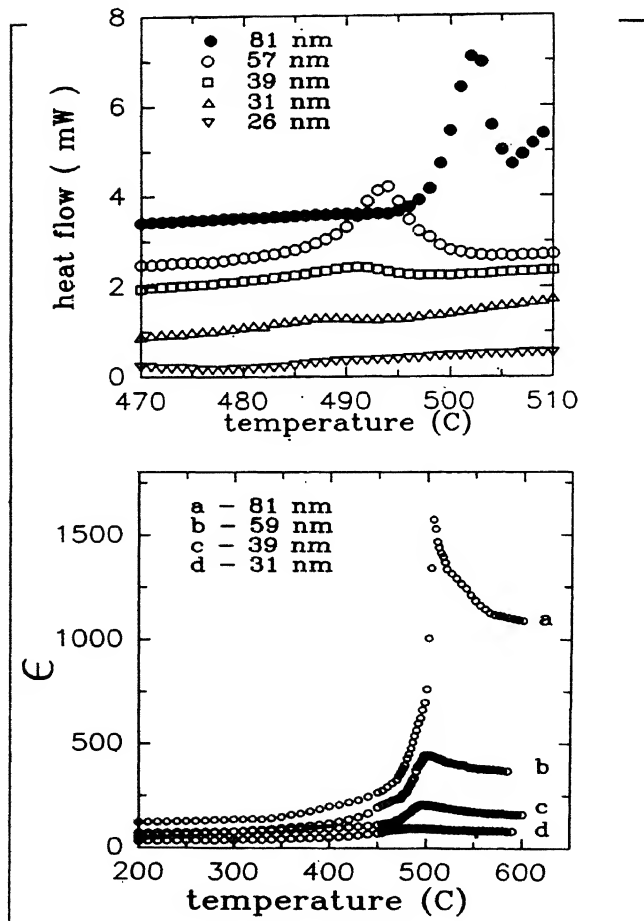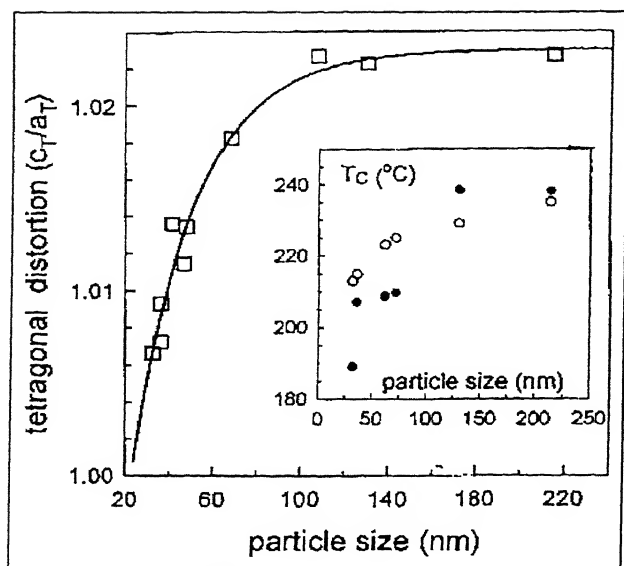

Fig. 4 (Bottom) Temperature dependence of the low frequency dielectric response in nanocrystalline $PbTiO_3$ for different sizes. (Top) Differential scanning calorimetric study of the effect of particle size on the ferroelectric transition in nanocrystalline $PbTiO_3$

Fig. 5 Dependence of the room temperature pseudo-tetragonal distortion (c_T/a_T) in $PbZrO_3$ on the particle size (d_{XRD}). The solid line is an empirical fit. Inset shows the size dependence of the T_c: measurements using DSC data are represented by filled circles, while those from dielectric data are shown by open circles

Ultrafine particles of $PbZrO_3$ (down to 30 nm) were prepared using a modified sol-gel technique. The dependence of the pseudo-tetragonal distortion (c_T/a_T) on the particle size is shown in Fig. 5. The crystallographic unit cell remains relatively undistorted (from the bulk) down to ≈ 100 nm, but below this size it shows an increasing tendency to become cubic. When the above data are extrapolated downwards, we are led to the conclusion that the crystal structure would become perfectly cubic below a size of 23 nm. The monotonic reduction in the T_C (obtained from dielectric and thermal measurements) with decreasing particle size is shown in the inset (Fig. 5). Overall, size effects in antiferroelectric $PbZrO_3$ were found to be qualitatively similar to those in the ferroelectrics $PbTiO_3$ and $BaTiO_3$.

3.4 Size Effects in Order-Disorder Ferroelectrics

It is clear from the preceding part of the review that nanoparticles of *displacive* systems such as $BaTiO_3$, $PbTiO_3$ and $PbZrO_3$ are found to show certain basic similarities, such as (i) a monotonic decrease in the T_C with particle size below ≈ 100 nm, (ii) existence of a critical particle size below which ferroelectricity cannot be observed, (iii) a broadening of the ferroelectric transition peak and behaviour

reminiscent of a diffuse phase transition at low sizes, and (iv) an interrelation between the T_C, the ferroelectric distortion, and the particle size.

The behaviour of a typical *order-disorder* system such as $NaNO_2$, however, does not fall into this pattern. Bulk $NaNO_2$ undergoes a first order ferroelectric-paraelectric transition at $165°C$, which is associated with a relatively large latent heat. Marquardt and Gleiter[19] prepared nanocrystalline $NaNO_2$ (down to 5 nm) by three different methods, and studied the ferroelectric phase transition by differential thermal analysis. Very little change in T_C was observed down to 5 nm, whereas displacive systems start showing deviations in the T_C at sizes as large as 100 nm. This clearly emphasizes the importance of the size-induced *structural distortions* in the nanoparticles of the displacive systems. The other obvious difference in the two types of system is that the thermal (as well as dielectric) phase transition is not at all observed in nanoparticles of displacive systems with a size below ≈ 25 nm, while even 5 nm $NaNO_2$ nanoparticles show a clear transition peak. Size effects, therefore, appear to be much weaker in order-disorder ferroelectrics.

4. Conceptual Understanding of Size Effects in Ferroelectrics

4.1 Brief Review

Till recently, the basic theoretical approach used to understand size effects in ferroelectric nanoparticles has been the Landau-Devonshire phenomenological theory. For a finite-sized, inhomogeneous ferroelectric with a second order phase transition, Zhong et al.,[20] write the total free energy in the form:

$$\int [\tfrac{1}{2}A(T-T_{C\infty})P^2 + \tfrac{1}{4}BP^4 + \tfrac{1}{2}D(\nabla P)^2]dv + \int \tfrac{1}{2}D\delta^{-1}P^2 dS \quad ...(4)$$

where P is the polarization, and $T_{C\infty}$ refers to the 'bulk' value of T_C. D is connected to the correlation length (ξ), $D = \xi^2|A(T-T_{C\infty})|$. The volume and surface integrals represent, respectively, the free energies of the interior and the surface. When compared to the analogous expression for an infinite and homogeneous ferroelectric, the extra terms that appear in eq. (4) are the gradient term and the surface term. The 'extrapolation length', δ, turns out be particle size dependent. It can then be shown that the polarization as well as the T_C decrease with decreasing size and ultimately both vanish as $d \rightarrow d_{crit}$.

Later on, Rychetsky and Hudák[21] analytically solved the phenomenological model for the second order phase transition in spherical ferroelectric particles and obtained the temperature and size dependent dynamical dielectric susceptibility. Both these treatments[20, 21], however, ignore the possible presence of a surface depolarization field. Shih et al.[22] have considered the effect of incorporating the depolarization energy in the Landau free energy density. They consider cubic particles with alternating domains separated by 180° domain walls. Not unexpectedly, they found that the presence of a depolarization field can substantially lower the ferroelectric T_C.

4.2 Size Induced Structural Phase Transitions - A Broader Perspective

In all the perovskite type oxide ferroelectrics studied, we observe a decrease in the tetragonal distortion with a reduction in particle size. It is important to note that this effect is *not* special to ferroelectrics, but appears to be a manifestation of a much more general phenomenon. Our earlier studies have shown that in a large number of partially covalent oxides, the crystal lattice tends to transform into structures of higher symmetry when the particle size is reduced[23]. In certain systems (e.g., Fe_2O_3 and Al_2O_3), the size-induced distortion is large enough to actually produce a crystallographic transition to a high-symmetry structure[24]. In other cases (such as the present one), there may be a gradual reduction in an asymmetry parameter (c/a −1) with decreasing size.

We have also shown, qualitatively, how a decrease in the particle size may cause a change in the bulk lattice parameters via surface stresses[25]. The anisotropic nature of the lattice expansion in the nanoparticle systems can be understood in terms of a tendency of such systems to become increasingly *ionic* with decreasing size[26]. As a result, the inter-ionic bonds lose their directional character and the crystal tends to assume a structure with comparatively higher symmetry. It is interesting to note that the size-dependence of many important physical properties (such as superconductivity and magnetism, in addition of course to ferroelectricity) are often directly or indirectly connected to the anisotropic lattice distortion that accompanies a reduction in the particle size[23].

4.3 Size Effects In Ferroelectric Nanoparticles: A Simple Microscopic Model

We now present a microscopic model[27] which

helps us to understand the nature of size-induced changes in displacive ferroelectrics. $PbTiO_3$ has been selected as a test system, though the results obtained should apply to other displacive systems as well. This model also allows us to make certain predictions about order-disorder ferroelectrics, which appear to be consistent with the data available for such systems. The model is based on two simplifying assumptions: (a) the finite sized ferroelectric system is quasi-free, i.e., it consists of loosely aggregated, unclamped nanoparticles, and (b) the ferroelectric nanoparticles are not electrically isolated. Under these conditions, we can ignore the effects of external strain and depolarization.

Most experiments show that a reduction in the size of ABO_3-type displacive ferroelectrics and antiferroelectrics is accompanied by a monotonic decrease in the ferroelectric T_C - the temperature at which the high symmetry paraelectric structure transforms to a low symmetry phase in which the B ions no longer occupy the centrosymmetric positions in the BO_6 octahedra. When the particle size is made sufficiently small ($d<d_{crit}$), the ferroelectric system reverts to the paraelectric phase, *however low the temperature*. In other words, the observations suggest that the ferroelectric to paraelectric transition may be made to occur as a function of increasing temperature or decreasing size. The following microscopic model naturally leads to a size-induced structural phase transition of the first order.

The displacement of the centrosymmetric B-ion to an off-centric position at the ferroelectric T_C, is accompanied by a distortion in the cubic (paraelectric) unit cell to one of lower symmetry, e.g. (in $PbTiO_3$), a tetragonal one with sides $a \times a \times c$. The tetragonal distortion (c/a −1) is experimentally found to scale with the order parameter. The displacement (d) of each such ion clearly requires some energy, and the system would undergo a ferrodistortive transition only when it gains a *larger* amount of energy from the interaction of the resulting dipoles, which are aligned in some particular fashion.

The dipolar interaction energy of the stable ordered phase, ($\sim Jzd^2$), should be comparable to kT, where z is the coordination number. So, the displacement (d) should be at least $\sqrt{(kT/Jz)}$, for dipolar alignment to take place. Note that this argument itself implies the possibility of driving the transition by varying either the temperature, or the system size (which

controls the average value of z). So, the model describes the temperature-driven transition in the bulk material, as well as the size-driven transition in finite systems.

The interaction energy between the nearest neighbour dipoles can be phenomenologically described by $Jd_id_j\alpha_i\alpha_j$, where $\alpha = \pm 1$ is an Ising variable, which accounts for the fact that the central ion can be displaced in two opposite directions. J is positive for ferroelectrics and negative for antiferroelectrics. The effective Hamiltonian for the problem is thus the sum of an elastic part and an Ising part. From symmetry considerations, we obtain:

$$H = \sum_i (\tfrac{1}{2}\lambda_2 d_i^2 + \tfrac{1}{4}\lambda_4 d_i^4) - J\sum_{i,j} d_i d_j \alpha_i \alpha_j \quad ...(5)$$

This Hamiltonian is solved by treating the Ising variable via an inhomogeneous mean-field theory (IMFT) and the displacement variable within a saddle point approximation. To bring out the difference between sites in the bulk and those near the surface of the finite system, the IMFT is carried out with *open* boundary conditions to study the size-driven transition and *periodic* boundary conditions to obtain the bulk transition. Finally, we obtain the free energy density in the form: $F(d) = E(d) + I(d)$, where the elastic part, $E(d)$, is given by:

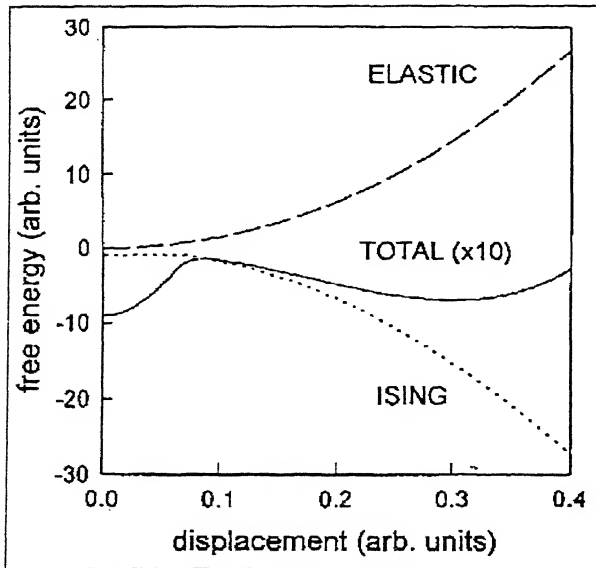$$E(d) = \tfrac{1}{2}\lambda_2 d^2 + \tfrac{1}{4}\lambda_4 d^4 \qquad ...(6)$$

and the Ising part, $I(d)$, is given by:

$$I(d) = \tfrac{1}{2}Jzm^2d^2 - T\ln 2\cosh(\frac{Jzmd^2}{kT}) \qquad ...(7)$$

where $m \equiv \langle\alpha\rangle = \tanh (Jzd^2m/T)$. The saddle point values of d, obtained by minimizing $F(d)$, are $d = 0$ and $d = d_0 = \sqrt{[(Jzm^2 - \lambda_2)/\lambda_4]}$. The nature of the variations of $E(d)$ and $I(d)$, and the presence of the two minima in $F(d)$ are shown schematically in Fig. 6. Clearly, it is this two-minima structure of the free energy that is responsible for the first order ferroelectric ($d = d_0$) to paraelectric ($d = 0$) transition.

For $PbTiO_3$, the model parameters (λ_2, λ_4 and J) were determined from our experimental data[17]. We can now plot the phase diagram in the temperature-size plane (Fig. 7) by calculating $d_0(T)$ for each L from $d_0 = \sqrt{[(Jz(L)m^2 - \lambda_2)/\lambda_4]}$. The phase boundary for displacive systems ($\lambda_2 > 0$, solid line) represents first order transitions for all $T > 0$. Thus, the theory predicts a suppression in T_C with reducing size. In systems with $\lambda_2 < 0$ (which usually describes order-disorder ferroelectrics), size effects are greatly suppressed, as shown by the dotted curve in Fig. 7. One would require to study very small particles at temperatures close to T_C, to observe such effects. This is also in agreement with experimental observations. We conclude that the observed size effects in ferroelectrics

Fig. 6 Schematic representation of the elastic energy and the Ising energy contributions to the total energy
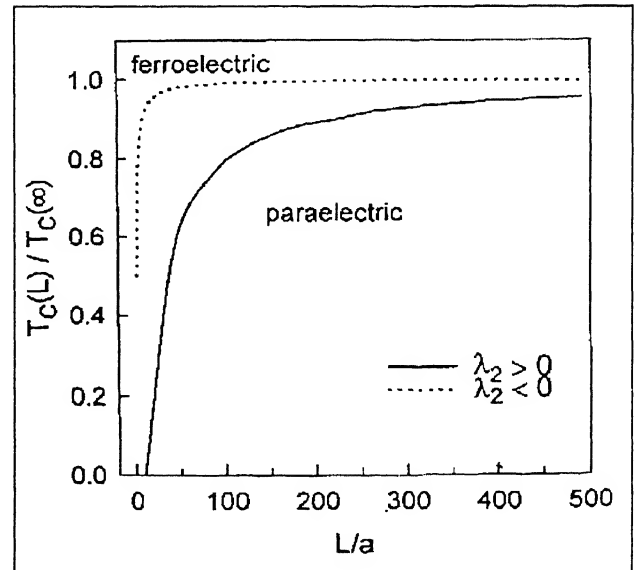

Fig. 7 Temperature-size phase diagram obtained from the model described in Section 4.3. Displacive and order-disorder systems are represented by the solid and dotted lines, respectively

appear mainly to arise from a lower average coordination number for the atoms close to the surface of a nanoparticle.

An important advantage of the model described above is that it has only three fitting parameters, while the phenomenological Landau theories[20,22] have about twice as many. Also, it can be easily extended to describe displacive-type *anti*ferroelectrics, simply by making J negative. It has been shown[27] that the nature of the size dependence in antiferroelectrics is the same as that in ferroelectrics (with J being replaced by $|J|$). This is also supported by the results on $PbZrO_3$ nanoparticles (Section 3.3).

4.4 Diffused Phase Transition in Ferroelectric Nanoparticles

We now consider another experimentally observed feature in ferroelectric and antiferroelectric nanoparticles. The dielectric studies (ε vs. T) on nanoparticles of ferroelectric $PbTiO_3$[17] and antiferroelectric $PbZrO_3$[18] can be summarized as follows. With a decrease in the particle size: (i) the peaks in the ε-T curve become broader, (ii) there is an increase in the separation between the peaks in the $\tan\delta$ vs. T and ε vs. T curves ($\tan\delta$ is the dielectric loss tangent), (iii) there is an increasing deviation from the Curie-Weiss law (discussed later), (iv) both the ε vs. T and $\tan\delta$ vs. T curves show marked frequency dispersion, (v) the decrease in the tetragonal distortion, c/a as $T\rightarrow T_C$ becomes more gradual in samples with smaller particle size, (vi) values of T_C obtained from different measurements (dielectric, thermal and structural) do not coincide, and (vii) with a decrease in frequency, T_C decreases while ε_{max} increases.

The broadening of the dielectric and thermal peaks at the ferroelectric transition as well as most of the other observed features are recognized characteristics of the so-called 'relaxor' ferroelectrics which exhibit a *diffused phase transition*[28-31]. The *diffuseness* of a ferroelectric phase transition can be quantitatively estimated[29] by fitting the part of the ε-T curve above T_{max} (where T_{max} corresponds to the peak in ε) with following equation:

$$\varepsilon^{-1} - \varepsilon_{max}^{-1} = C^{-1}(T - T_{max})^\gamma \qquad ...(8)$$

where C is a constant and the critical exponent $\gamma=1$ for a classical Curie-Weiss ferroelectric. According to the local compositional fluctuation model, we expect $\gamma=2$ for a system with a totally diffused

transition. For systems exhibiting intermediate degrees of diffuseness: $1<\gamma<2$. In the case of $PbTiO_3$,[17] the value of γ was determined from the slope of a straight line fitted to $\log(1/\varepsilon - 1/\varepsilon_{max})$ measured at 1 MHz as a function of $(T - T_{max})$. As expected, the ferroelectric transition was found to become increasingly diffuse with decreasing particle size. For bulk $PbTiO_3$: $\gamma = 1$, whereas it was 1.5 for the sample with $d_{XRD} = 31$ nm, below which the transition peak gets totally smeared.

Both dielectric and thermal measurements of T_C apparently indicate that the ferroelectric transition is *totally suppressed* in $PbTiO_3$ and $PbZrO_3$ when d_{XRD} is reduced below ≈ 30 nm. This appears to contradict the structural data since the ferroelectric distortion corresponding to 30 nm is rather large ($\approx 5\%$ in $PbTiO_3$) and it is not seen to vanish *even in the finest particles* studied. Note that in the isostructural $BaTiO_3$, a tetragonal distortion of only 1% is sufficient to stabilize the ferroelectric phase. We, therefore, suggest that the nonappearance of a peak in the dielectric
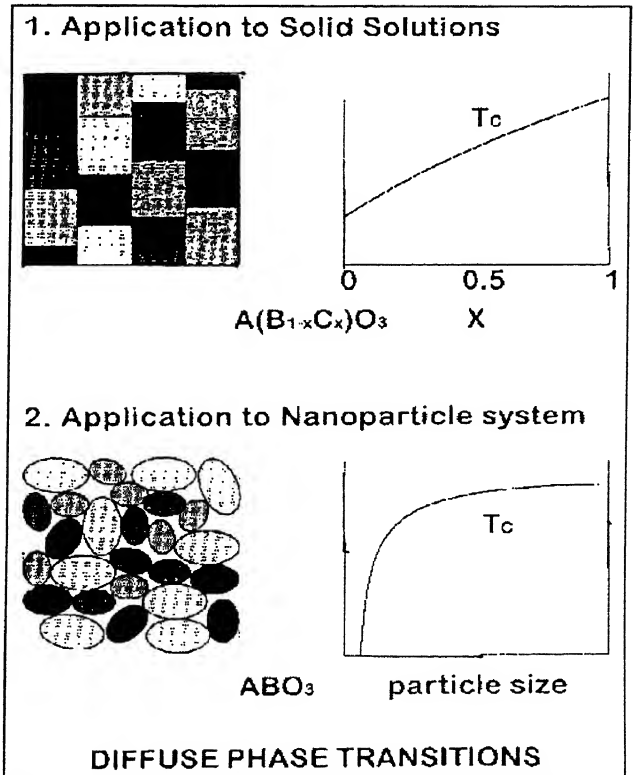

Fig. 8 A schematic comparison of diffuse phase transitions in a perovskite solid solution system (top) with local stoichiometry variations and a nanocrystalline system (bottom) with a particle size distribution

and thermal response need not be construed as an absence of ferroelectric (or antiferroelectric) ordering.

Diffuse phase transitions were discovered in perovskite solid solutions of the type $A(B_{1-x}C_x)O_3$, in which, generally, there is no long range crystallographic ordering of the B and C cations. Local compositional fluctuations are therefore present throughout the crystal, so that it could consist of microscopic domains of ABO_3 and ACO_3 (Fig. 8, top). Since ABO_3 and ACO_3 would - in general - have different values of T_C, this would lead to a micro-level T_C distribution about a central value corresponding to the T_C for $A(B_{1-x}C_x)O_3$. There could also be an intermixture of ferroelectric and paraelectric regions if only one of the constituents of the solid solution is ordered at the observation temperature. The scale of heterogeneity is believed to be ~10-20 nm[30].

The conceptual similarity between a solid solution and a nanocrystalline system can now be established. A nanocrystalline ferroelectric with an average size in the range of 10-50 nm would consist of a collection of crystallites with varying sizes (due to the inherent size distribution) centered around the mean size (Fig. 8, bottom). Recall, that in the size range being discussed, particles of different sizes also have different values of T_C. Since the variation of T_C with size is more conspicuous in smaller particles - the latter should exhibit a more diffused phase transition. We have earlier mentioned that the T_C distribution model had been invoked[7] to explain the dielectric behaviour of sintered ceramics, in which a complicated stress distribution occurs due to the high compaction. In the comparatively loosely aggregated nanocrystalline material studied by us, the observed strain and the T_C appear to depend directly on the particle size. However, in this case, the strain dependence is *inherently* a size effect and is not an artifact of sintering or high pressure compaction.

5. Finite Size Effects in Ferroelectric Thin Films

5.1 A Brief Review of Size Effects in Thin Films

An enormous amount of developmental work has been done on ferroelectric thin films during the present decade - as evidenced by the publication of seven large volumes of *Materials Research Society* Symposium Proceedings titled 'Ferroelectric Thin Films'. This has obviously been fuelled by the intense interest in the development of ferroelectric memory devices. A discussion of the technological aspects and the related synthesis problems are obviously not within the scope of the present review. In addition

to the MRS Symposium Proceedings, the readers interested in device applications may refer to the recent and excellent review by Scott[32]. Here, we will merely attempt to cover some aspects of inherent size effects in ferroelectric thin films. Then we will also present an interesting effect in antiferroelectric thin films, which appear to show ferroelectric behaviour below a critical thickness. This is included, because (as will be shown later) this is really a grain size effect rather than a thickness effect.

From a review of the experimental observations, it is possible to classify the size (thickness) effects into four distinct categories[33,34]. A decrease in the thickness (t) in ferroelectric thin films usually leads to (i) a sharp increase in the coercive field, (ii) a decrease in the remnant polarization, (iii) a drop in the dielectric constant, and (iv) a broadening of the ferroelectric transition. Such changes usually occur when the film thickness is below ~200 nm, but the actual value of this 'critical thickness' often depends sensitively on the nature of the microstructure, and hence on the synthesis conditions. One should also make allowances for film-substrate interfacial stresses, crystal quality, crystallographic orientation effects and epitaxy. Since the microstructure often changes continuously with t - thinner films being usually composed of smaller particles - it may be difficult to distinguish between particle size effects and thickness effects. Ren *et al.*[35] provide an example of this in their study of free standing polycrystalline $PbTiO_3$ films. They find that domain structure and dynamic response change drastically when the thickness is reduced below 200 nm, because the thinner films are composed of nano-sized, single-domain grains.

Most of the 'size effects' have a direct bearing on applications. One of the main problems involving ferroelectric thin film capacitors of finite area has been pointed out by Scott[32]. This arises from a reduction in the total quantity of switched charge due to the effect of fringing fields. Thus, in a circular disc of diameter $2\mu m$ and thickness 200 nm (aspect ratio = 10:1) the fringe fields produce a 7% reduction in the switched charge. But this effect increases non-linearly with decreasing aspect ratio, and is about 23% for an aspect ratio of 5:1.

5.2 Antiferroelectric to Ferroelectric Phase Transition in Thin Films

A ferroelectric is primarily characterized by the existence of a hysteresis in the polarization measured as a function of the applied electric field (P vs. E). This arises from the electrical switching of the ferroelectric domains. An antiferroelectric, on the other hand, is usually recognized by the existence of a *double*

hysteresis loop in the P vs. E diagram. Since the free energies of the antiferroelectric and ferroelectric modifications of a particular crystal are not too different, it is possible in certain cases to transform the former to the latter by applying a suitable electric field.

For the possible application of ferroelectric thin films as D-RAMS and NV-RAMS, one requires to fabricate integrated devices, requiring the growth of ferroelectric thin films on semiconductor substrates. In this context, the recent observation (outlined below) that antiferroelectric thin films deposited on a semiconductor substrates become ferroelectric when the film thickness is reduced below a characteristic value, appears to be quite significant[36].

This study involves the two antiferroelectric compounds: $BiNbO_4$, which has an orthorhombic stibiotantalite structure, and $PbZrO_3$, which has an orthorhombic perovskite structure. Normally, $BiNbO_4$ is antiferroelectric up to 360°C, ferroelectric between 360°C and 570°C, and paraelectric above 570°C. $PbZrO_3$ has a $T_C \approx 230$°C and transforms to the cubic paraelectric phase above T_C. But in high-purity $PbZrO_3$ samples, it is possible to stabilize a rhombohedral *ferroelectric* phase[37] in a temperature range of 220-230°C.

Phase-pure $BiNbO_4$ and $PbZrO_3$ films of different thickness (100 nm$\leq t \leq$900 nm) were grown on single crystalline Si(100) substrates using pulsed laser ablated deposition. The $PbZrO_3$ thin films were completely c-axis oriented, while the $BiNbO_4$ films were polycrystalline. Atomic force micrographs showed that an increase in film thickness was also accompanied by an increase in the average grain size in both systems.

Fig. 9 Dielectric hysteresis loops (P vs. E) in PbTiO$_3$/Si films of different thickness at 300°K

Dielectric hysteresis (P vs. E) curves for $PbZrO_3$ and $BiNbO_4$ thin films show that in both cases, the thicker films (above $t \approx 500$ nm) exhibit the expected 'butterfly' loops typical of *bulk* antiferroelectrics, while - below a characteristic thickness - they show ferroelectric-type hysteresis loops (Fig. 9). Note that the critical thickness (t_C) below which ferroelectricity is found to be stabilized is quite large - about half a micron. A study of the temperature-dependence of the dielectric hysteresis in the thinner films ($t < t_C$) shows that the ferroelectric- loop with a saturated spontaneous polarization persists between room temperature and T_C, while it behaves like a lossy dielectric above T_C. This proves the genuineness of the ferroelectric loops observed in the thinner films of $PbZrO_3$ and $BiNbO_4$ at room temperature.

The observed stabilization of ferroelectricity in thin films of normally antiferroelectric materials can possibly be ascribed to the effect of the electric field produced at the semiconductor-dielectric interface. A crystal surface can be viewed as an extended defect because surface atoms have unsatisfied bonds and may be displaced from their equilibrium positions. Also, the periodicity of the crystal potential is interrupted at the surface, and the resulting deviation of the electronic structure at the surface leads to the formation of localized surface electronic states. For a typical semiconductor-insulator interface, the interfacial field
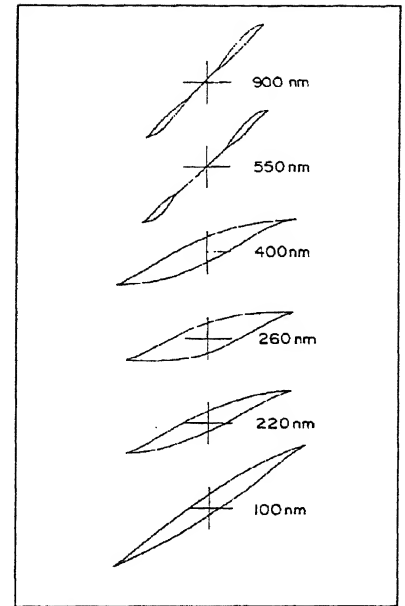
can be shown to be of the order of 100 kV cm^{-1}, which is high enough to induce ferroelectricity in many antiferroelectric crystals. The nucleation of $PbZrO_3$ and $BiNbO_4$ grains on the substrate actually takes place above their respective T_C's (the growth temperature being 700°C) and the samples were furnace-cooled in the presence of the large intrinsic electric field normal to the surface, which tends to orient the local dipoles along itself.

The antiferroelectric to ferroelectric transition can be understood as follows. The grains start nucleating on the Si substrate in the presence of the strong interfacial field (E_{if}). The first layer of single-domain grains polarizes the next, and so on. But, an increase in thickness is accompanied by increasing grain size. When the grain size becomes large enough, ferroelectric *domains* start to appear within each grain, leading to a net zero polarization over small volumes, and terminating the process of sequential polarization. Thicker films would therefore tend to show bulk-like (antiferroelectric) properties. In this model, the critical thickness is determined mainly by the nature of the antiferroelectric and the grain size (controlled by the growth conditions), and would not depend strongly on the magnitude of E_{if}.

It is significant to note that Batra *et al.*,[38] made an interesting prediction about a similar ferroelectric/ semiconductor system. They suggested that the

depolarization fields in such a system (arising due to lack of compensation) would increase with decreasing thickness and cause a reduction in the polarization. Ultimately, the polar state would be unstable below a certain thickness. A ferroelectric showing a second-order transition in the bulk should, according to these authors, exhibit a new type of first order transition due to the depolarization fields.

6. Conclusion

Even though Känzig's group made several key observations on size effects in ferroelectrics as far back as in the early 50s, the early data in this area suffered from inconsistencies due to imperfect materials as well as the presence of surface stresses. Much of the older data (50s through to 70s) referred to fine-grained sintered ceramics rather than to free or quasi-free nanoparticles and the observation of diffuse phase transitions in such systems by Martirena and Burfoot is noteworthy. Both experimental results as well theoretical modelling appear to suggest that size effects in displacive type ferroelectrics and antiferroelectrics

are dominated by the distortion in the crystal structure that occurs with a reduction in the particle size. The observed reduction in T_C and finally the destabilization of the dipolar ordering that occur with decreasing size, both appear to be related to the structural distortion. It follows that size effects would be much weaker in order-disorder ferroelectrics (in which structural distortions are of little or no significance), and this is indeed borne out by both experiment and theory. Nanocrystalline ferroelectrics also exhibit diffuse phase transitions.

The message to those interested in memory applications is that there exists an *inherent lower size limit* down to which a displacive ferroelectric is expected to retain its spontaneous polarization. However, this 'critical size' is rather small - only ≈ 10-20 nm. In very thin films with single-domain grains, the interfacial fields may actually tend to *stabilize* the ferroelectric order. On the other hand, if surface depolarization fields are present, they would try to reduce the polarization.

References

1   M E Lines and A M Glass *Principles and Applications of Ferroelectrics and Related Materials* Clarendon Press Oxford (1977) 10

2   M H Francombe *Physics of Thin Films: Mechanic and Dielectric Properties* (Eds. M H Francombe and J L Vossen) Academic San Diego (1993) 225

3   C Jaccard, W Känzig and M Peter *Helv Phys Acta* **26** (1953) 521

4   M Anliker, H R Brugger and W Känzig *Helv Phys Acta* **27** (1954) 99

5   W Känzig *Phys Rev* **98** (1955) 549

6   K Okazaki and K Nagata *J Am Ceram Soc* **56** (1973) 82

7   H T Martrena and J C Burfoot *J Phys C: Solid State Physics* **7** (1974) 3182

8   H Diamond *J Appl Phys* **32** (1961) 909

9   M R Srinivasan, M S Multani, P Ayyub and R Vijayaraghavan *Ferroelectrics* **51** (1983) 137

10 K Kanata, T Yoshikawa and K Kubota *Solid State Commun* **62** (1987) 765

11 K Uchino, E Sadanaga and T Hirose *J Am Ceram Soc* **72** (1989) 1555

12 S Schlag, H-F Eirke and W B Stern *Ferroelectrics* **173** (1995) 351

13 R Bachmann and K Bärner *Solid State Commun* **68** (1988) 865

14 K Ishikawa, K Yoshikawa and N Okada *Phys Rev B* **37** (1988) 5852

15 G Burns and B A Scott *Phys Rev Lett* **25** (1970) 167; *ibid Phys Rev B* **7** (1973) 3088

16 W L Zhong, B Jiang, P L Zhang, J M Ma, H M Cheng, Z H Yang and L X Li *J Phys: Cond Mat* **5** (1993) 2619

17 S Chattopadhyay, P Ayyub, V R Palkar and M S Multani *Phys Rev B* **52** (1995) 13177

18 S Chattopadhyay, P Ayyub, V R Palkar, A V Gurjar, R M Wankar and M S Multani *J Phys: Cond Mat* **9** (1997) 8135

19 P Marquardt and H Gleiter *Phys Rev Lett* **48** (1982) 1423

20 W L Zhong, Y G Wang, P L Zhang and B D Qu *Phys Rev B* **50** (1994) 698

21 I Rychetsky and O Hudák *J Phys: Cond Mat* **9** (1997) 4955

22 W Y Shih, W-H Shih and I A Aksay *Phys Rev B* **50** (1994) 15575

23 P Ayyub, V R Palkar, S Chattopadhyay and M S Multani *Phys Rev B* **51** (1995) 6135

24 P Ayyub, M S Multani, M Barma, V R Palkar and R Vijayaraghavan *J Phys C* **21** (1988) 2229

25 P Ayyub *Frontiers in Materials Modelling and Design* (Eds. V Kumar, S Sengupta and B Raj) Springer Verlag Heidelberg (1997) 228

26 V R Palkar, P Ayyub, S Chattopadhyay and M S Multani *Phys Rev B* **53** (1996) 2167

27 K Sheshadri, R Lahiri, P Ayyub and S Bhattacharya *J Phys Cond Mat* **11** (1999) 2459

28 G Smolenskii *J Phys Soc Jpn Suppl* **28** (1970) 26

29 K Uchino and S Nomura *Ferroelectrics Lett* **44** (1982) 55

30 L E Cross *Ferroelectrics* **76** (1987) 241

31 V S Tiwari and D Pandey *J Am Ceram Soc* **77** (1994) 1819

32 J F Scott *Ferroelectrics Review* **1** (1998) 1

33 R E Newnham, K R Udayakumar and S Trolier-McKinstry *Chemical Processing of Advanced Materials* (Eds. L L Hench and J K West) John Wiley (1992) 379

34 M H Francombe *Physics of Thin Films: Mechanic and Dielectric Properties* (Eds. M H Francombe and J L Vossen) Academic San Diego (1993) 225

35 S B Ren, C J Lu, H M Shen and Y N Wang *Phys Rev B* **55** (1997) 3485

36 P Ayyub, S Chattopadhyay, R Pinto and M S Multani *Phys Rev B* **57** (1998) R5559

37 B A Scott and G Burns *J Amer Ceram Soc* **55** (1972) 331

38 I P Batra, P Wurfel and B D Silverman *Phys Rev Lett* **30** (1973) 384

ELECTRICAL PROPERTIES OF NANOSTRUCTURED MATERIALS

S RAMASAMY[+] AND B PURNIAH[*]

+Department of Nuclear Physics, University of Madras, Guindy Campus, Chennai-600 025 (India)
*Materials Science Division, Indira Gandhi Centre for Atomic Research, Kalpakkam-603 102 (India)

The dielectric properties, electrical transport and Hall effect for nanostructured materials differ from those for micron sized materials due to increased interfacial atoms/ions and sinking of large amount of defects at/or near the grain boundaries. Each interface acts as a capacitor thus changing the dielectric value of the material. This change is highly pronounced in ceramics and compounds. The electrical conductivity in a polycrystalline material is the sum of the carrier transport under the applied field, in the grains and along/across the grain boundaries. The electrical conductivity can be studied by applying a d.c. voltage. However, if one is interested to investigate the dielectric property also, an a.c. voltage has to be applied and the variation of the impedance as a function of frequency must be measured. This gives in turn, both the a.c. conductivity and d.c. conductivity.

Metals and alloys do not have capacitative and inductive components. Hence the resistivity or the conductivity, is studied by applying a d.c. voltage. Ceramics and composites have capacitative components and hence the second method namely the impedance spectroscopy is often employed to investigate the electronic and ionic transport properties of these materials. In this article, under the heading impedance spectroscopy, the dielectric properties of nanostructured ceramics and composites will be reviewed; under the heading d.c. electrical conductivity, electrical conductivity of nanostructured metals, alloys, ceramics and composites will be reviewed. The role of grain boundary scattering of charge carriers is an important factor in the study of transport properties. There are arguments for and against in the literature about G.B. scattering. Transport properties include diffusion, Hall effect and thermoelectric power also. However, only passing remarks will be made in this paper on these properties in nanostructured materials.

Key Words: Nanostructured Materials; Metals; Alloys; Ceramics; Composites; Impedance Spectroscopy; Dielectric Properties; Electrical Conductivity

Introduction

Dielectric properties of ceramics and composites are important considering the application of these materials in electronics. The dielectric property gets modified due to defects, grain size, matrix of the composite, density distribution of the solute in the insulating matrix etc. Similarly the electrical resistivity which is related to the transport of charge carriers depends on the type of solids say metal, insulator or composite and also on the grain size, defects, doped impurities etc. The aim of this article is to review the status of these properties in nanostructured metals, alloys, pure and impurity doped ionic materials and composites. The first part will deal with the dielectric properties and the second part will deal with the electrical resistivity studies. The field of nanostructured materials has been reviewed by many authors[1-6] and the readers may refer to them for an overall view of these nanomaterials.

(A) Impedance Spectroscopy Studies

Electronic Ceramic Compounds

Barium Titanate, Zirconia, Zinc Oxide and Titanium dioxide may be considered to be the most important electronic ceramic materials studied in nano-structured form[7-20]. Apart from these, CeO_2[21], $Bi_4Ti_3O_{12}$[22], $Pb(In_{0.5}Nb_{0.5})O_3$[23], PZT on glass ceramics and metal particles like Cu, Ag[24, 25] on glassy matrix have also been studied by impedance spectroscopy. Pakhomov et al.,[26] have reported the dielectric studies of metal-insulator nanocomposites describing the observed results in terms of the percolation theory. Also Bursill et al.,[27] speak about the relationship between nanostructure and dielectric response function in $Pb(Sc, Ta)O_3$. Here the important results observed by various authors and their conclusion on the influence of the grain size and grain boundary on the dielectric property of the materials will be outlined.

Ferroelectric Ceramics

Barium Titanate is a multipurpose material; it can be used as a dielectric medium in a high voltage capacitor, as a positive temperature coefficient thermistor (PTCR) with certain rare earth ions like Gd^{3+} and also as a varistor although not frequently. It is a displacement type dielectric material with the transition temperatures at 120°C, -5°C and -95°C. Viswanath and Ramasamy[28] have studied the ferro- to paraelectric transition at 120°C as a function of grain size. Fig. 1 shows their results. Below the grain size of 32 nm, the material becomes amorphous and does not show any ferroelectric behaviour. Unlike in amorphous ferromagnetic materials where one can find spin ordering although the crystalline structure is in the amorphous state, in ferroelectric materials,
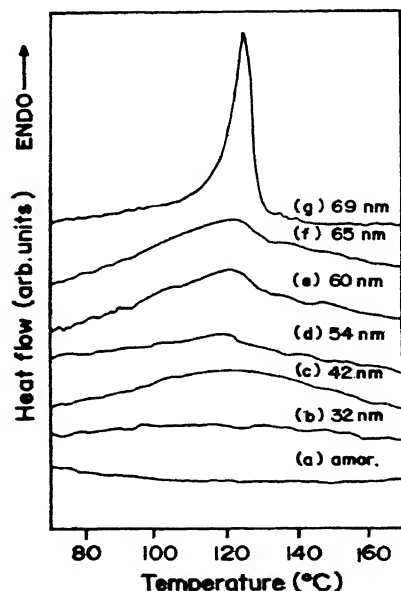

Fig. 1   DSC spectra of nanocrystalline $BaTiO_3$ (a) dried gel, (b-g) heat treated at 750, 850, 950, 1000, 1050 and 1250°C, respectively[28]

amorphous crystalline structure makes the electric dipole interaction very weak and hence no net ferroelectric ordering is observed. However, when the grain size exceeds 69nm the ferro to paraelectric transition becomes very sharp. In the recent literature one finds that in $BaTiO_3$, $PbTiO_3$, etc. in general the transition temperature T_c decreases with the decrease of grain size. This trend was attributed to the internal stresses that develop spontaneously in

small grains[29-32]. However as early as in 1954 an increase in T_c with decreasing particle size in $BaTiO_3$ has been reported[33]. The existence of domain walls or surface layers in fine particles was given as the reason for this phenomenon. The change of the ferro to paraelectric transition temperature thus seems to be due to competing effects of internal stresses and domain walls in small grains. In a recent study on $Bi_4Ti_3O_{12}$, Jiang *et al.*,[22] have reported that the diffusion of oxygen vacancies into the crystal lattice and clamping of domain walls are the reasons for the first increase and then decrease of T_c with continuous decrease of grain size in a ferroelectric material.

Viswanath and Ramasamy[28] have studied the behaviour of dielectric constant and the energy loss factor $\tan\delta$ in nanocrystalline $BaTiO_3$ sintered at 1250°C with grain size approximately 69 nm as a function of temperature as well as the measuring frequency. The dielectric constant shows slight decrease with increase of measuring frequency at all measuring temperatures. Addition of aliovalent impurities upto a maximum level of 8 at % destroys the ferroelectricity of the system. Creation of holes due to the dopants to substitutional position of Ti^{4+} and their diffusion to the surface regions such as grain boundaries have been cited to be the reason for such a suppression of ferroelectricity.

In the above paper, the role of grain boundary (GB) and the defects in the interfaces have not been considered. The influence of GB and defects on the dielectric property has been investigated by Viswanath and Ramasamy[34] in the varistor material zinc oxide. Pure ZnO is an n-type semiconductor. However when it is doped with impurities like Bi, Co, Sb, B, Cu and Sn in the form of oxides these impurities form an insulating coating layer on the surface of the ZnO grains and the consolidated material turns to be an insulator containing semiconductor ZnO cores which can be used as a varistor. Complex impedance spectra of nanostructured 96 at % ZnO + 4 at % dopants at room temperature and 300°C in Oxygen and Nitrogen atmospheres are given in Fig. 2. The Z' - Z" plots were fitted with two depressed semicircles. At RT the high frequency region gives a resistance of 10^5 ohms and the low frequency region gives a resistance of 10^7 ohms. The semiconducting ZnO grain core has a resistivity of 5-10 ohm - cm. Hence the high frequency region resistance has been considered
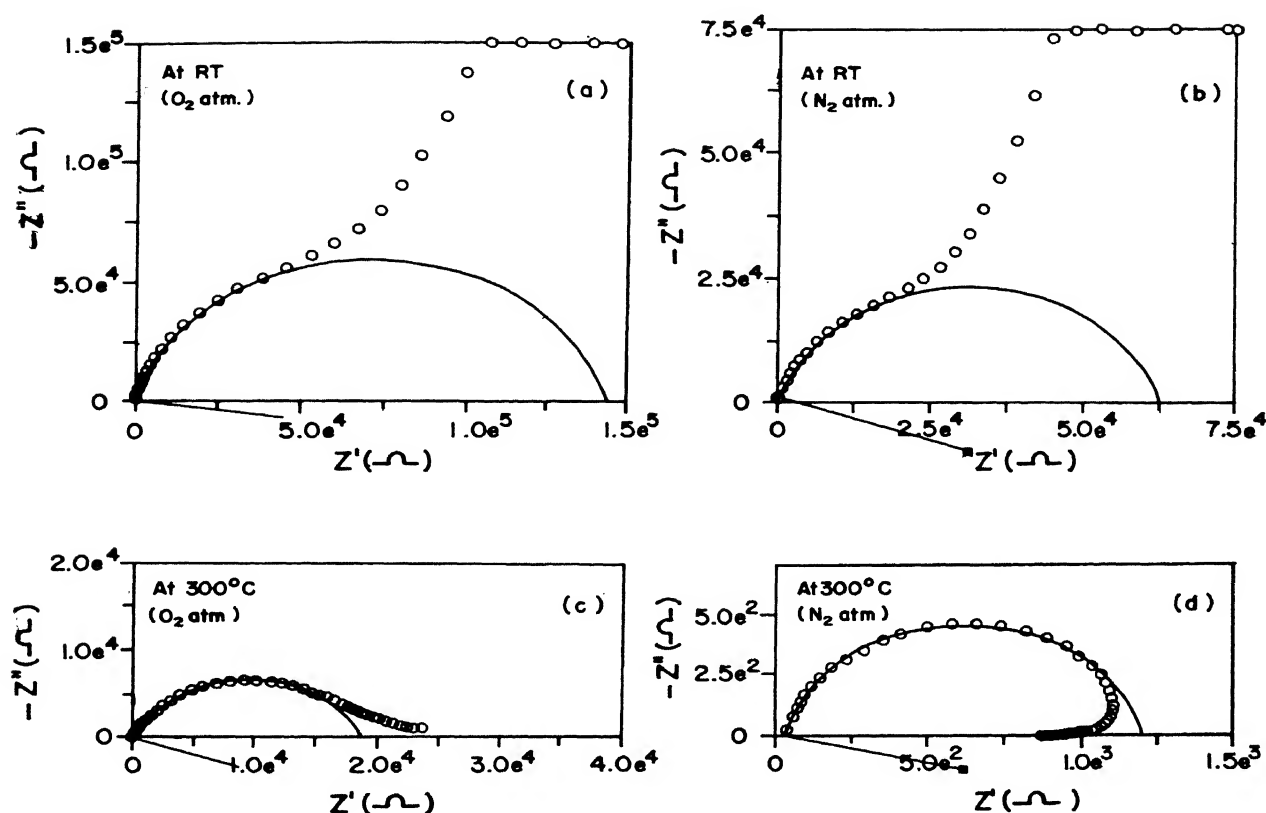
Fig. 2 CI spectra of NS 96% ZnO+4% dopants at RT and 300°C in O_2 and N_2 atmospheres[34]

as due to the diffused insulating layer on the ZnO grains. Then the low frequency region resistance has to be attributed to the G.B. The dielectric nature of the insulating layer has to be addressed to. Since the resistance R is the point where the imaginary part Z'' cuts the Z' axis and the frequency ω is known, the capacitance C has been calculated using the relation $\omega RC = 1$.

The electrical characterisation of nanostructured titanium dioxide (TiO_2) has been investigated systematically by Siddhartha Bhowmik et al.,[35] and Knauth and Tuller[36]. In the first case, the sample has been prepared by inert gas condensation technique, whereas in the second case the sulphate route has been used. Inert gas condensation gives about 95% rutile phase whereas the chemical route gives mainly anatase phase[18]. Thus a comparison of the results

of the two articles may be misleading since the ferroelectric domain structure in rutile phase and anatase may be different. Fig. 3 shows the impedance plot of the nanostructured TiO_2 sample with a grain size of about 10 nm studied by Siddartha Bhowmik et al. Polarisations for TiO_2/electrode/air interface, grain boundaries and grain interiors are clearly seen as three distinct semi-circles at low frequencies, intermediate frequencies and high frequencies respectively. The distortion of the semicircle at high frequencies corresponding to bulk region has been attributed to the presence of small amount of anatase phase along with the rutile phase. The authors have measured the impedance of microcrystalline TiO_2 also for comparison and it is shown in Fig. 4.

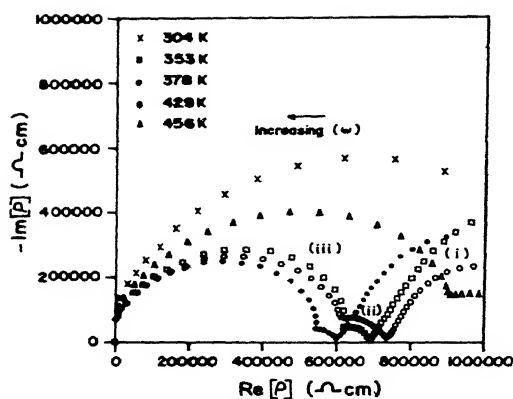Both the nano and microcrystalline TiO_2 show dominance in the resistivity of bulk region of the

Fig. 3   (a) Impedance vs frequency for a nanocrystalline TiO₂ Sample calcined at 400°C (673 K) at different temperatures. (b) Cole-Cole plot of nanocrystalline TiO₂ calcined at 400°C (673 K), showing the three major effects of (i) the electrode, (ii) the grain boundaries and (iii) the grain interior[35]
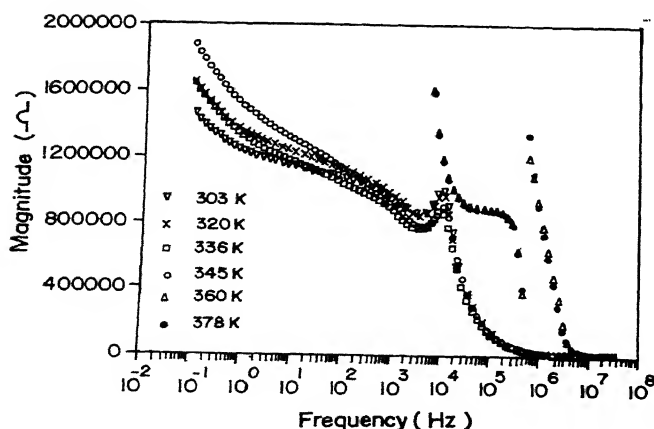

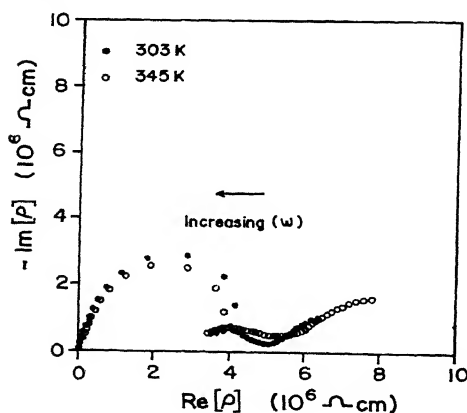Fig. 4   (a) Cole-Cole plot of microcrystalline TiO₂ sample calcined at 800°C (b) Impedance vs frequency for microcrystalline TiO₂ sample calcined at 800°C[35]

grains. Also the increased grain boundaries in nanocrystalline TiO_2 have the net effect of increasing impedance. The effect of sintering seems to reduce the grain boundary resistance. One important point to be noted is that the increased porosity and grain boundaries of the nanocrystalline TiO_2 result in the increased sensitivity of the frequency response. The tan δ for the nanocrystalline samples decreases with increased sintering temperature in the frequency range 1 Hz to 10^6 Hz and for samples calcined at high temperatures, this loss remains constant in the temperature range studied. The effects of interstitial Ti^{3+}, Ti^{4+} and Oxygen ion vacancies on the nature of impedance and electrical conductivity have posed a problem for these authors. Knauth and Tuller[36] have chosen nanostructured anatase TiO_2 to investigate the electrical and defect thermodynamics using impedance spectroscopy. The impedance spectra obtained by them for coarse grained ($d=1\mu m$) rutile TiO_2 and nanocrystalline ($d = 35$ nm) anatase (TiO_2) are shown in Fig. 5. Densities of the samples are said to be nearly 95% of bulk density 4.1 gm/cc. No phase change has been observed after impedance measurements at various temperatures. Coarse grained material shows two distinct semicircles corresponding to bulk and blocking grain boundaries. However, the nanostructured TiO_2 shows only one depressed semicircle probably, as the authors argue, because the time constants for bulk and blocking grain become closer in value when the grain size decreases. This is an indication to the fact that the grain boundary resistivity is orders of magnitude lower in nanocrystalline samples due to size effects.

The authors have studied the electrical conductivity both for conventional coarse grained and for nanocrystalline TiO_2 as a function of Oxygen partial pressure. Coarse grained TiO_2 shows regimes of p type as well as n type conductivity depending on whether the Oxygen partial pressure is high or low respectively and the titanium ions found to be in fully ionised (Ti^{4+}) in the interstitial positions with the characteristic exponent values +1/4 and -1/4. Thus the results have been interpreted by a defect model based on Cationic Frenkel disorder with fully ionised titanium interstitials. Unlike micron sized rutile TiO_2, the nanocrystalline TiO_2 gives a characteristic exponent of -1/2 for low oxygen partial pressures. This has been explained assuming doubly charged titanium interstitials. Further, the nanocrystalline TiO_2 shows a plateau of conductivity at high oxygen pressures.

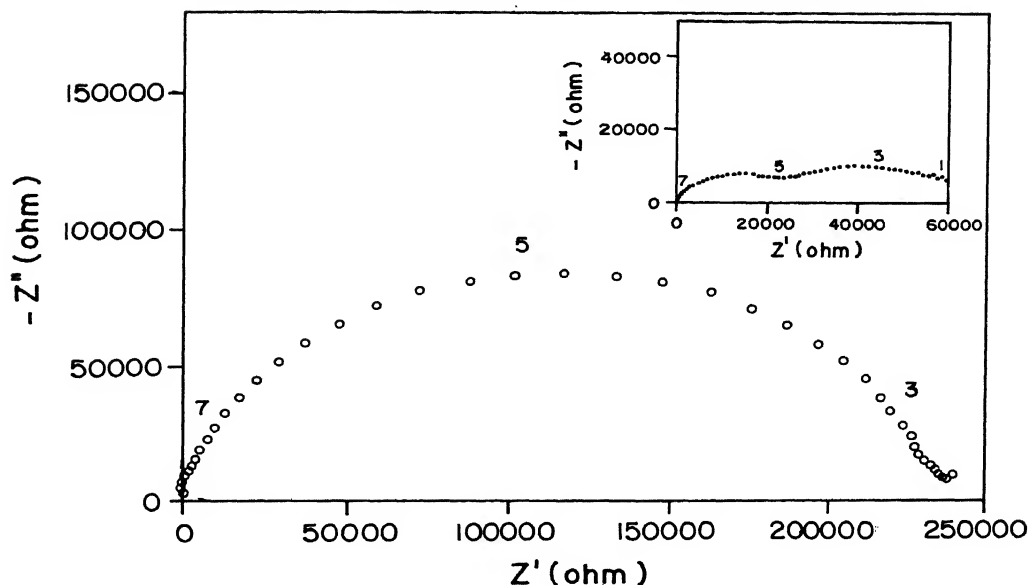Fig. 5 Impedance spectrum at 580°C in air of nanocrystalline TiO_2 (d≃35 nm). An impedance spectrum of a coarse-grained TiO_2 ceramic (d≃1 μm) is shown in the upper right corner. The numbers above the spectrum correspond to the logarithm of the measurement frequencies[36]

This has been interpreted as being a domain of ionic conductivity due to the high density of grain boundaries in nanocrystalline material which can act as preferred paths for diffusion of titanium ions at reduced temperatures. The low enthalpy of reduction of nano-TiO_2 (7.8 ± 0.4) eV is related to the reduced defect formation energies at the interfaces. The increased sensitivity at low oxygen pressures implies that the nano-TiO_2 can be used as an oxygen sensor.

Tschope[21] et al., have listed three important reasons as to how grain boundaries in polycrystalline semiconductors may be electrically active: (i) the formation of interfacial states as a result of broken symmetry, (ii) the altered defect thermodynamics at the grain boundary and (iii) the inhomogeneous distribution of charged defects resulting in a current-blocking space charge region. In nanocrystalline materials, the enhancement of all the above factors are high due to enhanced grain boundary densities. They have prepared oxygen nonstoichiometric cerium oxide, CeO_{2-x}, by inert gas condensation technique and recorded the complex impedance spectrum using HP4192A analyser. The impedance spectrum and the equivalent circuit are given in Fig. 6. The high frequency component is the bulk contribution and the second semicircle at low frequencies is the interfacial component since it appears above 10^5 Hz whereas electrode polarisation effect is expected to be below 10 Hz. In the present case the value of

bulk capacitance is approximately one order of magnitude larger than typical values for polycrystalline material. In the brick-layer model[37], the grain size and the width of the space charge layer determine the capacitance values in the equivalent circuit provided the permittivities in the bulk and the grain boundaries are similar. Hence as the grain size in a nanostructured material approaches the same order of magnitude as the space charge width, the capacitances
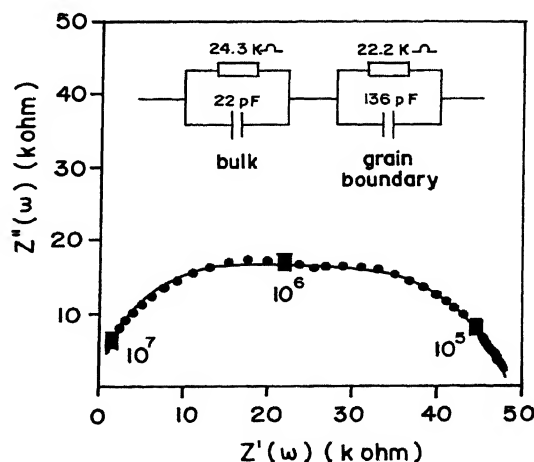

Fig. 6 Complex impedance spectrum of nanocrystalline CeO_{2-x} at 130°C in 1% H_2 /He. Full dots are measured data points and the solid line is the simulation by the indicated equivalent circuit. Measurement frequencies of 10^5, 10^6 and 10^7 Hz are indicated in the figure[21]

should become almost equal. Thus the result obtained for CeO_{2-x} illustrates that the distinction between bulk and grain boundary region tends to vanish as the grain size is reduced to the nanometer regime. The activation energy of the electrical conductivity for nanocrystalline CeO_{2-x} has been found to be 0.7 eV compared to the value of 1.97 eV reported for single crystal of CeO_2. Since the difference is much larger than the value of hopping mobility energy (0.4 eV), it has been proposed that the enthalpy of carrier formation is lower in nanocrystalline CeO_{2-x}.

Zirconia is one of the technologically important material which usually shows oxygen non-stoichiometry. Shusheng Jiang et al.,[38] have reported electrical conductivity studies of 4mol % yttria stabilised ZrO_2 prepared by combustion technique[39]. The impedance spectra have been recorded at various temperatures for samples with the grain size ranging from 10 nm to 200 nm. The relative density ranges from 68% to 98% of the theoretical density 6.1gm/cc, the stabilized crystal structure being tetragonal. The total effective resistivity and the effective resistivities of the grain and the grain boundary are found by measuring the distance between the vertical axis (Z″ axis) and the intercepting points of the impedance semicircles that correspond to the electrode, the grain and the grain boundaries respectively, with the horizontal axis (Z′ axis). The Arrhenius plots for the grain resistivity and the grain boundary resistivity are shown in Fig. 7 for the sample of grain size 100 nm. The activation energy for the oxygen vacancies in the grain boundary is found to be higher than that in the grain. However, the activation energies for the migration of oxygen vacancies in the grains and in the grain boundaries as a function of grain size remains almost constant for the grain size range 100 nm to 200 nm with relative density range 68% to 99%. The ratio of oxygen vacancy concentration in the grain boundary C_b to that in the grain Cg has been estimated experimentally from the impedance data. It has been found that, above 90 nm grain size, the oxygen vacancy concentration and the activation energy for the oxygen ion conduction do not change with grain size. The authors have arrived at the conclusion that in order to achieve the unusually high oxygen-vacancy concentration and to enhance oxygen-ion conductivity as reported in the literature[40], the grain size of the stabilised Zirconia should be reduced to less than 10 nm. Recent investigations reported by Ramamoorthy et al.,[41] support this
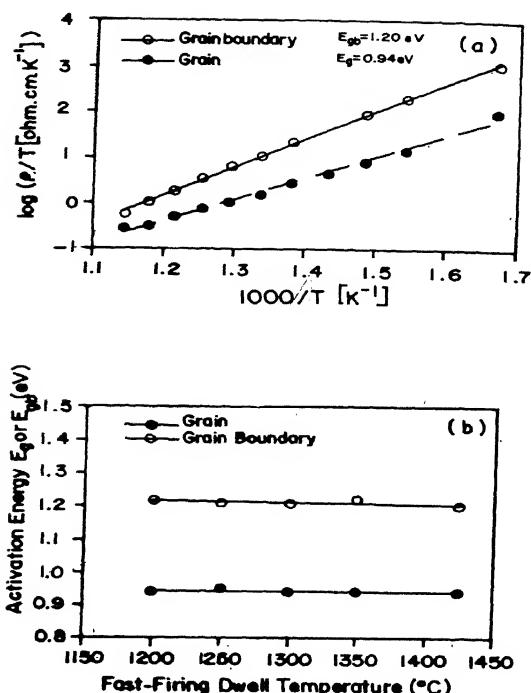

Fig. 7 (a) Arrhenius plots of the resistivities of the grain and the grain boundary for a Y-TZP sample (4 mol% Y_2O_3) following the fast-firing at 1200°C for 2 min. (b) The influence of the fast-firing dwell temperature on the activation energies of the oxygen-ion conduction in the grain and the grain boundary of Y-TZP sample (4 mol% Y_2O_3). A dwell time of 2 min was used in each case[38]

conclusion. The complex impedance spectra of yttria stabilised ZrO_2 at 573K obtained by these authors are shown in Fig. 8. The initial average grain size of the stabilised powders annealed at 1073K for 1 hour has been found to be around 10 nm. The Arrhenius plots of conductivity in grains, conductivity in the grain boundaries and the total dc conductivity are shown in Fig. 9. The Table I gives the corresponding activation energy values as a function of Yttria dopant mol%. The activation energies reported for grain conductivity 0.98 eV and for grain boundary conductivity 1.20 eV are in agreement with the values reported by Shusheng et al., (0.94 eV and 1.20 eV respectively). Since the activation energy for the total conductivity is almost equal to that for the grain boundary conductivity, it has been concluded that the conductivity in the nanostructurred stabilized ZrO_2 with grain size approximately 10 nm is mainly due to the oxygen ion conduction in the grain boundaries.
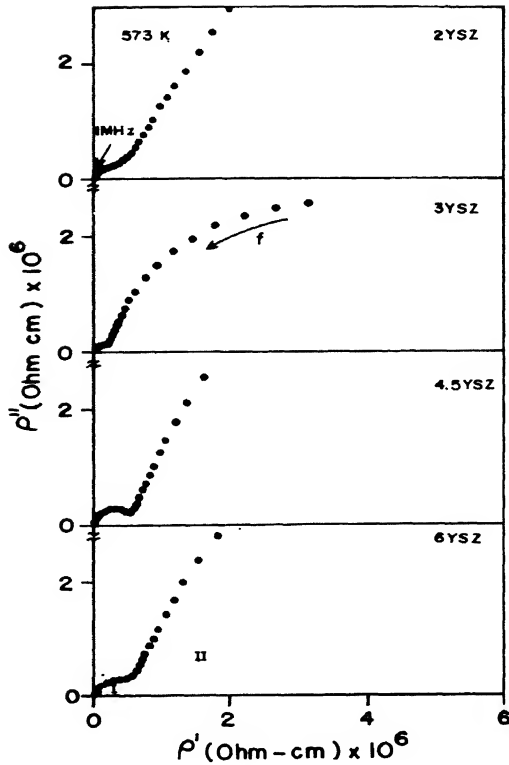
Fig. 8 Complex impedance spectra of YSZ at 573 K (the semi circle I corresponds to the intragrain polarization and II corresponds to the grain boundary polarisation[41]

Complex and Relaxor Ferroelectrics

So far impedance spectroscopy studies of some simple oxide ferroelectric materials in nanostructured form were discussed. Their applications have been mentioned in respective references. Bismuth Titanate is a material which shows potential applications such as nonvolatile memory devices and ferroelectric field effect transistor memory devices of nondestructive readout (NDRO) modes. The dielectric constant ε as a function of temperature for different grain sizes ranging from 15 nm to 56 nm for this material obtained by Jiang et al.,[22] is shown in Fig. 10(a). Knauth and Tuller[36] argue that the large dielectric constant of TiO_2 reduces the electrostatic interactions between point defects (i.e.) the formation of, $Ti^{ion} + O^{ion}$ dipole is minimal. However, for $Bi_4Ti_3O_{12}$, formation of oriented Bi interstitial ion + oxygen ion vacancy V_o^{2-} dipoles and their oriented polarisation seems to play a major role as the grain size is reduced down to 19 nm. The polarisation of these defect dipoles depends on the concentration of the defects on the grain surface
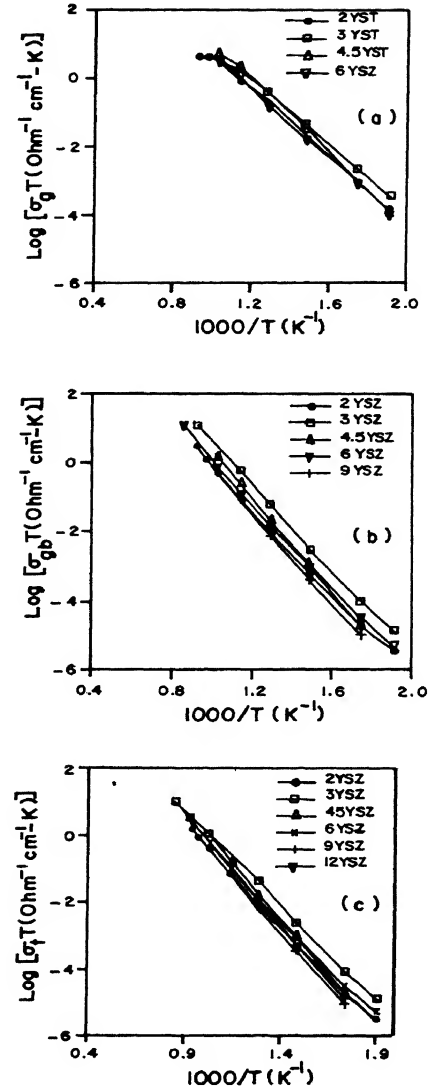

Fig. 9 Arrhenius plots of (a) conductivity in grains, (b) conductivity in grain boundaries and (c) total dc conductivity in YSZ[41]

Table I

Activation energies for ionic conduction in grains, grain boundaries and for total ionic conductivity in ultrafine grained YSZ systems with different yttria concentration

Y_2O_3 Concentration (mol%)	E_A (in grain) (eV)	E_A (in grain boundary) (eV)	E_A(total) (eV)
2	0.98	1.20	1.17
3	0.97	1.21	1.12
4.5	1.12	1.27	1.27
6	1.02	1.20	1.18
9	1.17	1.31	1.29
12	1.22	1.35	1.32

and hence it has maximum value for 19 nm grain size sample which will have maximum surface/ interface area. Since 56 nm gain size sample will have the minimum defect dipoles, the peak of ε-T curve corresponding to this vanishes. However, this peak reduces for 15 nm grain size sample also. Fig. 10(b) illustrates the grain size dependence of ferroelectric transition temperature T_c for this sample as measured by DSC. It is important to recall that Viswanath and Ramasamy[28] have not found any change in the T_c for the grain size range 69 nm down to 32 nm in $BaTiO_3$. In $Bi_4Ti_3O_{12}$ from 56nm to

26 nm the T_c increases. This is explained invoking "internal stress model"[30]. When the grain size is further reduced, T_c also decreases. This is argued as due to the dominance of domain wall pinning or clamping due to their lower mobility compared with internal stresses. The number of domains will decrease with decreasing grain size. The authors discuss that the combined effect of decrease in the number of domains and the clamping of domains by the defect dipoles and elastic dipoles (two different orientations of oxygen vacancies) may be the reason for the reduced value of dielectric constant for the sample with the grain size of 15 nm. Further research is needed to confirm the explanation given by these authors.

Relaxor type ferroelectric materials have the general chemical formula $Pb(B, B')O_3$. Their dielectric relaxation time and permitivity depend on the B^{n+} ion distribution in the octahedral sites. B and B' cations have different ionic radii. Pb $(Sc_{0.5}Ta_{0.5})O_3$ (PST), $Pb(Mg_{0.5}Nb_{0.5})O_3$ (PMN) and Pb $(In_{0.5}Nb_{0.5})O_3$ (PIN) are the examples. Elissalde et al.,[23] have prepared PIN material by 'fast firing'[42] process with grain size variation from 0.5 to $1\mu m$. The fast firing process has resulted in disordered structure of the system (i.e.) occupational positions of In^{3+} and Nb^{5+} have been altered. In this system In^{3+} seems to be inert for electrical polarisation and Nb-O-Nb chains give rise to the ferroelectric nature of the sample. The temperature dependence of the permittivity ε_r at different frequencies as measured by Elissalde is given in Fig.11. The TEM pictures show isolated polar clusters of size 1-2nm in the disordered matrix. At high temperature $T > T_c$, these clusters are supposed to give high frequency relaxation. Small values of the permittivity at high temperatures and at high frequencies can also be explained considering this isolated clusters. When the temperature decreases, the correlation length L_c for hopping of Nb^{5+} may increase thus increasing the size of the polar regions. A larger size of polar regions will lead to slower relaxation mechanism and higher permittivity. At a particular temperature say $T=T_c$ (lowest transition temperature) the relaxation frequency for disordered matrix $f_r(LF)$ will be different from that of the relaxation frequency $f_r(HF)$ for ordered (polar) regions. The reason is that the system is not completely ordered. Thus the dielectric properties of relaxor materials are related to nanostructure of polar regions. Similar polar domain regions have been observed in PST using HRTEM by Bursill et al.,[27].
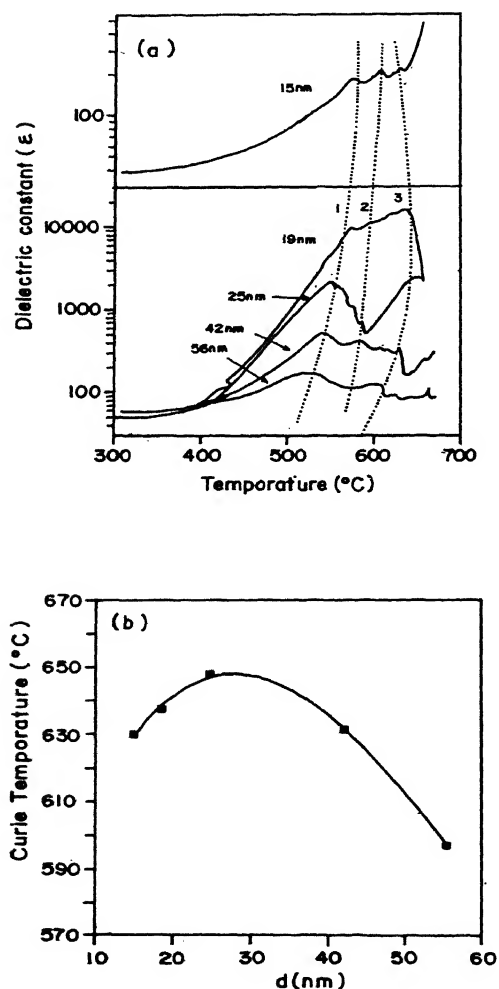

Fig. 10 (a)Temperature dependence of dielectric constant (ε) for $Bi_4Ti_3O_{12}$ samples with different grain sizes measured at frequency of 100 kHz. (b) Dependence of the Curie temperature (T_c) on the grain size (d) for crystalline $Bi_4Ti_3O_{12}$[22]
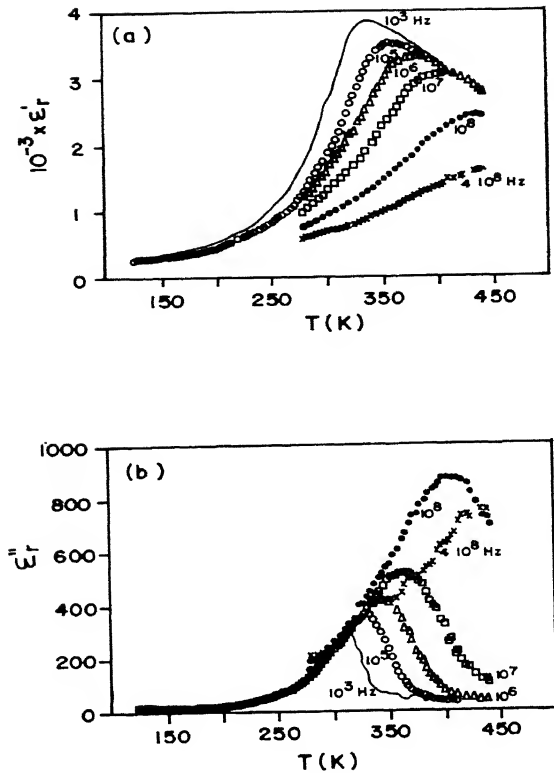
Fig. 11 (a) Temperature dependence of 'ε_r' at different frequencies (b) Temperature dependence of 'ε_r' at different frequencies[23]
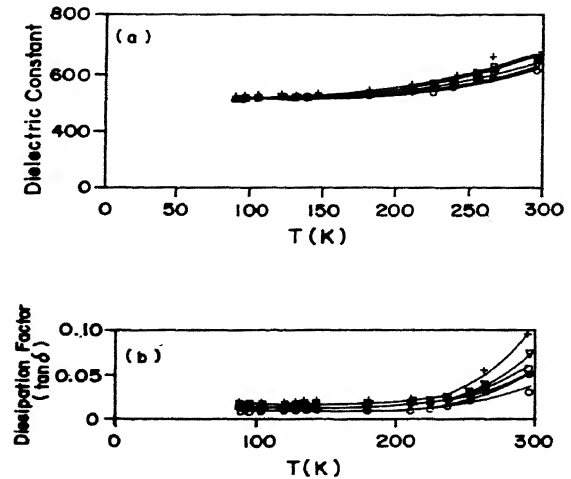

Fig. 12 (a) Variation of the delectric constant as a function of temperature for an ion-exchanged glass-ceramic sample reduced at 873 K for 30 min. (X) 2 KHz, (∇) 5 kHz, ($\square$) 10 kHz, ($\bullet$) 20 kHz, (Δ) 50 kHz and (o) 100 kHz (b) variation of the dissipation factor as a function of temperature for an ion-exchanged glass-ceramic sample reduced at 873 K for 30 min. (X)$\sqrt{2}$ kHz, ( ) 5 kHz, ($\square$) 10kHz, ($\bullet$) 20 kHz, (Δ) 50 kHz, and (o) 100 kHz[43]

Metal-glassy Matrix Nanocomposites

Chakravorty and his coworkers have been studying glass-ceramic metal nanocomposites from 1977 onwards. Roy and Chakravorty[43] have prepared metallic silver strands of about 15nm length as an aggregate of 3nm dia silver particles on a glass ceramic by ion exchange process and investigated the dielectric properties of the system. The dielectric constant versus temperature and loss factor versus temperature are shown in Fig. 12. Upto 200K, both the dielectric constant and the tanδ remain constant with slight variation as a function of measuring frequency. Beyond 200K there is dispersion in both the quantities. The low temperature dielectric permittivity is said to be electronic in origin. This fact combined with the formation of silver strands is believed to confirm Gorkov-Eliasberg anomaly[44], namely that the one-dimensional metallic box (interrupted strand model) could be regarded as the anologue of the ultrafine

metal particles having large spacing of electronic energy levels. The authors have assumed Maxwell-Wagner space charge mechanism[45] for the dispersion in dielectric permittivity at temperatures higher than 200K. A diagonal-layer model having alternative insulating and conducting layers has been assumed and a value of ε=676 at 5KHz has been theoretically estimated in good agreement with the experimental value of 680. One important factor to be considered here is that the loss factor is very low, the value being less than 0.1. Similar results have been obtained for silver nanoparticle-glass ceramic PZT composite by Kundu and Chakravorty[46]. However for this sample, there is finite temperature coefficient between 100 to 300 K in the dielectric permittivity for which the authors are unable to find any explanation. Further, the value of tanδ increases upto 1.

Recent work of Banerjee and Chakravorty[25] on Copper-Silica nanocomposites synthesized by electrodepositions is highly informative. They have prepared three samples with average copper grain size of 11.4 nm, 8.8nm and 3.2nm in silica matrix. The interparticle separations were estimated to be 14.4nm, 11.7nm and 2.8nm respectively for the three samples. The metal particles in the matrix have fractal structure. Experimentally observed a.c. conductivities

by impedance measurement as a function of frequency at various temperatures for all the three samples are given in Fig. 13. The conductivities for all the specimens obey the frequency dependence $\sigma_r(\omega) \propto (\omega)^n$, n being 0.62 independent of temperature. The theoretical model proposed for the a.c conductivity for fractal clusters of metal particles on insulating matrix

$$\sigma_r(\omega) \cong \omega^{t/(s+t)} \qquad \ldots (1)$$

where t is the power law exponent for d.c. conductivity above the percolation threshold and s describes the divergence of the dielectric constant at the percolation threshold. For the systems under study $s = 0.75$ and $\varepsilon = 1.95$. Substituting these values, the exponent n turns out to be 0.72 which is higher than the value obtained from the experimental results. This is the case for other systems also as per the authors. Hence it seems that the theory needs modification. The temperature-independent nature of the a.c. conductivity exponent is shown to be characteristics of quantum mechanical tunneling model in amorphous semiconductors. Assuming $Cu\text{-}SiO_2$ gel system as equivalent to a homogeneous random quantum mechanical tunneling material, the authors have fitted the a.c conductivity data using the radius of electron wave function localisation α^{-1} and $N(E_F)$ turns out to be $4.5 \times 10^{18}cc$. Since theoretical and experimental values are almost same, it is concluded that Cu nanoparticles in Silica gel constitute the localised sites for the electrons. The dielectric dispersion of these has been analysed in term of a stretched exponential relaxation function[47] using dielectric modulus data. Pakhomov et al.[26], have studied $(Ni_{85} Fe_{15})_x - (SiO_2)_{1-x}$ samples and suggested that the low-frequency behaviour may be due to a combination of metallic and tunneling conduction. Brouers et al.[48], have considered the influence of boundary scattering on transport phenomena in $(NiFe)_x (SiO_2)_{1-x}$ which is a ferromagnetic metal-dielectric nanocomposite. It may be more appropriate to add this factor in explaining the data obtained by Banerjee et al.,[25] and Pakhomov[26].

(B) D.C. Electrical Conductivity Studies

Metals

As early as in 1969 Fujita et al.[49], reported enhanced superconductivity in aluminium granular films prepared by means of inert gas condensation technique. The degree of enhancement depended on
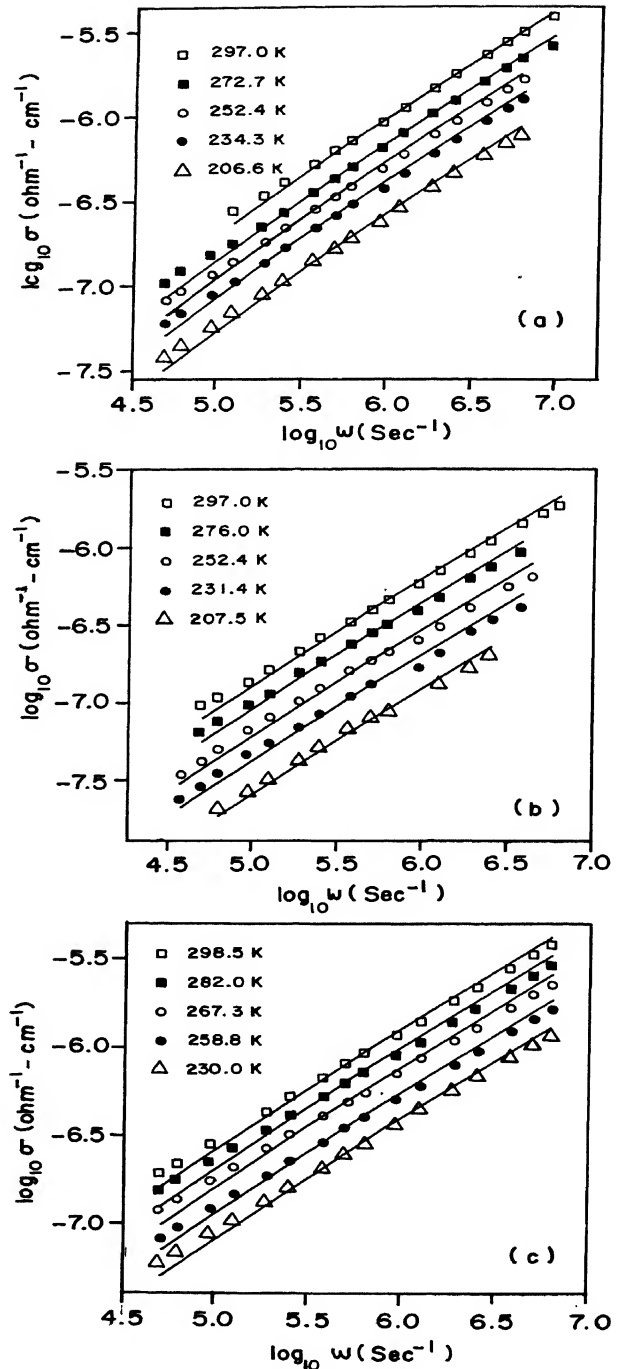

Fig. 13 Variation of ac conductivity as a function of frequency for different specimens (a) Specimen 1, (b) Specimen 2, (c) Specimen 3 [25]

the particle size and not on the thickness of the film. The mean size of the particles were estimated by XRD pattern to be less than 5 nm. The conductivities suggested that the particles were not insulated from each other but the electrical contact between them were perfect. As the particle size is much smaller than the electronic mean free path λ of bulk aluminium, in the granular film the λ was supposed to depend on the scattering at the junctions. Thus λ was assumed to be of the same order of magnitude with the mean particle size. Hence the conductivity was found to be independent of temperature below 100K. Fujita et al.[50], reported the d.c resistance of films of Ag and Al consisting of fine particles between 1.5 to 300K in 1976. For silver, the particle sizes were 10 and 30 nm respectively and for Al the size was 20 nm. The resistance for these specimen showed finite temperature dependence unlike for the sample containing 5 nm Al grains. When the particle size increases above 5nm the phonon scattering seems to increase thus giving rise to positive temperature coefficient of resistance. The fitting with Gruneisen's relation[51] gives lower Debye temperature compared to the bulk metals. This implies the lattice softening as the particle size is reduced Bakonyi et al.,[52] have investigated the temperature coefficient of resistivity in electrodeposited Ni in the grain size range 55 nm to 300 nm. As the grain size is reduced, volume fraction of grain boundaries which have a highly disordered structure increases. This structural disorder leads to an increase of temperature independent contribution to the resistivity causing a reduction of α as observed in Fig. 14. This is in agreement with the results reported by Fujita et al. in Al. Bakonyi et al.[52], have studied the thermoelectric powers also for nc-Ni and microcrystalline Ni. A value $S = -15.5$ μV/K to -18 μV/K for nc- Ni is less than the value $S(300\ K) = -19.52$ μV/K for fcc micro crystalline Ni. This difference is ascribed to an increased degree of disorder in the nanocrystalline state. Following the work of Bakonyi[52], Aus et al.[53], have repeated the resistivity measurements of electrodeposited Ni down to the grain size of 11 nm. They have observed the values of resistivity to increase with decreasing grain size. This excess resistivity has been shown to be directly proportional to the volume fraction of atoms in grain boundary and is associated with electron scattering events at the grain boundaries. These authors also have found the temperature coefficient of resistivity to decrease with decreasing grain size.
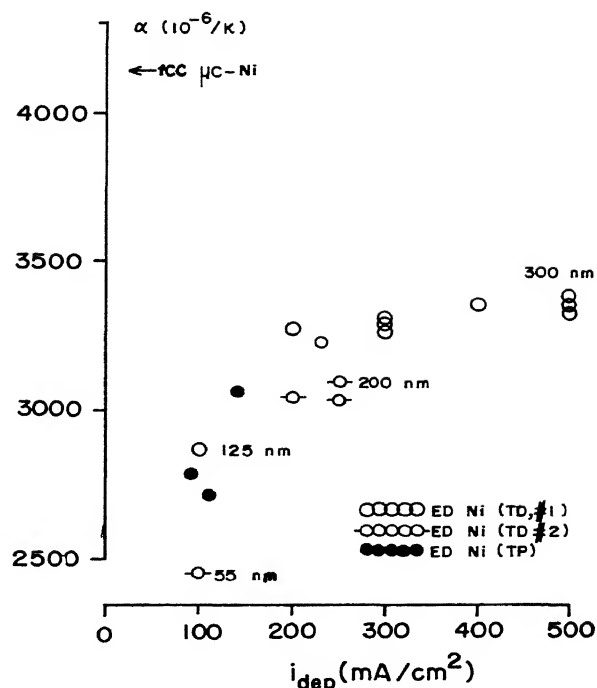

Fig. 14 Temperature coefficient of resistivity α versus deposition current density i_{dep} for the ED Ni foils. For the TP series, the time- averaged values of the plating current pulse amplitude have been used to calculate the assigned value of i_{dep}. The α value fo fcc μc-Ni[12] is indicated by the arrow on the ordinate. The numbers given for some data point symbols represent the average grain size determined for that sample by XRD and/or TEM[52]

Low temperature transport properties of nanocrystalline Cu, Fe and Ni have been reported by Pekala and Pekala[54] prepared by torsional deformation at quasihydrostatic pressure of 6 GPa (severe plastic deformation, SPD). For each metal, the nanocrystalline process causes a systematic increase in electrical resistivity which is accompanied by a suppression of the temperature coefficient of resistivity α. The temperature variation of electrical resistivity for the n-Ni and n-Fe exhibits a minimum around 30K and it seems to be of the Kondo type. The authors argue that the transport phenomena in these systems are strongly influenced by the electron scattering on the grain boundaries in agreement with the Mayadas-Shatzkes model[55]. The structural disorder in the nanocrystalline metals reduces the electron-phonon interaction as demonstrated by the suppressed thermoelectric power maximum in nanocrystalline Fe. Usually a minimum in resistivity versus temperature curve is observed due to spin-flip scattering (Kondo effect)[56] or Mott metal-insulator

transitions[57,58]. However, in nanocrystalline tungsten which is a nonmagnetic metal, with a typical grain size of about 10 nm, Ramansani, as cited by Sauer[59], has observed a minimum in resistivity at a temperature $T = 35K$. Sauer[59] has given a theory to explain this phenomenon based on conduction band width and says that this effect has its origin in the existence of a new length scale defined by the medium grain size in the nanostructured metal which leads to corrections to the conductivity tensor. These correspond to lowest-order quantum interference effects of conduction electrons at the grain boundaries. Whether such a resistivity can be seen in other nanostructured metals is yet to be experimentally seen. Results contrary to those discussed in the above paragraphs have been reported by Karpe et al.[60], on thin films of gold containing nanocrystals. These authors have found grain-boundary scattering in thin-film nanocrystalline gold to be relatively small inconsistent with a large volume fraction of a strongly disordered grain boundary phase. Further, the temperature dependence of the resistivity of the nanocrystalline films is found to be in close agreement with that of bulk gold indicating that the Debye temperature is not strongly grain-size dependent. They have also found the irradiation effects with 1MeV Xe^{2+} and 500 keV Ar^+ at room temperature to produce same saturation level of defects both in nanocrystalline film and in polycrystalline film. Thus the resistivity increase due to irradiation is not strongly grain-size dependent. The grain size of as deposited film was found to be 8 nm and that of the specimen annealed at 773K was 40 nm. Fitting the resistivity data with Bloch-Gruneisen formula[51] gives the Debye temperature $\theta_R = 185K$ which is within $\pm 10K$ for the bulk gold. Thus the electron scattering due to grain boundaries seems to play no role in the resistivity which is in total contradiction to the argument of Pekala and Pekala[54] whose experiment on n-Cu, n-Fe and n-Ni followed Mayadas and Shatzkes. Karpe et al.,[60] have found the transmission probability electron through the grain boundary to be larger than 95% using a semi empirical formula

$$\sigma = (ne^2 /m_e v_F)\ T^{\lambda/D} \qquad \ldots (2)$$

D being the grain size. Thus these authors argue that their results follow the results of Eastman[61] on n-Pd and not in agreement with the report of Huang et al.,[62] on a nanocrystalline consolidated copper. Since these results contradict many reports available in the literature in support of electron scattering by the grain boundary, it would be worthy to repeat the

experiment and analyse the validity of the empirical formula.

Birringer et al.[63], have measured the grain size dependence of the electrical resistivity in nanocrystalline Pd in order to investigate whether or not a critical grain size exists below which the grain boundary length couples to the grain boundary structure and energy. The results are depicted in Fig. 15. Seeger and Schottky[64] have argued that the electrical resistivity of a high angle GB is correlated to its excess volume and hence is directly related to its structure and energy. On the basis of the work of Mayadas and Shatzkes[55], Reiss et al.[65], have derived an exact expression for the resistivity ρ of a nanograined material as a function of the average crystallite intercept length $<L>$: (used for linear thermal expansion of nanocrystalline materials).

$$\ln \rho = k - (l_\infty/<L>)\ln T \qquad \ldots (3)$$

where k is a constant related to the electrical resistivity of a defect free single crystal of the same chemical composition as the fine-grained material, l_∞ is the electron mean free path in the defect free single crystal and T is a tranmission coefficient for electrons through GBs. According to Seeger and Schottky[64] the T of a given GB is correlated to its excess volume; hence the deviation from linear behaviour evident in Fig. 15 at small mean intercept length $<L> \leq 8$ nm implies a change in the average specific excess volume away from that typical of quasi-infinite boundaries.
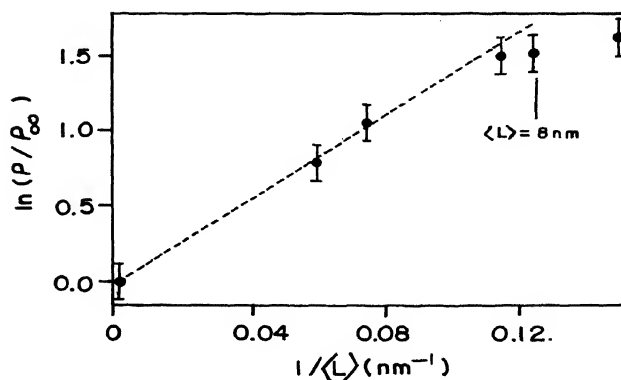
Fig. 15 Electrical resistivity ρ of nanocrystalline Pd as function of inverse average crystalline intercept length <L>. All resistivity values were normalized to the resistivity ρ_∞ = of coarse-grained Pd. The marked intercept length of 8nm (at which deviation occurs from the linear behaviour at larger sizes (---) corresponds to a (number-weighted) average grain size <D> = 7nm, assuming spherical grains and a log-normal size distribution with σ = 1.3 [63]

Surprisingly the average transmission coefficient T is larger and therefore, the specific excess volume is smaller for samples with the smallest grain sizes. Probably the experiment on Au as done by Karpe[60] may have to be carried out below certain critical grain size to find the GB effects.

Islamgaliev et al.[66], have done the resistivity measurements in Cu and Ni samples subjected to severe plastic deformation (SPD). One advantage in this method of producing nanocrystalline materials is that there will not be pores as in consolidated nanostructured specimens. However, density of dislocation will dominate the resistivity which is temperature independent. The mean grain sizes of SPD Cu and Ni are 109 nm and 121 nm respectively. These sizes are somewhat on the higher side to show the special properties of nanocrystalline materials. However, these authors were able to get reasonable change in GB electronic conductivity. They have used Mayadas-Shatzkes model[55] in which the product of the GB potential barrier width s by its height ϕ is given by

$$s \ \phi = (k/1-k) \ (h^2 v_F^2)/2 \qquad \ldots (4)$$

(k is the mirror reflection coefficient, h is plank constant, v_F is the Fermi velocity) to estimate the width of the GB potential barrier s. The values of potential barrier width obtained by this model are 2.1 nm and 3.7 nm for nanocrystalline Cu and Ni respectively. These values are considerably larger than the width of the GB for large crystals, which is less than 1 nm as determined by HRTEM. This difference is attributed to the presence of residual internal strains near the GB in nanocrystalline metals.

Alloys

One of the methods of obtaining nanocrystalline alloys without porous structure is by annealing the amorphous alloys. Pekale et al.[67], have found three stage crystallisation process in $Fe_{6.5-y}CuNb_ySi_{22.5-z}B_z$ amorphous alloy prepared by melt spinning method. Measurement of d.c. resistivity has been used as the tool to study the crystallisation behaviour. Nb seems to suppress the grain growth down to 13 nm thus speeding the creation of phase boundaries. In 13 nm grain sized samples, the mean free path of the electron is controlled by the grain size and the GB scattering increases. Hence, an increase in the resistivity with temperature has been noticed. When the grain size grows to 48 nm with zero Nb concentration the mean

free path of the electron increases giving sudden drop in the electrical resistivity. Influence of boron concentration on the grain growth has also investigated by these authors. The boron atoms destabilises the amorphous structure beyond 980K. Allia et al.,[68] point out that the electrical resistivity measurements can be used to study the nanostructure growth in an amorphous matrix.

Interface dependence on the electrical resistivity in Fe-Cu-Si-B amorphous alloy containing nanocrystals in the range 30-90 nm produced by crystallisation method has been investigated by Liu et al.[69]. The residual resistivity ρ_o (extrapolated to 0K) versus the average grain size and the temperature coefficient of resistivity versus mean grain size of nanocrystalline Fe-Cu-Si-B alloys are shown in Fig. 16. The residual resistance decreases from 50 to 20 $\mu\Omega$ cm as the average grain size increases from 30 to 90 nm. Electron scattering by an interface which can be regarded as a potential barrier with a certain width s and height ϕ as defined earlier decreases the conductivity of the nanocrystalline materials with respect to bulk single crystal. This is due to grain boundary scattering of electrons. However the behaviour of temperature coefficient of resistivity as function of grain diameter is contrary to the theoretical expectations. Quantum mechanical calculation of d.c. GB implies a decrease of TCR even to negative values[65]. However as in Fig. 16, TCR increases with decrease of grain size. The authors argue that this contradiction needs more
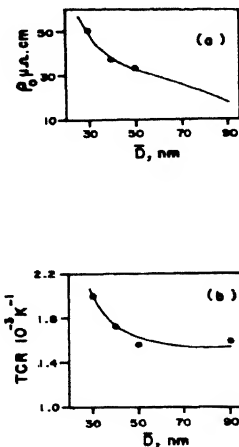

Fig. 16 (a) Plot of the residual resistivity ρ_o versus the average grain size of nanocrystalline Fe-Cu-Si-B alloys. (b) Plot of the temperature coefficient of resistivity (TCR) vs mean grain size nanocrystalline Fe-Cu-Si-B alloys[69]

detailed research. In Al-Y-Ni-Co Pekala *et al.*[70] report a decrease of relative resistivity with temperature for samples containing various volume fractions of nanocrystalline material. However, there is no direct correlation between TCR and average grain size to make any conclusive remark. A positive TCR of the resistivity versus temperature in the granular films of SiO_2 containing Ag nanograins (R = 2.35 nm and 2.5 nm) has been found by Juh Tzeng Lue *et al.*[71]. However, one cannot make a comparison of this result with the theory of Reiss *et al.*,[65] since the system is not a pure metal. The authors have also found an apparent break (resistivity minimum) of the R-T curve around 120K which is presumed to be due to the Kondo effect (spin flip scattering) when the number of metallic particles with odd spins is large enough to exhibit local magnetic moments.

Nanoceramics and Composites

Chakravorty and his coworkers have been carrying out systematic transport studies in metal-glassy matrix composites both by impedance spectroscopy and by d.c. electrical conductivity. D.C. electrical conductivity of fractal silver particles having grain sizes in a glassy matrix from 4.3 nm to 11 nm has been reported by Roy and Chakravorty[72]. The surface resistivity was found to vary linearly over the temperature range 120-300K, the slope of the curves increasing as the silver particle diameter becomes smaller. The linear variation of the resistivity with temperature is broken below 120K for which no explanation is found. May be the tunneling mechanism is the cause. As has been found earlier for metals, the effective Debye temperature decreases as the particle size of silver becomes smaller. This is ascribed to the softening of the phonon spectrum due to the effect of surface of the metal particles. Unlike in metals, where Mayadas-Shatykes model[55] is used, here the authors have used Ziman theory[73] for the lattice resistivity ρ_l of the bulk metal to study the effect of particle size on the electrical resistivity but the conclusions are the same as in the previous case. Nanoparticles of Cu and Ni have been synthesised again by Roy *et al.*[74] in bulk form by hot pressing sol-gel derived silica-metal nanoparticle composite powders. The particle sizes range from 9 to 17.5 nm. Adopting the same procedure as that for Ag particles to analyse the d.c. resistivity data, the authors have arrived at the conclusion that the specimens exhibit the characteristic behaviour of the metallic species in

their nanocrystalline form (*i.e.*) θ_D decreases with decrease of grain size implying phonon softening. Earliest work of Chakravorty's group on glass-metal nanocomposite is in 1977 when Chakravorty *et al.*,[75] reported the electrical properties of glassy system with Bi particles of size 5 to 50 nm and selenium particles of size 5 to 200 nm. The d.c. resistivity data at temperatures below 120°C indicated that a tunneling mechanism of charge carriers between the conducting Bi and Se granules is operative. The dielectric relaxation spectra confirmed this model of electron transport. Fig. 17 shows the log ρ against $1/T$ measured at various frequencies. The figure shows two linear portions having different slopes, the change occurring around 200°C except for the d.c. which has a switch over at 120K. These results indicate that there are two conduction mechanisms operative in these glassy-metal systems. At temperatures above 200°C, the transport seems to be due to the migration of sodium ions through the glassy matrix. The linearity of the curve log ρ against $1//T^{1/2}$ below 120°C provides confirmation of the tunneling mechanism between
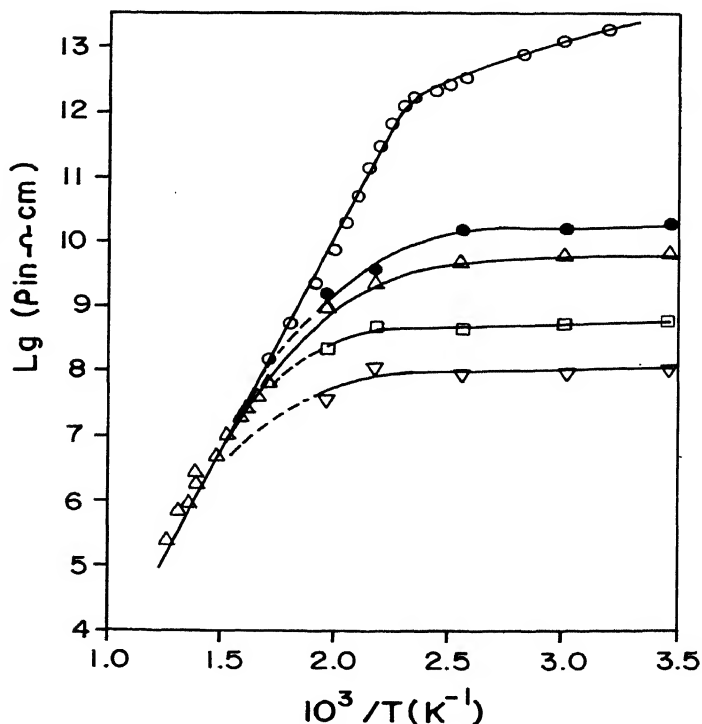

Fig. 17 Log ρ against $1/T$ for glass 1.1 measured at different frequencies: ● 500 kHz, △ 1kHz, □ 10 kHz, ▽ 50kHz[75]

the conducting grains, separated by a distance less than 5 nm.

The d.c. resistance data obtained by Banerjee and Chakravorty[76] for Cu particles with size 11.4 nm, 8.8 nm and 3.2 nm in silica gel medium prepared by electrodeposition is shown in Fig. 18. The data fits fairly well with the variable range hopping model[77] having the resistivity expression

$$\rho = \rho_0 \exp (T_0/T)^{1/4} \text{ with } T_0 = 8 \ b_c \ \chi^3/[fN(E_F)k]$$

$$... (5)$$

where b_c is a dimensionless constant 1.5, χ is the tunneling constant, f is a proportionality constant, $N(E_F)$ is the density of states at the Fermi level and k is the Boltzmann constant. The fitting has been done over the entire temperature range of measurement. In hopping mechanism, the activation energy arises due to the Coulomb energy needed to separate an electron from a metal cluster and place it on a neighbouring one at a distance of approximately 14.4 to 2.8 nm. The metal particles contributing to such high activation energies have diameters of the order of 2nm. In the report under discussion, the particles obey log-normal distribution with sizeable fraction of particles having 2nm grain size which control the variable range hopping mechanism of conductivity over the entire temperature range of measurement. Assuming $f = 1$, it has been shown that the $N(E_F)$ decreases drastically as the metal particle size is reduced to nanometer range. Reasonable agreement with the characteristic exponent $-1/4$ has to be compared with the studies of Knauth and Tuller[36] on nc- anatase TiO_2 at low oxygen pressures in which the exponent has been found to be $-1/4$ for electronic conductivity.

Anri Nagajima et al.[78] have recently used low energy Sn^+ ion irradiation process followed by thermal annealing to have 4.2 nm Sn layer at a depth of about 2 nm in SiO_2 thin film. This has been used to fabricate a single electron device for operation at high temperature (as a diode). Mukherjee et al.[79] have synthesised PbS particles of average diameters ranging from 9.9 to 18 nm within a polyacrylamide matrix. The percolative chains of PbS particles exhibit intrinsic semiconducting behaviour at temperatures above 340K. The estimated band gap for these particles are found to be much higher than that of bulk PbS being in the range 1.03 to 1.49 eV. The low temperature conductivity of these composites appears to be controlled by an electron tunneling mechanism.
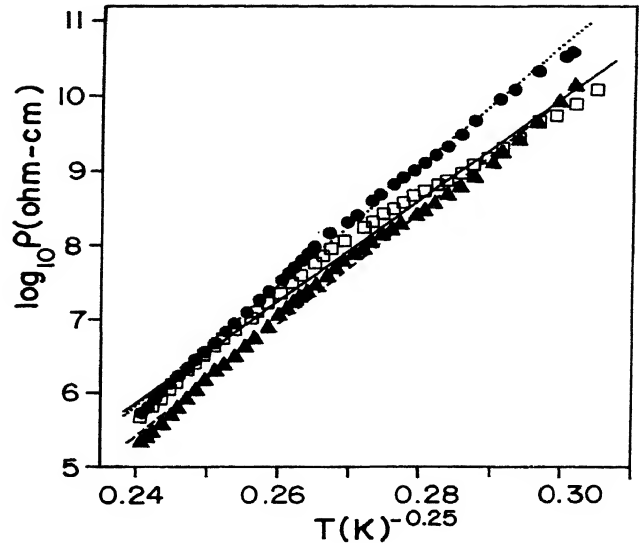

Fig. 18 Variation of logarithm of dc resistivity as a function of $T^{1/4}$ (T being the temperature in K) for different samples. Samples □ A, ● B and ▲ C Theoretical: — Samples A, ...B, and ----C[76]

So far, dielectric properties, a.c. and d.c. electrical transport properties, thermoelectric power have been discussed in terms of intrinsic carrier in the bulk single crystal, grain boundary potential and electron passage through it, defect dipole polarisation in grain boundary in addition to bulk polarisation, single electron tunneling due to localised electronic states, variable range hopping mechanism etc. There was no direct evidence for the potential barrier width and height in the grain boundary to explain either the linear or the non-linear properties. Johnson and Dravid have published their work on Nb doped $SrTiO_3$ bicrystal observing both static and dynamic attributes of the internal potentials. Nb doped $SrTiO_3$ is of interest because of the nonlinear grain boundary electrical behaviour of the bicrystals. Direct current electrical measurements on both single crystals and bicrystals reveal a much higher resistance due to the grain boundary. Bicrystal also show varistor behaviour, defined as a rapid decrease in the grain boundary resistance above a threshold voltage, towards the single crystal resistance. This non-linear behaviour is attributed to the breakdown of the internal grain boundary potentials. This breakdown potential has been found to be approximately 30 kV/cm in ZnO based varistor

by Viswanath *et al.*[81] with a non-linear exponent η around 50. The breakdown voltage per boundary has been estimated to be 0.06 V whereas the value reported in the literature for micron sized specimen is 2.6 V. Johnson and Dravid[80] have used electron holograpy to investigate the potential per boundary in Nb doped SrTiO$_3$ bicrystal. Electron holography is a field emission transmission electron microscope technique that records the electron wave function phase difference between coherent beam electrons and exit electrons that are perturbed by the specimen. A confined internal potential such as along a charged GB is detected as a difference in the electron phase at the interface compared to the shift resulting from perturbations by the grain interior. The magnitude, sign and width of this phase shift profile directly correspond to the magnitude, sign and width of the internal field. The voltage versus current curves of the Nb doped SrTiO$_3$ bicrystal, single crystal and TEM ready bicrystal are shown in Fig. 19(a) and 19(b). Electron holography on a static grain boundary revealed a positive phase shift peak centered on the GB plane corresponding to an internal potential of about 0.45V.

In accord with barrier breakdown, *in situ* applied current of 1mA resulted in a levelling of this phase shift peak. Thus the electron holography presents a direct real space evidence for breakdown of an internal grain boundary barrier. This will be useful in investigating the grain boundary controlled electroceramic varistor behaviour.

In summary, in this review article, the electrical properties of various types of nanocrystals electronic ceramics, composites, metals and alloys studied by both impedance spectroscopy and direct current electrical resistivity have been discussed. The readers are advised to refer to the references for detailed descriptions.

Acknowledgement

Fig. 19 (a) The dc electrical measurements compare the behaviour of Nb doped SrTiO$_3$, bicrystal (●), single crystal (■), and TEM ready bicrystal (O) samples. The dotted line indicates a linear fit to the single crystal data. The current density values only apply to the bulk samples. (b) After reconstructing the hologram a phase shift peak is detected for the static grain boundary (i) but with applied current the peak is absent (ii) indicating barrier breakdown[80]

References

1 H Gleiter *Prog Mater Sci* **33** (1989) 223

2 N Ichinose, Y Ozaki and S Kashy *Superfine Particle Technology* Springer-Verlag Limited (1992)

3 C Suryanarayanan *Bull of Mater Sci* **17** (1994) 307

4 R W Siegel *Sci Am* **74** (Dec 1996)

5 M J Mayo *Int Mater Rev* **41** (1996) 85

6 R Birringer *Mater Sci Engg* A**117**(1989) 33

7 R N Viswanath, S Ramasamy, K Shanmugam and R Ramamoorthy *J Mat Sci Lett* **14** (1995) 841

8 S Schlag and H F Eiche *Solid State Commn* **91** (1994) 883

9 S Chattopadhyay, P Ayyub, V R Palkar and M Multani *Phys Rev* B**52** (1995) 13177

10 R Ramamoorthy, S Ramasamy and D Sundararaman *J Mater Res* **14** (1999) 90

11 Y Maehara and T G Langdon *J Mater Sci* **25** (1990) 2275

12 H K Schmid *J Am Ceram Soc* **70** (1987) 367

13 A Dwivedi and A N Cormack *Phil Mag* **A61** (1990) 1

14 E Olsson and G L Dunlop *J Appl Phys* **66** (1989) 4317

15 L M Levison and H R Philip *J Appl Phys* **50** (1979) 2799

16 L M Levison and H R Philip *Ceramic Bull* **65** (1986) 639

17 R N Viswanath and S Ramasamy *Nanostructured Materials* **6** (1995) 993

18 R W Siegel, S Ramasamy, H Hahn, L Zongquan, L Ting and R Gronsky *J Mater Res* **3** (1988) 1367

19 H Hahn, J Logas and R S Averback *J Mater Res* **5** (1990) 609

20 J A S Ikeda and Y M Chiang *J Am Ceram Soc* **76** (1993) 2437

21 Andreas Tschope, Jackie Y Ying and Harry L Tuller *Sensors Actuators* **B31** (1996) 111

22 A Q Jiang, G H Li and L D Zhang *J Appl Phys* **83** (1998) 4878

23 C Elissalde, F Weillad and J Ravez *Mater Sci Engg* **B25** (1994) 85

24 B Roy and D Chakravorty *J Mater Res* **8** (1993) 1206

25 S Banerjee and D Chakravorty *J Appl Phys* **84** (1998) 799

26 A B Pakhomov, S K Wong, X Yan and X X Zhang *Phys Rev* **B58** (1998) 13375

27 L A Bursill, Peng Julin, Qian Hua and Nava Setter *Physica* **B205** (1995) 305

28 R N Viswanath and S Ramasamy *Nanostructured Materials* **8** (1997) 155

29 K Uchino, E Sadanaga and T Hirose *J Am Ceram Soc* **72** (1989) 155

30 W R Buessem, L E Cross and A K Goswami *J Am Ceram Soc* **49** (1966) 33

31 T Kanata, T Yoshikana and K Kubota *Solid State Commun* **62** (1987) 765

32 H T Martirena and J C Burfoot *J Phys* **C7** (1974) 3182

33 M Anliker, H R Brugger and W Kanzig *Helv Phys Acta* **27** (1954) 99

34 R N Viswanath and S Ramasamy *J Phys Chem of Solids* (*communicated*)

35 Siddhartha Bhowmik, Kristen P, Constant John, C Parker and M Ali *Mater Sci Engg* **A204** (1995) 258

36 P Knauth and H L Tuller *J Appl Phys* **85** (1999) 897

37 N M Beekmans and L Heyne *Electrochin Acta* **21** (1976) 303

38 Shusheng Jiang, Walter A Schulze, Vasantha R, W Amarakoon and Gregory C Stangle *J Mater Res* **12** (1997) 2374

39 D Huang, K R Venkatachari and S P Ostrander *J Mater Res* **10** (1995) 756

40 H Liu, L Feng, X Zhang and Q Xue *J Phys Chem* **99** (1995) 332

41 R Ramamoorthy, D Sundararaman and S Ramasamy *Solid State Ionics* **123** (1999) 271

42 N Yasuda, H Inagaki and S Imamura *Jpn J Appl Phys* **31** (1992) 574

43 B Roy and D Chakravorty *J Mater Res* **8** (1993) 1206

44 L P Gorkov and G M Eliasberg *Sov Phys JETP* **21** (1965) 21

45 K Yamamoto and H Namikawa Jpn *J Appl Phys* **28** (1989) 2523

46 T K Kundu and D Chakravorty *Appl Phys Lett* **67** (1995) 2732

47 P B Macedo, C T Moynihan and R Bose *Phys Chem Glasses* **13** (1972) 171

48 F Brouers, A Granovsky, A Sarychev and A Kalitsov *Physica* **A241** (1997) 284

49 T Fujita, K Ohshima and N Wada *J Phys Soc Japan* **27** (1969) 1459

50 T Fujita, K Ohshima and K Kurroishi *J Phys Soc Japan* **40** (1976) 90

51 F J Blatt *Physics of Electronic Conduction in Solids* Mc Graw Hill New York

52 I Bakonyi, E Toth, Kadar T, Tarnoczi L, K Varga, A Cziraki, I Gerocs and B Fogarassy *Nanostructured Materials* **3** (1993) 155

53 M J Aus, B Szpunar, U Erb, A M El-Sherik, G Palumbo and K·T Aust *J Appl Phys* **75** (1994) 3632

54 K Pekala and M Pekala *Nanostructured Materials* **6** (1995) 819

55 A F Mayadas and M Shatzkes *Phys Rev* **B1** (1970) 1382

56 G S Grest and S R Nagel *Phys Rev* **B19** (1979) 3571

57 N F Mott Can *J Phys* **34** (1956) 1356

58 N F Mott *Phil Mag* **6** (1961) 287

59 H M Sauer *Nanostructured Materials* **6** (1995) 759

60 N Karpe, G Lapogian, J Bottiger and J P Krog *Phil Mag* **B71** (1995) 445

61 J A Eastman, M Rr Fitzsimmons and L J Thompson *Phil Mag* **B66** (1992) 667

62 Y K Huang, A A Menovsky and F R De Boer *Nanostructured Materials* **3** (1993) 505

63 R Birringer, C E Krill and M Klingel *Phil Mag* **72** (1995) 71

64 A Seeger and G Schottky *Acta Metall* **7** (1959) 495

65 G Reiss, J Vancea and H Hoffmann *Phys Rev Lett* **56** (1986) 2100

66 R K Islamgaliev, K Pekala, M Pekala and R Z Valiev *Phys Stat Sol(a)* **162** (1997) 559

67 K Pekala, P Jaskiewiez, M Pekala and T Kulik *Mater Sci Forum* **179-181** (1995) 609

68 P Allia, M Baricco, E Bonetti, L Del Bianco, P Tiberto, G Valldre and F Vinai *Nanostructured Materials* **3** (1993) 433

69 X D Liu, B Z Ding, Z Q Hu, K Lu and Y Z Wang *Physica* **B192** (1993) 345

70 K Pekala, P Jaskiewiecz, J Latuch and A Kokoszkiewicz *Mater Sci Forum* **235-238** (1997) 439

71 Juh Tzeng Lue, Wen Chu Huang and Shav Kwen Ma *Phys Rev* **B51** (1995) 14570

72 B Roy and D Chakravorty *J Phys Condens Matter* **2** (1990) 9323

73 J M Ziman *Eletrons and Phonons* Clarendon Oxford (1960) 364

74 S Roy, A Chatterjee and D Chakravorty *J Mater Res* **8** (1993) 689

75 D Chakravorty, A K Bandyopadhyay and V K Nagesh *J Phys D Appl Phys* **10** (1977) 2077

76 S Banerjee and D Chakravorty *J Appl Phys* **84** (1998) 1149

77 P Sheng *Nanophase Materials* (Eds. G C Hadjipanayis and R W Siegel) Kluwer Netherlands (1994) 381

78 Anri Nakajima, Toshino Futatsugi, Hiroshi Nakao, Tatsuya Usuki, Naoto Horiguchi and Naoki Yokoyama *J Appl Phys* **84** (1998) 1316

79 M Mukherjee, A Datta and D Chakravorty *Appl Phys Lett* **64** (1994) 1159

80 Kevin D Johnson and Vinayak P Dravid *Appl Phys Lett* **74** (1999) 621

81 R N Viswanath, S Ramasamy, R Ramamoorthy, P Jayavel and T Nagarajan *Nanostructured Materials* **6** (1995) 993

NANOSTRUCTURE SEMICONDUCTORS: PHYSICS AND APPLICATIONS

S N SAHU* AND K K NANDA

Institute of Physics, Bhubaneswar-751 005 (India)

Semiconductor nanostructures with size in few nanometer range and comparable to Bohr exciton radius show quantum size effect (QSE). The consequence of QSE leads to discretisation of energy bands and results in widening of the band gap. Large surface to volume ratio and QSE in nanostructure semiconductors give rise to some of the unique semiconducting properties that are not normally found with bulk semiconductors.

The present review first describes some preparatory techniques to synthesize nanostructure semiconductors in particulate and thin film form. Composition, surface roughness, thickness, Structure, crystalline size, shape and thermodynamic properties often influencing the nanostructure properties are discussed with theoretical back ground and experimental results. Optical absorption, photoluminescence and Raman measurements demonstrate QSE, trap effect and size dependent properties. Finally, electrical, interfacial/device properties, stabilty and device applications of nanostructure semiconductors have been discussed.

1 Introduction

Nanometer range semiconducting materials have been a subject of intense study for last several years due to their size dependent physical and chemical properties[1-4] below a critical size characteristic of the material. Blue-shift in the optical absorption spectrum, size dependent luminescence, enhanced oscillator strength, nonlinear optical effects are some examples of the interesting properties exhibited by these nanocrystals. All these properties are various menifestations of the so called size quantization effect which arises due to the increasing quantum confinement of the electrons and holes with diminishing size of the crystallites and the consequent changes in the electronic structures. Their electronic structure is between that of a molecule and a bulk responsible to give rise to profound modification of the physical properties. Nanoparticles have been suggested for various potential applications in electronics where quantum confinement effects may be of advantage. For example, quantum confinement effects in nanostructured semiconductors results in widening the band gap of semiconductor and act as an efficient light emitter.

Recent reports suggest that nanoparticles can be used to produce light of various colours by band gap tuning using particle size effects[5]. As the life times of electrons in the excited states is large[6], efforts are being made to use in laser application. It has also got technological importance in the field of solar cells[7], catalysis[8], light emitting[9,10], resonant tunneling devices[11], lasers[12], gas sensors[13] and ultra violet sensors[14] etc. Experimental evidence for quantum size effects in all three dimensions was obtained by Ekimov and Onushchenko[15, 16] for microcrystallites of CuCl and CdS dispersed in a silicate glass. A blue shift in the absorption threshold and excitonic confinement effect resulted in theoretical development in these area by Efros and Efros[17] Consequently a large experimental activities spurted up to confirm quantum confinement effect using size controlled nanocrystalline semiconductors. A typical case of size quantisation effect is shown in Fig. 1 for CdSe[18]. Shift of absorption threshold to shorter wavelength is seen with decreasing crystalline size suggest the individual confinement of electron and hole for smaller crystallites whereas excitonic confinement is associated with larger crystallites (120A°). Based on the devlopment of both theory and well planned experiments, further
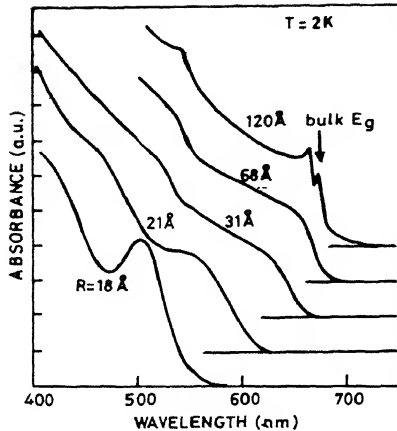
Fig. 1 Optical Absorption Spectra of CdSe with various radii at 2K. The arrow indicates the bulk CdSe

studies on structure, shape, luminescence, Raman, electrical, interfacial and device properties have been carried out. The durability of nanocrystalline semiconductors have been studied. The present review discusses some physics aspects of nanocrystalline semiconductors and their device applications.

The present review is divided into eight sections. Sections 1 to 3 give introduction, theoretical background and synthesis of semiconductor nanocrystals. Surface roughness, composition, impurity, fractals, structure, size and shape, thermodynamics and melting of semiconductor nanoparticles are discussed in Section 4. Section 5 describe the optical properties and provide some detailed information about optical absorption, spectral response, electrical, interfacial properties and photoluminescence excitation of nanostructured semiconductors. Stability, device physics and application of semiconductor nanostructures are discussed in Sections 6 to 8.

2 Theoretical Background

Depending upon the dimensionality of low-dimensional homogenous semiconductor one can consider three catagories of systems *viz*. the so called two dimensional (2D) system which include thin films, layer structures and quantum wells; the one dimensional (1D) system such as semiconductor wires; zero-dimensional system such as clusters, quantum dots and colloids.

The density ρ (E) of electronic states varies with energy as

$$\rho \ (E) \propto E^{d/2-1}, \ d = 1, 2, 3 \qquad ....(1)$$

where d is dimensionality. In case of three dimensional system, $\rho(E)$ is a smooth function of squre root of energy as shown in Fig. 2a[19]. In the case of $d=1$, and $d=2$, a number of descrete subbands apper due to quantum confinement effect and the density of states obeys eq. (1) within every subband. Due to the finite size of the nanocrystals, the continuous bands of the bulk crystal transforms into a series of discrete states resulting in widening of the effective band gap. Energy level diagram of the bulk and small clusters of semiconductors is shown in Fig. 2(b)[20]. The increase in the distance between valence states and excited levels is a consequence of quantum confinement. The energetic shifts of conduction and valence band states are not of equal magnitude as shown in the figure. Note that the surface traps have been descretized along with the valence band and conduction band for nano-clusters. As a result of the confinement of both electrons and holes, electrons in the conduction band and holes in the valence band are confined spatially and the lowest energy of optical transition from the valence band to conduction band increases resulting in an increase of effective band gap. Within a simple effective-mass approximation, the confined gap is given by[21];

$$E_{\text{confined gap}} = E_{\text{bulk gap}} + \frac{\hbar^2 \pi^2}{2} \left(\frac{1}{w_x^2} + \frac{1}{w_y^2} + \frac{1}{w_z^2} \right) \left(\frac{1}{m_c^*} + \frac{1}{m_v^*} \right) \quad ... (2)$$

where m_c^* and m_v^* are conduction and valence band effective masses, respectively. The other parameters w_x, w_y, w_z are the dimensions of a three-dimensional (3D) box. If $w_x << w_y$, and w_z, then the energy levels will mainly depend upon w_x, i.e. the size estimated from the blue shift corresponds to the lowest dimension of nanoparticle. In this case, the carriers are confined in one-dimension only. If $w_x \sim w_y << w_z$, then the confinement is two-dimensional and if $w_x \sim w_y \sim w_z$, the nano crystals are confined in all three dimensions.

Why Semiconducting Nanomaterial is Interesting?

In any material, substantial variation of fundamental, electrical and optical properties with size is observed when the diameter of the nanocrystals is comparable to or smaller than the diameter of the bulk exciton[11] such that the energy level spacing exceeds the thermal energy, kT. For a given temperature, this occurs at a very large

size in semiconductors, as compared to metals, insulators and van der Waals or molecular crystals. In the case of van der Waals or molecular crystals, the nearest-neighbour interactions are weak and the bands in the solid are very narrow and as a consequence not much size dependent optical and electrical properties are expected or observed in the nanocrystal regime. However, in case of metals, the edges of the band develops first and the centre develops last upon decreasing size. Further, the Fermi level lies in the centre of a band and the relevent energy level spacing is still very small and at temperatures above a few kelvin, the electrical and optical properties more closely resemble those of a continuum, even in relatively small sizes. In semiconductors, however, the Fermi level lies in between two bands, so that the edges of the bands dominate the optical and electrical behaviour. Thus, it is interesting to study the semiconductor nanocrystals.

Depending upon the crystalline size and shape of a semiconductor nanocrystals, different type of confinements can be realised. When the radius of the crystallite R is smaller than ~2 exciton Bohr radii, electrons and holes are considered as two confined particles, bound by an enforced Coulomb interaction and when the crystallite radius is larger than ~4 exciton radii, the ground exciton is treated as a rigid sphere, confined as a quasiparticle. In between these two limiting cases both the electron and hole confinement and their Coulomb interaction are considered. Bohr radius (a_B) of exciton is given as

$$a_B = \frac{\hbar^2 \epsilon}{e^2} \left[\frac{1}{m_e^*} + \frac{1}{m_h^*} \right] \quad \text{.........................(3)}$$

where ϵ is the dielectric constant of semiconductor material and m_e^*, m_h^* are the effective electron and hole masses respectively. Bohr exciton radius of different semiconductors, the bulk and effective band gap values are given in Table I.

3 Synthesis of Nanostructure Semiconductors

As discussed earlier, substantial variation in electrical and optical properties can be realized when the crystalline size is comparable to Bohr exciton radius. For most of these semicondcutors, Bohr exciton radius is less than 10-15 nm excepting few narrow gap semiconductors. Further, presence of a small amount of impurity causes dramatic changes in different properties of semiconductors.

Table I

Band gaps for different bulk and nanocrystalline semiconductors

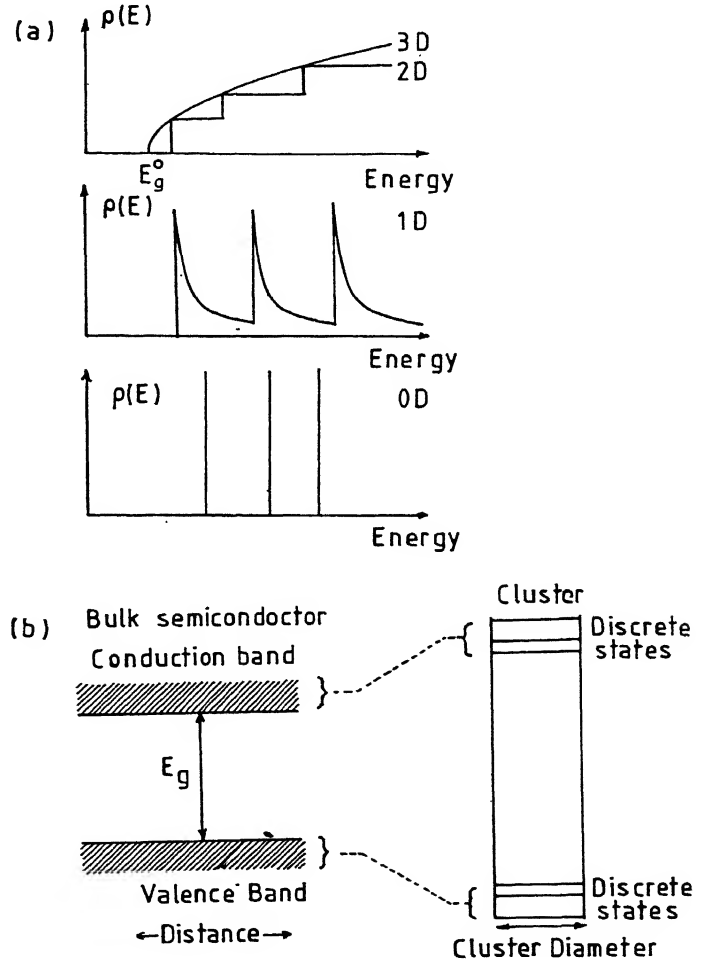| Material	Bohr radius a_B in ^{o}A	Bulk Band gap E_g in eV	band gap $E_{n,g}$ in eV
ZnS	15	3.5	~5.2
CdS	30	2.4	5.52
PbS	200	0.4	5.2
CdSe	~30	1.7	2.4
ZnTe	~60	2.26	3.2
GaAs	91	1.4	3.89
Ge	–	0.66	1.47
InSb	573	0.24	3.84
InAs	340	0.418	1.4

Fig. 2(a) Idealized density of states, ρ (E) of electrons for various dimensionalities. In the 3D case the energy levels are continuous, while in the "0D" case the levels are discrete; (b) Energy levels near the band gap for bulk and small clusters of semiconductors. The increase in the distance between valence states and excited levels is a consequence of quantum confinement

Thus, it is of great challenge to synthesise particles of nanometer dimension with narrow size distribution and without any impurity. Different ways to synthesize nanoparticles are chemical deposition[22-39], sol-gel[40], gas evaporation[41-43], electrostatic deposition[44,45], magentron sputtering[46,47] and electrochemical deposition[48,49] etc. Chemical bath deposition technique is relatively less expensive and convenient to prepare large area semiconductor thin films at moderate temperature. Materials can easily be prepared in the colloidal form which can subsequently be precipitated to give dry and stable powders or can be deposited in the thin film form onto different substrates. The growth process involves a controllable chemical reaction which proceeds at a low rate in an aqueous solution containing various reactants. The reaction rate in this technique is controlled by adjusting pH, solution temperature, and the relative concentrations of various reactants in the solution. However, a non-uniform surface is often obtained in chemical bath deposition process.

For the samples prepared by the chemical route, it is expected to have the size distribution which ultimately will influence the experimental results. For example, each spectrum obtained for optical absorption and photoluminescence is a summation of the spectrum of individual crystallite. So, the optical absorption and photoluminescence spectra observed for chemically prepared nanocrystallites samples do not show any sharp feature originating from individual crystallite but show wide terraces. Thus, it is most essential to restrict the size distribution in nanocrystalline samples. In order to arrest the agglomeration of the nanocrystallites, the crystallites are generally capped with polymers[22-30,44,45] such as thiophenol, mercaptoethanol, ethylene glycol etc. For example, the chemical synthesis of binary semiconductors can be carried out by mixing two salts each having one component. However, before mixing two salts to obtain the desired semiconductor, the organic capping agent is added to either of the salts that control the size of the nanoparticles. Electrodeposition also offer a novel way of synthesizing nanocrystalline semiconductors. The electrolysis parameters that controls the size of the particles are pH, current density, temperature and deposition time. The advantages of the electrodeposition technique over chemical bath

deposition is that it is possible to grow uniform films of nanocrystallites over large area conducting substrates. However, electrodeposition technique is not free from drawbacks[49]. Binary semiconductors having more and less noble components are difficult to be deposited simulteneously beacuse of large difference in their deposition potentials[50]. Hence, judicious choice has to be made to adjust the ionconcentration and electrolysis current density. Often an excess of noble component is deposited as is the case of Se in CdSe[51]. Hence stoichiometry and narrow size distribution[51] is difficult to maintain.

Most of the reports deal with the synthesis of binary semiconductors by chemical route. There are a few literatures available where nanocrystallites are prepared by evaporation method. There are two different evaporation processes for the deposition of the binary semiconductors. In one case, the same material is taken as the source and is evaporated by thermal heating[41], by magnetron sputtering[46, 47] or by electron gun[52]. For example CdS is taken for deposition of CdS[41] nanocrystallites and PbS[52] is taken for PbS nanocrystallites. The deposition rate, inert gas, pressure in the chamber controls the size of the nanocrystals. In the second method, the nanocrystals are synthesized by the co-evaporation of different constituents and then subsequnetly heated to obtain the semiconductors by chemical reaction. Different sized nanocrystals are obtained by annealing the deposit several times at different temperatures. However, vacuum deposited nanocrystalline semiconductors are often expected to show non-stoichiometry and size distribution. Nevertheless, a uniform deposit is obtained in vacuum deposition technique.

In order to have very narrow size distribution, besides polymer capping[28, 36], attempts have also been made to grow nanocrystalline semiconductors in Langmuir-blodget films[33,53], protien mono layers[54], and reverse Micelle[55] etc. Such nano crystals are mostly used for fundamental property studies.

Attempts have been made to synthesize elemental nano-crystalline semiconductors $viz.$ Si and Ge using various techniques. Nano-Si has been prepared by first depositing amorphous[55] Si on Si substrate and followed by an annealing treatment. Most of the cases nano-Si is prepared in an oxide matrix such as SiO_2 where the first precurser deposition is SiO_x:H or SiH species[56-58]. Annealing

treatment resulted in nano-Si in oxide matrix. This technique in particular is useful to avoid coagulation and size distribution in general is avoided. However, the best results were obtained with Si[59] and Ge[60-63] nanocrystalline films which are prepared by a novel cluster deposition technique. Excellent photoluminscence properties have been observed from these nanocrystals. In particular Ge[61-63] for the first time has been shown to exist in tetragonal phase contrary to the bulk diamond structure. Ge nanocrystals also show visible blue luminescence[61] under UV irradiation.

Cluster assembled nano-materials are in general produced by condensation of atom vapours generated by laser ablation or heating source followed by a supersonic expansion through a cooled nozzle. The metal clusters are carried away into the deposition chamber by an innert carrier gas Ar or He acting as nucleation centres. The free clusters then deposited onto different substrates. Cluster size is controlled by adjusting pressure of inert gas and nozzle diameter. The number of atoms in the cluster is studied by time of flight spectrometer.

4 Physical Properties

Physical properties such as structure, phase, thickness, composition, surface roughness, crystalline shape and size are known to influence the nanocrystalline semiconductor properties. The observation of quantum confinement effect, interfacial as well as device properties basically depend upon the above parameters. For example, off-stoichiometry and unterminated surface greatly· change the nanocrystalline properties and often the results are misleading.

4.1 Impurity Identification and Composition

As there are small number of atoms present in a cluster or nanostructure, the presence of impurity of foreign element or off-stoichiometry leading to structural defects causes dramatic changes in electrical and optical properties. For example impurities and off-stoichiometry in nanostructure semiconductors generate localized electronic energy levels within the forbidden gap. Due to quantum confinement effect these states are also quantized and form a continuum of localised states near the band edges and ultimately influence the optical properties. The localised states also participate in conduction mechanism of carriers and influence the electrical properties. Most commonly used tool to identify and estimate the impurity or composition are : particle induced X-ray emission (PIXE), energy dispersive analysis of X-rays (EDAX), Rutherford back scattering spectrometry (RBS), secondary ion mass spectrometry (SIMS), Auger electron spectroscopy (AES) and X-ray photoelectron spectroscopy (XPS). However, very popular technique to identify and estimate impurities at ppm level is PIXE where one would require to use an accelerator. Core shell ionization takes place when the sample is bombarded with highly energetic ions and X-ray is emitted from the element present in the material and are detected by a Si: Li detector. PIXE analysis has been carried for nanocrystalline CdS[31] and has identified no impurities even at ppm level. RBS is a non destructive technique which can measure relative atomic concentration, thickness of the sample as well as surface roughness. XPS, besides measuring the composition, also measures the core level shift. Quantum confinement effects can easily be studied by XPS where a valence band shift can be estimated.

4.2 Surface Roughness and Fractals

From the perspectives of application, surface roughness plays a major role in determinig optical scattering and absorption, electrical resistivity, thickness and photoluminscence properties. The interfacial properties are also influenced by the surface structure which often show deviation from ideal behaviour. Surface roughness in particular has pronounced effect in Raman scattering experiments which normally is expected to show size dependent feature. The surface phonon mode intensity is likely to increase with increasing surface roughness[64].

Hence, in the competing mechanism, one would expect for the Raman yield, is in between the surface roughness contribution and the contribution due to the excitation energy. It is known that the roughness depend upon the thickness of the film. As the thickness of a film increases the roughness increases irrespective of the sample preparation procedure[65-67]. Further, the measurement with different scanning length indicates that with increasing scanning length, the roughness increases and exhibits scaling behaviour over large variation of length scales. Normally a thin film surface is characterised by Atomic Force Microscopy (AFM), Scanning Electron Microscopy (SEM), Scanning Tunneling Microscopy (STM), Rutherford

Backscattering Spectrometry (RBS) and Ellipsometry etc. AFM picture for nano-crystalline CdS thin film of 35 nm thickness having crystalline size 11 nm is shown in Fig. 3[68]. The rms roughness is 8.95 nm which increases as the thickness is increased. The rms roughness for 50 nm thick film is 10.39 nm. Such surface roughness is resulted due to the chemi-adsorption[31] of colloidal CdS prepared by a chemical route. With increasing thickness of the film the crystalline size also increases which ultimately increases

the surface roughness. Besides the above, if AFM scan area is increased, one would also see an increased surface roughness value.

Rutherford Backscattering Spectrometry (RBS) is an alternative technique to AFM which can measure the surface roughness along with the composition and thickness of the sample. Fig. 4(a) shows the rough surface of a sample where the thickness is different at different regions[68]. E' and E'' are the incident energies corresponding to the atoms at distances t_{min} and t_{max} from the surface of the sample. It can be inferred that up to a distance t_{min}, atoms are uniformly distributed beyond which the density of the atoms decreases and becomes zero at a distance t_{max}. The RBS yield which depend on the density of the atoms starts decreasing from t_{min} and becomes zero at t_{max}. Because of this, a tail is expected in the low energy side of the RBS spectrum as shown in the Fig. 4 (S1) for CdS bulk sample. The tailing towards lower energy/ channel number will be less for low thickness samples as shown in Fig. 4 (S3 and S4). The CdS sample thickness for S1, S3, S4 are 1450nm, 50nm and 35nm respectively. From the tailing, the roughness of the sample can be estimated by adopting the following procedure. Corresponding to any energy between

Fig. 3 Surface topology, measured by AFM for CdS semiconductor sample having crystalline size as 12 nm and thickness 35nm

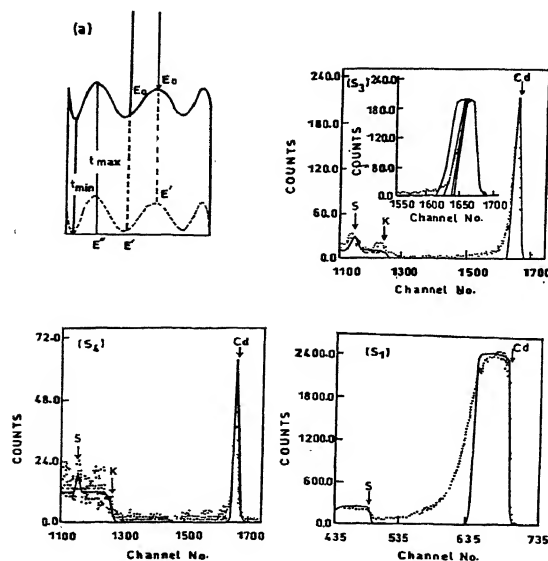

Fig. 4 Schematic diagram of a rough surface sample with incident ion beam energy E_0, E^I and E^{II} at different region. The RBS spectra of CdS samples S_4, S_3 and S_1 having thickness 35 nm, 50 nm and 1450 nm respectively. The He$^+$ ion beam energy for S_4 and S_3 is 3.04 M eV whereas for S_1, 5.06 M eV. Inset in S_3 is the theoretical fitting for different thicknesses

E' and E'' there is a thickness in between t_{min} and t_{max} i.e. each energy represents for one thickness. This gives the thickness of the sample at different places. Thus, the average thickness t_{av} and roughness, σ of the sample can be deduced using the relation

$$t_{av} = \frac{1}{N} \Sigma_{i=1}^{N} t_i \text{ and } \sigma = \sqrt{\frac{1}{N} \Sigma_{i=1}^{N} (t_{av} - t_i)^2} \qquad \cdots \quad (4)$$

similar to that of AFM used to estimate the roughness of the sample. The data were fitted with the theoretical expressions for the yield and obtained reasonable fit Fig. 4 (s3) up-to certain energies that corresponds to t_{min} and t_{max} (yield is almost zero), respectively. In this way a series of thickness values are obtained for sample S3 and the average thickness as well as the roughnesses have been estimated. The roughness for sample S4 is found to be 11 nm, whereas, it is 18.4 nm in case of sample S3, which are certainly higher as expected. These data were compared to that obtained from AFM measurement[68] and found to be comparable. However for thicker sample (Fig. 4 (s1)) RBS can not be employed to estimate the surface roughness as it is limited by struggling[69]. Hence, the surface roughness estimated for sample s1 by AFM and RBS are not comparable.

An unique feature of branched fractal surface morphology in nanocrystalline CdSe, PbS and CdS thin films prepared by electrodeposition[69] and chemical deposition[69] techniques were observed under optical microscope. Such fractal features are observable in samples whose thicknesses range is in between 30 to 50nms. Under optical microscope, the fractals appear to be diffusion limited aggregated (DLA) but when zoomed to higher magnification, they found to consist of several crystallites and this do not qualify to be called as DLA pattern. Quantum size effects were observed for these nanocrystalline films whose thicknesses were in the range 30 to 50nms and exhibit branched fractals. Shown in Fig. 5[69] is the optical micrographs of nanocrystalline semiconductor thin films, PbS (Fig. 5a) and CdSe (Fig. 5c) whereas Figs. 5 (b and d) are the optical micrographs of bulk PbS and CdSe respectively. Note that the fractal features disappear for bulk PbS and CdSe samples. Further, the surface coverage of fractal pattern is relatively more for CdSe (Fig. 5c) compared to PbS (Fig. 5a) which can be attributed to the high mobility of Cd^{2+} ion as compared to Pb^+ ion in the electrolytic process.
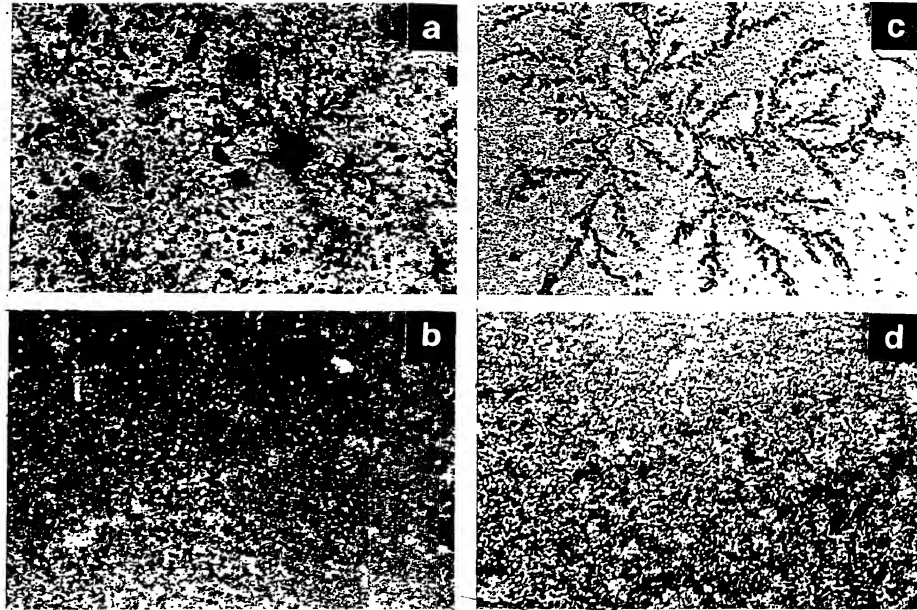

Fig. 5 Optical micrograph (X 1000) of PbS (a and b) and CdSe (c and d) showing branched fractal patterns for (a) and (c) and non-uniform surface for (a) and (d)

4.3 Structure, Size and Shape of Nanocrystals
Structure

The structure and phase of the nano-crystals are in general determined by X-Ray Diffraction (XRD) and transmission electron microscopic studies. The structure of the nanocrystals depend on the sample preparation procedure, lattice strain and pressure. For example, chemically prepared CdS at high temperature (363K) gives a hexagonal phase whereas that prepared at 300K show a cubic phase. Further, the XRD peak intensity and width decreases with decreasing crystalline size. The peaks may shift to the high diffraction angle if there is lattice contraction caused by narrowing the crystalline size. Generally, the information regarding crystalline shape and size can be estimated from electron micrographs (TEM) or AFM images wheras the structural information can be obtained from XRD or from TEM diffraction studies. The shape of the crystallite is decided by the internal bonding geometry. Thus, for covalent crystals, such as Si and InP tetrahedral shape characteristic of the zinc blend and diamond interior bonding is favoured. For ionic semiconducters viz. CdS or CdSe[70], hexagonal shape is favoured. Hence, CdS crystallites prepared by a chemical route show exclusively a hexagonal phase contrary to the bulk zinc blende/wurzite structure. Nano-crystalline semiconductor shape and size can also be identified by optical absorption studies[71-73]. Shown in Fig. 6(a) is the powder XRD spectra of In As[74] nanocrystals. Note that with increasing crystalline size, the full width at half maximum (FWHM) decreases and the XRD peaks go sharper.
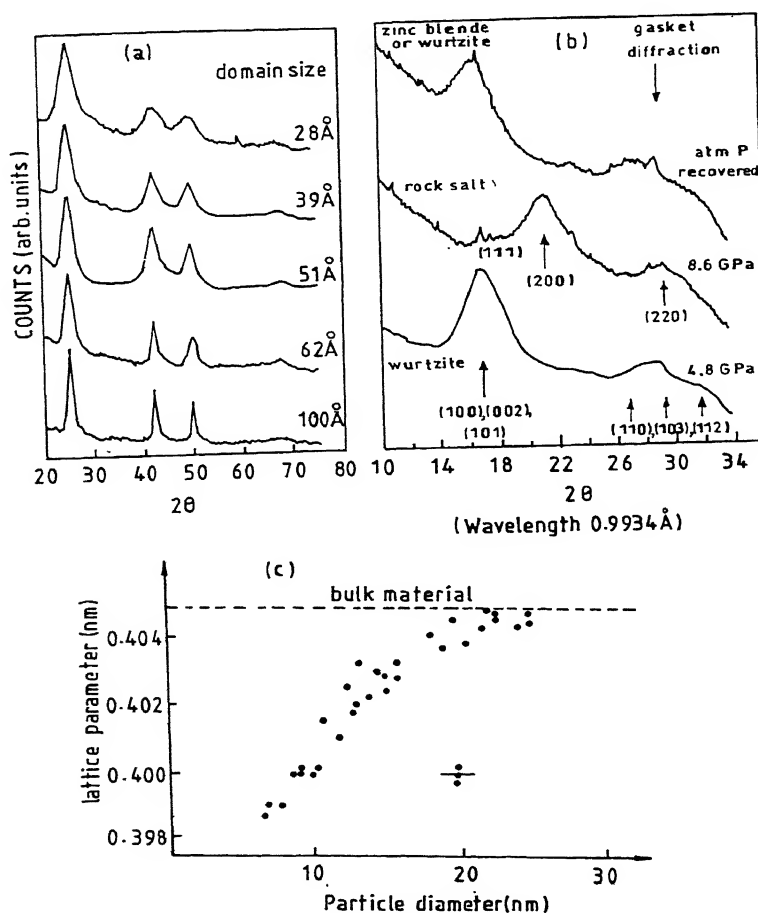
Fig. 6(a) Powder XRD spectra of In As nanocrystals of different crystalline size. XRD peak broadening occur with decreasing crystalline size; (b) High pressure XRD spectra of 1.9 nm CdSe nanocrystals showing untransformed wurtzite, transformed rocksolt and back to wurtzite or zincblende structure after release of the pressure. The arrow indicates diffraction from the metal gasket of the diamond cell. Multiple transitions does not show any change in domain size; (c) Dependence of measured lattice parameter on particle size

FWHM is the measure of crystalline size estimated using sherrer equation[28]. Structural phase transformation also does occur in semiconductor nanostructures like their bulk counterpart under pressure. However, the thermo-dynamics, and the kinetics of the transformation are significantlly different. In case of CdSe[75] nanocrystals the transition pressure varies from 3.6 to 4.9 GPa for the crystalline size ranging from 21 to 10A° in radius whereas for the bulk the pressure value is 2.0 GPa. Fig. 6(b) shows the high pressure XRD spectra of CdSe[75] nanostructure of size 1.9nm. The untransformed wurzite phase of CdSe (a direct band gap semiconductor) transformed to a rock salt phase (known to be an indirect band gap semiconductor) at high pressure but recovered to tetrahedral (wurzite or zincblende) phase when brought to atmospheric pressure. No significant X-ray line broadening observed even though CdSe nanocrystal goes through multiple transitions. Lattice parameter is another interesting feature to observe which decreases with decreasing crystalline size. This ultimately will influence the optical properties of nanocrystals. Lattice contraction leads to a shift of X-ray diffraction peaks to higher diffraction angles. Fig. 6(c) shows the variation of lattice parameter[76] as a function of particle diameter in the range 6 to 30nm. As shown in Fig. 6(c), below 6nm particle diameter, significant decrease in lattice parameter is found which amount to 1.5% for 6nm particle.

Classical Interpretation of Lattice Contraction

The lattice contraction associated with decreasing crystaline size can be understood by considering the crystallite as a liquid drop. The thermodynamical relation for a liquid drop in equilibrium is given by[76]

$$\Delta p dV = \gamma dF \qquad \text{... (5)}$$

where γdF is the surface energy (γ is the surface tension, dF is the surface area) and the $\Delta p dV$ is the work (Δp is the pressure inside the drop). For a sphere with particle diameter, d

$$\Delta p = 4 \gamma / d \qquad \text{... (6)}$$

If the small nuclei are crystalline with cubic structure and lattice constant a, then with the compressibility $K = \Delta V (\Delta p V_0)^{-1}$ and $V_0 = a^3$, from eq. (4) one obtains

$$\frac{\Delta a}{a} = \frac{4k \gamma}{3d} \qquad \text{... (7)}$$

It is evident from above equation that as the crystalline size decreases the change in the lattice

constant would be appreciable. In other words, as the pressure difference becomes more and then there is a decrease in the lattice constant. However, equation 7 gives only a qualitative prediction of lattice contraction as it does not consider the surface stress which is also a function of particle size.

4.4 Thermodynamic Properties, Melting of Semiconductor Nanostructures and Effect of Synthesis Temperature on Cluster Size

When a solid is heated, it melts and the melting temperature is normally considered as one of the most important characteristics of a material. Nanometer size crystals melt at much lower temperatures than extended ones. Reduced melting temperature has resulted beneficial effect in sintering which can be achieved at low temperature as compared to the bulk. This phenomena is being used to produce thin films, nanoelectronic devices and solar cells etc. It is well established that the change of melting temperature (T_m) with particle size is a surface initiated process[77,78] and decreases as the particle size decreases[79-87]. It has been shown by Castro et al.[82] that below 2.0 nm of size, the melting temperature does not decrease as the crystalline size decreases whereas for very small CdS particles 50% reduction in melting point is reported[70]. Recently, Schimdt et al.[88] have shown a variation of ±30 K in the melting temperature with sodium clusters containing 70 to 200 atoms. In order to understand the experimental data on size dependent lowering of T_m of small particles, some theoretical model based upon thermodynamic formulation[80-82,89-91] and molecular dynamic simulation[91-98] have been proposed and have predicted that the melting temperature, T_m decreases with particle size. As the particle size decreases, the surface tension plays an important role which would decrease the size of the small particle and thereby, lower the melting temperature. Shown in Fig. 7(a) is the melting temperature as a function of particle radius for CdS crystals. Note that 50% reduction in melting temperature is achieved for less than 20A° crystallite. Shown in Fig. 7(b) is the experimental data of Coombes[79] for Pb plotted as T_m versus inverse of the size of the particle. It can be noted from Fig. 7(b) that the plot is linear for particles of size larger than 14.0 nm (solid line) whereas, for particles of size less than 14.0 nm, the deviation from linearity have been observed which is ascribed to be due to nonspherical geometry of small particles.
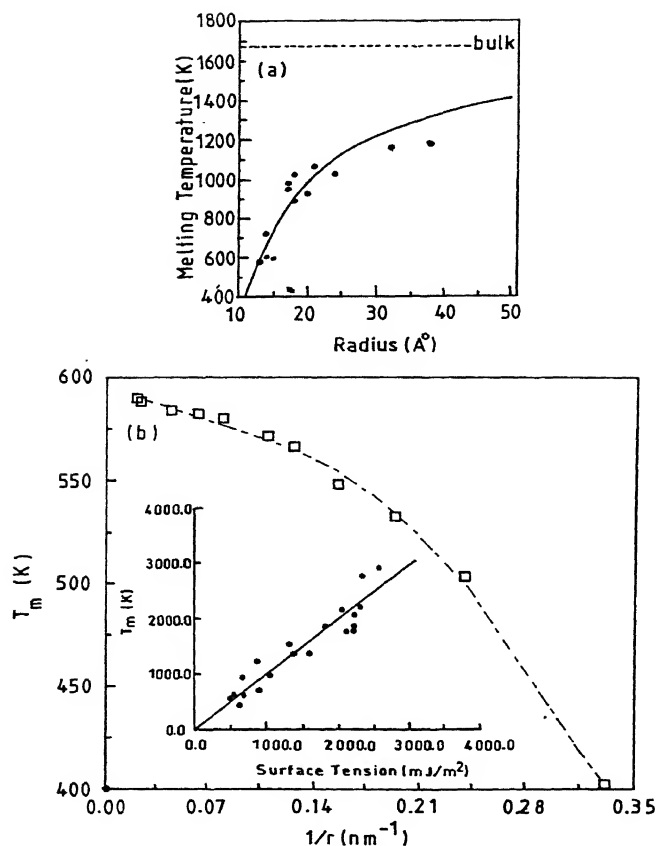
Fig. 7(a) Melting temperature of CdS as a function of crystalline radii; (b) Size dependent melting temperature of Pb particle
(C J Coombes *J Phys* F 2 (1972) 411) Inset shows melting temperature of large particles as a function of surface tension.
Different surface tension correspond to different elements

The effect of geometrical shape of nanocrystallites has also been studied experimentally by Kofman *et al*[84]. They have observed for an ellipsoid geometry of axes 2*a*, 2*b* and 2*c* (height) with 2*a* < 2*b* < 2*c* that as the temperature is increased, the particle starts melting and a decrease of axes 2*a* and 2*b* takes place, axis 2*c* remains constant. The continuous melting proceeds until 2*a* and 2*b* equals 2*c* and a spherical core is obtained. At that temperature an abrupt transition (first order) to a completely liquid state occurs. The melting temperature of Pb[84] as a function of the inverse of the size of the spherical core is shown in the inset of Fig. 7(b). Though the data points are scattered, it is fitted to a straight line and obtained a reasonable fit. A thermodynamical argument developed by them predicts that the diameter to height ratio increases as the crystalline size decreases. Similar cylindrical geometry with height less than the diameter of the particles have been reported for small as well as large size Pb particles[79]. For large size particles, the volume energy dominates and the melting temperature will be independent of the geometry. But, for nanoparticles the effect of surface is dominant resulting the decrease in the melting temperature. In contrast, Sheng *et al*.[86] have reported for Pb embedded in Al matrix that the melting temperature varies linearly with inverse of the size down to particle diameter 10 nm. The good agreement in this case implies a spherical geometry of the nanoparticles which is expected as the particles are synthesized by

ball milling. In this process small size particles are obtained from large size particles, whereas, reverse is the case with other techniques. Based on thermodynamic arguments and melting properties, cluster (consisting few atoms) size and deposition temperature can be considered.

If the incident cluster size is larger than the melting size (lowest size of the nanoparticle that does not melt at the deposition temperature) the cluster will be deposited as such. However, if the incident cluster size is smaller than the melting size, the clusters co-agulate to give rise a larger cluster. Once a larger cluster is formed, it solidifies and stops further coagulation. This implies that the deposition temperature should be as low as possible to obtain lower size cluster.

Applications

The ability to fuse nanoparticles at relatively modest temperature indicates that nanoparticles may provide a new low-temperature route to thin film growth. It can also be used as a soldering material which melts at low temperature.

5 Optical Properties

The most important properties of a semiconductor nanostructure is its optical behaviour to crystalline size. Optical properties may be absorption, spectral response, photoluminescence, photoluminescence excitation, electroluminescence, and Raman scattering whose optical properties respond to crystalline size. As the size is decreased, the electronic states are discretized and results in widening of the band gap and increases the oscillator strength. The radiative recombination life time of carrier is lowered from nanosecond to picosecond. These features known as quantum size effect (QSE) are observed in semiconductor nanocrystals. Hence one of the final product of QSE is the increased band gap. Depending upon the size of the crystallites, two types of confinement *viz.* weak and strong can be considered where the particle radius is few times larger or smaller than Bohr exciton radius[98, 99]. QSE were explored by many authors to look for individual bands smeared by in- homogenous broadening[100, 101]. Size dependent optical absorption specrta of different semiconducting nanomaterials belonging to the II-VI[55, 101-109], III-V[110-112], III-VI[113, 114], IV-VI[52, 115-117], II-V[118] group and some elemental semiconductors[63, 119, 120] have been reported in literature. Band gaps atleast three times that of the bulk have been reported for the nanocrystalline semiconductors.

5.1 Optical Absorption

Varieties of techniques have been used for the determination of the band gap (Eg) of a semiconductor. The best values of the band gap are obtained from optical absorption measurements which also envisages the size quantization effect (QSE). A blue shift in the optical absorption edge and series of maxima in the absorption spectra are observed as a consequences of QSE. For bulk samples, the band gap is estimated from the $(\alpha h\nu)^2$ vs $h\nu$ plot, where α is the absorption coefficient and $h\nu$ is the photon energy. But for nanocrystalline samples the band gap is determined from the absorption maxima. The other method to estimate the band gap is the spectral response of the semiconductor in which a device has to be fabricated. Excepting optical absorption other methods have limitations. There are two different models that are used to understand the variation of band gap with particle size: (i) effective mass approximation and (ii) hyperbolic band model. Electrons in the conduction band and holes in the valence band are confined spatially. As a result of the confinement of both electrons and holes, the lowest energy of optical transition from the valence band to the conduction band increases resulting in the increasing of effective band gap. According to the effective-mass approximation, the confined gap is given by[21]

$$\Delta E = \frac{\hbar^2 \pi^2}{2r^2} \left[\frac{1}{m_e^*} + \frac{1}{m_h^*} \right] - \frac{1.786 e^2}{\epsilon r}$$
$$- \frac{0.124 e^4}{\hbar^2 \epsilon^2} \left[\frac{1}{m_e^*} + \frac{1}{m_h^*} \right]^{-1} \quad \text{..............(8)}$$

where r is the cluster radius, m_e^* is the electron effective mass, m_h^* is the hole effective mass and ϵ is the dielectric constant.

A hyperbolic band model has recently been proposed to explain the change of energy gap as a function of particle radius and shown to be used to calculate the size dependent optical band gap of PbS clusters[28]. The equation derived for the change in band gap ΔE according to this model is given by

$$\Delta E = [E_g^2 + 2\hbar E_g \ (\pi/r)^2 \ / \ m^*]^{1/2} \quad \text{...(9)}$$

where E_g is the band gap for the bulk semiconductor, r is the particle radius, and m^* the effective mass of electron. Once, the band gap isknown, the corresponding particle size can easily be determined. In this context, it is worth pointing out that in most of the cases size determined from AFM/TEM or XRD does not.match with that obtained from the blue shift.

The discrepency in the size estimated from AFM/XRD/TEM and blue shift will be discussed in a latter section.

Optical Absorption and Pancake Structure of the Nanocrystallites

Fig. 8(a) shows the optical absorption spectra of CdS thin films of different crystalline size/thickness. Here, the sample was prepared from a chemical route[31] where the small crystallites dissolve to give the larger ones with increasing thickness/deposition time period[4]. Samples S_4, S_3 and S_1 have the crystalline sizes 11 nm, 15 nm, and 75 nm respectively corresponding to the thickness values 35 nm, 50 nm, 1450 nm respectively. The nanocrystalline film S_4 shows an absorption maximum at 395 nm which corresponds to the band gap of 3.14 eV. QSE is clearly refflected here. The peak at 395 nm is due to 1s-1s transition as suggested by Brus[121]. With increasing crystalline size, the peak structure slowly disappears and attains a normal interband transition spectrum for the bulk CdS (S1) having crystalline size 75 nm and band gap 2.4eV. Clearly a blue shift of 0.74eV has been achieved in this case. The tailing towards the longer wavelength without any sharp absorption suggests that the spectra are of powder CdS sample and has size distribution. From the blue shift, the crystalline sizes have been estimated and Fig. 8(b) shows the band gap as a function of size/thickness. Note that the band gap for CdS decreases with increasing crystalline size/thickness.
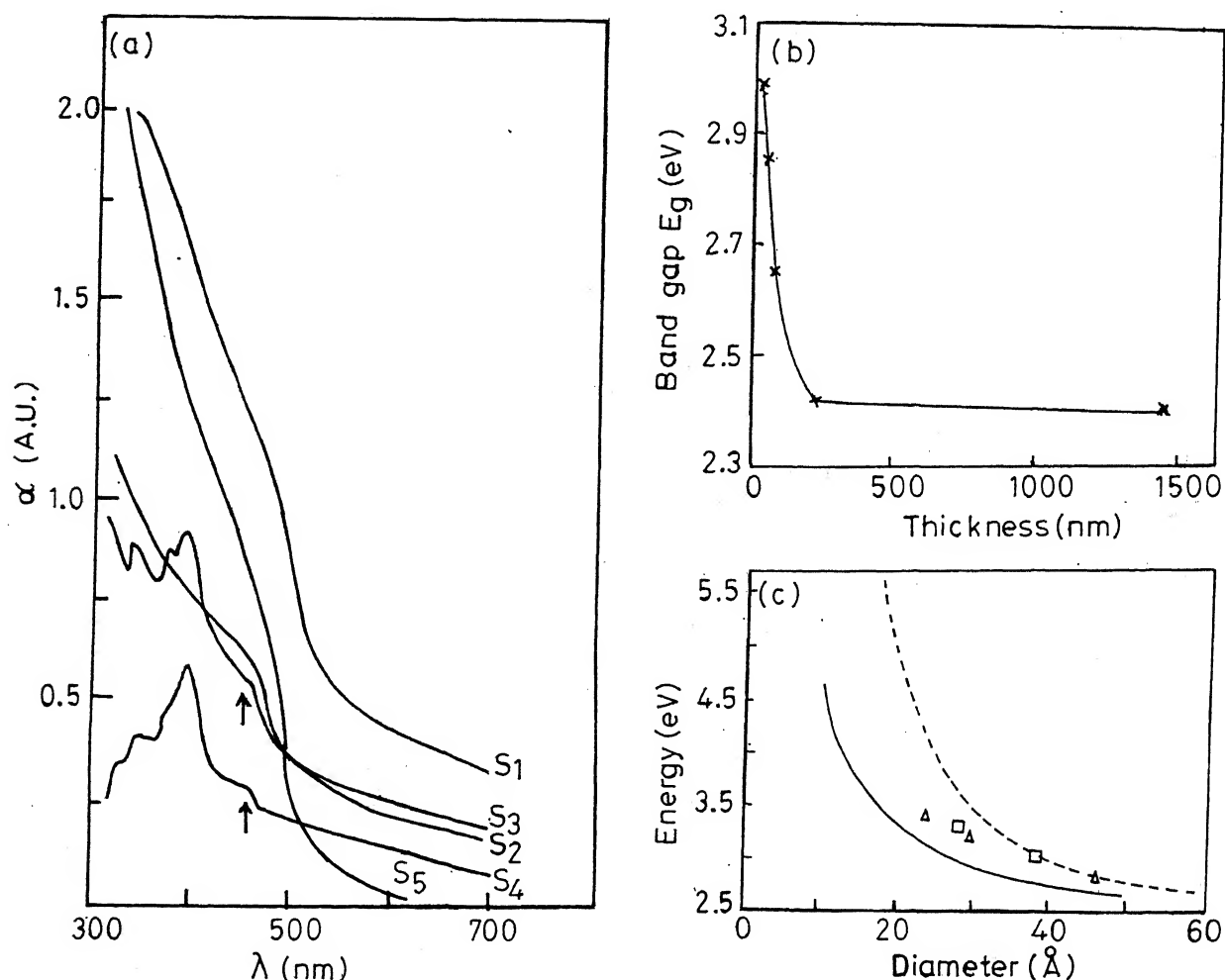
Fig. 8(a) Optical absorption spectra of CdS with varying thickness, t/crystalline size S_1: t=1450 nm, S_2: t=75 nm, S_3: t=50 nm, S_4: t=35 nm and S_5: t in between S_2 and S_3. As the thickness increases, the crystalline size increases; (b) The thickness/size dependence of the band gap; (c) Comparison with experimental data for CdS. Solid curve is from tight binding approach and dashed curve is from effective mass approximation. Δ and ▢ are experimental data points

A hyperbolic band model has been proposed to explain the change of energy gap as a function of particle size[28]. The equation derived for the band gap, E_{gn} of nanocrystallites according to this model is given by

$$E_{gn}= [E_{gb}^2 + 2\hbar^2 \, E_{gb} \, (\pi/R)^2/m^*]^{1/2} \qquad \ldots \quad (10)$$

where E_{gb} is the band gap for the bulk semiconductor, R is the particle radius, and m^* the effective electron mass. If E_{gn} is known, the particle size can be estimated from the blue shift using eq. (10). Taking $m^*/m_e = 0.2$ for CdS[31], where m_e is the mass of a free electron and E_{gb}=2.4 eV, the crystalline sizes of different samples are estimated using eq. (10). Shown in Fig. 8(c) is the band gap energy of CdS[122] as a function of particle diameter obtained from effective mass approximation[21] (dashed curve) and hyperbolic band model[28] (solid curve) calculation. The trend, increase of band gap with decreasing particle diameter for both the models are similar. However, when compared with experimental data[123] points from well characterised samples with narrow size distribution are found to agree only for large particle diameter. The failure of the above two models in the low size regime is due to the failure in taking proper account of dielectric constant, surface structure and shape of the crystallite. For example, the effective dielectric constant of CdS get reduced for very small CdS particles[28]. In order to confirm the above, the present authors[31] have measured the crystalline size experimentally by atomic force microscopy (AFM), and compared their size estimation data obtained from the blue shift. Fig. 9 shows the AFM picture of chemically prepared CdS. The nanocrystallites Fig. 9 (top) have the size in the range 9 to 12 nm whereas the bulk crystallites are in the range of 71 to 75 nm (Fig. 9 (bottom)). The size
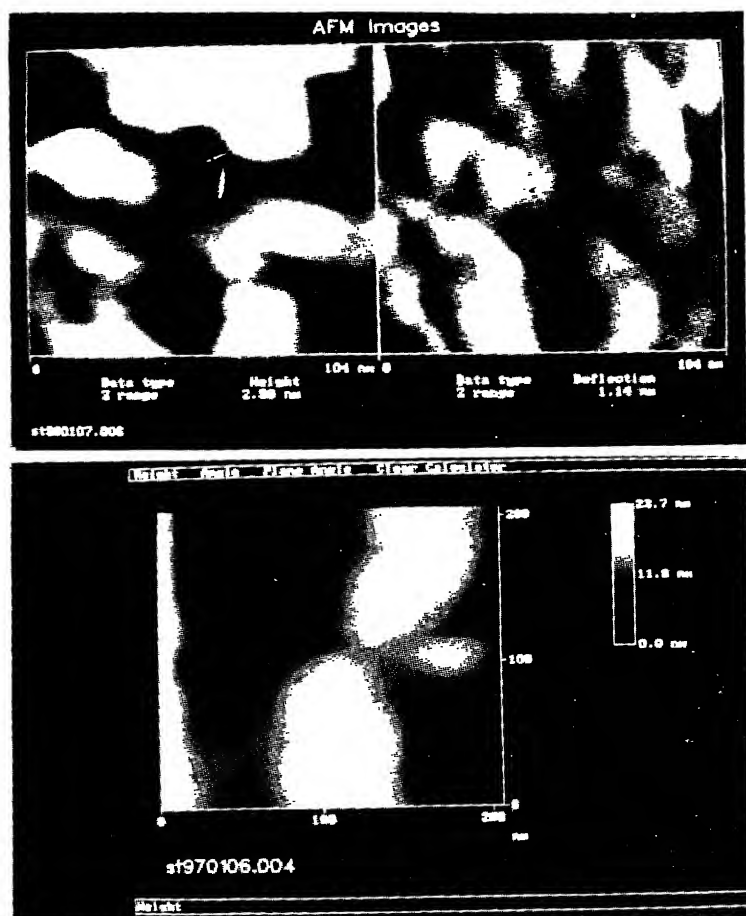

Fig. 9 AFM picture of CdS nanocrystalline sample (top) with size 12 nm and bulk CdS (bottom) with size 75 nm

estimated from AFM analysis do not agree with that obtained from the blue shift, predominantly associated with nano-CdS samples. In fact, the experimentally measured crystalline sizes in the small size regime does not agree well with the size estimated from blue shift as discussed earlier. One possibility for this discrepancy associated with nano-CdS samples could be the non-spherical geometry of nanoparticles. Electrons in the conduction band and holes in the valence band are confined spatially. As a result of the confinement of both electrons and holes, the lowest energy of optical transition from the valence band to the conduction band increases resulting in the increase in effective band gap. Within a simple effective-mass approximation, the confined gap is given by[21]

$$E_{confinedgap} = E_{bulkgap} + \frac{\hbar^2\pi^2}{2} \left[\frac{1}{w_x^2} + \frac{1}{w_y^2} + \frac{1}{w_z^2} \right] \left[\frac{1}{m_c^*} + \frac{1}{m_v^*} \right]$$

... (11)

where m_c^* and m_v^* are the conduction and valence band effective masses, respectively. The other parameters w_x, w_y and w_z are the dimensions of a three-dimensional (3D) box. If $w_x << w_y$ & w_z then the energy levels will mainly depend upon w_x i.e. the size estimated from the blue shift corresponds to the lowest dimension of the nanoparticles. The results from AFM analysis in case of nano CdS (Fig9 (top)) shows a lateral dimension of 11 nm considered as the diameter of the nano-CdS. On the other hand from the optical absorption study, the dimension of the nano-CdS is found to be 4.0 nm implying to a pancake geometry of the nanocrystallites. In fact, in case of nano-materials the binding energy per atom decreases with decreasing crystalline size which would result in a nonspherical geometry of the particles. Hence, one would expect a pancake structure for uncapped samples in chemically prepared nano CdS. Fig. 10 shows the size dependent band gap of some of the nanostructure semiconductors[124] whose Bohr exciton radii are different. Note that for low band gap semiconductor with large Bohr exciton radius, e.g. GaAs (see Table I), the band gap increases sharply as the size is decreased.

5.2 Photoluminescence and Photoluminescence Excitation

Photoluminescence (PL) is a process in which an electron excited by a monochromatic photon beam of certain energy undergoes nonradiative/radiative recombination either at valence band (band edge
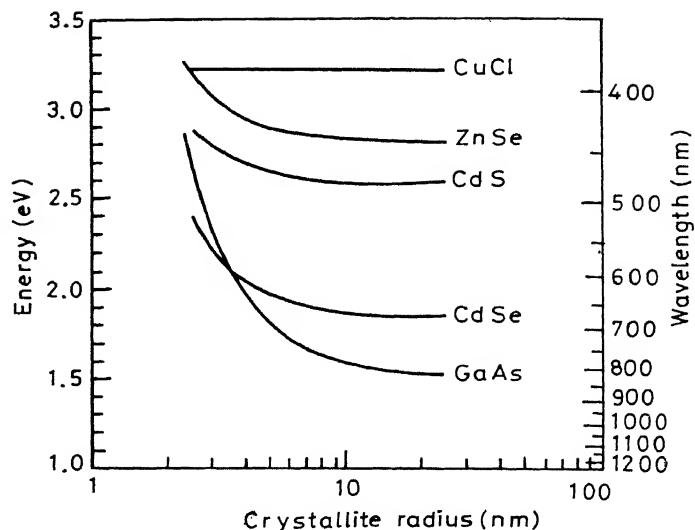

Fig. 10 Energy of the absorption onset as a function of crystalline radius for different semiconducting materials

luminescence) or at traps/surface states (normally red shift) within the forbidden gap. The band edge luminescence in general are weak whereas efficient luminescence transfer occurs at traps/surface states. Hence, PL essentially provide an estimation of band gap and identifies the presence of traps within the band gap. Attempts have been made to study PL properties[125-130] of nano-crystalline semiconductors which shows that with decreasing crystalline size the band edge luminescence or excitonic recombination yield decreases. The red shift band intensity in general is found to increase with decrease of crystalline size[125, 126]. The increase in PL yield of red shifted band is ascribed to the increase in surface state density[127]. In fact, when the crystalline size decreases, the surface to volume ratio increases which ultimately increases the surface state density[127]. The PL yield in general is found to increase with decreasing crystalline size if the transition is from the surface state to the valence band or to the acceptor state[128, 129]. However, both the band edge and the red shifted bands shift to blue with decreasing crystalline size. In some noncrystalline semiconductors the band edge luminescence is completely absent and is caused by the non-radiative decay of free electrons to the trapped state[130]. Shown in Fig. 11 is the photoluminescence spectrum of CdS of different crystalline size/thickness. The excitation wavelength is 488nm Ar+ laser. S_1, S_2, S_3 and S_4 are CdS samples whose crystalline sizes are in decreasing order. The crystalline size of S_4 is 11nm where the
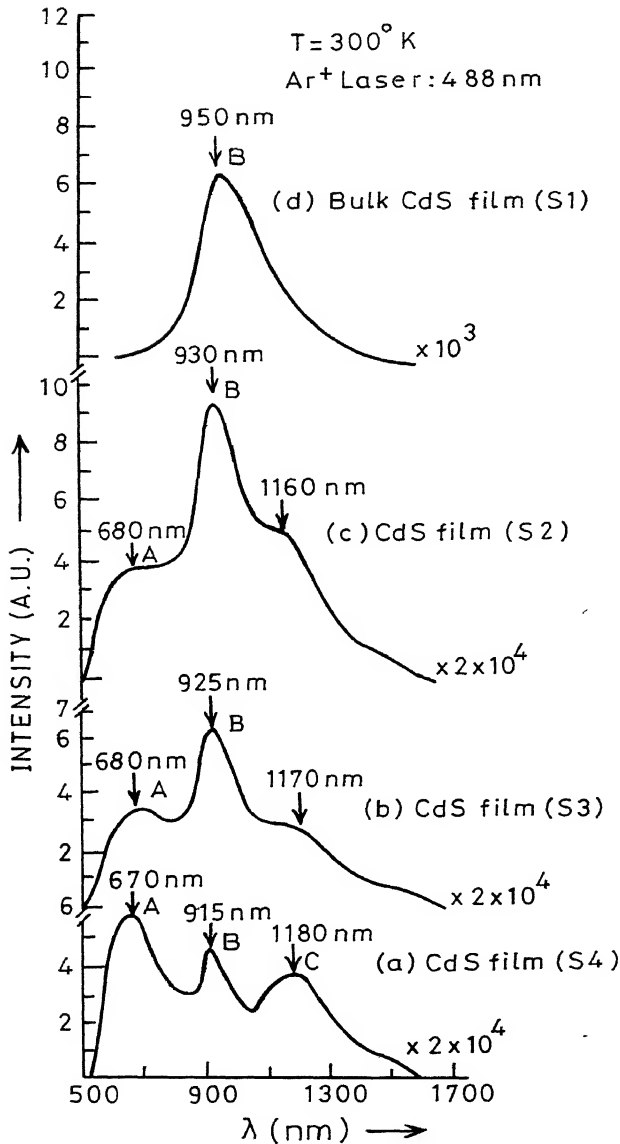
Fig. 11 Photoluminescence spectra of CdS at 300K taken for different sample thickness/crystalline size. The crystalline sizes are of the order a < b < c < d. The crystalline size for sample (a) is 12 nm and that of (d) is 75 nm

transition from donor state to surface state. With increasing crystalline size the A band is slowly suppressed due to decrease in donor state concentration. In fact, in the present case excess Cd in CdS acts as an acceptor and Cd-O as a donor. With increasing crystalline size, the concentration of Cd in CdS become less in chemically grown nano CdS. Hence, in the present case the PL studies essentially demonstrates the optimisation of nanocrystalline CdS growth conditions.

Photoluminescence excitation (PLE) technique in general is used to estimate the band gap as well as to study the discrete states in the semiconductor nanostructure[127]. Shown in Fig. 12 is the PL and PLE of Mn doped $21A^0 ZnS^{131}$ nano-crystal. The band gap is found to be 4.1 eV. It is obvious that the excitation is at 312nm whereas PL emission is at 600 nm. The PL and PLE spectra are very strong and suggest a very narrow size distribution in the sample.
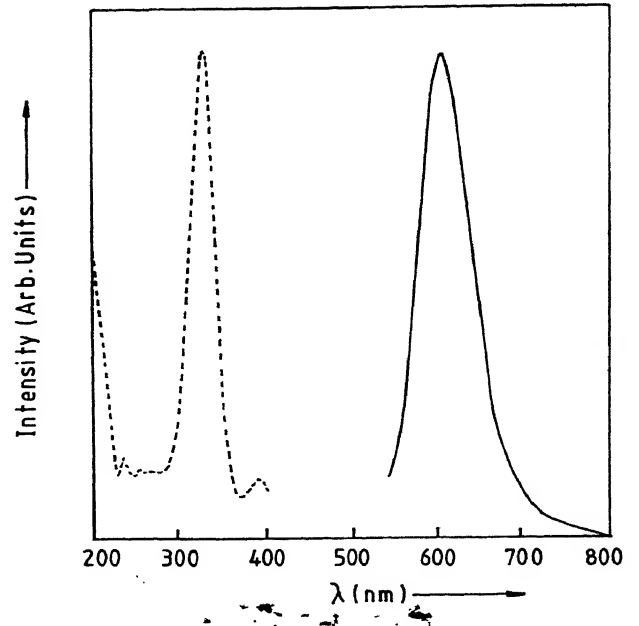
Fig. 12 Excitation (dashed line) emission spectra (solid line) of Mn doped 21+ 2A⁰ ZnS nanoparticle

crystalline size of S_1 is 75 nm. Note that the A and B bands shift to lower energies, whereas the shift of C band is opposite to that of A and B bands with increasing crystalline size. The B band PL yield decreases with decreasing crystalline size whereas that of A and C band increases. The A band at 670 nm is due to the transition from donor state to the valence band which give an efficient luminescence transfer with decreasing size. The B band is due to the donor-acceptor transition whereas the C band is due to the

5.3 Raman Scattering

Light scattering experiments is an useful tool to study nanostructure semiconductors. Of specific importance is the Resonant Raman scattering which has been extensively used for studying the size quantization effect[132] and surface phonon (SP) mode in nanocrystallites. The possibility of observing the

surface phonon (SP) mode in these class of materials using Raman spectroscopy is of considerable interest and a number of studies have been reported[4, 60, 120, 133-141]. It is believed that the SP mode can be observed if the size of the crystallites are small so that the surface to volume ratio is large and disappears in case of bulk sample. Further, if the nanoparticles are non-spherical, the surface to volume ratio will be large which would result in the enhancement of the surface mode intensity. Again, it has also been shown[137] that intensity and FWHM of Raman peak due to surface phonon increases with increasing surface roughness with no appreciable change in the frequency. From the above discussion, it can be concluded that both surface roughness as well as the crystalline size plays important role in modifying the Raman spectra[49, 64, 71, 134, 141, 142].

Fig. 13 shows the resonant Raman spectra of CdS[136] thin films S_1, S_2, and S_3 having crystalline sizes 75 nm (E_g = 2.405 eV), 7.5 nm (E_g = 2.65 eV) and

5.5 nm (E_g = 2.85 eV) respectively. The excitation wavelength used was 457.9 nm (2.7 eV) Ar$^+$ laser. First order longitudinal optical phonon (ILO) marked as p1 at 305cm^{-1} and a left wing shoulder at 295cm^{-1} surface phonon (SP) mode marked as p2 are identified for sample, S_1. Note that the ILO (p1) Raman yield gradually decreases with decreasing band gap of the samples S_2 and S_3. The excitation 2.7 eV satisfies the resonance condition for the samples S_1 and S_2 (2.4 eV and 2.65 eV) respectively whereas it fall short of 0.15 eV in case of samples S_3 (E_g = 2.85 eV). Hence, it is expected that at resonance the ILO peak will be enhanced and will mask the weak SP mode resulting a broad ILO peak. To test this, the author[136] varied the excitation energy and fixed the band gap (E_g = 2.65 eV). The sample S_2 was excited with two other wavelengths: 488nm and 514.5nm respectively. The effect was clearly seen as shown in Fig. 14 with decreasing excitation. Note the reduction in the Raman yield of ILO phonon (P1) with decreasing excitation energy Fig. 14 (b and c) which can be

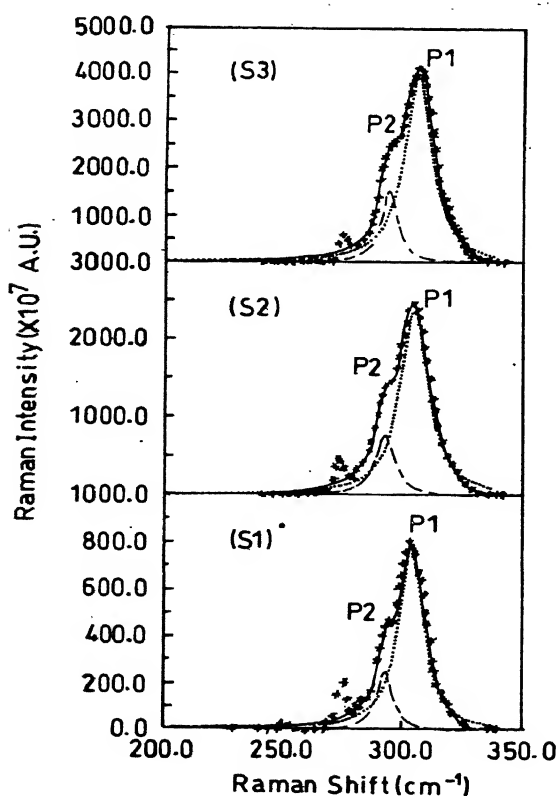Fig. 13 Resonant Raman Spectra of CdS samples (S_1-S_3) at 300K. The excitation source is 457.9 nm Ar$^+$ laser. The crystalline size for S_1=75 nm, S_2=7.5 nm and S_3=5.5 nm
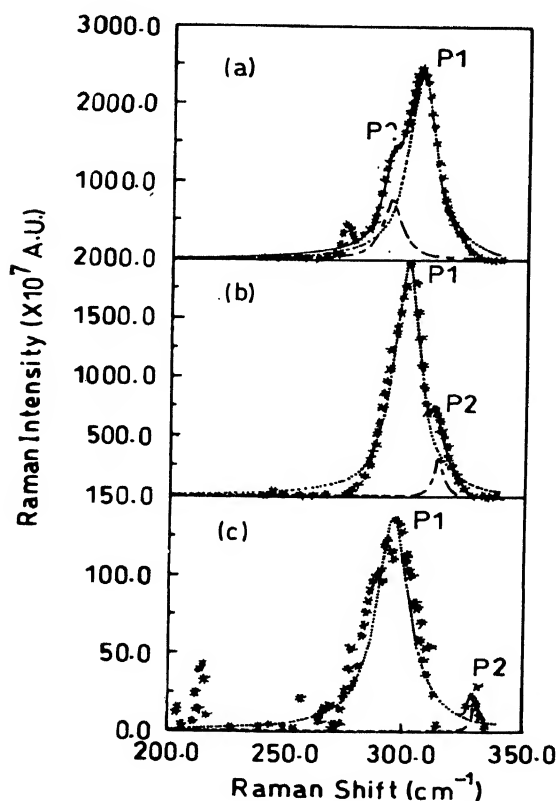
Fig. 14 Raman spectra of CdS sample (crystalline size, 7.5 nm, E_g= 2.65 eV) as a function of different excitation wavelength. (a) λ_{exc}= 457.9 nm; (b) λ_{exc}= 488 nm and (c) λ_{exc}= 514.5 nm

ascribed to the same reason that the excitation fall short of the band gap value. However, one peculiarity is that with decreasing excitation energy the SP mode shift to the higher frequency. Attempts have been made by the author[137] to explain this through some models shown in Fig. 15 (a and b). The author had adopted a chemical route[31] to synthesize nanocrystalline CdS where excess Cd which forms acceptor states in CdS is invariably present. The excess Cd content decreases with increasing crystalline size/thickness. Besides excess Cd in nano-CdS, the samples has size distribution. Based on this, the energy band scheme for bulk CdS, nano CdS without acceptor state, nano-CdS with acceptor states are shown in Fig. 15(a). The localised acceptor states, due to quantum size effect are shown as continuum of localised acceptors near the valence band. The excitation energy being lower than the band gap, the Raman shifted phonon intensities
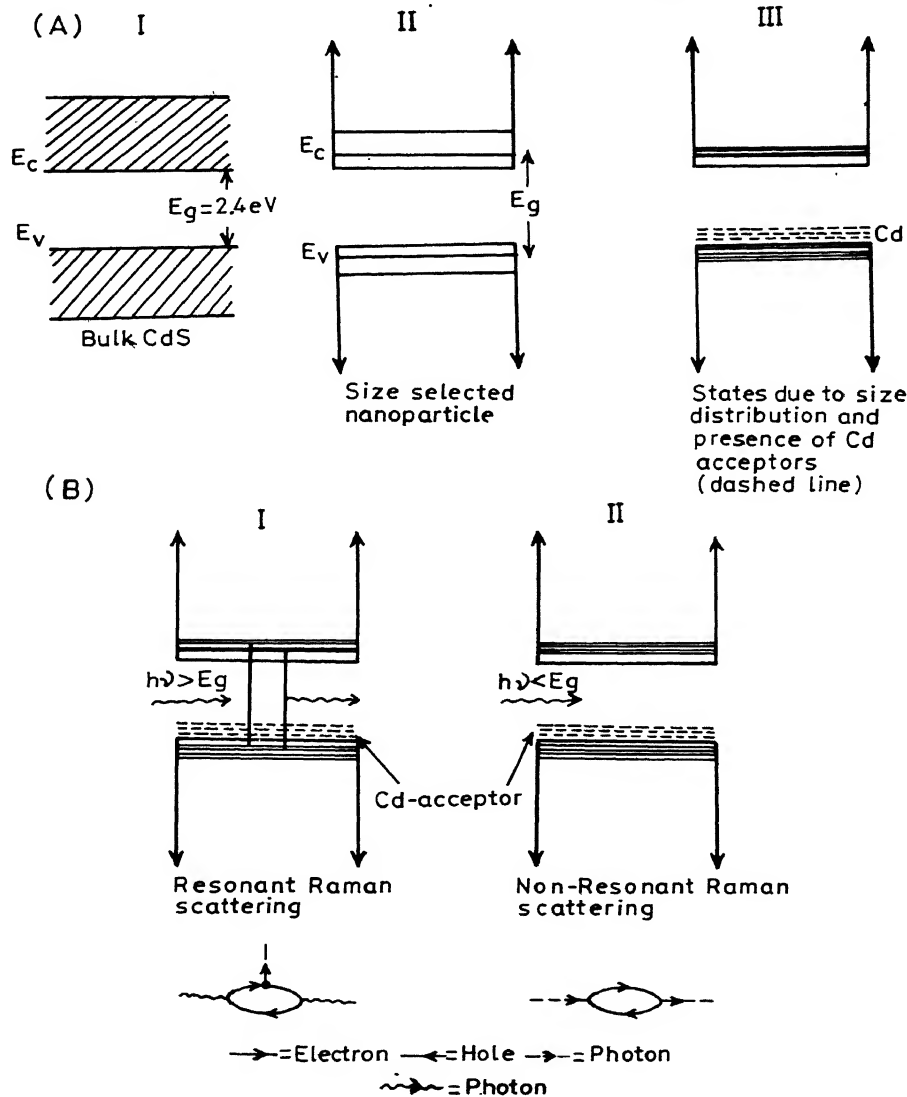
Fig. 15(a) Schematic diagram of CdS (I) bulk, (II) Size selected nano-particles showing discrete states and (III) Size distributed nano-particles and the presence of Cd acceptor results in bunching of electronic states (b) (i): Resonant Raman scattering process for which the energy of laser beam is greater than the band gap. In this process electron-hole pairs are produced by photon absorption and emit a phonon before recombination to give a photon; (ii) Excitation is less than the band gap and is non-resonant process. Excitation energy is not sufficient to excite electrons from the valence band but states are available for phonon to interact. Thus, electron-hole pairs are created in the continuum of localized states. The phonon acquires a self energy as explained by Feynman diagram

are shifted due to off resonance effect. However, the phonon, now can interact with electrons in the valence band which can excite the electron-hole pair in the continuum of acceptor states and reemit a phonon. In this way phonon gains the self energy, hence get shifted to higher frequency with decreasing excitation energy as shown in Fig. 15(b). The Fyneman diagram is self explanatory. A similar resonance effect of decreasing Raman yield with decreasing excitation energy is also observed with electrochemically prepared 18 nm crystallite PbS[49] and 2.0 nm PbS crystallites[138,139] prepared through chemical route. However, the surface effects, as described in ref. [49], plays a crucial role in determining the Raman yield, shift and widths. In particular the surface phonon mode is highly influenced by surface roughness[49].

5.4 Spectral Response

Spectral response technique essentially provide information regarding estimation of band gap, quality of the semiconductor and also device performances. A semiconductor device is excited by different wavelength light and the corresponding photocurrent is recorded in this technique. A plot of square of photocurrent as a function of photon energy in case of direct band gap semiconductor gives an estimation of the band gap. The photocurrent in this technique depends upon the photon absorption. A wide range of wavelength absorption by the device will obviously generate larger number of photo carriers which totally will contribute to the photo current. By this the quantum efficiency will increase. However, in case of bulk semiconductors[142] excited with shorter wavelength, the majority carriers diffuse to the interface to recombine with minority carriers. and the photocurent falls. Hence, a wide range wavelength can not be used for absorption. In case of nanocrystalline semiconductors *e.g.* CdSe[143], the sample is able to absorb a wider range of wavelength and thus generates a large number of photocarriers and contribute to the photocurrent. The quantum efficiency is thus increased and attains a flat spectral response of the system for nanocrystalline device. The surface effect is believed to play a crucial role in attaining the flat spectral response.

6 Electrical and Interfacial Properties

Study of electrical and interfacial properties of nanostructured semiconductors are essential for technological applications. Attempts have been made

to measure the resistivity of the sample in order to find the activation energy *vis-a-vis* the band gap of the material as well as to understand the conduction mechanism. Similarly, any device, before it goes for application, the interface has to be characterized first. As the surface to volume ratio for nanostructure semiconductor is large, introducing huge grain boundaries, the resistivity is expected to be very high. Caped PbS[36] of different crystalline sizes were subjected to resistivity studies as a function of temperature. In the resistivity curve, two distinct regions above and below 340°K show different conduction mechanisms. The high temperature (above 340°K) conductivity arise due to intrinsic semiconducting behaviour of PbS controlled by large activation energy process whereas below 340°K the conduction is controlled by low activation energy process. Resistivity as high as 10^{15} Ω cm was obtained for such PbS nanocrystallites. Further, the resistivity increases with decreasing crystalline size. The band gap values for different crystalline sizes have been estimated and found to increase with decreasing crystalline size as expected. The low temperature activation energy is believed to arise due to electron tunneling between nanocrystalline particles. Similar feature is also reported for CdS[47] and ZnTe[144] nanocrystalline samples prepared by d.c. magnetron sputtering. Shown in Fig. 16 is the conductivity data of ZnTe as a function of temperature for two different
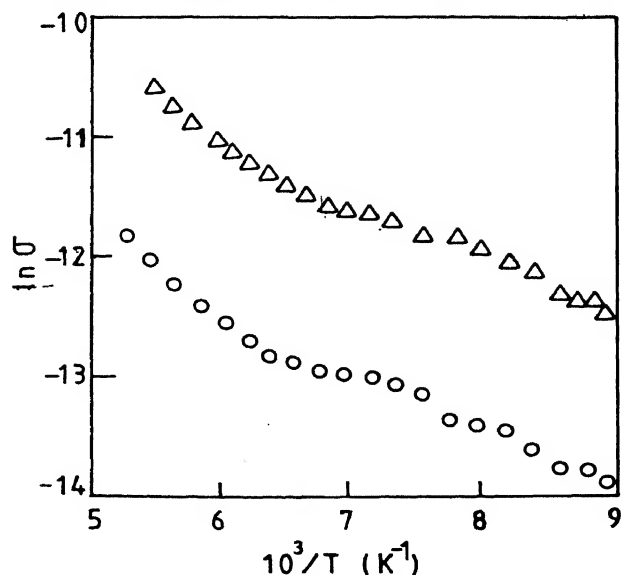

Fig. 16 Variation of Electrical conductivity (σ Ω cm) with temperature for two ZnTe samples prepared at 0– (273K) and Δ– (283K)

crystalline sizes. Samples prepared at 283K are smaller in size as compared to that prepared at 273K. The smaller crystallites show higher resistivity compared to that of 4.5 nm size prepared at 273K. From the conductivity curve two distinct regions, one at low temperature and the other at high temperature result two different slopes. The conduction mechanism remains the same as described in ref. [36]. Similar results were also obtained for nanocrystalline CdS[47]. Careful analysis of the data for CdS[47] or ZnTe[144] films under illumination show a different behaviour. In fact, the low temperature photoconductivity data for CdS[47] show two more slopes instead of one as discussed earlier. Thus, the low temperature photoconductivity data of CdS[47] indicate two activation energy processes for conduction with nominal activation energies (10^{-3} eV to 10^{-2} eV) which suggests that the conduction switches from variable hopping to tunneling through the potential highly resistive regions under illumination.

Reports of interfacial characterization of semiconductor nanostructures available in the literature show that the dominant control over device performance is based upon interfacial properties. The semiconductor nanomaterial has a high surface to volume ratio along with unsaturated dangling bonds which will introduce a high density of surface traps at the interface and can influence the interfacial properties. In general the interface is characterized by current (I) -voltage (V), and capacitance (C) -voltage (V) characteristics. Some of the common interfaces studied are CdS/Au[145], CdS/Ag[146], porous GaP/Au[147] and porous SiC/electrolyte junction[148]. It is wellknown that nanostructure semiconductors exposed to air or kept in ambient are prone to oxidation. Presence of such an oxide layer introduces a series resistance to the device. Hence, the applied voltage is supposed to be distributed[145-151] both across the space charge and the oxide layer. Hence, when a device is characterized the series resistance effect has to be taken into account and necessary corrections are to be made with the I-V characteristics.

The corrected relation for nano-CdS/Au Schottky junction is given as

$$I=I_0[exp\ (q(V-IR_s)\ /nKT) -1] \qquad ... (12)$$

with dynamic resistance r as:

$$r= \frac{dV}{dI}\ (nKT/qI_0)\ exp\ (-q(V-IR_s)/nKT) + R_s$$

$$= nKT/qI_0 + R_s \qquad ... (13)$$

Where the quantities; I, I_0, V, R_s, n and q are respectively

the current flow across the junction, reverse saturation current, applied voltage, series resistance, ideality factor and electronic charge. Shown in Fig. 17 is the $\ln J$ vs V plot for the nano-CdS/Au[146] Schottky junction where J is the current density. Note two ideality factors n=6.0, 1.8 in the high and low forward biased regions respectively of the nano-CdS/Au[146] junction. Ideality factor exceeding 2 is often found for schottky junction where the interface consists of a thin oxide layer. Presence of an oxide layer introduces high density of surface states to the interface. The applied potential will be distributed across the space charge and oxide layer. The inset shows the $\ln J$ vs $\ln V$ plot. A straight line plot with slope, m=6.6 suggests the hopping conduction for electrons through the nanocrystalline film.

The C-V plot of nano CdS/Au[145] and bulk CdS/Au[145] at 1kHz frequency along with the model explaining the electric field penetration into the interface under forward bias is shown in Fig. 8(a). Note that the capacitance of nano CdS/Au junction is large as compared to that of bulk CdS/Au which suggests that a large surface area of contact exists for nano CdS/Au junction. As discussed earlier from Fig. 17 that a high density of surface states are present at the

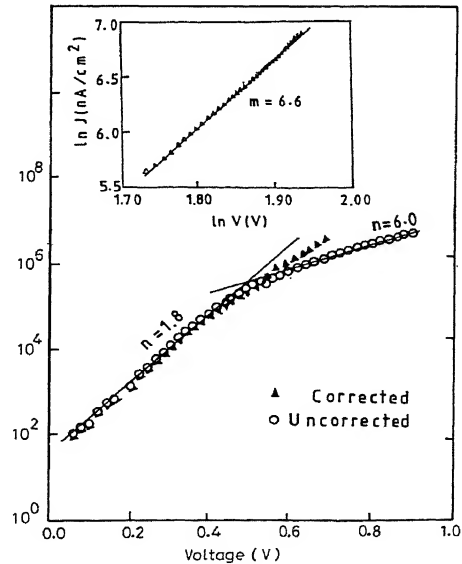Fig. 17 I-V characteristics of nano-CdS/Au junction plotted as ln (J)-V. Two ideality factors in the low and high forward bias are seen. *Inset:* the same data plotted as ln (J) Vs ln (V) and fitted into a straight line. The slope is estimated to be 6.6

interface. Presence of high density of surface states, under high forward bias may inject minority carriers which can diffuse across the junction and will contribute to the junction capacitance. Hence, region A is the contribution both from depletion and diffusion layer capacitance whereas region B of the C-V curve is due to the diffusion layer capacitance alone. However, when the frequency of the applied A.C. signal is increased, the surface states will not follow it and the diffusion capacitance contribution will be insignificant. Shown in Fig. 18(b) is the C-V plots for different frequencies. Note that the diffusion capacitance contribution become insignificant, for frequencies above 1kHz.

7 Stability of Semiconductor Nanostructures

Nanocrystalline semiconductors belonging to II-VI group are prone to oxidation when exposed to light and oxygen. In particular nanosemiconductors *viz.* CdS and CdSe are very unstable[70]. Upon exposure to visible light or oxygen the chalcogenides (S or Se) at the surface is oxidised to sulphate or selenate and oxides being volatile, evaporates from the surface as a molecular specy and leaves behind the sample element belonging to the 2nd group (*i.e.* Cd, Zn, Hg). This has been confirmed from XPS experiments[151].

Hence nanocrystalline semiconductors belonging to II-VI group has limitation for applications unless a protective coating is applied onto the surface. On the other hand the nanocrystalline semiconductors belonging to III-V group such as In P, form stable oxide at the surface and may find use in application. Aging[152] effect of nano-CdS thin film prepared by a chemical route[31] has been tested by photoluminescence studies. Shown in Fig. 19(a) is the photoluminescence spectra of nano-CdS sample with aging recorded at 300K. The excitation energy is 2.78 eV. The spectra provide two PL bands, A and B. Note that for fresh samples, the PL band, A has FWHM 0.17 eV. With increasing of the time of exposure of the sample to the atmosphere the FWHM of the B band decreases from 0.6 eV to 0.49 eV along with a shift towards lower energy. On the other hand, in case of band A, neither the peak position nor the FWHM changes upon aging. Further, note that both the bands, A and B, are red shifted and the transition is believed to be between donor, acceptor or surface states. The energy band scheme is shown in Fig. 19(b) to explain the above. Narrowing of B band with aging suggest the growth of crystallites with time. The band gap of the aged sample will be small due to crystallite growth upon aging. The energy band scheme shows the presence of shallow traps, deep
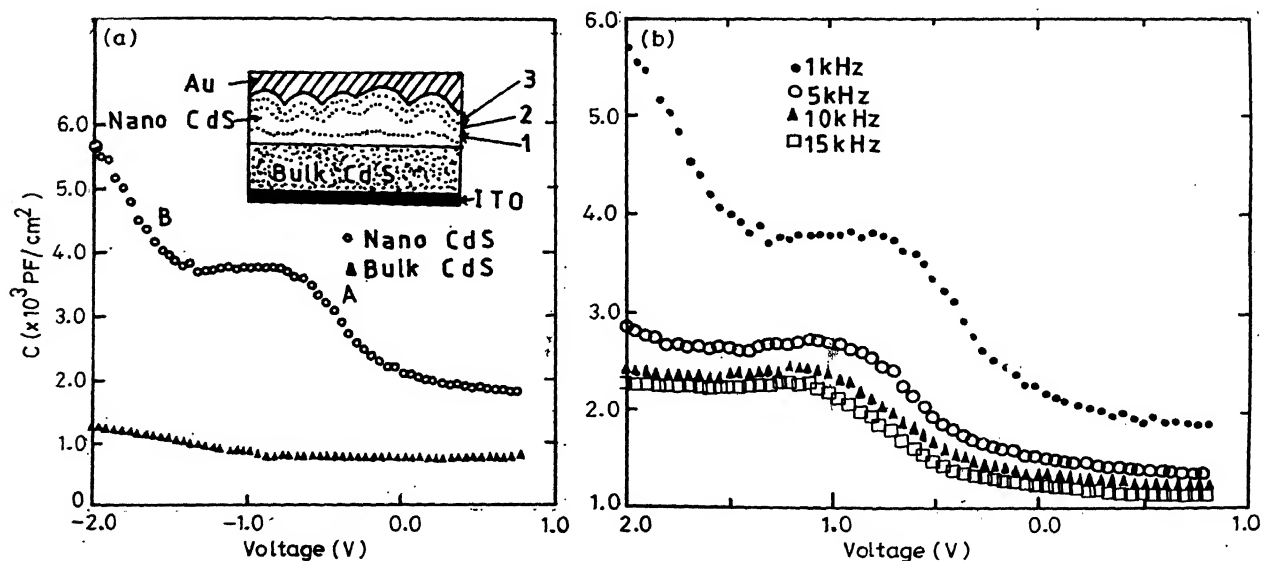
Fig. 18(a) C-V characteristics of nano-CdS/Au(o) and Bulk CdS/Au (Δ) at 1 KHz frequency. The inset shows a schematic representation of ITO/bulk-CdS/nano-CdS/Au junction. The solid line represents the nano-CdS/Au interface and the dashed line represents the inner edge of the depletion layer. Lines 1, 2, 3 are electric field penetration with increasing forward bias; (b) C-V Characteristic of nano-CdS/Au junction at different frequencies

traps and surface traps. Upon aging the band gap become small, hence the shallow traps will move along the band edges. Hence, a shift of the band B to the lower energy is expected whereas the A band arising due to the deep traps has no effect on aging. So, niether the FWHM nor the peak position changes with aging.

Fig. 19(c) shows a 15 days old samples excited with two different photon energies. The crystalline size of the fresh CdS sample is around 12nm. Note that the A band has no effect with change of excitation energy but the B band peak shift to the higher energy when the excitation energy is increased. Further, the B band

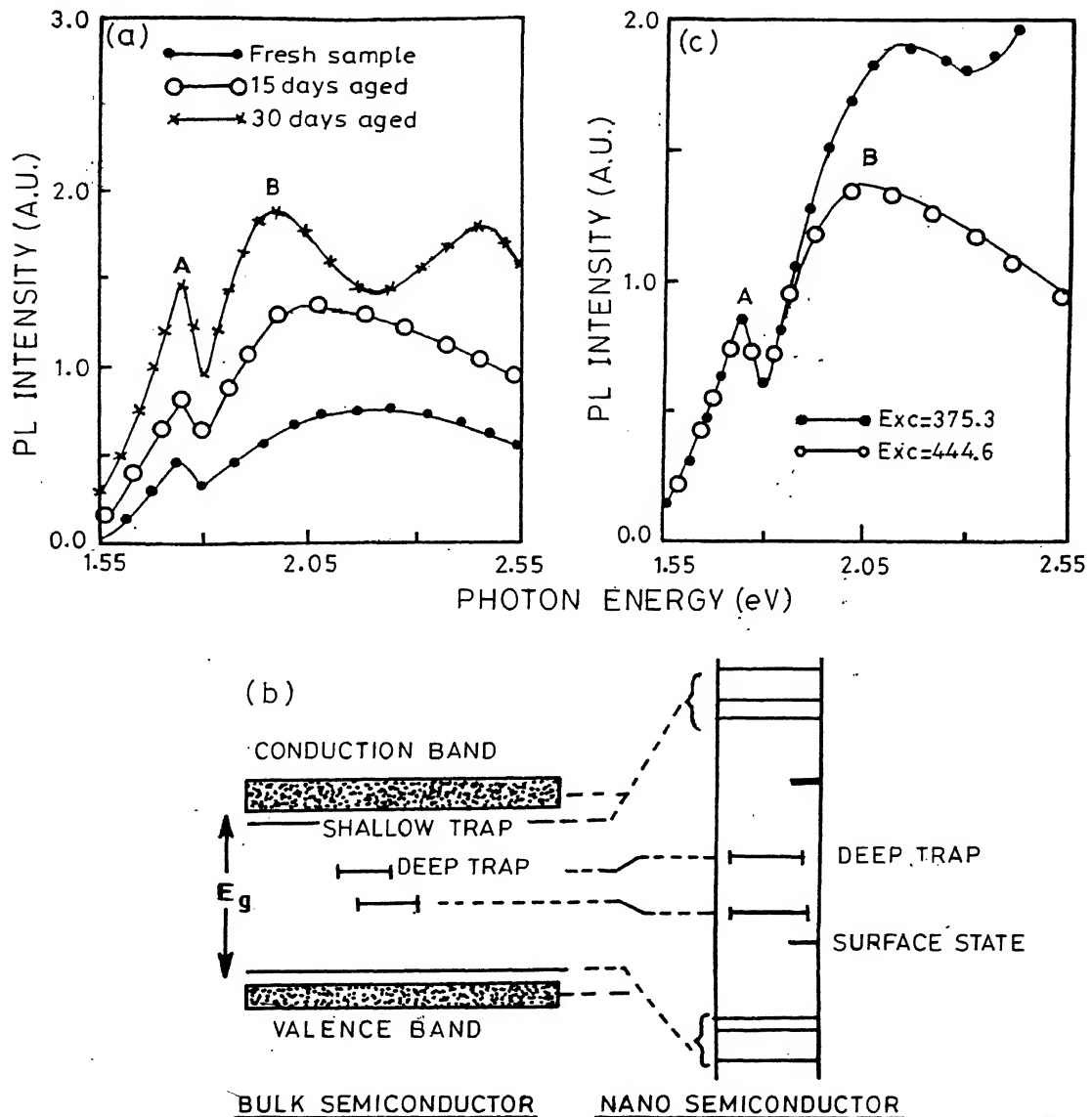Fig. 19(a) The effect of photoluminescence spectra of nanocrystalline CdS with aging recorded at 300K. The excitation energy is 2.78 eV; (b) Energy level diagram of bulk and nanocrystalline semiconductor. Surface states arise due to increased surface to volume ratioi as shown in the figure; (c) Photoluminescence spectra of 15 day old nano-CdS sample with two different excitations (375.3 nm and 444.6 nm) recorded at 300K

intensity is increased considerably which suggests that the excitation energy is above the luminescence band. Overall picture shows that with increasing aging time the nanocrystallites grow in their size.

8 Nanostructure Devices and Applications

Visible Light Emission

It is well known that the oscillator strength increases with decreasing crystalline size[21]. Thus, light emission from the nanocrystals is expected through a radiative recombination process of charge carriers generated by higher energy photon absorption. The emission colour can be tailored by changing the crystalline size and appropriate doping[9]. In fact, the dopants create different energy levels within the band gap of the host material which influences the luminescence properties. Further, in case of nanocrystallites, the enhanced surface to volume ratio increases the density of surface states that take part in efficient luminescence transfer process[61,128,129,153,154]. Thus, the impurity levels at appropriate position in the band gap is beneficial to efficient luminescence. The impurity levels can be created by doping or by natural defects.

The first experiments on Mn-doped ZnS nanocrystals revealed a drastic change in spontaneous decay rate of Mn^{2+} ions embedded in nanocrystals as compared with ZnS monocrystals. In case of bulk crystal the decay life time is aout 2 msec, whereas, it is of the order of nanoseconds in case of nanocrystals. Therefore, the efficiency of luminescence is rather high. In ZnS: Mn nanocrystals the quantum yield is found to be about 20 per cent, showing a monotonic increase with decreasing size. Thus, doped nanocrystals are believed to offer a set of commercial phosphors and laser media in the near future.

CdS nanocrystals showing quantum size effect[31] also emit red light when exposed to UV excitation even at room temperature[14,154]. However, the intensity of luminescence increases by many fold when the sample is cooled down to 80 K. Shown in Fig. 20(a) is the colour photographs[154] of CdS bulk and nanocrystalline sample[31] prepared by chemical route. Note that a clear change of crystallite colour from orange (crystalline size is 75nm) to yellow (size less than the bulk), and then to pale yellow (size 8 to 12nm and shows quantum size effect) is clearly seen. Fig. 20(b, c and d) are the photographs taken under UV radiation. Red light emission under UV is for nano-CdS sample clearly seen but absent for bulk CdS. Along with red emission, there are also green emitted particles which are collected, put together and exposed to UV radiation. Green emission is shown in Fig. 20(c). Nanocrystalline samples are cooled to 80K and exposed to UV, emission intensity increases by manyfold as shown in Fig. 20(d). Different colour light emission suggest a size distribution in the nanocrystallites. The reason for light emission is described in ref.[154]. A similar visible light emission is also seen from Si[119] nanostructures. Although Si is an indirect band gap semiconductor, being very small in size the states are quantised due to three dimensional confinement and behave as a direct band gap Si. This results in visible luminescence.

Applications

As a consequence of efficient light emission upon irradiation by UV light, it can be used as an UV sensor.

Nanoelectronic Device

The solid state nanoelectronic devices take the advantage of quantum confinement effect. The essential structural feature for the device have in common is a small "island" composed of semiconductor in which electrons are confined. Based on the extent of confinement the solid state nanoelectronic devices can be classified in three categories viz. (a) Quantum dots[155] (artificial atoms): here, the island confines the electrons with zero degree of freedom remaining, (b) Resonant Tunneling Devices[156], where the island confines electrons with one or two classical degrees of freedom and (c) Single Electron Transistor[157,158] where the island confines the electron with three degrees of freedom.

a) Quantum Dots (QD) (Artificial Atom)

Quantum dots can be synthesized by lithography, self organisation of droplets or nanocrystallites grown in-situ in film. As in QD the electrons are three dimensionally confined, the quantum energy level, $\Delta\varepsilon$ for electrons are widely spaced and is comparable to the changing energy, u. In that case the interaction among the electrons on a QD and the energy level for each individual electron influence the current flow. as a result, a sequence of current steps are observed as the bias voltage is varied.

b) Resonant Tunneling Devices (RTD)

In this case island is long and narrow the structure may be a "wire" or a "pancake" with dimension 5-10 nm. Here, the quantum energy level, $\Delta\varepsilon$ is large
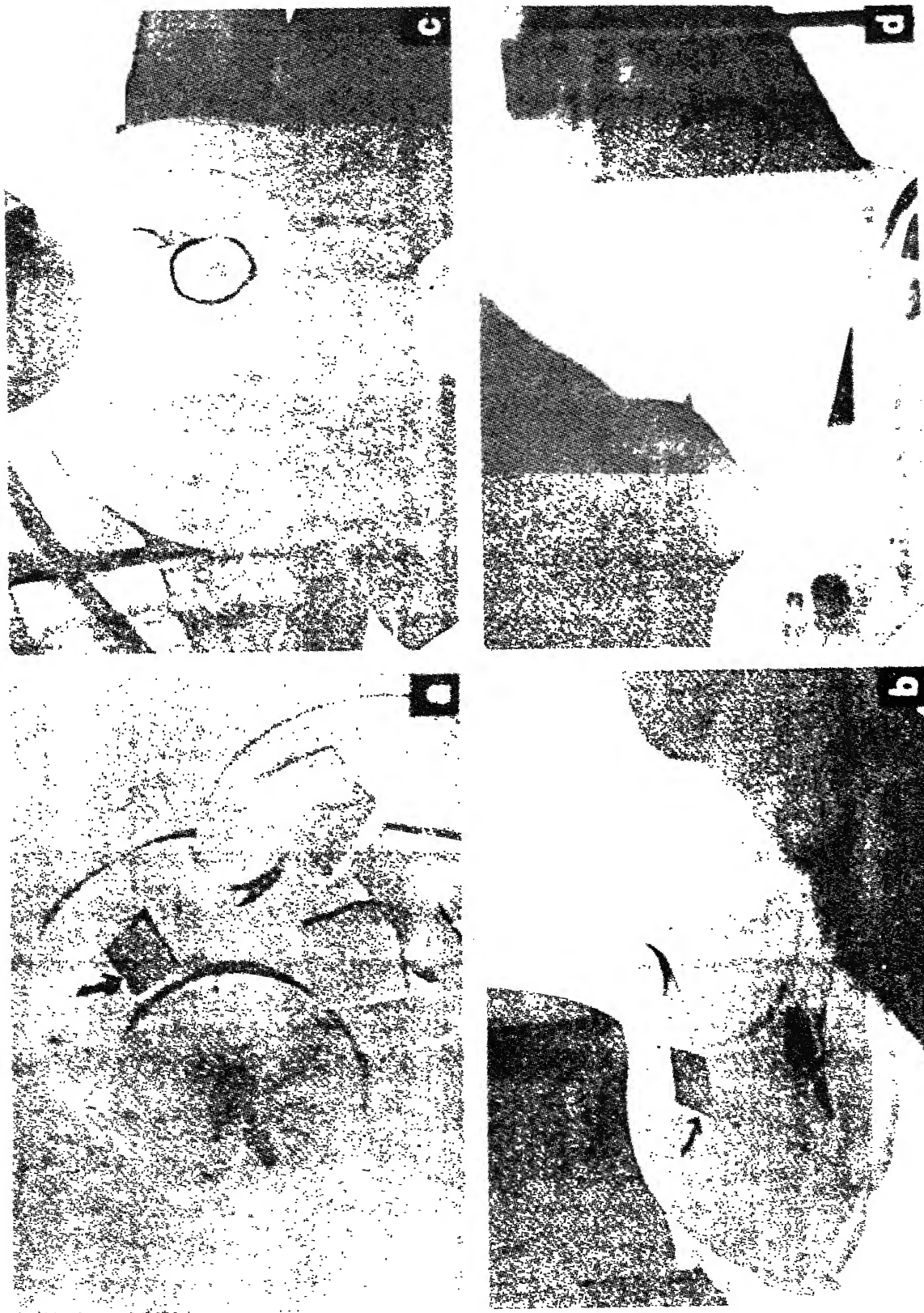
Fig. 20 Optical colour photograph of visible light emission from CdS on filter paper taken at 300K. (a) Photograph taken under visible light. Orange crystallites are bulk-CdS (75 nm size) E_g=2.405 eV, yellow crystallites are again bulk-CdS with E_g = 2.65 eV and faint yellow crystallites are nano-crystals of size 12 nm, E_g = 3.14 eV; (b) Photograph taken under U V radiation for sample as in (a). The nanocrystallites emit red light whereas bulk does not; (c) Crystalline size <12 nm emiting green under U V radiation (circled); (d) CdS nanocrystallites size 12 nm cooled to 80K and exposed to U V. The emission intensity increased by many fold

as compared to charging energy, u. Hence, the current flow is totally controlled by quantum energy levels when a bias voltage is applied between the source and the drain. So, one gets a current peaking structure.

c) Single Electron Transistor (SET)

SET is a three terminal device having gate, source and drain whereas RTD and QD are two terminal devices. As SET switches the source to drain current on and off in response to small changes in the charge on the gate amounting to a single electron. For island to be short, the quantum energy level, $\Delta\varepsilon$ are well separated for the electron, so the island for the semiconductor to be around 100 nm. In SET, $\Delta\varepsilon \ll u$. Coulomb interactions among the electrons (represented by U) block electron from tunneling to the island at low bias voltage is known as "coulomb blockade". Thus the current flow is associated with a threshold bias voltage, U. Increasing the bias gate voltage, a current suddenly flow from source to drain, increasing further, U turns off the current flow. Again increasing U the cycle is repeated. The current flow is in off means no extra electron can tunnel to the island due to coulomb blockade. Shown in Fig. 21(a) is the conductance, G of a SET[158] device as a function of gate voltage. With increasing gate voltage, G increases, give a peak structure and than falls back to zero. The conductance peak is due to the coulomb oscillation. Insets show current, I vs voltage, V plot taken at two fixed values of the gate voltage. The conductance is suppressed when applied voltage is small whereas the voltage applied corresponding to the conductance peak have some finite and linear response even when the applied voltage is small. For detail see ref. [158].

A Schottky device using nano-crystalline CdS (Size= 44A° and E_g=2.7 eV) have been fabricated in the configuration of ITO/CdS/Al[159]. Here, ITO stands for indium tin oxide. The dark and photocurrent (I)-voltage (V) characteristics of the Schottky diode, ITO/CdS/Al[159] is shown in Fig. 21(b). For photo I-V characteristics, the monochromatic excitation is 3.0 eV which is close to the absorption threshold. Open circuit photovoltage and short-circuit photo-current of 0.1V and 100 nA respectively were obtained from such a device. The symmetric dark I-V characteristic (inset) shows a large dark reverse current. The rise of photocurrent only occurred after a threshold applied voltage. A large dark current and a threshold applied voltage for photocurrent to flow

suggests the presence of high density of surface traps or may be due to a series resistance effect.

Electroluminescence

Electroluminescence of nanocrystals is of great practical importance because it may be used for various light emitting device applications. The main problem in obtaining efficient electroluminescence is to get a dense ensemble of nanocrystals in a proper conducting and transparent environment providing charge carrier injection and migration. To date CdSe[39] and CdS[160] nanocrystals embedded in a conducting polymer and of nano-Si[161] in SiO$_2$ matrix electroluminescence devices have been fabricated. Colvin et al.[39] has reported on electroluminescence from CdSe nanocrystals. A nearly monodisperse assembly of nanocrystals was embedded in a matrix of polyvinylcarbazole and an oxidiazole derivative and sandwiched between ITO and Al electrodes. Electroluminescence was observed both at room temperature and at cryogenic temperatures featuring an intrinsic emission spectrum similar to that observed with optical excitation. Typical voltage applied to the structure was about 20 V. Artemyev et al.[160] obtained electroluminescence (EL) from a thin film structure containing close-packed CdS particles of size 1-2 nm. with Schottky configuration, ITO/CdS/Ag. The electroluminescence characteristic at different forward bias is shown in Fig. 21(c). Note that at low forward bias EL was obtained in the red region. But as the forward bias is increased from 20 V to 36.5 V the EL with very high yield is blue shifted. At a voltage above 36.50 V an EL spectrum similar to PL was obtained which suggests similar localized states participating in the luminescence process.

Photovoltaics

Nanocrystals are well-suited for photoelectrochemical cells because they provide a high surface area. Further, the ability to tune the band gap readily by varying the size suggests that inexpensive multi bandgap solar cells, analogous to very high-efficiency but expensive quantum well based photovoltaics, may be realizable with nanocrystals. O'Regan and Gratzel[7] have reported an efficient (12%) and inexpensive photovoltaic cells based on a film of partially fused TiO$_2$ nanocrystals coated with an extremely robust sensitizer molecule. The device takes advantage of the large surface area but does not make use of the quantum-size effect to tune band gaps.
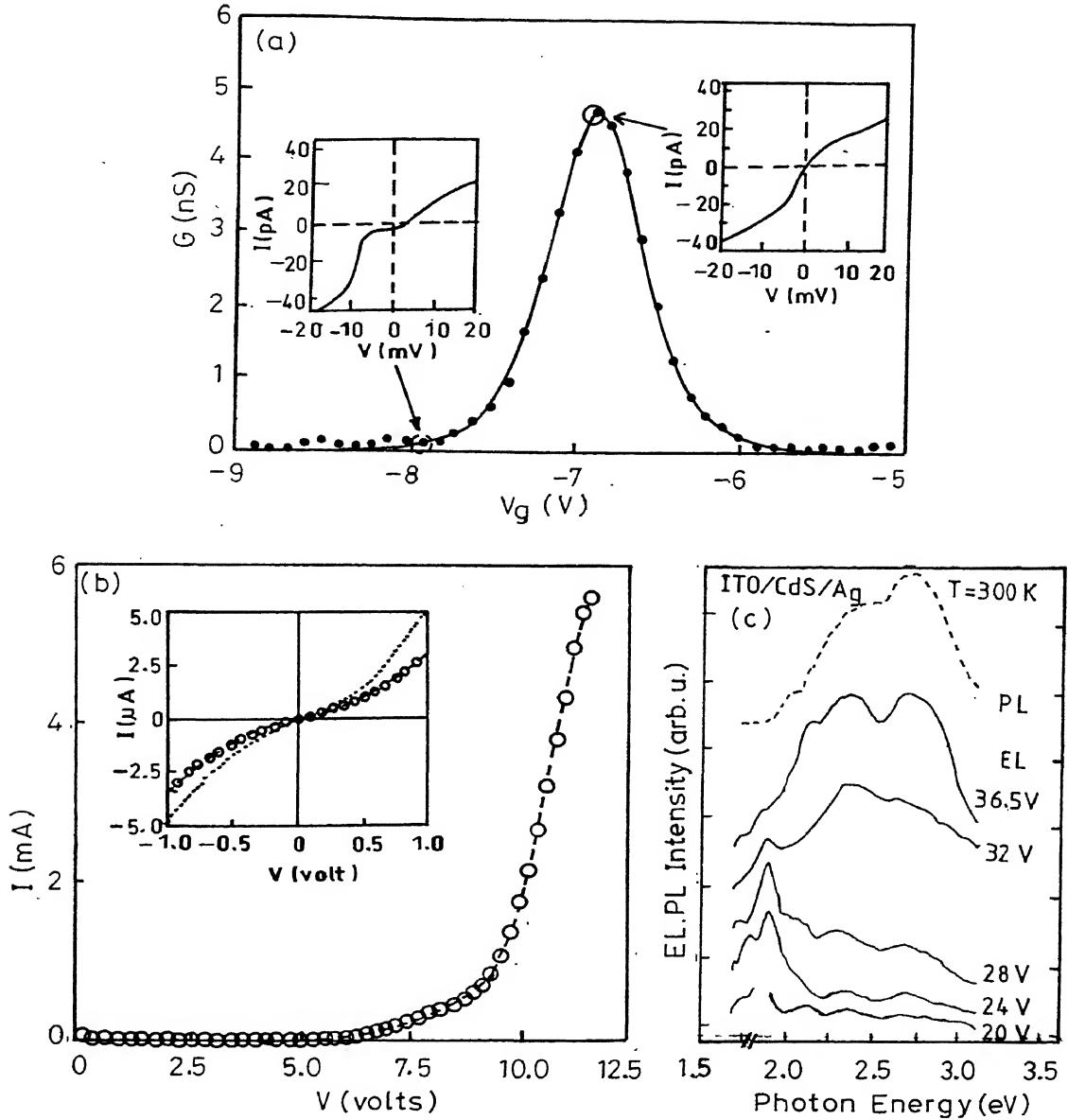
Fig. 21(a) Conductance, G plotted against gate voltage, V_g for a single electron transistor at 4.2K. The condutance shows a peak when the charge state of the CdSe nanocrystals (size 5.5 nm) changes by one electron. The dots are the measured values and solid line is the fit to the data. Insets; I-V characteristics measured at the gate voltages indicated; (b) I-V characteristics of ITO/ CdS (44A°) /Al device. The inset is the dark current and the total current with incident light (3.0 eV, 0.7 µW/cm²) VS Voltage response at a magnified lower range; (c) Room temperature electroluminescence spectra of ITO/CdS (quantum confined) /Ag Schottky device for different forward bias voltage as indicated. The dashed line is the PL spectum at 300K

Photovoltaic effects are also seen with CdS nanocrystalline semiconductors[31], where a reasonable photovoltage can be obtained. However, no appreciable photocurrent was observed due to highly resistive nature of the samples.

Acknowledgements

References

1 J Woltersdorf, A S Nepijko and E Pippel *Surf Sci* **106** (1981) 64

2 S B Qadri, J Yang, B R Ratna, E F Skelton *Appl Phys Lett* **69** (1996) 2205

3 N Herron, Y Wang and H Eckert *J Am Chem Soc* **112** (1990) 1322

4 R Rossetti, S Nakahara and L E Brus *J Chem Phys* **79** (1983) 1086

5 R Seigel *Scientific American* **275** (1996) 74

6 C Weisbuch and B Vinter *Quantum Semiconductor Structures: Fundamentals and Applications* Academic Press San Diego (1991)

7 B O'Reagan and M Gratzel *Nature* **353** (1991) 737

8 G M Panjonk *Appl Catal* **72** (1991) 217

9 R N Bhargava, D Gallagher, X Hong and A Nurmikko *Phys Rev Lett* **72** (1994) 416

10 Y Maeda *Phys Rev B* **51** (1995) 1658

11 E H Nicolian and R Tsu *J Appl Phys* **74** (1993) 4020

12 S Schmitt-Rink, D A B Miller and D S Chemla *Phys Rev B* **35** (1987) 8113

13 R L Holtz, V Provenzano and M A Imam *Nanostructured Materials* **7** (1996) 259

14 K K Nanda, S N Sarangi and S N Sahu *Curr Sci* **72** (1997) 110

15 A I Ekimov and A A Onushchenko *JETP Lett* **35** (1981) 345

16 A I Ekimov and A A Onuschenko *JETP Lett* **40** (1984) 1136

17 Al L Efros and A L Efros *Sov Phys Semicond* **16** (1982) 722

18 A Nakamura, T Tokizaki, H Akiyama and T K Kataoka *J Luminescence* **53** (1992) 105

19 S V Gaponenko *Optical Properties of Semiconductor Nanocrystals* Cambridge Univ Press (1998) Ch 1

20 N Chestnoy, T D Harris, R Hull and L E Brus *J Phys Chem* **90** (1986) 3393

21 Y Kayanuma *Phys Rev B* **38** (1988) 9797

22 R Rosseti, R Hull, J M Gibson and L E Brus *J Chem Phys* **82** (1985) 552

23 R Rosseti, R Hull, J M Gibson and L E Brus *J Chem Phys* **83** (1985) 1406

24 Y Wang, N Herron, W Mahler and A Suna *J Opt Soc Am B* **6** (1989) 808

25 N Herron, Y Wang and H Eckert *J Am Chem Soc* **112** (1990) 1322

26 V L Colvin, A P Alivisatos and J G Tobin *Phys Rev Lett* **66** (1991) 2786

27 C J Sandroff, D M Hwang and W M Chung *Phys Rev B* **33** (1986) 5953

28 Y Wang, A Suna, W Mahler and R Kawoski *J Chem Phys* **87** (1987) 7315

29 A P Alivisatos *Science* **271** (1996) 933

30 J Nanda, B A Kuruvilla, K V P M Shafi and D D Sarma In *Physics of Semiconductor Nanostructures* (Ed. K P Jain) Narosa Publishing House New Delhi (1997)

31 K K Nanda, S N Sarangi, S Mohanty and S N Sahu *Thin Solid Films* **322** (1998) 21; K K Nanda, S N Sarangi and S N Sahu *Nanostr Mater* **10** (1998) 1401

32 Y Tian, C Wu, N Kotov and J H Fendler *Adv Mater* **6** (1994) 959

33 X K Zhao and L D McCormick *Appl Phys Lett* **61** (1992) 849

34 S Gallardo, M Gutierrez, A Henglein and E Janata *Ber Bunsenges Phys Chem* **93** (1989) 1080

35 M T Nenadovic, M I Comor, V Vasic, O I Micic *J Phys Chem* **94** (1990) 6390

36 M Mukherjee, A Datta and D Chakravorty *Appl Phys Lett* **64** (1994) 1159

37 Y Wang and N Herron *J Phys Chem* **91** (1987) 257

38 Y Wang and N Herron *J Phys Chem* **92** (1988) 4988

39 V Colvin, A Schlamp and A P Alivisatos *Nature* **370** (1994) 6488

40 H Mathieu, T Richard, J Allegre, P Lefebvre and G Arnaud *J Appl Phys* **77** (1995) 287

41 C Kaito, K Fujita and M Shiojiri *J Appl Phys* **47** (1976) 5161

42 T Arai, H Fujumura and I Umezu *Jap J Appl Phys* **28** (1993) 484

43 D Nesheva and Z Levi *Semicond Sci Tech* **12** (1997) 1319

44 O V Salata, P J Dobson, P J Hull and J L Hutchinson *Thin Solid Films* **251** (1993) 1

45 O V Salata, P J Dobson, P J Hull and J L Hutchinson *Advanced Materials* **6** (1994) 772

46 R Pal, D Bhattacharya, A B Maity, S Choudhury and A K Pal *Nanostr Mater* **4** (1994) 329

47 P Gupta, R Pal, D Bhattacharya, S Choudhury and A K Pal *Phys Stat Solidi* **148** (1995) 459

48 E A Ponomarev, A Albu-yaron, R Tenne and C Levy Celement *J Elec Soc* **144** (1997) L277

49 K K Nanda and S N Sahu *Phys Rev B* **58** (1998) 15405

50 R K Pandey, S N Sahu and S Chandra *Handbook of Semiconductor Electrodeposition* Marcel Dekker Inc (1996)

51 Y Golan, B Alperson, J L Hutchinson, G Hodes and I Rubinstein *Advanced Mater* **9** (1997) 236

52 R Thielsch, T Bohme, R R Eiche, D Schlafer, H D Bauer and H Bottcher *Nanostr Mater* **10** (1998) 131

53 K C Yi and J H Fendler *Langmuir* **6** (1990) 1519

54 J Y Wang, R A Uphaus, S Ameenuddin and D A Rintoul *Thin Solid Films* **242** (1994) 127

55 L Motte, C P Petit, L Boulanger, P Lixon and M Pileni *Langmuir* **8** (1992) 1049

56 X Zhao, O Schoenfeld, Y Aoyagi and T Sugano *J Phys D: Appl Phys* **27** (1994) 1575

57 M Zhu, G Chen and P Chen *Appl Phys A* **65** (1997) 195

58 Y He, C Yin, G Cheng, L Wang and X Liu *J Appl Phys* **75** (1994) 797

59 P Melinon, P Keghelian, B Prevel, A Perez, G Uiraud and J LeBrusq *J Chem Phys* **107** (1997) 10278

60 C E Bottani, C Mantini, P Milani, M Mafredini, A Stella, P Toginini, P Cheyssac and R Kolman *Appl Phys Lett* **69** (1997) 2409

61 S Nozaki, S Sato, A Denda, H Ono and H Morisaki *Mat Res Soc Symp* **358** (1995) 133

62   S S Sato. S Nozaki. H Morisaki and M Iwase *Appl Phys Lett* **66** (1995) 3176

63   S Nozaki. S Sato. H Ono. H Morisaki and M Iwase *Nuclear Instr Method Phys Res B* **121** (1997) 455

64   K K Nanda and S N Sahu *Appl Surf Sci* **119** (1997) 50

65   A Iwamoto, T Yoshinobu and H Iwasaki *Phys Rev Lett* **72** (1994) 4025

66   H You. R P Chiarello. H K Kim and K G Vandervoort *Phys Rev Lett* **70** (1993) 2900

67   G W Mbise. G A Niklasson and C G Granqvist *Solid State Commn* **97** (1996) 965

68   K K Nanda, S N Sarangi and S N Sahu *Appl Surf Sci* **133** (1998) 293

69   S N Sahu, S N Sarangi, D Sahoo, B Patel, S Mohanty and K K Nanda *Novel Materials Design and Properties* (Ed. B K Rao and S N Behera) Nova Publisher New York (1998) 236

70   A P Alivisatos *J Phys Chem* **100** (1996) 13226

71   M C Klein, F Hache, D Ricard, C Flytzanis *Phys Rev B* **42** (1990) 11123

72   N F Borrelli, D W Hall, H J Holland and D W Smith *J Appl Phys* **61** (1987) 5399

73   N R Kulish. V P Kunets and M P Lisitsa *Superlattices and Microstructures* **22** (1997) 341

74   A A Guzellian, U Banin, A V Kadavanich, X Peng and A P Alivisatos *Appl Phys Lett* **69** (1996) 1432

75   S H Tolbert and A P Alivisatos *J Chem Phys* **102** (1995) 4642

76   J Woltersdorf, A S Nepuko and E Pippel *Surf Sci* **106** (1981) 64

77   R W Cahn *Nature* **323** (1986) 668

78   J Maddox *Nature* **330** (1987) 599

79   C J Coombes *J Phys F* **2** (1972) 441

80   P Buffat and J-P Borel *Phys Rev A* **13** (1976) 2287

81   P R Couchman and W A Jesser *Nature* **269** (1977) 481

82   T Castro, R Reifenberger, E Choi and R P Andres *Phys Rev B* **42** (1990) 8548

83   A N Goldstein *Appl Phys A* **62** (1996) 33

84   R Kofman. P Cheyssac, R Garrigos, Y Lereah and G Deutschar *Z Phys D* **20** (1991) 267

85   T Ben David *et al Philoshophical Magazine A* **71** (1995) 1135

86   H W Sheng, Z Q Hu and K Lu *Nanostructured Materials* **9** (1997) 661

87   P M Valov and V I Leiman *JETP Lett* **66** (1997) 511

88   M Schimdt, R Kusche, B V Issendorff and H Haberland *Nature* **393** (1998) 238

89   P Pawlow *Z Phys Chem* **65** (1990) 1

90   K J Hanszen *Z Phys* **157** (1960) 523

91   M Wautelet *Eu J Phys* **16** (1995) 283

92   C L Briant and J J Burton *J Chem Phys* **63** (1975) 2045

93   R D Etters and J Kaelberer *J Chem Phys* **66** (1977) 5112

94   J Jellinek, T L Beek and R S Berry *J Chem Phys* **87** (1987) 545

95   R S Berry, J Jellinek and G Natanson *Phys Rev A* **30** (1984) 919

96   F Ercolessi. W Andereoni and E Tosetti *Phys Rev Lett* **66** (1991) 911

97   R R Roy and B P Nigam *Nuclear Physics Theory and Experiment* John Wiley & Sons Inc New York (1967) Ch 5

98   S V Goponenko *SPIE Proc* **2801** (1995) 2

99   S V Goponenko *Semiconductors* **30** (1996) 577

100 A Henglein *Chem Rev* **89** (1989) 1861

101 L E Brus *Appl Phys A* **53** (1991) 465

102 D Gallagher, W E Heady, J M Racz and R N Bhargava *J Cryst Groth* **138** (1994) 970

103 S Mahamuni. A Z Khosravi. M Kundu. A Kshirsagar, A Bedekar. D B Avasare, P Singh and S K Kulkarni *J Appl Phys* **73** (1993) 5237

104 W Vogel. J Urban, M Kundu and S K Kulkarni *Langmuir* **13** (1997) 827

105 Y Golan, B Alperson, J L Hutchinson and G Hodes *Advanced Matter* **9** (1997) 236

106 D J Norris and M Bawendi *J Chem Phys* **103** (1995) 5260

107 P Roussignol, D Ricard, C Flytzavuis and N Neuroih *Phys Rev Lett* **62** (1989) 312

108 N Kumbhajkar, S Mahamuni, V Leppert and S H Risbud *Nanostr Mater* **10** (1998) 117

109 A M de Paula. L C Barbosa, C H B Cruz, O L Alves, J A Sanjurjo and C L Cesar *Superlattices and Microstru* **23** (1998) 1103

110 K Zhu, J Shi and L Zhang *Solid State Comm* **107** (1998) 79

111 U Banin. J C Lee, A A Guzelian, A V Kadavanich and A P Alivisatos *Supper Lattice and Microstru* **22** (1997) 559

112 H Uchida, C J Curtis and A J Nozik *J Phys Chem* **95** (1991) 5382

113 N M Dimitrijevic and P T Kamat *Radiat Phys Chem* **32** (1988) 53

114 Y Nosaka, N Ohta and H Miyama *J Phys Chem* **94** (1990) 3752

115 X K Zhao and L D McCormick *Appl Phys Lett* **61** (1992) 849

116 B G Potter and J H Simon Jr *Phys Rev B* **37** (1989) 10838

117 E A Ponomarev. A Albu-Yaron, R Tenne and C Levy-Clement *J Electrochem Soc* **144** (1997) L277

118 A Kornowski, R Eichberger, M Giersig, H Weller and A Eychmuller *J Phys Chem* **100** (1996) 12467

119 S Furukawa and T Miyasato *Jpn J Appl Phys* **27** (1988) L2207

120 H Miguez, V Fornes, F Meseguer and C Lopez *Appl Phys Lett* **69** (1996) 2347

121 L E Brus *IEEE J Quan Electron* **22** (1986) 1909

122 P E Lippens and M Lannoo *Phys Rev B* **39** (1989) 10935

123 R Rossetti, J L Ellison. J M Gibson and L E Brus *J Chem Phys* **80** (1984) 4464

124 S V Gaponenko *Optical Properties of Semiconductor Nanocrystals* Cambridge Press (1998) Ch 2

125 T Arai. T Yoshida and T Ogawa *J Appl Phys* **26** (1987) 396

126 T Arai. H Fujumura. I Umezu. T Ogawa and A Fuji *Jpn J Appl Phys* **28** (1989) 484

127 W Chem. Y Xu. Z Lin, Z Wang and L Lin *Solid State Commn* **105** (1998) 129

128 M Agata, H Kurase, S Hayashi and K Yamamoto *Solid State Commun* **76** (1984) 1061

129 I Umezu, T Ogawa and T Arai *Jpn J Appl Phys* **28** (1989) 447

130 P Roussignol, D Ricard, K C Rustagi and C Flytzanjs *Opt Commn* **55** (1985) 143

131 A A Khosravi, M Kundu, B A Kuruvilla, G S Sekhawat, R P Gupta, A K Sharma, P D Vijas and S K Kulkarni *Appl Phys Lett* **67** (1995) 2506; *Phys Rev B* **40** (1989) 5544

132 S Hayashi and H Kanamori *Phys Rev B* **26** (1982) 7079

133 A Mlayah, A M Brugman, R Carles, J B Renucci, M Ya Valakh and A V Pogorelov *Solid State Commn* **90** (1994) 567

134 S Hayashi, H Sanda, M Agata, and K Yamamoto *Phys Rev B* **40** (1989) 5544

135 S Ushioda, A Aziza, J B Valdez and G Mattei *Phys Rev B* **19** (1979) 4012

136 K K Nanda, S N Sarangi, S N Sahu, S K Deb and S N Behera *Physica B* **262** (1999) 31

137 G C Papavassilou *J Solid State Chem* **40** (1981) 330

138 T D Krauss, F W Wise and D B Tanner *Phys Rev Lett* **76** (1996) 1376

139 T D Krauss and F W Wise *Phys Rev B* **55** (1997) 9860

140 M Rajalakshmi, T Sakuntala and A Arora *J Phys Condens Matter* **9** (1997) 9745

141 B Champagnon, B Andrianasolo and E Duval *J Chem Phys* **94** (1991) 5237

142 S N Sahu, M J Antonio and C Sanchez *Solar Energy Mater and Solar Cells* **43** (1996) 223

143 G Hodes, J D Howell and L M Peter *J Electrochem Soc* **139** (1992) 3136

144 A B Maity, D B Bhattacharya, S R Sharma, S Choudhury and A K Pal *Nanostr Mater* **5** (1995) 717

145 B K Patel, K K Nanda and S N Sahu *J Appl Phys* **85** (1999) 3666

146 M V Artemyev, V Sperling and U Woggon *J Appl Phys* **81** (1997) 6975

147 D Vanmaekelbergh, A Koster and F I Martin *Adv Mater* **9** (1997) 525

148 J Van de Lagemaat, M Plakman, D Vanmaekelbergh and J J Kelly *Appl Phys Lett* **69** (1996) 2246

149 H P Maruska, F Namavar and N H Kalkhoran *Appl Phys Lett* **61** (1992) 1338

150 A M Cowley *J Appl Phys* **37** (1966) 3024

151 U Rothlisberger, W Andreoni and M Perrinello *Phys Rev Lett* **72** (1994) 665

152 K K Nanda and S N Sahu *Soild State Comm* (1999) 671

153 T Arai, T Yoshida and T Ogawa *J Appl Phys* **26** (1987) 396

154 K K Nanda, S N Sarangi and S N Sahu *J Phys D Appl Phys* **32** (1999) 2306

155 M G Bawendi *et al. Phys Rev Lett* **65** (1990) 1623

156 A C Seabaugh, J H Luscomb and J N Randal *J Future Electron Dev* **3** (1993) 9

157 M A Kastner *Rev Modern Phys* **64** (1992) 849

158 D L Klein, R Roth, A K L Lim, A P Alivisatos and P L Mc Euen *Nature* **389** (1997) 699

159 J Nanda, K S Narayan, B A Kuruvilla, G L Murthy and D D Sarma *App Phys Lett* **72** (1998) 1335

160 M V Artemyev, V Sperling and V Woggon *J Appl Phys* **81** (1997) 6975

161 T Toyama, Y Kotani, H Okamoto and H Kida *Appl Phys Lett* **72** (1998) 1489

OPTICAL PROCESSES IN NANOCRYSTALLINE SEMICONDUCTOR MATERIALS

S CHAUDHURI AND A K PAL

Department of Materials Science, Indian Association for the Cultivation of Science, Calcutta-700032 (India)

Optical processes in nanocrystalline semiconductors with special reference to the absorption and photoluminescence phenomena are discussed. Recent developments in the areas of several II-VI semiconductors *e.g.* ZnS and ZnSe along with their alloy ZnS_xSe_{1-x} (x~0.05) in nanocrystalline form are specially focussed in this report.

Key Words: Nanocrystalline Films; Optical Process; II-VI Semiconductors; Absorption; Photoluminescence

Introduction

In recent years advances in the areas of synthesis and characterization of semiconductors indicated that more exciting opportunities are lying ahead if the structure be scaled down to nanometer level[1-5]. Below a critical grain size, the characteristic properties of a material changes and become quite different from the corresponding bulk solid. Depending on the material concerned, the size dependent properties of interest may be related to mechanical, optical, electrical, electronic and optoelectronic applications. Considerable research activities in these areas have recently been demonstrated for different nanostructured semiconducting materials. The nanoparticles may be obtained as colliods, free standing powders as well as thin films. Structural and optical properties of the nanocrystalline materials may be investigated by different techniques such as, X-ray diffraction, transmission electron microscopy, atomic force microscopy, photoluminescence, optical transmittance, Raman studies etc. Due to the three dimensional carrier confinement there may be interesting properties[4,6-8] involving singularities in the density of states and improved linear and nonlinear optical responses[9,10]. From technological point of view II-VI semiconductors in nanocrystalline thin film form are of current interest for the realization of frequency selective lasers and photodetectors[11,12] whose performances may be modulated drastically by the shapes and sizes of the nanocrystallites. In addition, semiconductor nanostructures may be used to fabricate memories and microprocessors resulting in computer revolution. Possibility of obtaining quantum wells and quantum wires have practically revolutionized the semiconductor device physics. In semiconductor nanocrystallites or zero dimensional quantum dots a considerable fraction of the atoms reside on the surfaces of the devices or quantum dots and they consist of as few as 10^3–10^6 atoms. The carrier confinement resulting from band structure modification produces interesting physical properties with potential application in optical devices. The dependence of the electronic states of the quantum dots on the surrounding medium are not clearly understood till now. The optical properties of the quantum dots show blue shift due to carrier confinement. The quantum confinement stabilizes the excitonic effect and photoluminescence due to excitonic recombination may be expected at a higher temperature.

The experimental observations published so far on nanocrystalline materials were mainly on the elemental or binary compound semiconductors. Wide gap II-VI semiconductors, specially zinc chalcogenides, were the subject of numerous studies[9-10,13-17] in the past due to their high potential for various device applications. It may be mentioned here that the preparation of high quality doped ZnS has an inherent problem due to self-compensation effect. Most of the previous works on ZnS were concentrated on understanding and solving the problem of effective doping. Growth of ZnS layers on foreign substrates like GaAs was also the subject of many investigations in the past due to its use as thin film electroluminescent devices for flat panel displays[9]. Chen *et al.*[18] studied the absorption and luminescence in ZnS nanocrystals prepared by chemical precipitation route. They attributed the observed broad absorption band below the

absorption edge to the surface states present in the film. *Scholz et al.*[19] prepared ZnS nanocrystalline powders by using a chemical route and observed that the optical extinction spectra could be explained adequately by Mie scattering theory[20]. There is a need for more meaningful studies on this important material in nanocrystalline form so that the electron transport and optical processes in the material could be understood more faithfully. In recent times, ZnSe and ZnS_xSe_{1-x} alloys have also been extensively studied[21-26] for the realization of blue-light emitting diodes (LED) and laser diodes (LDs). Effective control of the electrical properties through doping (especially p-type) and reduction of lattice mismatch with GaAs substrate were the key issues to be investigated critically before these materials could be fruitfully exploited in the device technology. ZnS_xSe_{1-x} layers with x ~ 0.05-0.08 on GaAs which are perfectly lattice matched to the substrate[21,26] are well suited for fabricating LEDs and optoelectronic device applications in the blue-green spectral region.

A considerable progress has taken place in the theoretical understanding of the optical processes in nanocrystalline semiconductors, in general. Studies on the coherent transient optical effects in semiconductor nanostructures irradiated by lasers is one of the most interesting areas in current years. Here, we review the optical processes in nanocrystalline semiconductors, in general, with emphasis on two binary II-VI semiconductors ZnS and ZnSe and their alloy ZnS_xSe_{1-x} (x~0.05).

Preparation of Nanostructured Material

For the deposition of nanostructured materials different workers have used different techniques. High pressure sputtering, colloidal suspension, insertion of nanoparticles in porous zeolites, inclusion in glass prepared by conventional melting process etc. are worth to mention. CdS nanocrystallites having average size of 2.2 nm and 4.4 nm were synthesized by Nanda *et al.*[27] by a high temperature synthetic route. Focussed ion beams were also adopted by the workers for attaining structures below one micron. In fact, ionic exposures are useful to generate close packed structures with certain dimensional variation (100-600 nm). Deep UV radiation may also be used as a structure resolving tool. Among different techniques mentioned above, high pressure sputtering[27] is most attractive for preparing nanostructured

material in thin film form and this technique is discussed here in some detail.

It is known that during sputtering the substrate temperature increases due to the impact of the particles ejected from the target particularly when the deposition is carried out at a stretch for a time longer than several minutes. This results in the increase of grain size through the increase of the adatom mobilities culminating in the coalescence of the crystallites. So, in order to get nanocrystalline films, sputtering should be done intermittantly at regular intervals of time to allow the oncoming adatoms to release their thermal energy before a second deposition is made. An electronically controlled shutter may be logically connected to the output of a thermocouple for this purpose, so that, the deposition is automatically stopped by the shutter whenever an increase in substrate temperature is recorded. This sequential sputtering is very useful for obtaining nanocrystalline films with controlled grain sizes throughout the thickness. Banerjee *et al.*[28] and Mandal *et al.*[29] have reported studies on optical and electrical properties of ZnSe[28,29] and ZnS[30] in nanocrystalline thin film form by using this sequential sputtering technique where the crystallite size was comparable to or less than the bulk exciton Bohr radius. Properties of $ZnS_{0.05}Se_{0.95}$ films, prepared by the same technique, have been studied by Gangopadhyay *et al.*[31].

(i) ZnS Films

Mandal *et al.*[29] deposited ZnS films onto quartz and freshly cleaved NaCl substrates by d.c. magnetron sputtering of a ZnS target (99.999%) in argon plasma at system pressure of ~40 Pa. The films were deposited at different substrate temperatures (210-300 K) and the duration of deposition was varied. The substrates were placed on a heavy copper block which could be cooled by liquid nitrogen or heated electrically to attain the desired temperature during deposition. The temperature of the substrate could be monitored and controlled by a copper-constantan thermocouple using an on/off electronic temperature controller. Before starting the actual deposition, the target could be pre-sputtered with a shutter located in between the target and the substrate. This shutter was also used to control the deposition time. All the depositions were performed at 1.5 kV and 50 mA with the target (2.5 cm dia) to substrate distance of ~2.5 cm.

Three sets of nanocrystalline ZnS films with different thicknesses of the order of ~10 nm, 15 nm and 40 nm were deposited by Mandal et al.[29] with substrate temperature within 210-300 K, corresponding to deposition times of ~8, 15 and 30 minutes respectively. An increase in substrate temperature by 5 K could be observed if the films were sputter-deposited continuously for 5-7 minutes. This rise in temperature was found to be localised at the film surface and no evidence of increase in the temperature of the copper substrate holder was observed. This culminated in unavoidable agglomeration of the adatoms and the films thus deposited did not have the signature of the nanocrystallites. To overcome this, the films were deposited in sequence of one minute by allowing them to dissipate their thermal energy for the next minute or so before the next deposition was started. Size quantization could be retained by depositing the films in the above sequence. The extent of size quantization remains the same for films having different thicknesses when deposited at a particular set of substrate temperature and system pressure in the plasma chamber. The films deposited onto quartz substrates were used for electrical/optical studies while the films deposited onto NaCl substrates were used for TEM observation.

(ii) ZnSe Films

Banerjee et al.[28] deposited nanocrystalline ZnSe films by d.c. magnetron sputtering of a ZnSe pellet (99.999% purity) in argon plasma at system pressures of 20 and 30 Pa. The films were deposited at 1.5 KV and 100 mA with target to substrate distance ~2.5 cm. Glass (Corning) or quartz (fused silica) and NaCl crystals were used as the substrates for optical and microstructural studies respectively.

(iii) $ZnS_{0.5}Se_{0.95}$ Films

Films with pre-assigned thicknesses were deposited by Ganguly et al.[31] by using the sequential sputtering technique, discussed above. Three sets of films with different thicknesses were deposited with substrate temperatures (T_s) of 203, 233 and 263 K. For each of these T_s values, films were deposited for two different deposition times (20 and 25 minutes) and for each deposition time and substrate temperature, the pressure of the plasma chamber was varied between 15-30 Pa. The thicknesses of the films, thus produced varied within 10-40 nm. Films were simultaneously deposited on quartz (for optical transmittance measurement), microscope grid

(for microscopy) and GaAs (for photoluminescence measurement).

Microstructure of Nanocrystalline Films

The ZnS nanocrystalline films exhibited (Fig. 1) a zinc blende crystal structure as depicted by transmission electron diffraction pattern. The diffraction pattern showed three broad rings which could be assigned to the (111), (220) and (311) planes. The ring for (111) planes was most intense and broad. The intensity of the ring for (220) planes was weaker than those for both the rings. The widths of the rings for films deposited at lower substrate temperature (i.e. films having lower crystallite size) were broader than that for films deposited at higher substrate temperature. Fig. 2 shows the variation of crystallite size (D) with deposition temperature (T_s) for ZnSe films deposited
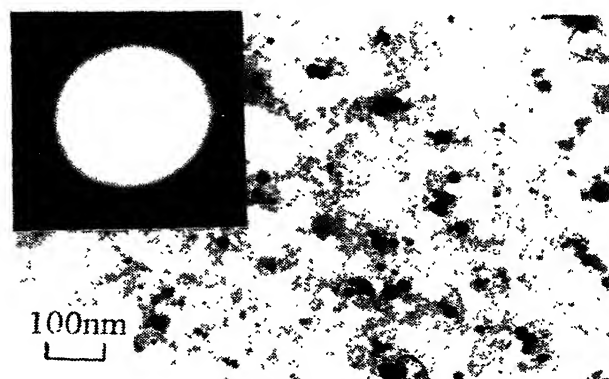

Fig. 1   TEM micrograph and corresponding diffraction pattern of a representative nanocrystalline ZnS film deposited at substrate temperature T_s = 233 K and pressure ~40 Pa
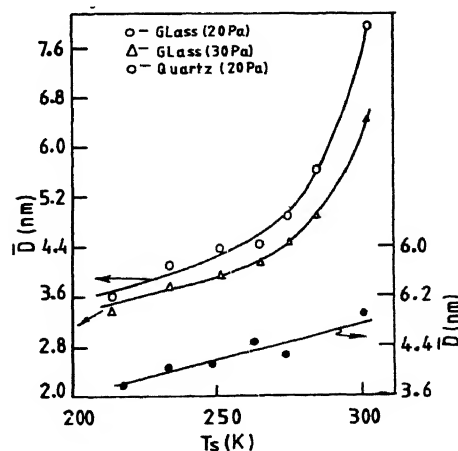

Fig. 2   Variation of crystallite size (D) with deposition temperature (T_s) for nanocrystalline ZnSe films deposited on glass and quartz substrates

on glass and quartz substrates. Fig. 3 (a & b) shows the TEM micrographs and the corresponding electron diffraction pattern of two representative $ZnS_{0.05}Se_{0.95}$ films deposited onto microscope grids at 233 K (15 Pa for 25 minutes) and 203 K (30 Pa and 20 minutes). One can observe that the films consisted of discrete nanocrystallites of dimensions varying between 1.7-2.1 nm and the diffraction patterns are mainly dominated by faint rings with a central halo. The films exhibited zinc blende structure and the rings could be identified as arising from (111), (220) and (311) planes.

Optical Absorption in Nanocrystalline Film

The absorption coefficients (α) of the nanocrystalline ZnS, ZnSe and $ZnS_{0.5}Se_{0.95}$ films were evaluated by measuring transmittance and reflectance[32] by a UV-VIS-NIR spectrophotometer (Hitachi U-3410). The band gaps (E_g) were determined by extrapolating $(\alpha h\nu)^2$ versus photon energy ($h\nu$) plots. The absorption trace for a representative film of nanocrystalline ZnS deposited at a substrate temperature of ~213 K with 30 minutes of deposition time is shown in Fig. 4. It may be noted that the variation of the absorption (α)
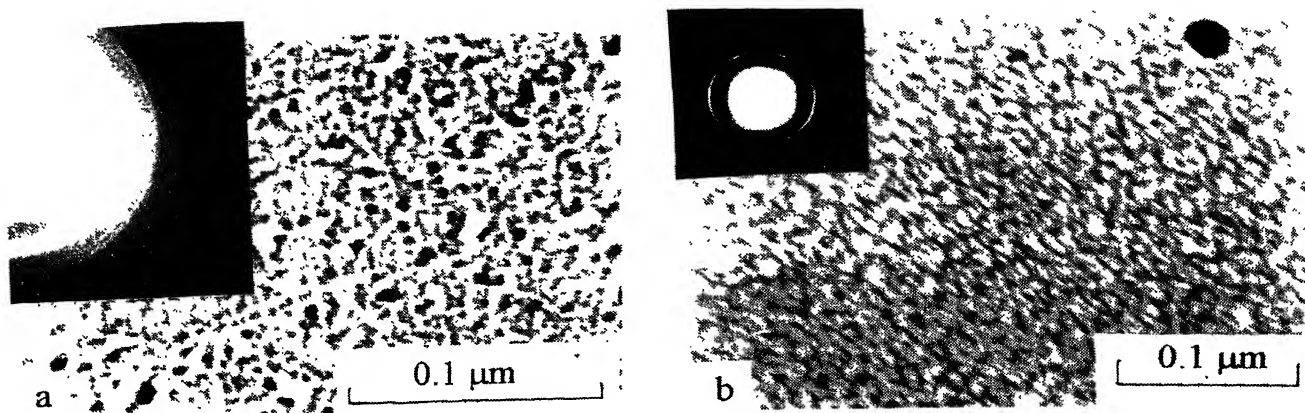

Fig. 3   TEM micrographs and corresponding diffraction patterns of two representative nanocrystalline $ZnS_{0.05}Se_{0.95}$ films deposited at (a) T_s=233 K (15 Pa for 25 minutes) and (b) T_s=203 K (30 Pa for 20 minutes)
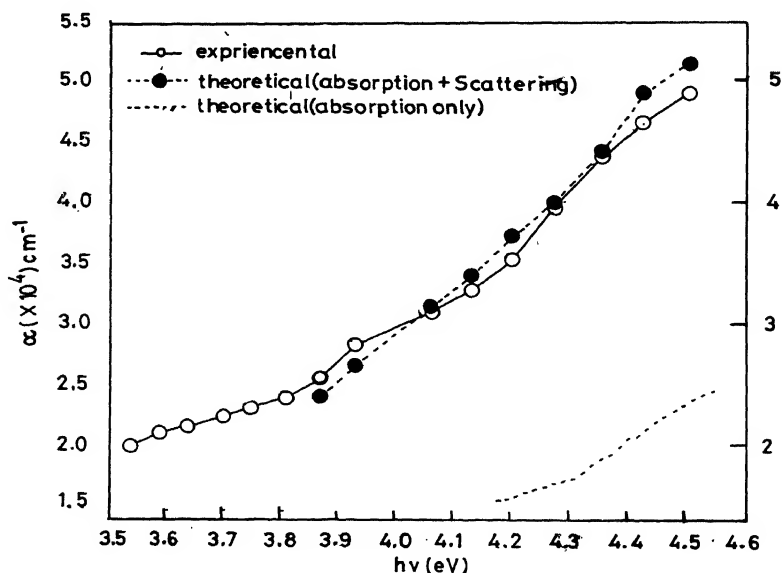

Fig. 4   Absorption trace of a representative nanocrystalline ZnS film deposited at a substrate temperature of ~213 K with 30 minutes of deposition

with the wavelength (λ) of the incident radiation were nearly the same for all the films. It was noticed that the fall of the absorption tail was sharper for films deposited for higher deposition time than those deposited for lower duration (*i.e.* for thinner films).

Fig. 5 shows the variation of band gaps of several nanocrystalline ZnS films deposited at different substrate temperatures and deposition times. The band gap values were always found to be higher compared to the bulk value. It may be noted that the films deposited at 213 K showed the maximum shift ($\Delta E_g = E_g - E_{g\,Bulk}$) of band gap from its bulk value (3.6 eV). The amount of shift in the band gap (ΔE_g) decreased substantially as the deposition temperature was increased. This is basically due to the fact that the films deposited at lower substrate temperature had smaller sizes of the nanocrystallite which was reflected in larger blue shift. Presence of smaller crystallite sizes would indicate the presence of an increasing amount of amorphous phase mixed with the nanocrystallites. This has been reflected in the gradual departure of the sharpness of the fall of the trace of

transmittance (T_r) versus wavelength (λ) for films deposited at lower substrate temperatures. The average particle size, ($\overline{R}$), was measured from TEM studies and also from the curve fitting of the absorption data. It was observed that for a constant gas pressure in the chamber, the average particle size, ($\overline{R}$), increased (Fig. 6) with the increasing substrate temperature (T_S) upto ~300 K after which a sharp increase in the grain size was observed with increasing T_S. No agglomeration was observed till T_S ~300 K as the gas pressure probably did not cross the threshold limit for agglomeration. The crystallite size did not vary significantly as the deposition time was increased. The measurement of the band gaps of ZnS films deposited at higher temperature (> 320 K) indicated the films to be polycrystalline with band gap nearly equal to that of the bulk material.

Fig. 7 shows the room temperature optical absorption spectrum of a representative ZnSe film with band gap E_g=2.93 eV (for film deposited on glass). The shift of the fundamental band gap (due to the quamtum size effect) to the higher energy side in
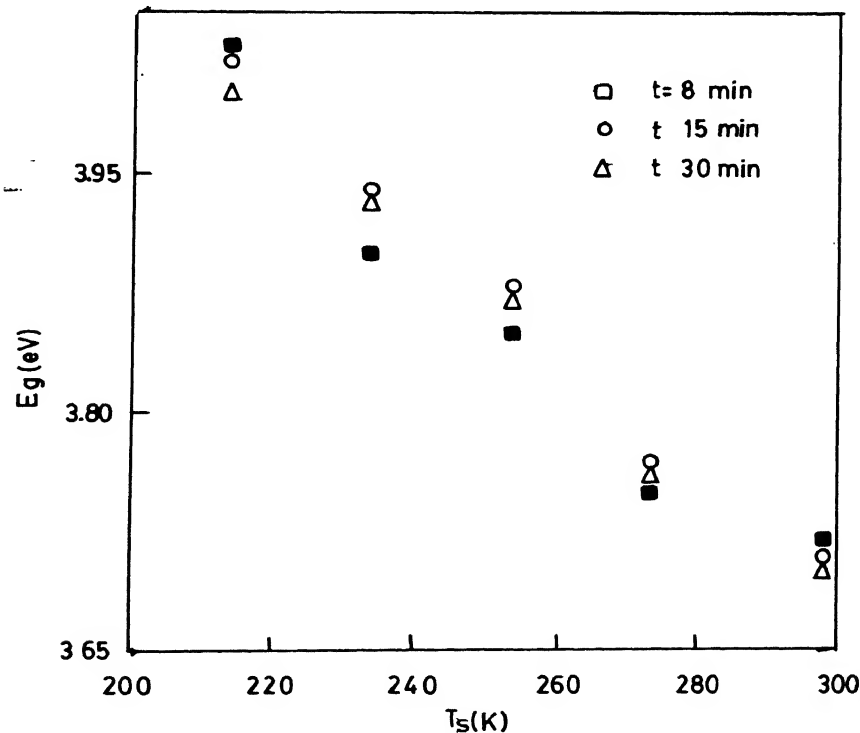

Fig. 5   Variation of band gap (E_g) of nanocrystalline ZnS films with substrate temperature (T_s) when deposited with various deposition times
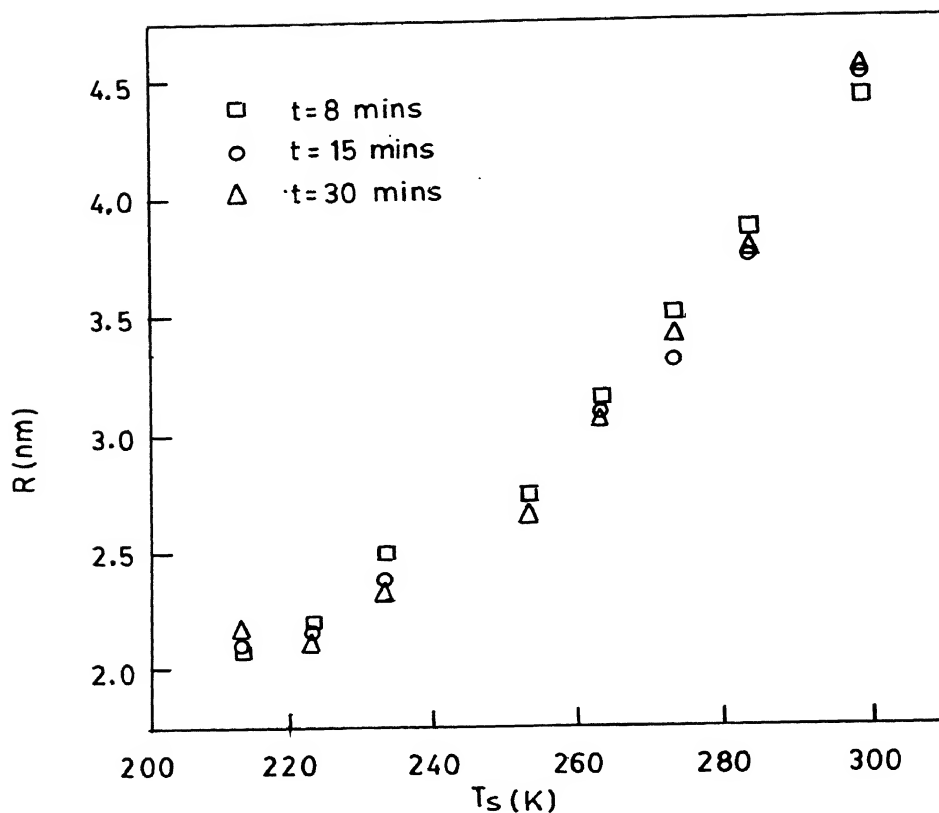
Fig. 6 (a) Variation of crystallite size (R) with substrate temperature (T_s) for nanocrystalline ZnS films deposited at various deposition
        times

comparison to the bulk value $E_g^0 = 2.7$ eV[33], may be
noted. Table I shows the band gap (E_g) and crystalline
radius (R) for different films deposited on glass
substrate. As the films consisted of large number of
nanocrystallites with different sizes and shapes, the
absorption peak corresponding to level to level interband
transitions was less sharp due to inhomogeneous
broadening and room temperature phonon broadening
effects[6,34,35]. Similar observations in other II-VI
nanocrystallites have already been reported[4,6,34,36,37].

It may be noted that for $ZnS_{0.5}Se_{0.95}$ films the
variation of the absorption coefficient (α) with energy
$(h\nu)$ of the incident radiation was nearly same for all
the films. The fall of the absorption tail was sharper
for films deposited for higher deposition time than
those deposited for lower duration $(i.e.$ for thinner
films). The band gap (E_g) values of the nanocrystalline
$ZnS_{0.05}Se_{0.95}$ films were always found to be higher
(Table II) compared to the bulk value of 2.71eV
obtained from the bulk values for ZnS and ZnSe

Table I

*Values of band gap (E_g) grain size (R) estimated from the optical
absorption studies of ZnSe films deposited on glass substrates at
substrate temperature (T_s)) and pressure P. Values of grain size
(R) from TEM studies (on NaCl substrate) are given*

| Film No.	T_s	P (Pa)	E_g (eV)	R (nm) Optical	R (nm) TEM
ZnSe-1	213	20	3.45	1.82	1.80
ZnSe-2	233	20	3.28	2.08	2.06
ZnSe-7	250	20	3.21	2.20	2.19
ZnSe-4	263	20	3.20	2.24	2.23
ZnSe-6	273	20	3.10	2.46	2.45
ZnSe-9	283	20	3.00	2.84	2.85
ZnSe-10	300	20	2.85	4.00	4.01
ZnSe-18	213	30	3.56	1.70	1.70
ZnSe-22	233	30	3.38	1.90	1.92
ZnSe-20	250	30	3.33	1.98	2.00
ZnSe-15	263	30	3.28	2.08	2.10
ZnSe-12	273	30	3.20	2.24	2.25
ZnSe-17	283	30	3.10	2.46	2.45
ZnSe-19	300	30	2.93	3.30	3.29
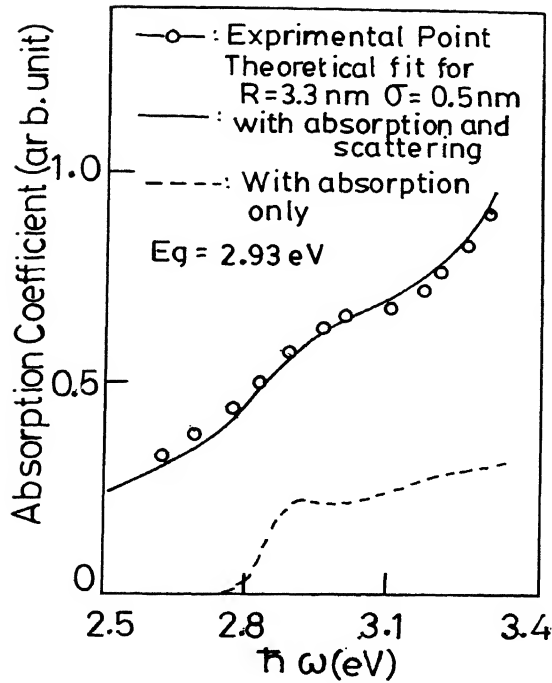
Fig. 7   Absorption spectra for a representative nanocrystalline ZnSe film deposited on glass at 300 K and 30 Pa

Table II

Values of average grain size (R) and band gap of nanocrystalline ZnS$_{0.05}$Se$_{0.95}$ films deposited at different conditions

Sample	Deposition Conditions	Band Gap E$_g$ (eV)	Grain Size (nm)
ZSS-2	15 Pa 25 mins. 203 K	3.38	1.99
ZSS-1	15 Pa 25 mins. 233 K	3.46	1.88
ZSS-3	15 Pa 25 mins. 263 K	3.30	2.12
ZSS-4	20 Pa 20 mins. 203 K	3.36	2.02
ZSS-5	30 Pa 20 mins. 203 K	3.58	1.74
ZSS-7	15 Pa 20 mins. 203 K	3.32	2.09
ZSS-8	15 Pa 20 mins. 233 K	3.55	1.78
ZSS-9	15 Pa 20 mins. 263 K	3.40	1.96

using bowing relation given by Newbury *et al.*[25]. It may be noted that the films deposited at ~203 K and 30 Pa showed the maximum shift ($\Delta E_g = E_g - E_{g\ Bulk}$) of band gap from its bulk value. The average particle size, ($\bar{R}$), was measured from TEM studies and also from the curve fitting of the absorption data. It was observed that the average particle size, ($\bar{R}$), did not show significant variation with the substrate temperature of deposition or gas pressure in the chamber. No agglomeration was observed till T_S ~300 K as the gas pressure probably did not cross the threshold limit for agglomeration. This observation is similar to that of nanocrystalline ZnS films. The crystallite size did not vary significantly as the deposition time was increased. It may be mentioned here that the bulk values of μ and E_g° for ZnS$_{0.05}$Se$_{0.95}$ were computed from the value of the bowing parameter[4] along with the value of ε_o obtained from the linear extrapolation of the bulk values of ZnS and ZnSe.

The increase of the fundamental band gap of the nanostructred materials due to the quantum size effect (QSE) is well established. For the sake of comparison, we estimated the band gaps of these nanocrystalline films from

$$E_g = E_g^0 + \frac{\hbar^2\pi^2}{2\mu R^2} - 1.786 \frac{e^2}{4\pi\varepsilon_o R} - 0.248 E_{RY}^* \qquad ... \quad (1)$$

for the strong confinement limit (*i.e* $R << a_B$) of QSE in nano material. For weak confinement limit (*i.e,* $R >> a_B$) we have:

$$E_g = E_g^0 + \frac{\hbar^2\pi^2}{2MR^2} - E_{RY}^* \qquad (2)$$

where $M = m_e + m_h$, m_e and m_h being the electron and hole effective masses respectively. In equation (1), R is the radius of the nanocrystallites, $E^*_{RY}(= e^2/4\pi\varepsilon_o a_B)$ is the effective Rydberg energy for the bulk exciton with a$_B$ as the corresponding Bohr radius ($= 4\pi\varepsilon_o \hbar^2/\mu e^2$), $\mu = [m_e m_h/(m_e + m_h)]$ being the reduced mass. E_g° and ε_o are the band gap and low frequency dielectric constant respectively of the bulk material. By utilizing the average particle size, ($\bar{R}$), values as obtained from TEM measurements, the E_g values of different films were estimated from the above equation which were found to agree well with those obtained directly from the absorption spectra.

As the nanocrystalline films consist of large number of nanocrystallites with different sizes and

shapes, the absorption peak corresponding to level to level interband transitions will be less sharp (Fig. 2) due to the enhanced phonon broadening and inhomogeneity broadening effects[34,35]. The origin of the broadening due to inhomogeneity is generally ascribed to the fluctuation in the shape and size of the grains in the film. The deviation from the perfectly spherical shape of the particles would likely modify the selection rule and the transitions forbidden for the spherical form might appear in real situation. More over, the size distribution of the nanocrystallites would culminate in the fluctuation in the energy subbands as inferred from eqs. (1) and (2). Thus, the superposition of all the discrete absorptions due to these combined effects will result in broadening of the experimentally observed spectrum. It may be mentioned here that in this treatment, we have not taken into account the effect of the fluctuation in the shape of the crystallites on the absorption spectrum due to the inherent complexity of the problem.

The broadening due to phonon would also exist besides the above inhomogeneous broadening. This intrinsic broadening would have a finite value at room temperature. Klein et al.[38] considered this energy broadening due to phonon interaction in nanocrystalline systems and assuming the nanocrystallites to be spherical in shape having Gaussian size distribution, the total absorption was expressed as[34,37]:

$$\alpha = \int_{R_{min}}^{R_{max}} P(R) \; \alpha \; (R) \; dR \qquad \text{... (3)}$$

where $P(R)$ is the probability of size distribution given by[34,39]:

$$P(R) = (R-R_{min}) \; (R_{max}-R) \; \exp \left(-\frac{R^2}{\delta^2}\right) \qquad \text{... (4)}$$

where R_{max} and R_{min} are the maximum and minimum diameters and δ is the half width of the distribution. $\alpha(R)$ is the absorption coefficient due to a nanocrystallite of radius R and can be written as[34,35]:

$$\alpha(R) = \frac{\omega}{n_o c \varepsilon_o} \; (C_o/V) \; \frac{\hbar\Gamma}{(E_g-\hbar\omega)^2 + (\hbar\Gamma)^2} \qquad \text{... (5)}$$

with,

$$C_o = \frac{2\pi e^2 \hbar^2}{m_e^2 (\hbar\omega)^2} \; |p_{cv}|^2 \qquad \text{... (6)}$$

where $\hbar\omega$ is the photon energy, n_o is the refractive index, c is the velocity of light, V is the volume of the spherical nanocrystallite and p_{cv}, the bulk optical matrix element, is given by[4]:

$$|p_{cv}|^2 = (m_e/3) \; \frac{E_g \; (E_g+\Delta)}{(E_g+2\Delta /3)} \qquad \text{.................(7)}$$

Δ being the spin-orbit splitting factor.

Optical Loss Due to Scattering

It is apparent from Fig. 4 that the optical absorption solely cannot explain the shape and magnitude of the experimental absorbance spectra at room temperature. It is true that a large amount of incident light would be scattered by the ultra small crystallites. In this case, the total intensity (I_{SC}) of the scattered light per unit volume for normal incidence may be given by using the Mie scattering theory[20]. In the limit where the crystallite dimensions are much less than the optical wavelength (λ):

$$I_{sc} = \int P(R) \; I_{sc}(R) \; dR \qquad \text{... (8)}$$

$$\text{with } I_{sc}(R) = (2/V) \left[(2\pi/\lambda) \; R^3 \; \frac{(n_o^2-1)}{(n_o^2-2)} \right]^2 \qquad \text{... (9)}$$

It may be noted that the authors did not consider the absorption due to surface traps and other impurities in these calculations as pointed out by Sekikawa et al.[40]. The theoretically simulated absorbance spectra for ZnS nanostructured films were obtained by using the eqs. (3) and (8) and are shown in Fig. 4. The amount of the optical loss due to scattering effect is easily estimated from the comparison between the theoretically simulated absorption curves. The values of different parameters utilized to compute the above simulated absorbance spectra for ZnS are as follows.

E_g=3.68 eV; m_e=0.27m_o; m_h=0.58m_o; ε_o=8.1; ε_∞=5.13; Δ=0.067; ω_{LO}=10.44 THz.

where, m_o is the free electron mass. It can be observed that the simulated spectra fitted well with $\overline{R}$ value of 3 nm (with a mean fluctuation of $\pm$ 0.5 nm) for ZnS. This also agreed well with the nanocrystallite sizes determined from the transmission electron microscopy (TEM) and shift in the band gap[30].

Fig. 7 shows the absorption spectra of nanocrystalline ZnSe films. The values of different parameters[33] utilized to compute the theoretical absorption spectra for comparison with the experimental spectra of nano-ZnSe films are[33,41]:

E_g^0=2.7 eV; m_e=0.16 m_o; m_h=0.6 m_o; ε_o=9.14; ε_∞=6.3; Δ=0.403 and ω_{LO} =7.59 THz.

Similar studies on ZnTe and CdS in nanocrystalline were reported by Mandal et al.[42a]. Kulkarni et al.[42b] synthesized sulphide nanoparticles with particle diameter <5 nm using a chemical route.

Photoluminescence of Nanocrystalline Films

(i) ZnS

Photoluminescence (PL) spectra of the ZnS nanocrystalline films were recorded at 100 K with an exciting wavelength of 300 nm. The PL spectra of the films had a peak in the range of 350-400 nm. It can be seen (Fig. 8) that the line shapes of the PL spectra are asymmetric and broad. The film deposited at lower substrate temperature showed broader PL peak. Shift of these PL peaks to higher energies for films deposited at lower substrate temperature (i.e. with lower crystallite size) was visible for all the films irrespective of their thickness (e.g. deposition time).

The appearance of the PL peaks at energies substantially lower than the band gap suggests that transitions from energy states in the band gap are being favoured for the luminescence process in these nanocrystalline ZnS films. This observation
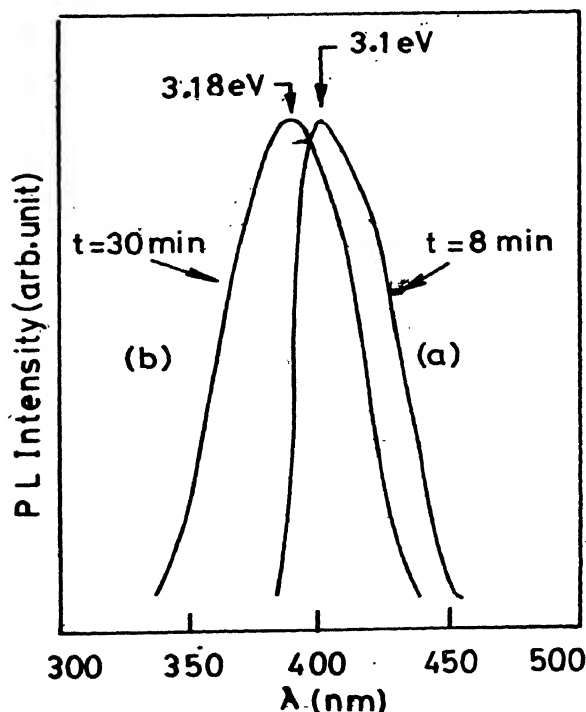

Fig. 8   PL spectra of two representative nanocrystalline ZnS films deposited at 233 K for (a) 8 minutes and (b) 30 minutes

may be ascribed to the presence of surface states of ZnS nanocrystallites constituting the film. This observation agrees well with that by Chen et al.[18]. The assignment of the surface states for the observed PL peak position at energies lower than band gap energy was also supported by the fluorescence and thermo-luminescence measurements made by them. The density of surface states in nanocrystalline films would increase with the decrease in crystallite size constituting the film due to the increase in surface to volume ratio in films having smaller crystallites. This would reduce the probability of excitonic emission via nonradiative surface recombinations[18,40]. The band edge or excitonic emission will thus be effectively overlapped with the absorption of the surface states and as such would show photoluminescence at energies less than the band gap. The position of the PL peak would depend on the size of the nanocrystallite i.e. the substrate temperature during deposition. It was observed that the films deposited at lower temperature had lower crystallite size and the PL peak was shifted to higher energies. It is also interesting to note that thinner films deposited at a particular substrate temperature indicated peak position (Fig. 8a) at lower energies than that for a thicker film (Fig. 8b) deposited at the same substrate temperature. This is in commensurate with the fact that the surface to volume ratio will be higher for thinner films than that of thicker films. Thus the observed PL spectra supports the so-called trapped luminescence arising from the surface states. Similar crystallite size dependence of the shift of surface emission has also been reported by Chestnoy et al.[43].

(ii) ZnSe

The room temperature photoluminescence (PL) spectra for three representative ZnSe films deposited on quartz at 233, 273 and 300 K are shown in Fig. 9. The shift of the PL peak to higher energies for films deposited at lower T_S with lower grain sizes is quite clear from this figure. Similar changes in the peak position of PL spectra of other nanocrystalline semiconductors have already been reported by several groups[44-47]. Considering the fact that the PL spectrum is due to the radiative recombination of the lowest lying excited states of the nanocrystallites, the semi-quantitative estimation of the dependence of PL peak position on the average grain radius $\bar{R}$ may be obtained from the frame-work of effective mass relation as given by eq. (1) for grains with $R < a_B$ (a_B being the Bohr radius).

(a) o at 300 K
(b) △ at 273 K
(c) ▫ at 233 K
—— Theritical fit with
(a) R=2.7 nm σ=0.35 nm
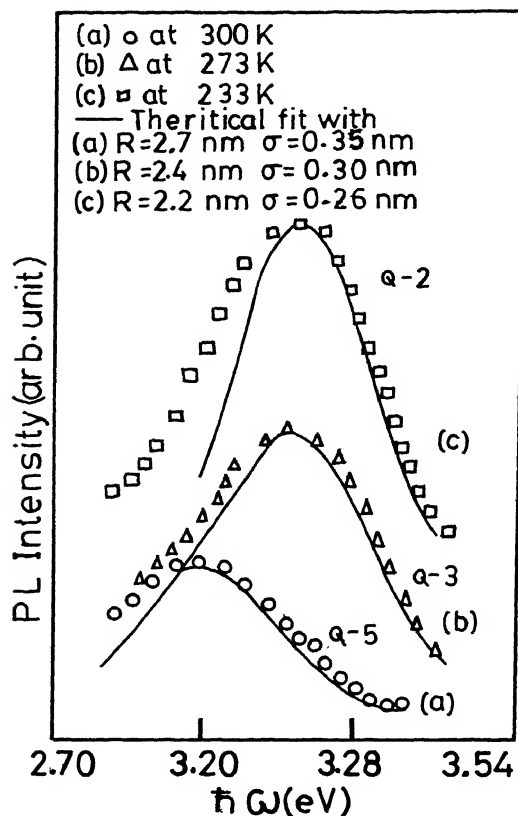(b) R=2.4 nm σ= 0.30 nm
(c) R=2.2 nm σ =0·26 nm

Fig. 9 Photoluminescence spectra of three representative nanocrystalline ZnSe films deposited on quartz substrate at 20 Pa and at different substrate temperatures as indicated in the figure

In general, the carrier confinement effect in semiconductor nanocrystallites stabilizes both excitons and corresponding luminescence due to excitonic recombinations even at room temperature. Systematic studies by different groups[48-50] indicated the presence of characteristic luminesence due to excitonic recombination in association with the significant contributions from impurities and surface states at the lower energy side of the PL spectrum. With the gradual decrease of the sizes of the nanocrystallites, the luminescence has been found to be dominated by band impurity and surface state transitions over the excitonic luminescence. However, the relative intensities depend on the excitation intensity. Ekimov et al.[44] have shown that with higher excitation intensity (so that the inter impurity luminescence becomes saturated) the transitions associated with the band to band free

electron and hole would dominate in the PL spectra even for samples with smaller (~5.7 nm) grain size. Although the intensity dependence of PL studies were not done (due to the limitation of our present experimental set-up), it is believed that in the ZnSe specimen the highly intense PL peak is mainly due to excitonic recombination. This is guided by the fact that in the reverse situation (i.e. if it is due to impurity and surface states, for the sake of argument), the excitonic emission would arise at still higher energy side of the PL spectra. Consequently, the theoretically estimated grain size would be smaller than that obtained from the TEM and optical absorption studies. Similar treatment have been done earlier by Kohno et al.[47] for Si nanocrystallites.

Besides the peak position, the line shape of the PL spectrum is essentially given by the inhomogeneous broadening which is due to the size distribution of grains. The theoretical line shape $I(\hbar\omega)$ of the PL spectrum between the lowest energy state of the electron and hole ($1s_e \rightarrow 1s_h$) in a quantum dot with radius R may be expressed as[47]:

$$I(\hbar\omega) \propto \int g(R)|f(R)|^2 \ \delta[\hbar\omega - E_L(R)] \ P(R) \ dR \quad \dots \ (10)$$

where $g(R)$ is the carrier recombination probability, $P(R)$ is the grain radius distribution function, $f(R)$ is the oscillator strength and $E_L(R)$ is the emission energy which is given by eq. (1). Within the frame work of the effective mass approximation[46], the parameter $|f(R)|^2$ is proportional to R^{-9}. Following Kohno et al.[47], the explicit form of carrier recombination probability $g(R)$ is given by

$$g(R) = 1 \quad \dots \ (11)$$

for $R > \overline{R}$, while for $R < \overline{R}$ we have :

$$g(R) = 2/\left[1 + (R/\overline{R})^2 \exp\left\{q\left(\frac{1}{R^2} - \frac{1}{\overline{R}^2}\right)\right\}\right] \quad \dots \ (12)$$

where

$$q = E_d/3\hbar\rho \ V_s \quad \dots \ (13)$$

Here E_d is the deformation potential due to electron phonon interaction, ρ is the mass density and V_s is the velocity of sound in the material. Using eqs. (1), (10), (11), and (12), together with the parameters[33] E_d = 8.6 eV, ρ = 5.28 g cm^{-3} and V_s = 4.4 km sec^{-1}, the theoretical fits of the line shape of PL spectra corresponding to the ZnSe films deposited at 233 K, 273 K and 300 K on quartz substrates are shown in Fig. 9. The estimated average crystallite size, obtained from this best fit to the PL line shape, also agreed well

with that obtained from the absorption spectra and TEM studies.

From Fig. 9 it also appeared that the PL line shape becomes asymmetric for films having relatively, smaller grain sizes. Andrianasolo et al.[48] reported similar observation and by deconvolution of such asymmetrical PL spectrum they suggested the presence of additional peak at lower energy side due to carrier recombination between surface states. Moreover, in all cases we have noticed a small Stoke's shift between the peaks due to absorption and PL effects. Such shift is prominent for films having relatively smaller grain sizes, as is evident from Fig. 10. It is speculated that this might be due to the enhanced carrier recombination from relatively larger amount of surface states in smaller nanocrystallites. Similar observation have also been noticed by other workers in different nanocrystalline systems[47-50].

The existence of surface states in the fundamental band gap region is in fact not surprising for films having small grain size. Hache et al.[50] also pointed out the possibility of pair-state formation of the surface states, one near the valence band and the other near the conduction band. With the decrease of grain size, the ratio of the surface states to the volume states (i.e. size quantised states) would increase. This is due to
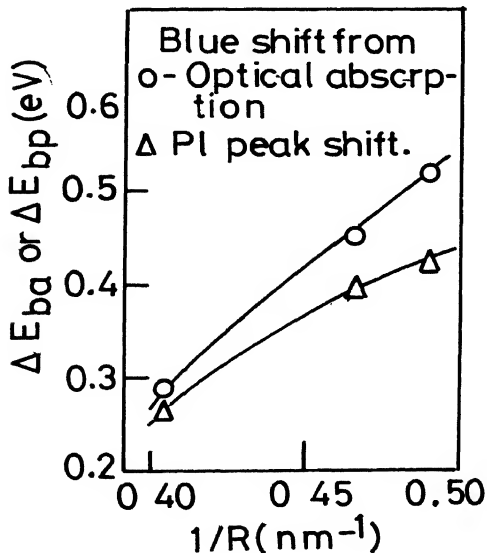
the fact that many more atoms will reside at the surface of the grain rather than at a volume site. It is important to note that these surface states are intrinsic states and delocalized over the entire surface of the sphere. In this way they participate in the optical processes similar to the volume states[50].

(iii) $ZnS_{0.05}Se_{0.95}$

Photoluninescence (PL) spectra of the nanocrystalline $ZnS_{0.05}Se_{0.95}$ films deposited on GaAs (100) were recorded (Fig. 11) at 300 K with an exciting wavelength of 300 nm. The PL spectra of the films are dominated by a peak in the range of 360-370 nm with a distinct shoulder around 397 nm. It can be seen that the line shapes of the PL spectra are asymmetric and broad. Shift of these PL peaks to higher energies for films having lower crystallite size was visible for all the films irrespective of their thicknesses (i.e. deposition time).

Fig. 10 Dependence of the blue shifts (ΔE_{bp} and ΔE_{ba}) of nanocrystalline ZnSe films, obtained from the optical absorption (ΔE_{ba}) and PL peak shift (ΔE_{bp}), on the 1/R, R being the average radius of the crystallites
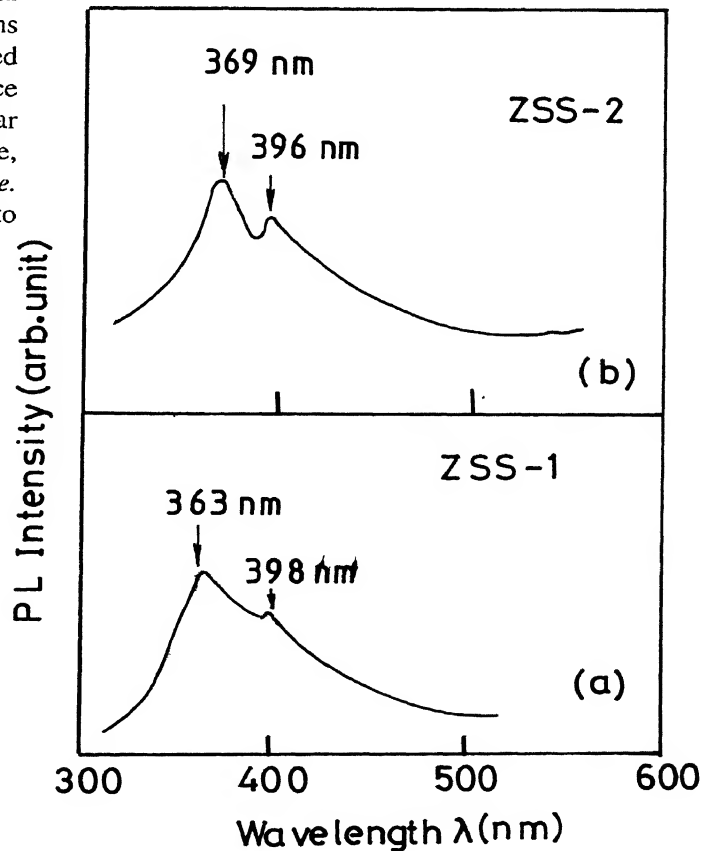

Fig. 11 PL spectra for two representative nanocrystalline $ZnS_{0.05}Se_{0.95}$ films deposited at 15 Pa for 25 minutes with substrate temperature : (a) 233 K and (b) 203 K

It could be observed that the sharp excitonic structure observed in the case of binaries (ZnS and ZnSe bulk) is replaced by a single, broad PL spectra for these nanocrystalline $ZnS_{0.05}Se_{0.95}$ films. This broadening may arise mainly due to alloy broadening and defect broadening. Alloy broadening may arise due to random distribution of sulphur atoms on selenium sites in these nanocrystalline films and as such an excited particle moving about the lattice would sense a varying local composition. As the lattice mismatch is small for films deposited onto GaAs, the broadening effect due to defects arising out of lattice mismatch may be minimal. But the surface states arising out of the enhanced ratio of surface atoms to the atoms constituting the main bulk of the $ZnS_{0.05}Se_{0.95}$ films would be very significant to cause defect related broadening. Similar observation for exciton line broadening in $ZnS_{0.05}Se_{0.95}$ epilayers grown on GaAs was reported by Newbury et al.[25]. The appearance of the shoulder at ~397 nm suggests the presence of transitions due to donor-acceptor (DA) pair formation. The origin of the DA transition may arise from Zn interstitials and/or sulphur vacancies causing donor levels and Zn vacancies causing acceptor states.

Conclusion

Nanocrystalline films of ZnS, ZnSe and $ZnS_{0.5}Se_{0.95}$ were deposited by high pressure magnetron sputtering technique. Films with different crystallite sizes were obtained by varying the substrate temperature during deposition and the thickness of the films could also be varied without sacrificing the blue shift. The films exhibited predominant zinc blende structure with intense rings for (111), (220) and (311) planes. The absorption behaviour in nanocrystalline films could not be explained from level to level transitions due to size quantization only. Significant contributions from

inhomogeneity and phonon broadening effects along with optical losses due to scattering are required to be considered to explain the observed absorption behaviour. The PL spectra for nanocrystalline films indicated a presence of a broad absorption band at energy less than band gap energy. This suggested that transitions from energy states in the band gap are being favoured for luminescence process which could be attributed to the surface states present in these films. The thinner films indicated PL peaks at lower energies than those of thicker films in agreement with the higher surface to volume ratio for thinner films.

The PL spectra for nanocrystalline $ZnS_{0.05}Se_{0.95}$ films indicated the presence of a broad excitonic peak around 365 nm with a distinct shoulder around 397 nm. This broadening was attributed to the combined effects of alloy broadening and defect broadening due to enhanced surface states. The origin of the shoulder may be ascribed to DA transitions.

In reality, the exact nature of emission mechanism in semiconductor nanocrystallites is very much complex and a clear picture has not yet been emerged. Works done[51,52] in this area indicated that a significant role is played by the complicated strain distribution in the vicinity of the nanocrystallites and several fundamental mechanisms of carrier relaxation like multiphonon and Auger-like processes should be considered. Thus, the theoretical fit to the experimentally observed luminescence spectrum demands careful inclusion of all these effects.

Acknowledgements

References

1   J Gutowski, N Presser and G Kudlek *Phy Stat Solidi (a)* **120** (1990) 11

2   H Hingerl, A Pesek, H Sitter, A Krost, D R T Zahn, W Richter, G Kudlek and J Gutowski 1990 *Proc SPIE : Physical Concepts of Materials for Optoelectronic Device Applications* **1361** (1990)

3   J M Hays, W Shan, X H Yang, J J Song and E Cantwell *Semicond Sci Technol* (1992) 1470

4   A D Yoffe *Adv Phys* **42** (1993) 173

5.   W Gleiter *Nanostructured Mater* **1** (1992) 1

6   U Woggon and SV Goponenko *Phys Stat Solidi (b)* **189** (1995) 285

7   L Banyai and S W Koch *Semiconductor Quantum Dots, Series on Atomic, Molecular and Optical Physics* (World Scientific Publishing Co Singapore) **2** (1993)

8   L J Geerligs, C J Harmans and L P Kouwenhoven (Eds.) *The Physics of Few-electron Nanostructures, Physica (Utrecht)* **189 B**, (1993)

9   O N Djazovski, S Tanaka, H Kobayashi, N N Semienov and V V Pasynkov *Jpn J Appl Phys* **34** (1995) 4819

10   Y Chubachi *Thin Solid Films* **224** (1993) 184

11 W T Tsang *Semiconductors and Semimetals* (Eds: R K Willardson and A C Beer) Academic Press New York **24,** (1987) 397

12 S Schmitt-Rink, D S Chemla and D A B Milier *Advances in Physics* **38** (1989) 89

13 H Kinto, M Yagi, K Tazunori, T Yamada, H Uchiki and S Iida *J Cryst Growth* **117** (1992) 348

14 M Nagano, H Kanie, I Yoshida, M Sano and M Aoki *Jap J Appl Phys* **30** (1991) 1915

15 S Iida, T Yatabe, H Kinto and M Shinohara *J Cryst Growth* **101** (1990) 141

16 R Mach and G O Muller *J Cryst Growth* **86** (1988) 866

17 R H Mauch, R Menner and H W Schock *J Cryst Growth* **86** (1998), 885

18 W Chen, Z Wang, Z Lin and L Lin *J Appl Phys* **82** (1997) 3111

19 S M Scholz, R Vacassy, J Dutta and H Hoffmann *J Appl Phys* **83** (1998) 7860

20 M Born and E Wolf *Principles of Optics* (Pergamon Press) (1959) 664

21 C Thiandoume, O Ka, A Lusson, C Cohen, A Bouanani, M Rommeluere, A Tromson-Carli and O Gorochov *J Cryst Growth* **184/185** (1998) 149

22 I Suemune, K Yamada, H Masato, Y Kan and M Yamanishi *Appl Phys Lett* **54** (1989) 981

23 K Nakanishi, I Suemune, H Masato, Y Kuroda and M Yamanishi *Jpn J Appl Phys* **29** (1990) L2420

24 X H Yang, J M Hays, W Shan, J J Song and E Cantwell *Appl Phys Lett* **62** (1993) 1071

25 P R Newbury, K Shahzad, J Petruzello and D A Cammack *J Appl Phys* **66** (1989) 4950

26 H Hong, W A Anderson, J Haetty, A Petrou, E H Lee, H C Chang, M H Na, H Luo, J Peck and T J Mountziaris *J Appl Phys* **82** (1997) 4994

27 J Nanda, B A Kuruvilla, K V P M Shafi and D D Sarma *Physics of Semiconductor Nanostructures* (Ed. K.P Jain Narosa) New Delhi (1997) 25

28 S Banerjee, R Pal, A B Maity, S Chaudhuri and A K Pal *Nanostructured Materials* **8** (1997) 301

29 S K Mandal, S Chaudhuri and A K Pal *Nanostru Mater* **10** (1998) 607

30 S K Mandal, S Chaudhuri and A K Pal *Thin Solid Films* **350** (1999) 209

31. A Ganguly, S K Mandal, S Chaudhuri and A K Pal (comm)

32. D Bhattacharyya, S Chaudhuri and A K Pal *Vacuum* **43** (1992) 313

33 *Landolt Bornstein Numerical Data and Functional Relationships in Science and Technology* (Eds. O Madelung and M Schulz) New Series Group III Springer Verlag **22a,** 117

34 R Pal, D Bhattacharyya, A B Maity, S Chaudhuri and A K Pal *Nanostru Mater* **4** (1994) 329

35 S Schmitt-Rink, D A B Miller and D S Chemla *Phys Rev B* **35** (1987) 8113

36 L Brus *Appl Phys A,* **53** (1991) 465

37 J Allegre, G Arnaud, H Mathieu, P Lefebvre, W Granier and L Boudes *J Cryst Growth* **138** (1994) 998

38 M C Klein, F Hache, D Ricard and C Flytzanis, *Phys Rev B* **42** (1990) 11123

39 D Bhattacharyya, S K Bhattacharyya, S Chaudhuri and A K Pal *Vacuum* **43** (1992) 1201

40 T Sekikawa, H Yao, T Hayashi and T Kobayashi *Sol State Comm* **83** (1992) 969

41 M S Tyagi *Introduction to Semiconductor Materials and Devices* John Wiley & Sons (1991) 646

42a S K Mandal, D Bhattacharyya, S Chaudhuri and A K Pal *Physics of Semiconductor Nanostructures* (Ed. K P Jain, Narosa) New Delhi (1997) 37

42b S K Kulkarni, A A Khosravi, P Borse, N Deshmukh, W Vogel and J Urban *Physics of Semiconductor Nanostructures* (Ed. K P Jain) Narosa New Delhi (1997) 73

43 N Chestnoy, T D Harris, R Hull and L E Brus *J Phys Chem* **90** (1986) 3393

44 A I Ekimov, I A Kudryavtsev, M G Ivanov and Al L Efros *J Lum* **46** (1990) 83

45 M G Bawendi, P J Corroll, W L Wilson, and L E Brus *J Chem Phys* **96** (1992) 946

46. Y Osaka, K Tsunetomo, F Toyomura, H Myorer and K Kohno *Jap J Appl Phys* **31** (1992) L365

47 K Kohno, Y Osaka, F Toyomura and H Katayama *Jap J Appl Phys* **33** (1994) 6616

48 B Andrianasolo, B Champagnon, M Ferrari and N Neuroth *J Lum* **48-49** (1991) 306

49 M Danek K F Jensen, C B Murray and M G Bawendi *J Cryst Growth* **145** (1994) 714

50 F Hache, M C Klein, D Ricard and C Flytzanis *J Opt Soc America B* **8** (1991) 1802

51 S Farad, R Leon, D Leonard, J L Merz and P M Petroff *Physics Rev B* **52** (1995) 5752

52 Al L Efros, V A Kharchenko and M Rosen *Sol State Comm* **93** (1995) 281